Development of lanthanide probes for the monitoring of pH and the physiological redox environment, and insights into the crystal field



A thesis submitted for the degree of

Doctor of Philosophy

in Inorganic Chemistry

Rhodri Mir Williams

Keble College University of Oxford

October 2023

Cydnabyddiaethau

Fe dywedodd John Donne; ‘Does yr un dyn yn ynys,’ felly does yr un dim a wnaiff dyn, wedi ei gyflawni'n gyfan gwbl ganddo ef ar ei ben ei hun. Gan ystyried hynny, hoffwn i gydnabod a gwerthfawrogi cyfraniad nifer o bobl:

Yn gyntaf, hoffwn diolch yr Athro Stephen Faulkner am fy nerbyn i'r grŵp labordy, gan fy helpu i gael cyllid a goruchwylio fy ymchwil.

Yn ail, hoffwn ddiolch aelodau grŵp Faulkner am eu cwmni a'u cyngor. Fe hoffwn ddiolch Dr. Adam Sedgwick, Ms. Charlotte Simms, Mr. Eric Yang a Dr Daniel Kovacs yn arbennig am eu cyfraniad a'u cyngor. Oni bai amdanyn nhw ni fyddai Penodau 3 a 4 wedi'u gorffen ar amser. Rydwyf yn gobeithio bod ein cydweithrediad wedi bod mor ffrwythlon iddyn nhw ag yr oedd i mi.

Yn drydydd, hoffwn gydnabod Ymddiriedolaeth James Pantyfedwen ac UKRI am gyllido fy DPhil.

Hefyd, hoffwn ddiolch fy nheulu am eu cefnogaeth, eu hanogaeth a'u hamynedd dros y blynyddoedd.

Yn olaf, hoffwn ddiolch fy nyweddi a chyn bo hir i fod yn wraig, Ms. Brooke Martin, am ei chefnogaeth, ei gofal a'i hoffter di-gwestiwn dros y blynyddoedd. Hebddo, byddai'r dasg Ercwlffaidd hon wedi bod yn gwlwm Gordinaidd.

Agradecimientos

Como dijo John Donne "No hay hombre que una isla sea", es decir, los logros del hombre nunca se consiguen de forma aislada. En reconocimiento de esta verdad, quisiera agradecer a varias personas su contribución a esta tesis.

En primer lugar, me quisiera agradecer al profesor Stephen Faulkner por admitirme al grupo de laboratorio, ayudarme a obtener fondos y supervisar mi trabajo de investigación.

En segundo lugar, me gustaría dar las gracias a los miembros del grupo Faulkner por su compañía y asesoramiento. Quisiera agradecer en especial al Dr. Adam Sedgwick, a Doña Charlotte Simms, a Don Eric Yang y al Dr. Daniel Kovacs por sus aportaciones y sus consejos. Sin sus aportaciones, los capítulos 3 y 4 quizás no se hubiesen completado a tiempo. Espero que nuestra colaboración haya sido tan fructífera para ellos como lo fue para mí.

En tercer lugar, me gustaría agradecer a Ymddiriedolaeth James Pantyfedwen y a UKRI por financiar mis estudios doctorales.

Además, me gustaría agradecer a mi familia por su apoyo, aliento y paciencia a lo largo de los años.

Finalmente, me quisiera agradecer a mi prometida, Doña Brooke Martin, por su incuestionable apoyo, cuidado y afecto a lo largo de los años. Sin ella, esta tarea Hercúlea habría sido un nudo Gordiano.

Acknowledgements

John Donne said, “no man is an island”, therefore nothing made by man is truly done in isolation. In consideration of this, there are many people whose contribution I would like to acknowledge and appreciate.

Firstly, I would like to express my gratitude to Professor Stephen Faulkner for accepting me into the lab group, aiding me in obtaining funding and supervising my research.

Secondly, I would like to thank members of Faulkner group for their company and advice. I would especially like to give thanks to Dr. Adam Sedgwick, Ms. Charlotte Simms, Mr. Eric Yang and Dr. Daniel Kovacs for their collaborations and advice. Had it not been for them Chapters 3 and 4 may not been finished on time. I hope that our collaboration was as fruitful for them as it was for me.

Thirdly, I would like to acknowledge Ymddiriedolaeth James Pantyfedwen and UKRI for funding my DPhil.

Furthermore, I would like to thank my family for their support, encouragement and patience over the years.

Finally, I would like to thank my fiancée and soon to be wife, Miss. Brooke Martin, for her unquestioning support, care, and affection over the years. Without which, this Herculean task would have been a gordian knot.

Abstract

Physiological pH and redox homeostasis are both locally altered by a number of conditions including cancer and infection. These may be monitored by lanthanide probes.

The work detailed in this thesis deals with the interaction between a lanthanide probe and its local environment and how these interactions affect the crystal field of said probe. This work produced a series of pH sensitive complexes, a valid synthesis for a redox sensitive probe, a chapter on the crystal field of lanthanides and how solution structures may be obtained for lanthanide complexes by Bleaney theory.

The probes discussed in Chapter 2: On pH probes, are based on a DO3A-3-acetylpyridynyl ligand. These probes have a pH sensitivity range of pH6-10. This was characterised by fluorescence and NMR titrations. The changes in the crystal field and anisotropy of the lanthanide ion in the probe, caused by the local pH environment, are also discussed and evaluated.

Chapter 3: On redox probes, describes the synthesis for an azo dye based redox probe. This describes the successful syntheses of two redox probes in an overall good yield over 5 steps.

Chapter 4: On CF parameters, presents the idea of correlating crystal fields and ligand pKa, a solution structure for $[Eu(DTtBuMA)]^{3+}$ and considers why solution structures could not be obtained for the other analogues presented in this chapter. This was achieved by the parametrisation of the fluorescence emission spectrum of $[Eu(DTtBuMA)]^{3+}$, the calculation of the hydration number from phosphorescence decay data and the application of the Stevens parameters to the NMR spectrum of the complex by Bleaney theory of magnetic anisotropy. This was done as part of a collaboration with Dr. Adam Sedgwick and Miss Amy-Grace Berger as part of their research into paraSHIFT probes.

In conclusion, this work considers the response of lanthanide probes to the local pH and redox environment as well as how these responses alter the probes' crystal/ligand field and how the crystal field data along with Bleaney theory can be used to obtain solution structures for lanthanide complexes.

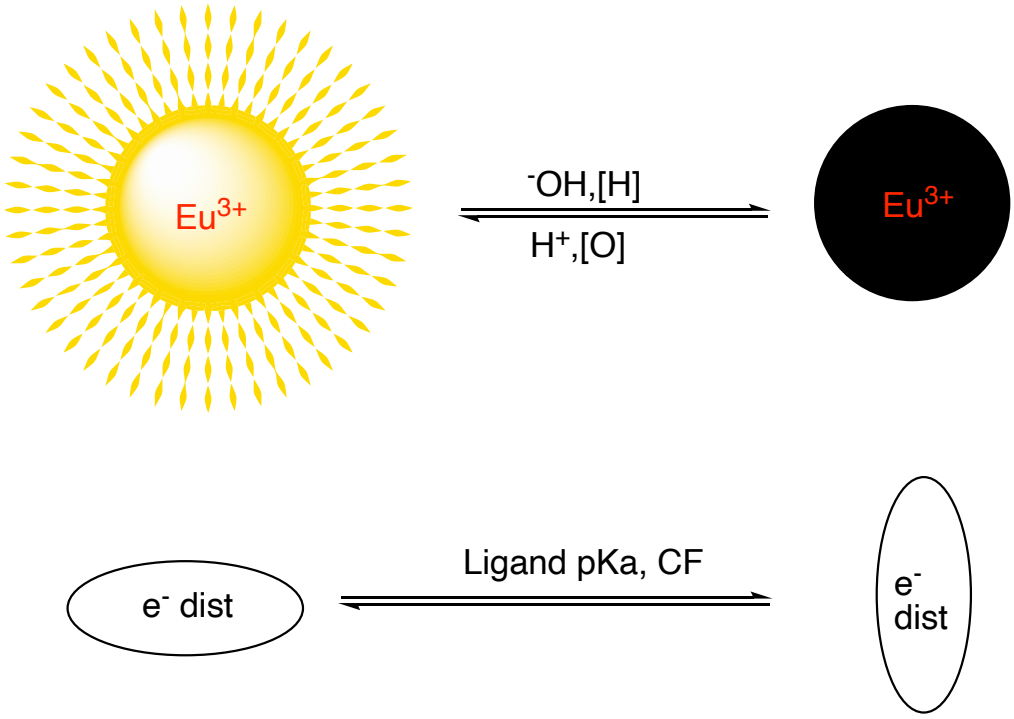


Table of Contents

Cydnabyddiaethau ..... ***I***

Agradecimientos ..... ***II***

Acknowledgements ..... ***III***

Abstract ..... ***IV***

Chapter 1: General Introduction ***1***

Lanthanoids or lanthanides? **1**

Discovery of the rare earths 1

Chemical properties **3**

Valency 3

Minerals and extraction 4

Complexation of lanthanide ions 5

DOTA based complexes 6

Luminescent and magnetic properties **8**

LS coupling 8

JJ Coupling and intermediate coupling 9

Magnetism 9

Luminescence 10

Molecular probes or sensors 12

Aims **19**

References **20**

Chapter 2: On pH probes ***26***

Introduction **26**

pH and the physiological environment 26

Lanthanide pH probes 27

Aim 31

Results and discussion 32

Ligand synthesis 32

Titrations 35

Characterisation of the conjugate base and analyses of NMR Spectra (NMR/Crystal Field analysis) 45

Conclusion 54

References 55

Chapter 3: On redox probes 58

Introduction 58

Physiological redox 58

Azo dyes 59

Redox behaviour of azo dyes 59

Aim 60

Synthesis 61

Conclusion 67

References 68

Chapter 4: On CF parameters 69

Introduction 69

CF parameters 69

Current CF-LF theories 71

Lanthanide anisotropy and parametrisation 74

Correlation of between pKa and B02 79

Effect of the lanthanide ion on the crystal field strength 82
Axial donors 82
Maximum values of $B02$ 83
Aim 84
Results and discussion 85
Analysis of luminescence spectra 85
Calculation of solution structure from NMR 85
Conclusions 91
References 92
Chapter 5: Conclusion 95
Experimental 97
General procedures 97
DO3A-tBu 99
DO3A-tBu-3-acetylpyridine (first synthesis) 101
DO3A-tBu-3-acetylpyridine 102
DO3A-3-acetylpyridine first synthesis 103
DO3A-3-acetylpyridine second synthesis 104
General method for complexation (first syntheses) 108
Eu-DO3A-3-Acetylpyridine (first synthesis) 108
Dy-DO3A-3-Acetylpyridine (first synthesis) 110
Y-DO3A-3-Acetylpyridine (first synthesis) 112
General complexation method (second syntheses) 117
Eu-DO3A-3-Acetylpyridine (second synthesis) 117
Dy-DO3A-3-Acetylpyridine (second synthesis) 120
Er-DO3A-3-Acetylpyridine 123

Sm-DO3A-3-Acetylpyridine 126

Nd-DO3A-3-Acetylpyridine 128

Gd-DO3A-3-Acetylpyridine 129

Rough titration data 130

MES, CHES, HEPES Titration 137

Excitation spectra 137

Emission spectra 139

UV-Vis spectrum of **5**Dy 141

Direct Excitation 143

Redox 149

Synthesis of 4'azidoacetophenone 149

Bromination of 4'azidoacetophenone 151

Synthesis of DO3A-tBu-1-(4'-azidophenylethanone) 155

Synthesis of DO3A-tBu-4'-aminoacetophenone 158

Synthesis of DO3A-4'-aminoacetophenone 160

Synthesis of [LuDO3A-4'-aminoacetophenone] 161

Synthesis of [Lu(4-((4-hydroxyphenyl diazenyl)phenyl)-2-oxoethyl-DO3A] 162

Synthesis of [PrDO3A-4'-aminoacetophenone]] 168

Synthesis of [Pr(4-((4-hydroxyphenyldiazenyl)phenyl)-2-oxoethyl-DO3A] 170

Complex review 172

Fluorescence spectra 172

Phosphorescencent decay 173

Complex NMR spectra and crystal structure 177

References 185

Appendix I: Crystal field parameters and pKa values for the ligands used to propose a correlation between the CF parameters and pKa. 186

Appendix II: Crystallographic data 195

[Er(DTtBuMA)]$^{3+}$ 195

[Eu(DTtBuMA)]$^{3+}$ 203

Appendix III: Unsuccessful reactions 205

pH probes: unsuccessful synthesis attempts 206

DO3A-4-acetylpyridine 206

DO3A-4-acetylpyridine 206

DO3A-4-acetylpyridine 207

Redox: Attempted 'arm' syntheses 210

Synthesis of 1-(4-((4-hydroxyphenyl)diazenyl)phenyl)ethan-1-one 210

MOM protection of OH group (1-(4-((4-(methoxymethoxy)phenyl)diazenyl)phenyl)ethan-1-one) 212

Brominations 214

Reductions of azido group 217

Chapter 1: General Introduction

Lanthanoids or lanthanides?

Lanthanides (more correctly referred as lanthanoids) are a series of 14 elements found on the first row of the f-block. They are often mistakenly referred to in the media simply as rare earth elements. This term refers to the lanthanides as well as yttrium and scandium.[1] All these elements are very similar to each other in respect of their chemistry. Due to this, they have all been classed together under the term *rare earths*. Lanthanides are usually found in nature as impurities in minerals which contain trivalent ions such as monazite,[2–4] bastnäsite[2–4] and xenotime.[3]

Discovery of the rare earths

In 1778, Lieutenant Carl Axel Arrhenius found a black rock at a quarry in the Swedish town of Ytterby.[1,5–7] In 1798, this mineral was investigated by Johan Gadolin, who discovered that 38% of the mineral was composed of an unknown substance.[5,7] He named the oxide of this substance yttria. The chemical formula of the mineral, now known as Gadolinite ($Be_2FeY_2Si_2O_{10}$),[8,9] is indeed 38% yttrium by mass. Yttrium was the first rare earth to be discovered.[5,7]

In 1803, the mineral cerite was investigated by Klaproth. He discovered that this mineral had another oxide which he named ceria.[5,10] This oxide was also independently discovered by Berzelius and Hisinger.[5]

Both the ceria and yttria produced from these minerals were further investigated by Mösander and found not to be pure metal oxides.[5] He heated a sample of cerium nitrate and found that only part of the sample dissolved in dilute nitric acid. He called the oxide, which dissolved in water, “lanthana” and the insoluble oxide, ceria.[5,10] He then further treated

lanthana (lanthanum oxide) with nitric acid and found that it gave a pink coloured solution which, he thought, contained the oxide of an element which he called didymia.[5,10–12] This 'earth' was later separated into 2 new element oxides (neodymium oxide and praseodymium oxide) by Baron von Welsbach.[5,10,12] In 1843, Mösander found that yttria, which had had all cerium oxide, lanthanum oxide and dydimia removed, contained two other oxides.[5,7,11] These were erbium oxide and terbium oxide.[1,5,6,10]

Cleve noticed that the atomic weights of samples of 'pure' erbium oxide were not consistent.[5,10,13] This suggested that the samples contained other elements.[5] This led to the discovery of two metal oxides: thulium oxide and holmium oxide.[5,10,13]

In 1878, Marignac separated ytterbium oxide from an impure sample erbium.[9] The year after, Boisboudran discovered that didymia, if basified with ammonium hydroxide, produced another 'earth'. He named this 'earth' samaria (samarium oxide).[5,10,14] In 1880, Marignac separated gadolinium oxide from a sample of the mineral samarskite ($(Y, Ce, U, Fe)_3(Nb, Ta, Ti)_5O_{16}$).[5,8,10,15]

In 1885, Von Welsbach separated didymia into neodymium oxide and praseodymium oxide.[5,12] The following year Boisboudran separated dysprosium oxide from a supposedly pure sample of holmium oxide.[5,10] In 1901, Demarçay separated europium oxide from samarium magnesium nitrate.[5,10,14,16] Six years later, Urbain separated impure ytterbium oxide into two earths, one kept the name ytterbium oxide and the other received the name lutecium oxide.[5,9,10,17]

It would not be until 1945 that promethium would be synthesised at the Oak Ridge National Lab by Marinsky, Glendenin, and Coryell.[4,18,19]

We can see in the brief history presented above that the lanthanides can be split into a 'yttrium' group and a 'cerium' group. The heavier lanthanides were all isolated from yttrium

oxide and the lighter lanthanides from cerium oxide. This makes sense as the lighter lanthanides have similar ionic radii to Ce^{3+}(1.196 Å) and heavier lanthanides have ionic radii similar to Y^{3+}(1.075 Å).[20] (see Figure 1.2)

Chemical properties

Valency

Overall, lanthanides are all chemically very similar to each other. The most common and stable oxidation state of all lanthanides is +3 (Ref.[1,21]. Most of their chemistry revolves around this oxidation state. Other oxidation states are possible, ranging from +5 to +2. The +2 oxidation state has been observed for all lanthanides[22] and +4 oxidation state has been observed for Ce, Pr, Nd, Tb and Dy.[23] The reason for +3 being the most stable oxidation state becomes apparent when comparing the ionisation energies of metals (see Figure 1.1).

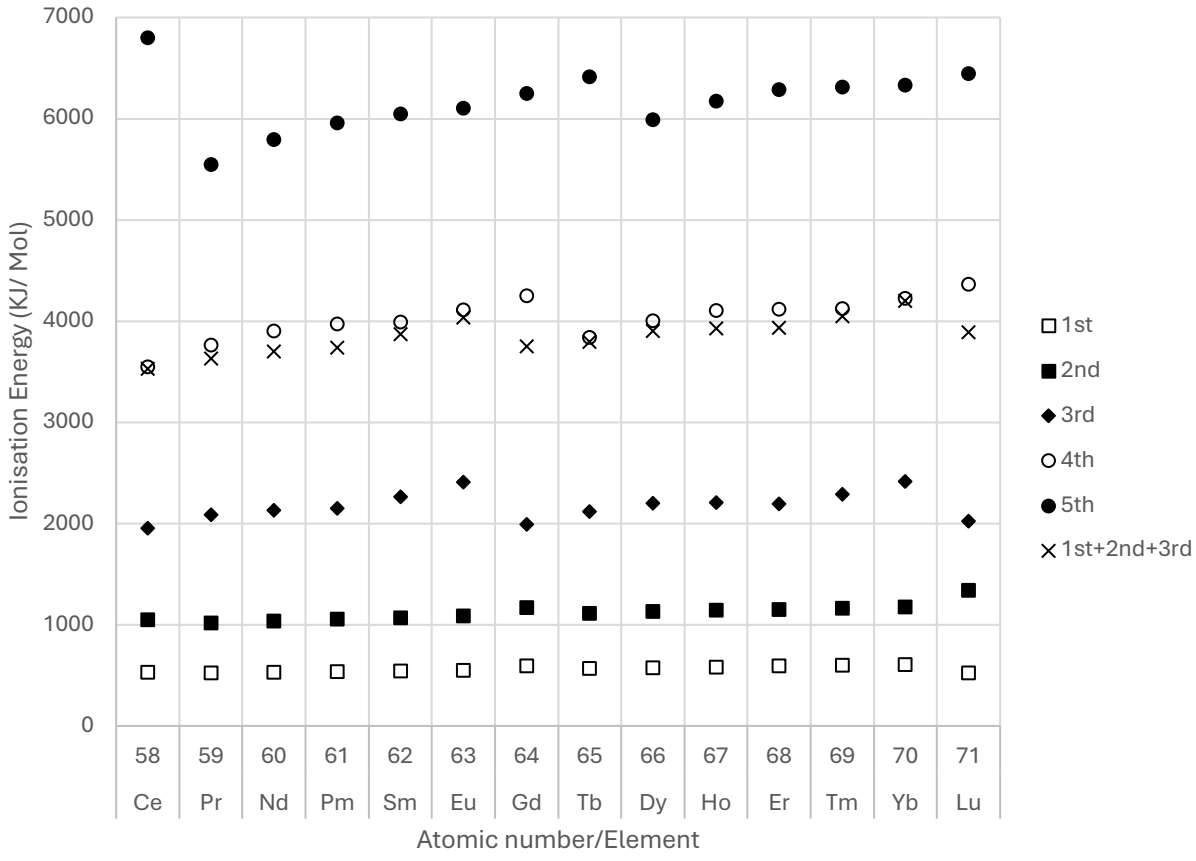


Figure 1.1: Ionisation energies of the lanthanoids.[4]

The first two ionisation energies are from electrons being removed from the outer shell of the metals (6s orbitals). These are the farthest from the nucleus and due to the low effective nuclear charge do not require much energy to be removed.[21]

The +2 oxidation state is stable in aqueous solution only for Eu(II), although it slowly oxidises to Eu(III), this is because it has a higher third ionisation energy than the rest of the lanthanides (see Figure 1.1), giving in the case of Eu(II), a half filled 4f-shell.[24,25]

Ce(IV) is stable in aqueous solution as it has a noble gas configuration (f^0).[21] This configuration can be obtained as the sum of its first three ionisation energies is very similar to that of its fourth, meaning it is within what can be provided by a chemical reaction.[24]

Pr(IV), Nd(IV), Tb(IV) and Dy(IV) and are stable in the solid state.[21,24] These have configurations of f^1, f^2, f^7 and f^8 accordingly.[21] As we can see their 4th ionisation energies (I4) are similar to the sum of the previous three, meaning that, for these elements, these oxidation states can be obtained by chemical reactions.

Pr(V) has been reported[12,21,23,26] , PrO_2^+ was detected in the mass spectroscopic analysis of Pr/O_2 in a xenon matrix.[26]

Minerals and extraction

The main ores of these metals are monazite, xenotime and bastnäsite.[25,27] These have the formulae RE-PO_4 and RE-CO_3F respectively.[4,25,27] In these minerals, the lanthanides and rare earth ions occupy square antiprismatic holes in these structures.[28] Due to the similarities in size of the RE^{3+} ions (see Figure 1.2), these ions substitute each other in these minerals and therefore these ions occur as "impurities" in these minerals.[27]

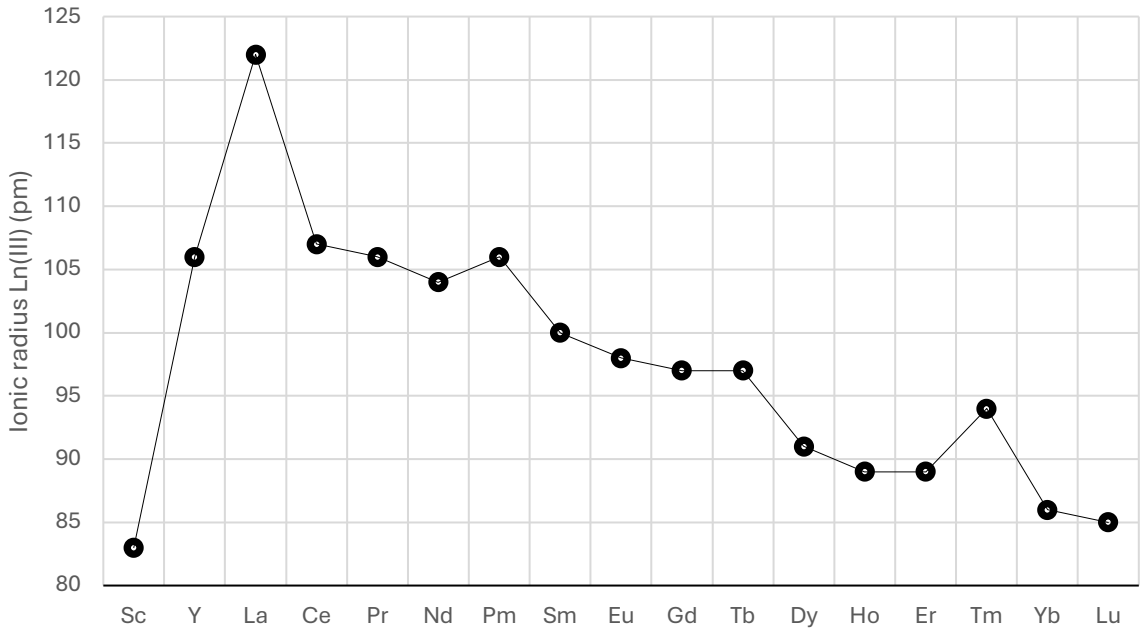


Figure 1.2: Ionic radii of the Ln(III) ions.[4]

The extraction of these minerals involves dissolving the ores in a solution of sodium hydroxide to form a slurry. This slurry is then boiled in hydrochloric acid, this causes the thorium ions found in these ores to precipitate out of solution as THO_2. [24] This chloride solution is combined with a sulfate salt and barium chloride to precipitate radium ions from the solution.[24] This results in a solution of rare earth (RE) ions.[24] These ions are separated from each other by several methods including crystallisation, solvent extraction and chromatography.[24,25]

Complexation of lanthanide ions

In solution, complexed lanthanide ions tend to form labile bonds with monodentate ligands.[24] Kinetically inert complexes can be formed by the use of "rigid" ligands such as DOTA.[29] The complexes presented in this thesis are all based on DOTA in order to obtain kinetically stable complexes.[30] If this were not the case, this would hinder the use of these complexes as probes, as free lanthanide ions are toxic and may substitute the usual metal

ions found in metalloproteins, such as calcium.[31–33] In humans, gadolinium(III) from contrast agents has been found to cause nephrogenic systemic fibrosis.[33–36]

DOTA based complexes

The lanthanide probes presented in this thesis are DOTA-based complexes. DOTA type ligands are based on cyclen (1,4,7,10-tetraazacyclododecane) which has been alkylated with residues containing carboxyl groups (see Figure 1.3).

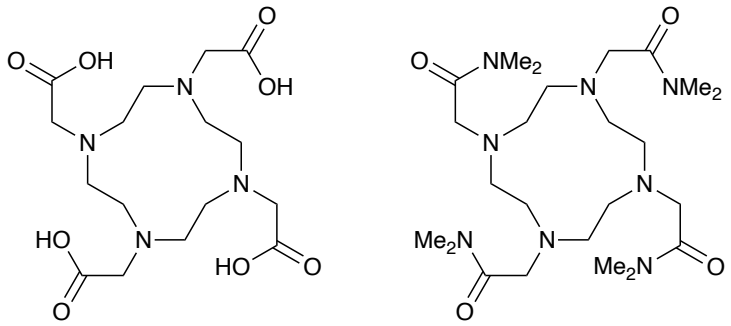


Figure 1.3 : Structural formulae of DOTA and DOTTA.

DOTA complexes form 4 exchanging conformational isomers, these being: SAP (Square Antiprismatic), CSAP (Capped SAP), TSAP (Twisted SAP) and CTSAP (Capped TSAP).[37,38] The properties of each conformer are shown in Table 1.1. The capped isomers are in fast exchange with the corresponding uncapped isomers but the SAP and TSAP isomers are in slow exchange.[37,38]

Table 1.1 : Properties of different conformational isomers of $[LnDOTA]^-$, where CN is the coordination number and q is the hydration number.[37]

	Capped	Uncapped
SAP	CN = 9, q = 1, large tilt angle	CN = 8, q = 0, large tilt angle
TSAP	CN = 9, q = 1, small tilt angle	CN = 8, q = 0, small tilt angle

The size of the cavity formed by the cyclen ring and the carboxyl groups decreases in the order CTSAP>CSAP>TSAP>SAP.[37] The ratio of TSAP to CSAP isomers in solution varies with the size of the ligated lanthanide ion.[37](See Figure 1.4) It should be noted that for lanthanide DOTA complexes, the change from $[La(DOTA)(H_2O)_x]^-$ to $[Sm(DOTA)(H_2O)_x]^-$ results in a change in the preferred conformer form CTSAP to CSAP:

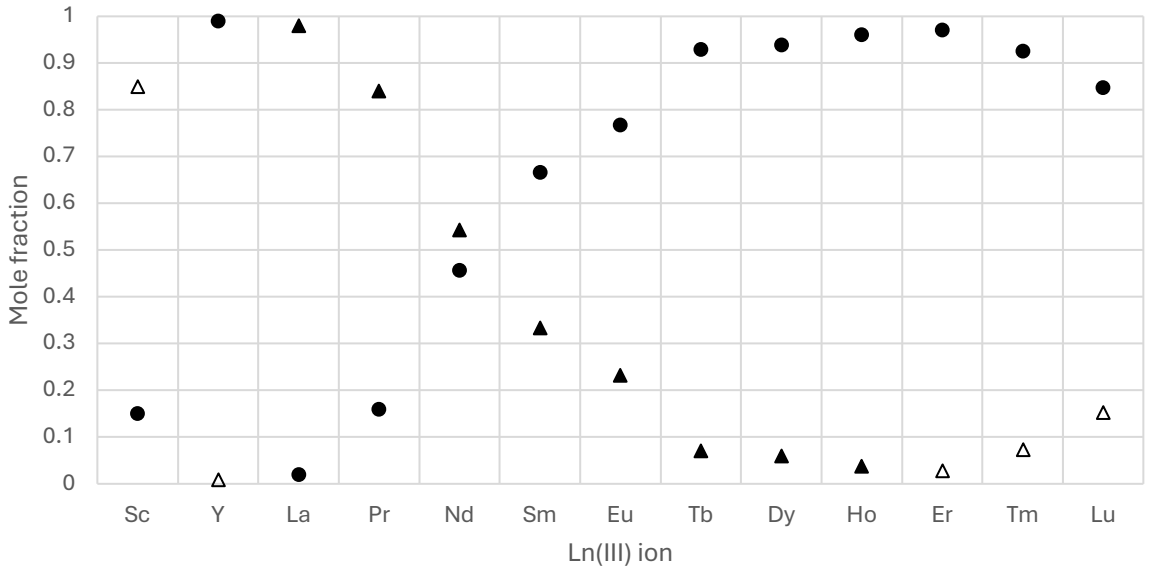


Figure 1.4: Mole fractions of different $[Ln(DOTA)(H_20)_n]$ conformers in aqueous solution. Where circular markers are CSAP, filled triangles are CTSAP and empty triangles are TSAP.[39]

However, the ligand itself may favour a particular geometry, for example, DOTA based ligands with tertiary amides (DOTTA) preferring TSAP conformations.[40] The main difference between TSAP and SAP is the tilt angle between the plane formed by the ligating oxygen ions and the ligating, this also applies to the CTSAP and CSAP conformers[37] (See Figure 1.5). The ideal square antiprism would have a tilt angle of 45° , in contrast to a twisted square antiprism which has a tilt angle closer to that found in a square prism (0°).

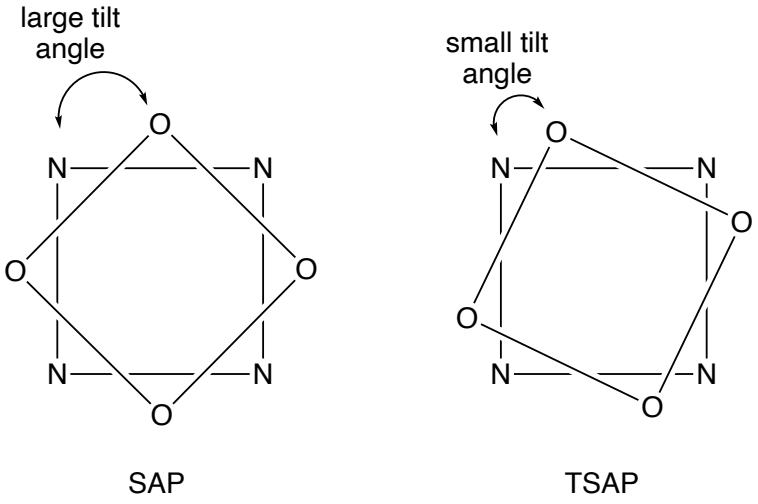


Figure 1.5 : differences between SAP and TSAP twist angles

Luminescent and magnetic properties

The main uses of lanthanide compounds, except for catalysis tend to make use of the lanthanide ions' luminescent and magnetic properties which arise from their electronic configurations.

LS coupling

LS coupling (also known as Russel-Saunders coupling) is the coupling between the spin of an electron in an atom/ion, given by S (spin quantum number) and the angular momentum of said electron, given by L (angular momentum quantum number).[41] These give rise to a number of energy levels with a quantum number J (total angular momentum quantum number) associated with each one. These take values of J = J, J-1, ...0 or 1/2.[41] For atoms/ions with less than half-filled shells: J=|S-L|, for atoms/ions with more than half-full shells: J=|S+L|. Each J state can be separated into several m_J states, these are split by the crystal field in lanthanides (this is described more thoroughly in Chapter 4: On Crystal Field Parameters).[41] These take values (separated by +1) of 0 or 1/2 to J.[41] These m_J states can then by split by the Zeeman interaction into $+m_J$ and $-m_J$ states.[41] The splitting of these energy levels for Eu^{3+} is shown in Figure 1.6. This coupling scheme is used when the spin-

orbit coupling is small in comparison to the repulsion between electrons.[42] When this is not the case the JJ Coupling scheme is used.[42]

JJ Coupling and intermediate coupling

JJ Coupling is used to describe the energy levels of heavy elements such as the actinides.[41,43] For these elements the spin-orbit coupling interaction is greater than those caused by electron repulsion.[41,43] LS coupling and JJ coupling are extremes; this must be considered when analysing fluorescence spectra.[41,42]

Magnetism

All lanthanide(III) ions except for lanthanum and lutetium have unpaired electrons. This means that all isolated Ln(III) ions are paramagnets. The magnetic susceptibility of lanthanide ions is described by Equation 1.1 as opposed to the spin only formula:[44]

Equation 1.1 : the Landé formula. Where μ_b is the Bohr magnetron.

$$\chi = g_J \mu_b \sqrt{J(J+1)}\,, g_J = \frac{3}{2} + \frac{S(S+1) - L(L+1)}{2J(J+1)}$$

This is because strong crystal/ligand fields quench the angular momentum (L) of the electrons in the d-orbitals of transition metals.[44,45] In general, in lanthanide compounds the crystal field is much weaker and so the quenching is much weaker, therefore the Landé formula is valid.[44]

The crystal field also causes stark splitting in these ions, causing them to have magnetic anisotropy when complexed.[41] This is discussed further in Chapter 4: On Crystal Field Parameters. The magnetic anisotropy of these ions seems to follow an n+7 rule where n is the number of f-electrons in the ions.[46] This rule states that different lanthanide ions in the same crystal field have the same position of their magnetic axis as the lanthanide 7 positions ahead/after of it in the series (e.g., Eu^{3+} and Yb^{3+}).[46]

Luminescence

Dexter exchange and the antenna effect

f-f transitions are weak as they are forbidden by the Laporte selection rule.[47] This rule only strictly applies to centrosymmetric complexes (i.e., those with an inversion centre).[47] The antenna effect is often used to partially circumvent this. Luminescent emission from f-f can be enhanced by means of the antenna effect.[48,49] The antenna effect is the use of a chromophore to indirectly excite a lanthanide ion by means of the dexter effect.[48,49] Figure 1.6 summarises the processes involved in the antenna effect.

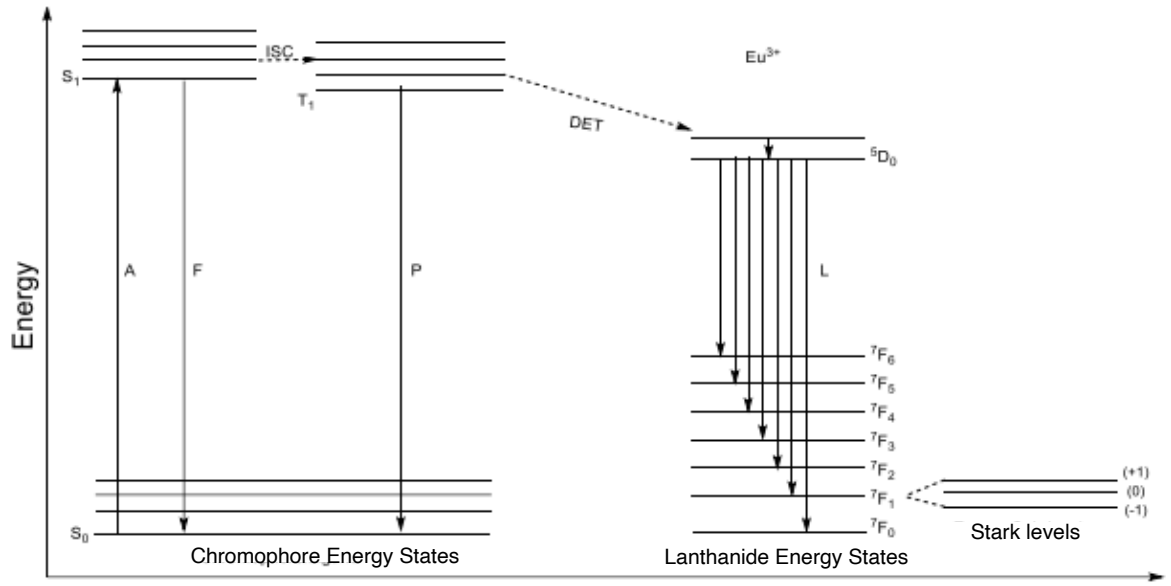


Figure 1.6: Jablonski diagram describing the antenna effect in Eu^{3+}ions.[47,50]

The antenna effect starts with the irradiation of a chromophore (A). The chromophore is excited into its singlet excited state (S_1).[47,50] The chromophore's excited state undergoes an intersystem crossing (ISC) into the chromophore's triplet state (T_1).[47,50] Then an electron from the chromophore is then exchanged with one from the lanthanide ion via Dexter Electron Transfer (DET) (as shown by Figure 1.7); this results in the chromophore returning to the ground state (S_0) and an excited lanthanide ion ($^5D_1$in the case of Eu^{3+}).[47,50,51] The ion

returns to the ground state by radiative emission (L).[47,50] Dexter electron exchange relies on a chromophore whose triplet state has a long lifetime and is higher in energy than the lanthanide ion's receptive energy level to ensure effective energy and electron transfer to the lanthanide ion, [52–54] as well as good orbital overlap between the chromophore and the lanthanide ion.[48,55]

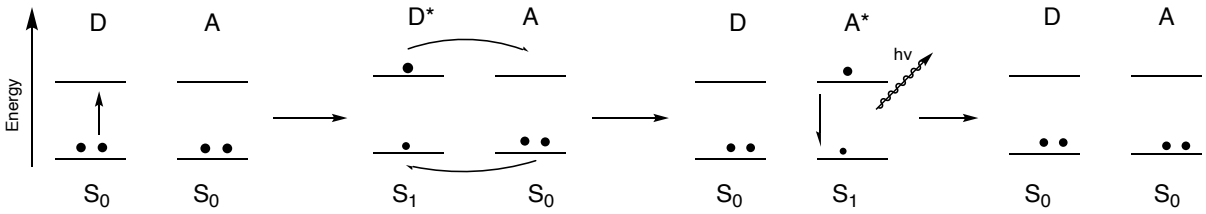


Figure 1.7 : Dexter Electron Transfer (DET) process. Where D is the orbitals of the donor species and A is the orbitals of the acceptor species, S_1 and S_0 are the excited and ground states.

In the case of europium complexes, the triplet state must be between 17,200 – 25,000 cm^{-1} above the chromophore's ground state.[50,56]

Förster exchange

Like many physiochemical phenomena (e.g. polarisation transfer via the Overhauser effect), excitation transfer may occur via a process which does not require direct physical contact between the donor species and acceptor species. In the case of electronic excitation transfer this process is referred to as Förster exchange (FRET).[57] This process relies on dipole-dipole interactions in order to transfer energy between donor and acceptor species.[57–59] The transfer rate is inversely proportional to the 6^{th} power of the distance between the species involved; in comparison to dexter exchange this is a smaller dependency on distance although FRET still requires proximity between the donor and acceptor species to be efficient.[51,57,58,60] Other properties required for a greater rate of FRET are a large spectral overlap between the donor and acceptor species, a donor species with a high radiative rate and an acceptor species with a large absorption coefficient.[57–59]

Fluorescence imaging

Fluorescence imaging is the use of a chromophore to cause specific tissues to fluoresce under upon irradiation by UV radiation to generate contrast.[61] The emission of these chromophores may vary with the cellular environment.[62] If the chromophore shows different fluorescent/phosphorescent emission in reaction to as specific substrate, these are known as optical probes/chemosensor.[53,63,64] A common example of a responsive optical probe are pH/redox indicators as these change colour in response to the chemical environment.

Molecular probes or sensors

Molecular sensors/probes are substances whose optical, magnetic and/or electrochemical change upon interaction with an analyte[63,64] These interactions may be permanent, such as the formation of a strong covalent bond or more labile, such as hydrogen bonding.[64] In order to be useful as a probe these changes must be specific for an analyte.[64] In the case of an optical probe this may be a change in the UV spectrum or fluorescent emission of the probe.[64–66] Figure 1.8 shows a probe which has specificity for fluorophosphates.[65]

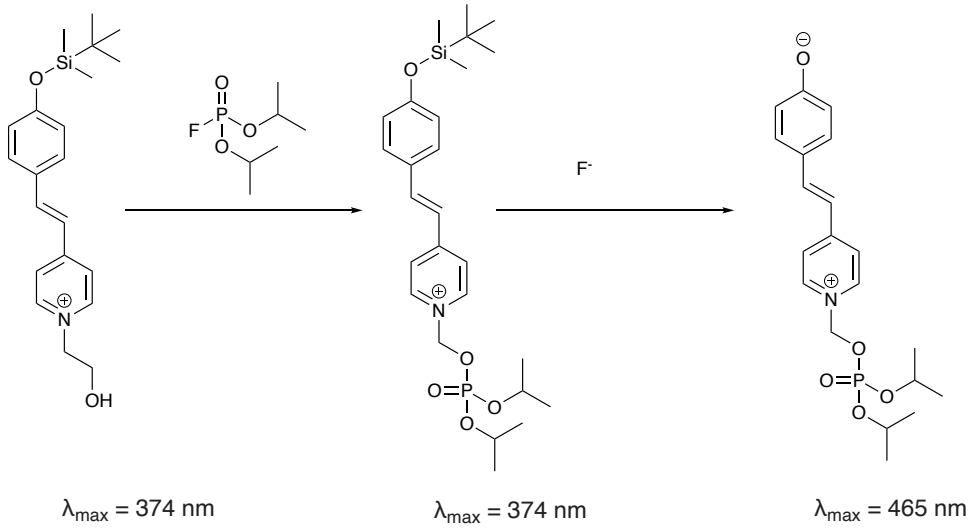


Figure 1.8: Fluorophosphate sensitive probe. λ_{max} is the point of maximum absorbance observed in the samples UV-Vis spectra between 300 nm and 700 nm.[65]

This probe works by having two interactions necessary for changes to be observed in its UV-Vis spectra.[65] The first is the binding of the fluorophosphate and the second is the hydrolysis of the silyl ether by the fluoride released when the phosphate binds the probe.[65] This causes a bathochromic shift in the probe's UV-Vis spectrum.[65] The interactions also cause a downfield shift in the NMR shifts of the aromatic protons of the probe.[65] Lanthanides combined with a chromophore can be used as chemical probes.

Lanthanide probes

Lanthanide probes are chemical sensors which are composed of two parts a lanthanide ion with specific magnetic and luminescent properties and a ligand which is sensitive to the environment around the complex.[67] These come in two general types, luminescent and magnetic probes.

Lanthanide responsive optical probes

In the case of a lanthanide optical probe, changes optical properties (i.e. fluorescence or phosphorescence) may be achieved in many ways such as changing the energy of the chromophore´s triplet state, changing the hydration number and contact with the lanthanide and transformation of the chromophore.[49,53,68,69]

Modulation of the triplet state

Dexter Electron Transfer requires a chromophore with a triplet excited state which is higher in energy than the receptive energy level of the emissive lanthanide ion.[50,56] This triplet state may be modulated in a number of ways such as the reduction or oxidation of a functional group on the chromophore.[49,54,69] This changes the efficiency of energy transfer between the chromophore and the lanthanide ion, causing the fluorescent emission from the lanthanide to be reduced or increased according to the difference in energy between thee receptive

energy level and the triplet state.[49,54,69] This varies the emission obtained from the probe depending on the amount of Figure 1.9 shows two examples of such probes.[69]

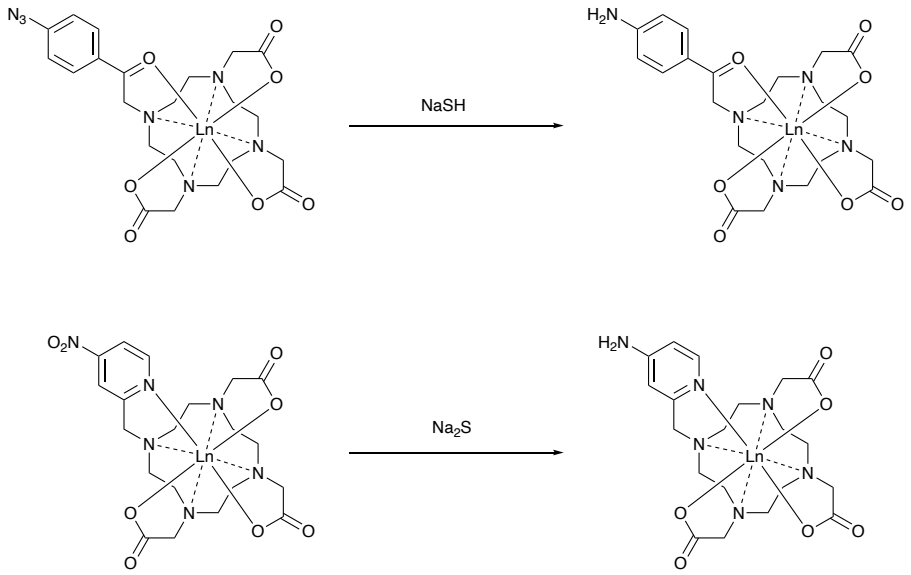


Figure 1.9 : lanthanide probes for the detection of hydrogen sulfide.[49,69] Where Ln is a lanthanide ion.

Chemical transformation of the chromophore

Another way in which the luminescent emission of a lanthanide probe may be changed is by the chemical transformation of the chromophore.[54,68–70]

Another possibility is the disruption of the Dexter electron transfer process. An example of this is shown by the probe described by Figure 1.10.[68] The emission of this probe is modulated by the interference caused by the reversible nucleophilic addition of cyanide ions to the chromophores ketone group.[68] This removes any electronic overlap between the chromophore and lanthanide ion, making it impossible for dexter electron exchange to occur.[51,68]

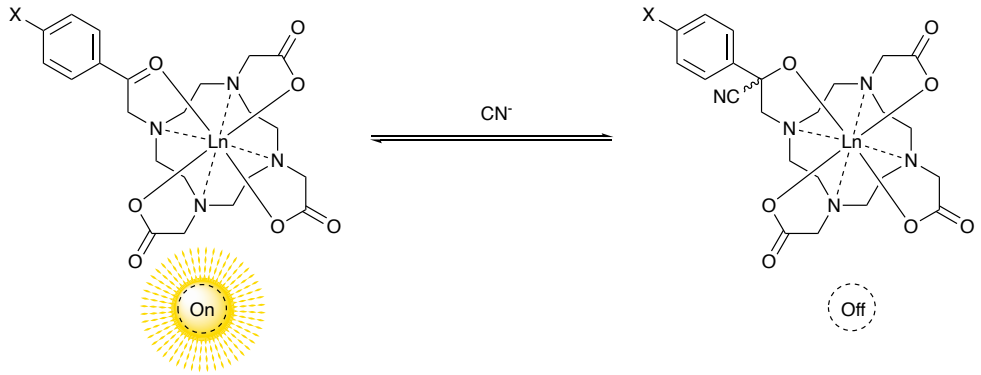


Figure 1.10: probe for detecting cyanide ions.[68] *Where Ln is a lanthanide ion and X is a halogen.*

Hydration and contact with lanthanide ion

An increase in the hydration number causes the rate of phosphorescent decay to increase due to the quenching effect of the ligated water molecule.[71–73] This will be more thoroughly covered in Chapter 2: On pH probes. The rate of Dexter Electron Transfer is dependent on the amount of overlap between the lanthanide ion and the chromophore and the distance between them.[48,51,60] An example of this is seen in Figure 1.10.

Magnetic probes

Magnetic probes are those whose magnetic properties (i.e. anisotropy, relaxivity and NMR spectrum) change in response to the local chemical environment. These include relaxivity, paraCEST and paraSHIFT probes.

MRI

Magnetic resonance imaging is a non-invasive scanning technique which makes use of the. Magnetic resonance of protons in water to generate an image, which may be used to diagnose a patient.[74] This technique may require a contrast agent in order to produce useful images of rapidly moving fluids such as blood as shown by Figure 1.11 where blood vessels can be seen as small white lines.[75]

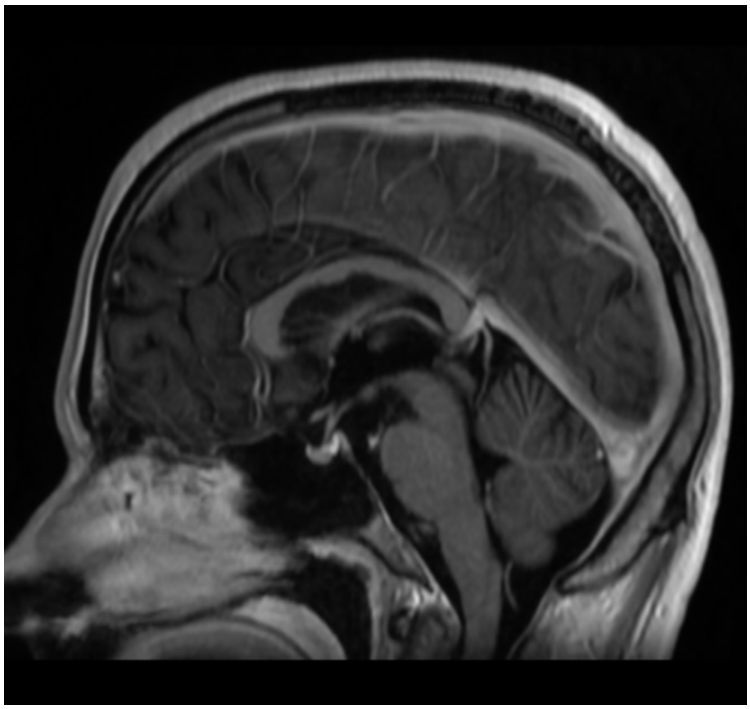


Figure 1.11 : Sagittal MPR MRI of a patient with contrast. Blood vessels appear as small white lines . MRi performed at the Churchill Hospital's radiology department, Oxford University Hospitals, Oxford.

paraCEST

Chemical Exchange Saturation transfer (CEST) is the use of a molecule with a functional group which is able to exchange protons with water to produce a chemical shift separate from that of the bulk water.[76,77] These labile proton groups must have a slow exchange regime.[76,77] Paramagnetic Chemical Exchange Saturation Transfer (paraCEST) is the use a CEST agent which has a paramagnetic ion.[76] These agents use the pseudocontact interaction to increase the magnitude of the shift of the labile proton with respect to bulk water.[76] CEST agents will usually alter the labile proton shifts within 5 ppm of the water shift while paraCEST agents can alter the chemical shift by several hundred ppms.[76]

ParaSHIFT

A paraSHIFT probe is one which uses the alteration of the chemical shifts by the change in the size of the pseudocontact interaction experienced by that proton[78] (an explanation of

the pseudo contact interaction as parametrised by Bleaney is to be found in Chapter 4: On Crystal Field Parameters). This may be caused by changes in the position of said proton in relation to the paramagnetic metal centre or changes in the crystal field.[78] To make this change in the chemical shifts more sensitive, tert-butyl and methyl groups on the molecule are used as reporter groups.[78]

Relaxivity probes

For the diagnosis of several conditions MRI is used as described in section MRI. Contrast agents are used to increase the relaxation rate of the water protons in physiological tissue.[36] This depends on the concentration of the probe in the tissue, the amount of water molecules bound to the contrast agent's lanthanide ion (usually gadolinium) and the tumbling rate of the contrast agent.[36] Equations 1.2 and 1.3 show how the proton relaxation rate is affected by these factors.

Equation 1.2 : Longitudinal relaxation rate formula.[79] Where T1 is the longitudinal relaxation time, $T_{1,d}$ is the diamagnetic longitudinal relaxation time, r_1 is the longitudinal relaxivity and [Gd] is the concentration of the contrast agent.

$$\frac{1}{T_1} = \frac{1}{T_{1,d}} + r_1[Gd]$$

Probes whose relaxivity is altered by the local chemical environment may change their hydration number or their tumbling rate amongst other factors.[34,54,79]

Equation 1.3 : Longitudinal relaxivity of contrast agent. Where r_{1IS} and r_{1OS} are the inner and outer sphere relaxivities, q is the hydration number, $[H_2O]$ is the concentration of the water in the solution, T_{1M} is the longitudinal relaxation rate of the bound water molecule and τ_m is the residence time of the water molecule on the complex. The longitudinal relaxation rate of the bound water molecule is inversely proportional to the tumbling rate. [79]

$$r_1 = r_{1IS} + r_{1OS}$$

Where:

$$r_{1IS} = \frac{q/[H_2O]}{T_{1m} + \tau_m}$$

An example of the concentration of complex being of diagnostic tool, is the dating of MS lesions as active or recently active lesions allow the contrast agents to cross the blood brain barrier.[80] Figure 1.12 shows an example of one such enhancement.

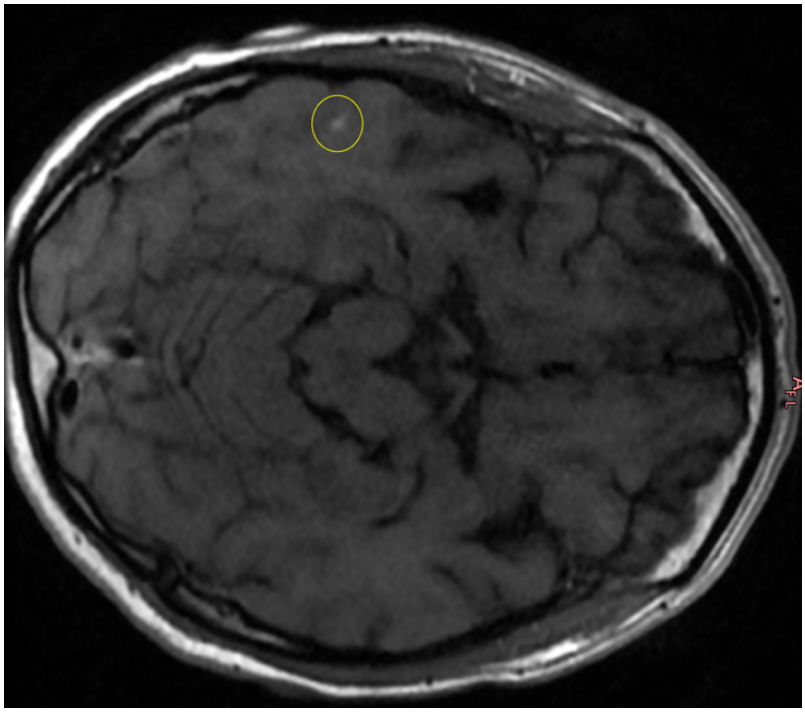


Figure 1.12 : T1 weighted MRI of a patient with an active MS lesion circled in yellow. MRi performed at Churchill Hospital's radiology department, Oxford University Hospitals, Oxford.

In Figure 1.12 we see a small white spot (yellow circle) and some lighter patches on the lower left hemisphere. These are regions where the contrast agent has crossed the blood brain barrier due to active demyelination events being present.[80]

Hyperpolarised MRI

In order to observe a number of metabolic processes (including changes in pH), hyperpolarised 13C probes may be of use.[81] These probes work by making use of dynamic nuclear polarisation (DNP) (See Figure 1.13) to produce and Overhauser effect between the ^{13}C nuclei and unpaired electrons from free radicals which may be produced by neurodegenerative conditions.[81,82]

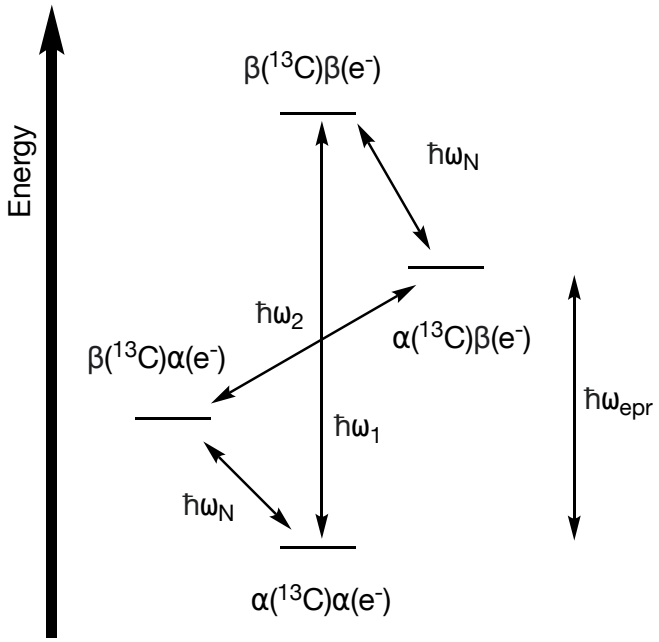


Figure 1.13 : Energy transitions involved in DNP.[82] Where α is uninverted spin, β isinverted spin, ω_N is the nuclear larmor frequency, ω_{epr} is the electronic Larmor frequency, ω_1 is the sum of the nuclear and Larmor frequencies and ω_2 is the subtraction of the nuclear from the electronic Larmor frequency and ħ is the reduced Planck's constant.

Aims

The aims of the work presented in this thesis are to synthesize probes for the monitoring of the physiological pH and redox environments and to consider the relation between the crystal field and ligand chromophore with the physical (i.e. luminescence spectra, NMR spectra) and chemical (i.e. pKa, redox) properties of the probes.

References

1 G. Deng, *Nat Chem*, 2018, **10**, 110–110.

2 M. Willbold, ed. W. M. White, Springer International Publishing, Cham, 2018.

3 F. Xie, T. A. Zhang, D. Dreisinger and F. Doyle, *Miner Eng*, 2014, **56**, 10–28.

4 J. Emsley, *The elements*, Oxford University Press, Third., 1998.

5 M. E. Weeks, *The discovery of the elements, the rare earths*, 1945, 414–438.

6 C. Piguet, *Nat Chem*, 2014, **6**, 370–370.

7 P. Dinér, *Nat Chem*, 2016, **8**, 192–192.

8 J. Emsley, *The Elements*, Oxford University Press, Oxford, 3rd edn., 1998.

9 A. Skelton and B. F. Thornton, *Nat Chem*, 2017, **9**, 402–402.

10 M. R. Ganjali, V. K. Gupta, F. Faridbod and P. Norouzi, in *Lanthanides Series Determination by Various Analytical Methods*, Elsevier, 2016, pp. 1–36.

11 B. F. Thornton and S. C. Burdette, *Nat Chem*, 2019, **11**, 188–188.

12 A. Dingle, *Nat Chem*, 2018, **10**, 576–576.

13 J. L. Marshall, *The Hexagon*, 2015, 72–77.

14 S. Strekopytov, *Nat Chem*, 2016, **8**, 816–816.

15 P. Pyykkö, *Nat Chem*, 2015, **7**, 680–680.

16 E. Demarçay, *Comptes rendus*, 1901, **132**, 1484–1486.

17 L. Öhrström, *Nat Chem*, 2018, **10**, 372–372.

18 J. A. Marinsky, L. E. Glendenin and C. D. Coryell, *J Am Chem Soc*, 1947, **69**, 2781–2785.

19 S. Cantrill, *Nat Chem*, 2018, **10**, 1270–1270.

20 R. D. Shannon, *Acta Crystallographica Section A*, 1976, **32**, 751–767.

21 D. A. Johnson and P. G. Nelson, *Found Chem*, 2018, **20**, 15–27.

22 M. R. Macdonald, J. E. Bates, J. W. Ziller, F. Furche and W. J. Evans, *J Am Chem Soc*, 2013, **135**, 9857–9868.

23 T. P. Gompa, A. Ramanathan, N. T. Rice and H. S. La Pierre, *Dalton Transactions*, 2020, **49**, 15945–15987.

24 N. Kaltsoyannis and P. Scott, *The F elements*, Oxford University Press, 1st edn., 1999.

25 H. C. Aspinall, *Chemistry of the f-block elements*, Gordon and Breach Science Publishers, 2001, vol. 5.

26 Q. Zhang, S.-X. Hu, H. Qu, J. Su, G. Wang, J.-B. Lu, M. Chen, M. Zhou and J. Li, *Angewandte Chemie*, 2016, **128**, 7010–7014.

27 D. Kołodyńska, D. Fila, B. Gajda, J. Gęga and Z. Hubicki, in *Applications of Ion Exchange Materials in the Environment*, Springer International Publishing, Cham, 2019, pp. 161–185.

28 Y. Ni, J. M. Hughes and A. N. Mariano, *American Mineralogist*, 1995, **80**, 21–26.

29 T. J. Sørensen and S. Faulkner, *Acc Chem Res*, 2018, **51**, 2493–2501.

30 J. C. Rodriguez-Ubis and E. Brunet, in *Encyclopedia of Metalloproteins*, Springer New York, 2013, pp. 1077–1087.

31 K. Nesmerak, in *Encyclopedia of Metalloproteins*, eds. R. H. Kretsinger, V. N. Uversky and E. A. Permyakov, Springer New York, New York, NY, 2013, pp. 1091–1097.

32 K. Nesmerak, in *Encyclopedia of Metalloproteins*, eds. R. H. Kretsinger, V. N. Uversky and E. A. Permyakov, Springer New York, New York, NY, 2013, pp. 1098–1101.

33 H. S. Thomsen, S. K. Morcos, T. Almén, M.-F. Bellin, M. Bertolotto, G. Bongartz, O. Clement, P. Leander, G. Heinz-Peer, P. Reimer, F. Stacul, A. van der Molen, J. A. W. Webb and ESUR Contrast Medium Safety Committee, *Eur Radiol*, 2013, **23**, 307–18.

34 V. Jacques, S. Dumas, W.-C. Sun, J. S. Troughton, M. T. Greenfield and P. Caravan, *Invest Radiol*, 2010, **45**, 613–624.

35 Y. Forslin, S. Shams, F. Hashim, P. Aspelin, G. Bergendal, J. Martola, S. Fredrikson, M. Kristoffersen-Wiberg and T. Granberg, *American Journal of Neuroradiology*, 2017, **38**, 1311–1316.

36 L. M. De León-Rodríguez, A. F. Martins, M. C. Pinho, N. M. Rofsky and A. D. Sherry, *Journal of Magnetic Resonance Imaging*, 2015, **42**, 545–565.

37 S. Aime, M. Botta, M. Fasano, M. P. M. Marques, C. F. G. C. Geraldes, D. Pubanz and A. E. Merbach, *Inorg Chem*, 1997, **36**, 2059–2068.

38 S. Hoeft and K. Roth, *Chem Ber*, 1993, **126**, 869–873.

39 S. Aime, M. Botta and G. Ermondi, *Inorg Chem*, 1992, **31**, 4291–4299.

40 K. J. Miller, A. A. Saherwala, B. C. Webber, Y. Wu, A. D. Sherry and M. Woods, *Inorg Chem*, 2010, **49**, 8662–8664.

41 W. G. Richards and P. R. Scott, *Structure and spectra of atoms*, John Wiley & Sons, Ltd., London, 1976.

42 C. W. Haigh, *J Chem Educ*, 1995, **72**, 206.

43 T. P. Softley, *Atomic spectra*, Oxford University Press, Oxford, 1st edn., 1994.

44 R. Skomski, P. Manchanda and A. Kashyap, in *Handbook of Magnetism and Magnetic Materials*, Springer International Publishing, 2021, pp. 1–83.

45 J. H. van Vleck, *Physical Review*, 1937, **52**, 1178–1198.

46 M. Briganti, E. Lucaccini, L. Chelazzi, S. Ciattini, L. Sorace, R. Sessoli, F. Totti and M. Perfetti, *J Am Chem Soc*, 2021, **143**, 8108–8115.

47 K. Binnemans, *Coord Chem Rev*, 2015, **295**, 1–45.

48 A. K. R. Junker, L. R. Hill, A. L. Thompson, S. Faulkner and T. J. Sørensen, *Dalton Transactions*, 2018, **47**, 4794–4803.

49 A. G. Cosby, J. J. Woods, P. Nawrocki, T. J. Sørensen, J. J. Wilson and E. Boros, *Chem Sci*, 2021, **12**, 9442–9451.

50 C. Spangler and M. Schäferling, *Lanthanide Luminescence chemical sensors*, Springer Berlin Heidelberg, Berlin, Heidelberg, 2011, vol. 7.

51 D. L. Dexter, *J Chem Phys*, 1953, **21**, 836–850.

52 J.-C. G. Bünzli and S. V. Eliseeva, in *Lanthanide Luminescence. Springer Series on Fluorescence, vol 7, Basics of lanthanide photophysics*, eds. P. Hänninen and H. Härmä, Springer, Berlin, Heidelberg, Berlin, Heidelberg, 2010, pp. 1–45.

53 D. Parker, J. D. Fradgley and K.-L. Wong, *Chem Soc Rev*, 2021, **50**, 8193–8213.

54 M. C. Heffern, L. M. Matosziuk and T. J. Meade, *Chem Rev*, 2014, **114**, 4496–4539.

55 A. D. McNaught and A. Wilkinson, *IUPAC Compendium of Chemical Terminology*, 1997.

56 F. S. Richardson, *Chem Rev*, 1982, **82**, 541–552.

57 In *The IUPAC Compendium of Chemical Terminology*, International Union of Pure and Applied Chemistry (IUPAC), Research Triangle Park, NC, 2014.

58 A. J. Mork, M. C. Weidman, F. Prins and W. A. Tisdale, *The Journal of Physical Chemistry C*, 2014, **118**, 13920–13928.

59 C. Chen, L. Ao, Y. Wu, V. Cifliku, M. Cardoso Dos Santos, E. Bourrier, M. Delbianco, D. Parker, J. M. Zwier, L. Huang and N. Hildebrandt, *Angewandte Chemie International Edition*, 2018, **57**, 13686–13690.

60 McNaught A. and Wilkinson A., *The IUPAC Compendium of Chemical Terminology*, International Union of Pure and Applied Chemistry (IUPAC), Research Triangle Park, NC, 2019.

61 D. W. Piston, G. H. Patterson, J. Lippincott-Schwartz, N. S. Claxton and M. W. Davidson, Introduction to fluorescent proteins, https://www.microscopyu.com/applications/live-cell-imaging/introduction-to-fluorescent-proteins, (accessed 22 August 2023).

62 A. Ettinger and T. Wittmann, *Methods Cell Biol*, 2014, **123**, 77–94.

63 R. Martínez-Máñez, *ChemistryOpen*, 2014, **3**, 232–232.

64 J. Krämer, R. Kang, L. M. Grimm, L. De Cola, P. Picchetti and F. Biedermann, *Chem Rev*, 2022, **122**, 3459–3636.

65 S. El Sayed, L. Pascual, A. Agostini, R. Martínez-Máñez, F. Sancenón, A. M. Costero, M. Parra and S. Gil, *ChemistryOpen*, 2014, **3**, 142–145.

66 M. A. Caldwell, C. R. Brue, T. J. Whittemore and T. J. Meade, *RSC Adv*, 2020, **10**, 8994–8999.

67 J.-C. G. Bünzli, *Chem Rev*, 2010, **110**, 2729–2755.

68 J. D. Routledge, X. Zhang, M. Connolly, M. Tropiano, O. A. Blackburn, A. M. Kenwright, P. D. Beer, S. Aldridge and S. Faulkner, *Angewandte Chemie International Edition*, 2017, **56**, 7783–7786.

69 M. Tropiano and S. Faulkner, *Chem. Commun.*, 2014, **50**, 4696–4698.

70 M. A. Caldwell, C. R. Brue, T. J. Whittemore and T. J. Meade, *RSC Adv*, 2020, **10**, 8994–8999.

71 W. D. Horrocks and D. R. Sudnick, *Acc Chem Res*, 1981, **14**, 384–392.

72 R. M. Supkowski and W. DeW. Horrocks, *Inorganica Chim Acta*, 2002, **340**, 44–48.

73 D. Parker, *Coord Chem Rev*, 2000, **205**, 109–130.

74 National Institute of Biomedical Imaging and Bioengineering (NIBIB), MRi, https://www.nibib.nih.gov/science-education/science-topics/magnetic-resonance-imaging-mri, (accessed 22 August 2023).

75 G. Morana, C. Cugini, G. Scatto, R. Zanato, M. Fusaro and A. Dorigo, *Cancer Imaging*, 2013, **13**, 350–359.

76 I. Hancu, W. T. Dixon, M. Woods, E. Vinogradov, A. D. Sherry and R. E. Lenkinski, *Acta radiol*, 2010, **51**, 910–923.

77 P. C. M. Van Zijl and N. N. Yadav, *Magn Reson Med*, 2011, **65**, 927–948.

78 P. Harvey, A. M. Blamire, J. I. Wilson, K.-L. N. A. Finney, A. M. Funk, P. K. Senanayake and D. Parker, *Chem Sci*, 2013, **4**, 4251.

79 S. Dumas, V. Jacques, W.-C. Sun, J. S. Troughton, J. T. Welch, J. M. Chasse, H. Schmitt-Willich and P. Caravan, *Invest Radiol*, 2010, **45**, 600–612.

80 M. A. Sahraian and E.-W. Radue, in *MRI Atlas of MS Lesions*, eds. EW. Radü and M. Sahraian, Springer Berlin Heidelberg, Berlin, Heidelberg, 2007, pp. 45–74.

81 V. Z. Miloushev, K. R. Keshari and A. I. Holodny, *Topics in Magnetic Resonance Imaging*, 2016, **25**, 31–37.

82 G. Parigi, E. Ravera, M. Bennati and C. Luchinat, *Mol Phys*, 2019, **117**, 888–897.

Chapter 2: On pH probes

Introduction

pH and the physiological environment

pH is a parameter which describes the negative logarithm of concentration of protons in solution.[1] pH is an important indicator of the health of a tissue.[2,3] Physiological pH is affected by a number of ailments[4] including cancer,[3,5,6] vaginosis,[7,8] and traumatic brain injury.[9,10] The extracellular pH of healthy human cells and blood lies between pH 7.2 and 7.4, but in cancerous tissue, the extracellular pH becomes acidic. In the case of vaginosis, an alkaline pH[7,8] is a marker for infection, whilst an acidic pH is a sign of a healthy pelvic organ.[7] The cerebrospinal fluid of a healthy brain has a pH is around 7.3.[11] In a trauma injured brain, the pH of the fluid becomes more acidic.[10]

Acidosis

Acidosis is the increased acidity of blood and other physiological tissues.[12] There are a number of causes for this imbalance, including renal, respiratory ailments and diet.[12] It may also occur in localised tissue due to inflammation,[12] hypoxia,[13] and tumours.[14] There are two types of acidosis respiratory and metabolic.

Metabolic acidosis is caused by a myriad of conditions including chronic kidney disease[15] and cancer.[16] Respiratory acidosis can be caused by insufficient pulmonary ventilation.[17] Lactic acidosis is caused by the overproduction and/or impaired metabolization of lactate.[17] It is usually confirmed by measuring the concentration of lactate in the serum in question.[17]

Alkalosis

Alkalosis is the decreased concentration of hydrogen ions in physiological fluids leading to a pH higher than the normal pH for that fluid.[17–19] In the case of blood, this is below pH 7.45.

(Ref.20) This condition is common in people who are in intensive care units.[20,21] Alkalosis is caused by an increase in the bicarbonate concentration in blood, which in turn causes the concentration of chloride ions to decrease and the Cl^-:Na^+ to be less 1:1.4. (Ref.20) The increased intake of sodium bicarbonate, vomiting and breathing more than required for the activity being performed, are amongst the causes of this condition.[19]

Lanthanide pH probes

Lanthanide probes are lanthanide complexes which show a change in luminescent or magnetic resonance in response to its local physiological environment. These can be split into two general categories: optical and magnetic resonance probes.[22] The physical requirements of these probes and the antenna effect have been described in Chapter 1: General Introduction. pH may alter the emission intensity and NMR behaviour of a lanthanide probe in a number of ways. These include modifying the hydration number,[23] separating the antenna chromophore from the lanthanide ion,[24] protonation,[25] and the formation of an enol.[26]

Modifying the hydration number

The hydration number (q) is the number of water molecules bound on to the metal centre.[22,27] The value for europium complexes can be calculated by use of the modified Horrocks equation as shown in Equation 2.1.[28–30]

$$q = 1.2\left(\frac{1}{t_{H_20}} - \frac{1}{t_{D_20}} - 0.25\right)$$

Equation 2.1 : Horrocks equation as presented in Ref.[30]. Where q is the hydration number, t_{H2O} and t_{H2O} are the emission lifetimes in water and deuterium oxide.

The emission intensity is inversely affected by the hydration number as it shortens the emission lifetimes.[22,27,29] This is due to the bound water molecules providing a non-emissive pathway for deexcitation of the excited state of the metal centre.[27,29] This pathway de-excites the metal centre by vibrations of the O-H bond.[27] Equation 2.1 gives a value for q by comparing the lifetimes of emission of the complex in D_2O and H_2O. The reason for the difference in lifetimes in D_2O and H_2O lies in the difference in the energy of vibrionic energy levels between the hydrogen and deuterium atoms in the O-H bond and the O-D.[27] This causes de-excitation to be less effective if D_2O is the axial ligand than if it is H_2O.[27]

The hydration number is important for magnetic resonance probes as its relaxivity increases with its hydration number.[22]

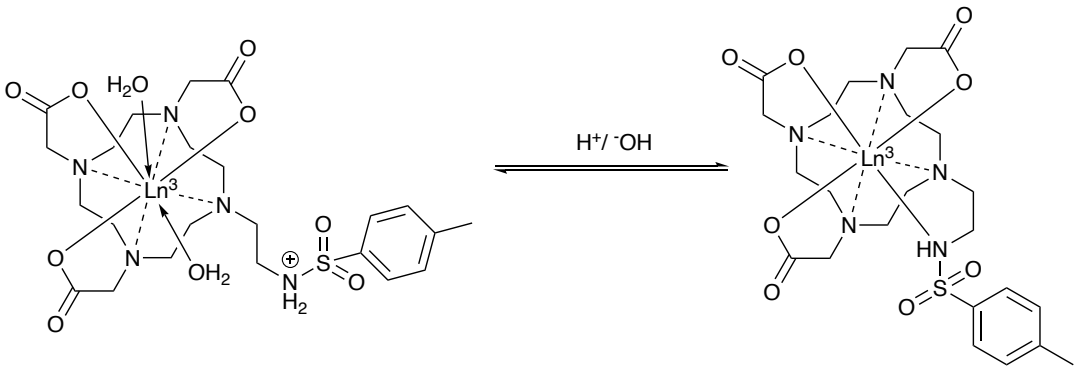


Figure 2.1 : Dual magnetic resonance/optical probe.[23,24]

Figure 2.1 shows a magnetic resonance probe which makes use of a change in hydration with pH. The increase in pH changes the hydration from q = 2 to q = 0, this increases the rate of longitudinal relaxation. [23]

Separation of the chromophore

In Figure 2.1 we saw how the protonation of a sulfonamide ligand is used to make relaxivity probe.[23] This same process resulted in the luminescent emission of the europium analogue of the sulfonamide probe to increase as pH decreases, due to the chromophore being pulled away from the lanthanide.[23,24] This causes a decrease in the efficiency of indirect excitation causing a reduction in fluorescent emission.[24] The same process changed the rate of phosphorescent emission decay of the probe, allowing for the hydration numbers to be quantified via the Horrocks equiation.[23,24] There are many such examples of pH responsive lanthanide probes which interact in a similar way.

Protonation of the chromophore

Protonation of a pyridine based chromophore has been used to synthesise a pH probe (see Figure 2.2).[25] This probe has its fluorescent emission intensity and NMR shifts altered by the protonation of the probe's pyridyl chromophore.[25] The protonation of pyridyl chromophore causes an hypsochromic shift in the probe's UV-Vis spectrum due to changes in the

chromophore's electronic structure.[25,31] This leads to a decrease in luminescent emission with an increase in pH.[25] The NMR spectrum showed an increase in the absolute size of the paramagnetic contribution to the chemical shifts with an increase in pH.[25]

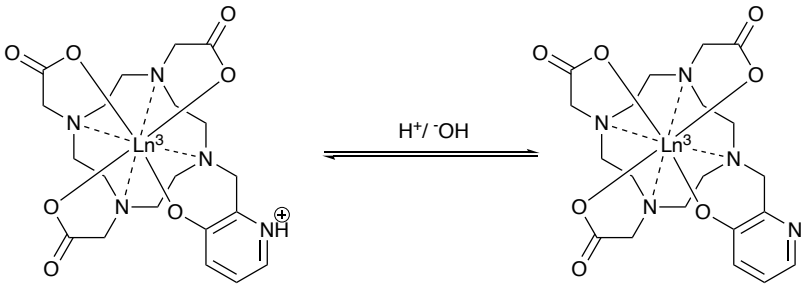


Figure 2.2: Optical probe whose fluorescent emissoin is altered by protonation.[25]

Formation of an enol

The ligand system around a lanthanide ion may form and enol at higher pH conditions (see Figure 2.3).[26] These can have a significant effect paraCEST behaviour of a probe. [26] This is due the formation of the enol causing changes in the chemical shift of water molecules,[26] possibly due to changes in the crystal field due to the increase in the number of another anionic ligand. This probe also showed a bathochromic shift in its UV-Vis spectrum as pH was increased.[26]

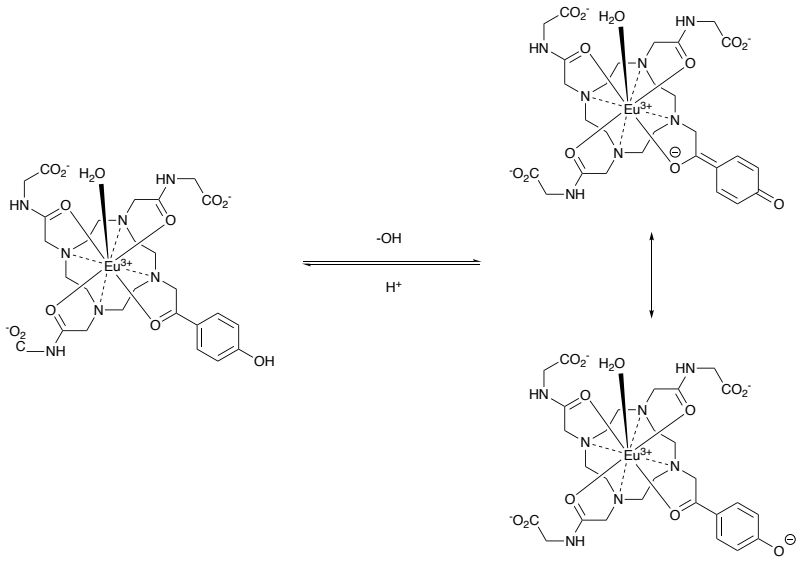


Figure 2.3 : 3-hydroxypyridine probe whose paraCEST behaviour is modulated by the formation of an enol.[26]

Aim

The aim of this work is to produce pH probes based on a DO3A-3-acetylpyridine ligand and assess its pH sensitivity range for use as a pH probe for use for measuring physiological pH. 3-acetylpyridine was selected as a chromophore because its UV-vis spectrum shows absorptions at 225 nm (42,553 cm^{-1}) and 265 nm (37,736 cm^{-1}) this is above the 17,200 cm^{-1} required for efficient dexter exchange between the chromophore and a Eu^{3+}. [32–34]

These probes are expected to show changes in luminescence and their NMR spectra with pH as it has the possibility of forming a ketal or an enol by nucleophilic addition or deprotonation respectively. We will also determine whether either or both occur under basic conditions (see Figure 2.4).

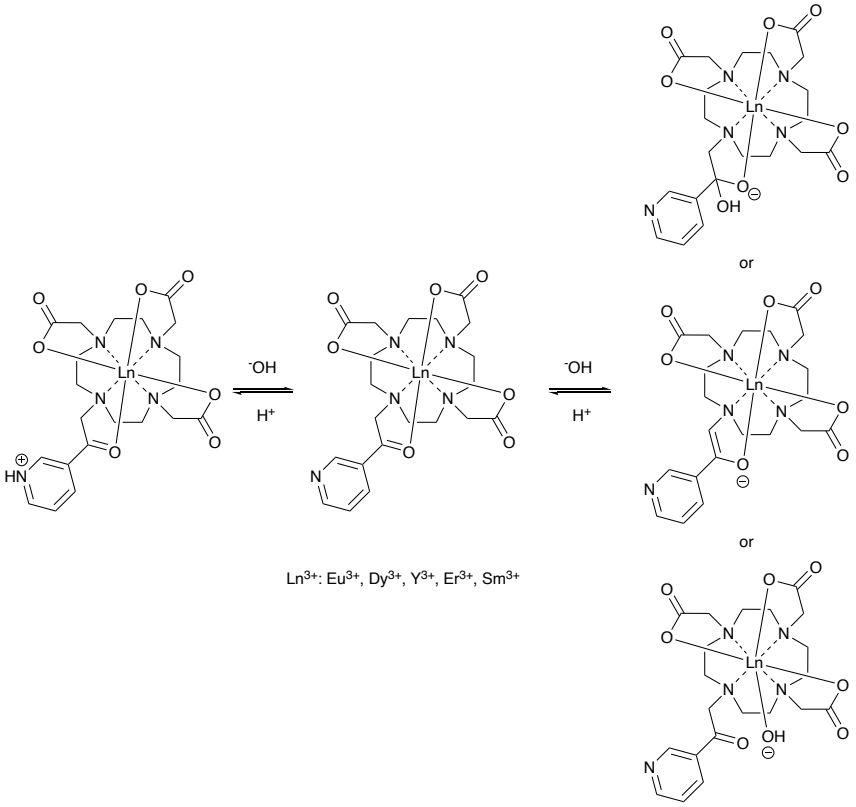
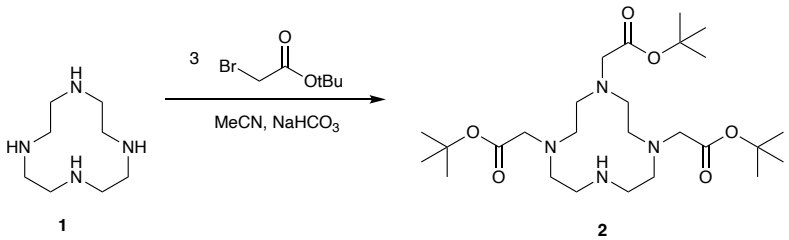


Figure 2.4 : Possible conguagte acid/base pairs of target compund.

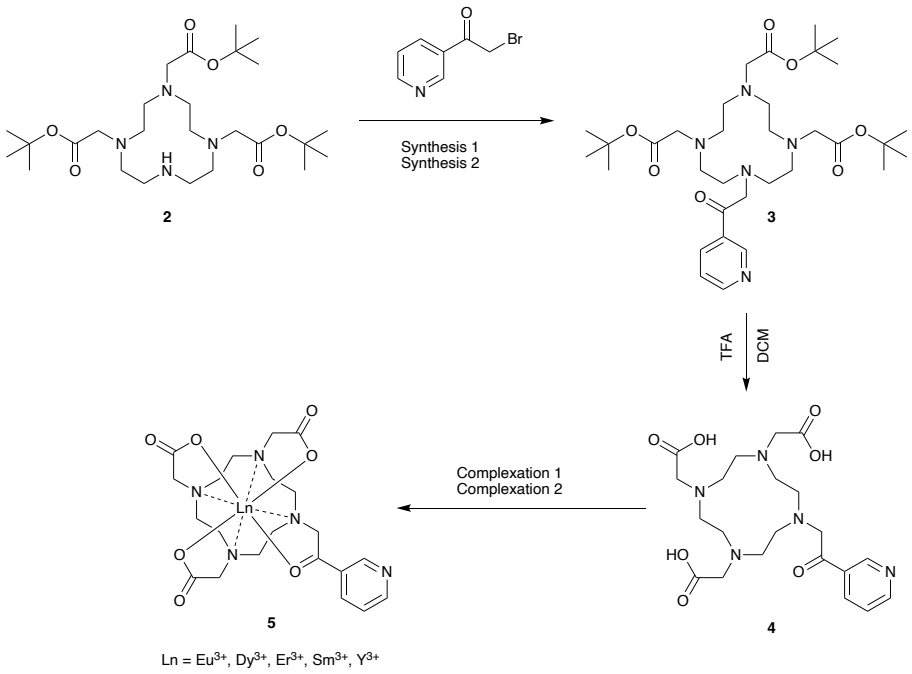
Results and discussion

Ligand synthesis



*Scheme 2.1 : synthesis of triester (DO3A-tBu)(**2**).*

All syntheses in this thesis involve the synthesis of **2** as shown in Scheme 2.1**.** Triester (**2**) is used as a starting material throughout all syntheses in this thesis.



*Scheme 2.2 : syntheses of **5**Ln, the synthetic target from **2**. Synthesis 1: Cs_2CO_3/MeCN. Synthesis 2: K_2CO_3/MeCN. Complexation 1: $Ln(OTf)_3$, NaOH in MeOH/H_2O 1:1, 60°C. Complexation 2: $LnCl_3$, NaOH in MeOH, reflux.*

The synthesis of the ligand from cyclen involved two alkylations and one deprotection step. The yields of these alkylations were low (<60%). Although only two sets of conditions for the alkylation of **2** are presented in Scheme 2.2, to achieve this alkylation many different reaction conditions were tested. These different conditions involved changing the solvent, the temperature and the base. In the end, the reaction which resulted in a successful

alkylation used MeCN as solvent and potassium carbonate as a base although this was only noted during the second attempt at synthesising the ligand.

For the first synthesis, caesium carbonate in MeCN was used. In this synthesis of the ligand, the alkylation and deprotection was carried out as a single step because during an attempted purification step acid was added to try to purify the product of the alkylation by solvent extraction. Unfortunately, this did not work, and it was suspected that some partial deprotection had occurred. Therefore, it was decided that the purification of the ligand after the deprotection was to be done by HPLC; this yielded the synthetic target as a light brown solid once concentrated under reduced pressure. The overall yield of the first synthesis was 7.2%.

A second synthesis of the ligand was carried out to improve the yield and obtain more ligand to prepare dysprosium, erbium, samarium and yttrium analogues.
This was done by carrying out the alkylation with potassium carbonate in MeCN at room temperature. Contrary to the previous synthesis, the product of this reaction was purified by silica gel chromatography. This produced a cleaner sample of the protected ligand (61%) as a brown solid. NMR confirmed the presence of the desired ligand with copious amounts of solvent even after several days of drying under high vacuum. It was therefore decided to deprotect the ligand and not count the protected ligand as having been isolated (although NMR data, HPLC-MS and HRMS on this compound is available in the experimental section of this thesis). The deprotection was carried out under the same conditions as in the first synthesis. This yielded DO3A-3-acetylpyridine as a light brown/yellow solid in 35% yield, giving an overall 21% yield from DO3A-tBu (**2**), a significant improvement in comparison to the yield of the first synthesis (7%).

Complexations

Initial complexations

For the formation of **5**Eu, initially europium chloride and europium trifluoromethanesulfonate were used. The complexations were carried out by refluxing equimolar quantities of metal salt and ligand and refluxed in methanol : water solutions. The reaction was then concentrated and dialysed in water for several days, any solid formed was passed through a syringe filter. The resulting solution was concentrated to yield a light yellow/brown solid. In the end, during the first syntheses of **5** (Eu, Dy and Y analogues) it was decided to use the trifluoromethylsulfonate salt as the source of the RE(III) ions for the syntheses because chloride ions may affect the luminescence of the complex.

Final complexation conditions

Complexations from ligand produced in the second synthesis were carried out under different conditions. These being the reflux of equimolar quantities of ligand and lanthanide (III) chloride or lanthanide(III) triflate in methanol depending on which salt was available. pH was monitored during the complexation. A solution of low pH (c.a. 3) formed as the reaction progressed. Three equivalents NaOH (1M) solution were added to neutralise the resulting solution. This resulted in the desired complexes in seemingly quantitative yields after the removal of solvent. The crude products were purified by dialysis and the removal of any solids formed by filtering through a syringe filter. NMR of Eu and Dy analogues of Ln-DO3A-3-acetylpyridine looked identical to those obtained from the first complexation and HRMS (high resolution mass spectrometry) confirmed the identity of these complexes. This method was used in the complexations of Er^{3+}, Sm^{3+}, Gd^{3+} and Nd^{3+} with **4**. These were all characterised by HRMS, HPLC-MS, IR and HNMR. The data for **5Gd** and **5Nd** can be found in

the experimental section of this thesis. The response of **5Nd** to pH was not characterised due to the difficulty measuring its fluorescent emission. The **5Gd** analogue was to be used to measure the antenna's triplet state and observe any change in relaxivity due to pH but due to time restrictions this was not possible. Accurate yields for the complexations could not be recorded due to not being able to identify the hydration number of the complexes.

Titrations

Several titration methods were tested, including an unbuffered method and others based on buffers. In the end, the unbuffered method (i.e. adding small amounts of acids and base to alter the pH and then measuring the UV-Vis and fluorescent response) was used to obtain a rough idea of the sensitive ranges and a method using CHES, HEPES and MES buffers.

UV-Vis

"Rough" titration

UV-Vis data suggests that there are three species present during the titration due to there being 3 different spectra at different pHs (see Figure 2.5). Between pH 1.95 and pH 4.01 we see an hypsochromic shift and a marked hyperchromic shift c.a. 240 nm. This is as expected for the deprotonation of a pyridinyl nitrogen.[25] Between pH 4.01-9.82 we see a large decrease in absorbance around 240 nm and the absorbance at 270 nm becoming broader. This is seen again in the UV-Vis measurements of titration of the Dy analogue (see Figure 2.6). The three different UV-Vis spectra suggests that there are 3 different species produced in this titration.

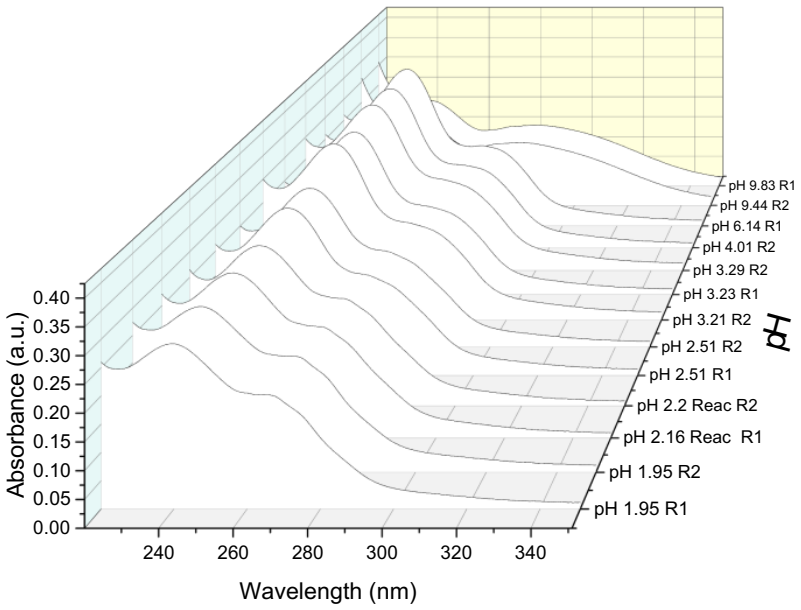


*Figure 2.5 : UV-Vis of preliminary titration of **5Eu** with the unbuffered method. R1 and R2 stand for replicates 1 and 2, Reac stands for reacidification after the highest pH was attained.*

HEPES, CHES and MES titration

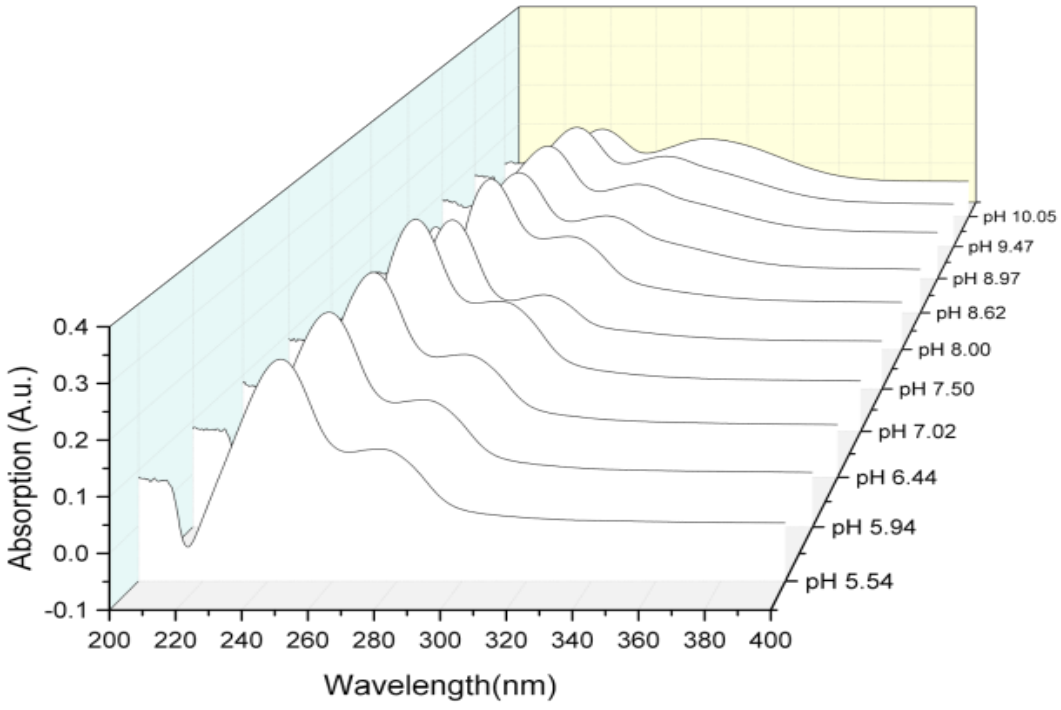


*Figure 2.6: UV-Vis spectra of **5**Dy at different pHs.*

The UV-Vis and fluorescent data was recorded again using a series of buffers (HEPES, CHES and MES) to obtain more accurate and reproducible values for the pKa of the complexes. The UV-

Vis spectra of this titration show a great similarity to those recorded in the “rough” titration. These spectra clearly show 2 different absorption spectra. This suggests that that there are 2 species present at pH 5.5 and pH 10.05. Table 2.1 shows the change in absorbance and position of the maxima observed in Figure 2.3. The absorbance at 243 nm undergoes a hypochromic shift as pH increases. We also see that the second absorption peak becomes broader and shifts from 274 nm to 289 nm. The bathochromic shift of the 274 nm maximum as pH increases suggests an increase or the conservation of the number of conjugated orbitals within the chromophore. This is expected if an enol is being formed.[26]

The pattern in intensity observed in the absorbance of the maxima in Figure 2.6 and Table 2.1 is imitated by the excitation and emission spectra of **5**Eu, **5**Dy and **5**Sm. This implies that the changes in emission between pH 6-10 are caused by changes in the complexes’ chromophore.

Table 2.1: Maxima observed in the UV-vis spectrum of 5Dy and their absorbance.

pH of buffer	*Maximum 1 (nm)*	*Abs. Maximum 1 (A.U.)*	*Maximum 2 (nm)*	*Abs. Maximum 2 (A.U.)*
5.54	243	0.301	274	0.138
5.94	244	0.305	274	0.140
6.44	244	0.302	275	0.141
7.02	244	0.333	273	0.166
7.50	244	0.258	277	0.100
8.00	246	0.274	274	0.145
8.62	243	0.212	277	0.121
8.97	243	0.212	278	0.122
9.47	243	0.190	280	0.120
10.05	242	0.120	289	0.095

Fluorescence spectra

"Rough" titration

The emission intensity of the $^5D_1$-$^7F_1$ (592 nm) transition in different pHs was plotted against the pH at which they were recorded. This shows that the probe has 2 pKas, one around pH 2 and another between pH6-10 (see Figure 2.7). This data is preliminary, subsequent titrations focused on the physiologically relevant pH range to obtain a more accurate value for the higher pKa value.

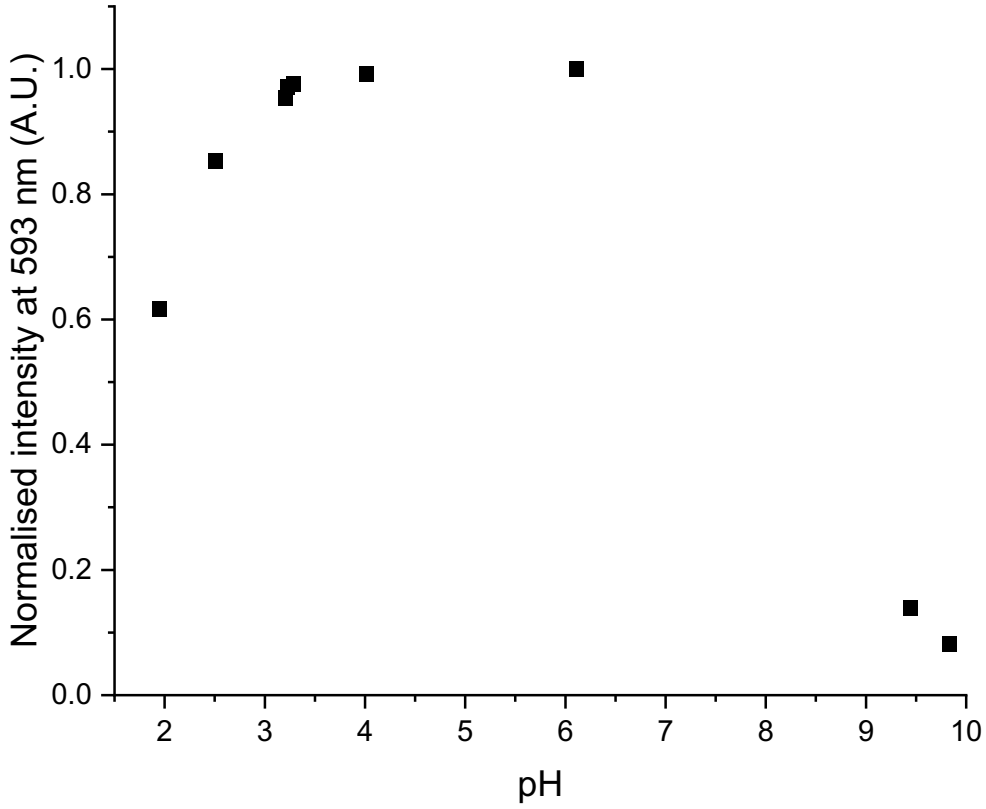


*Figure 2.7: emission intensity of the $^5D_1$-$^7F_1$ (593 nm) transition of **5Eu** plotted against the pH of the titrate.*

HEPES, CHES and MES titration

Fluorescence spectra

5Eu

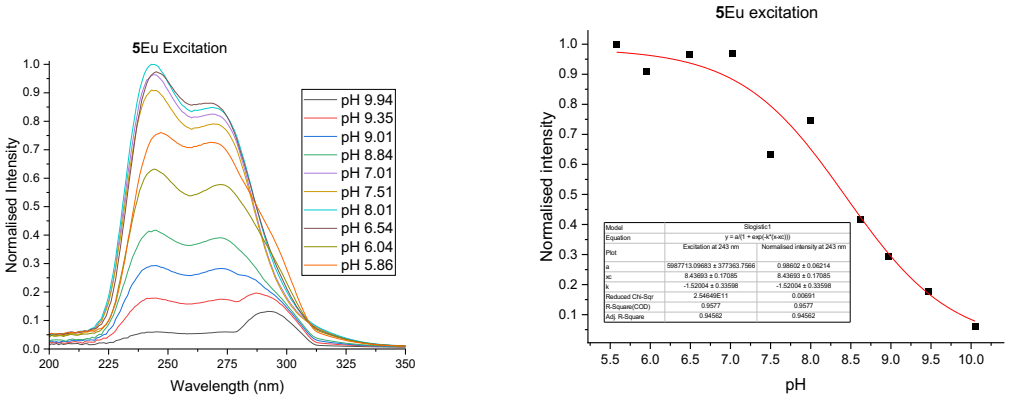


Figure 2.8 : excitation spectrum of the $^5D_0 \rightarrow {}^7F_1$ transition of 5Eu and the change of intensity with pH of this transition (λ_{em}: 592 nm).

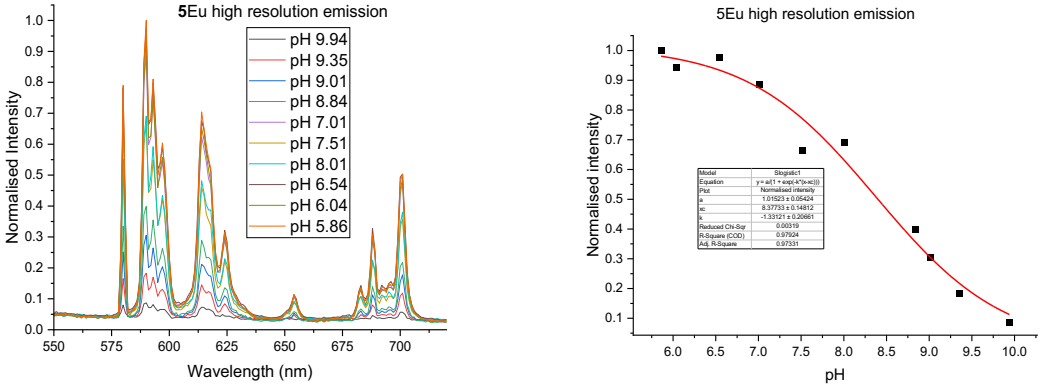


Figure 2.9 : high-resolution emission spectrum of 5Eu (λ_{exc}: 241 nm) and the intensity of the $^5D_0 \rightarrow {}^7F_1$ transition (λ_{em}: 590 nm) plotted against pH. The position of the components of the manifolds shown in the Experimental.

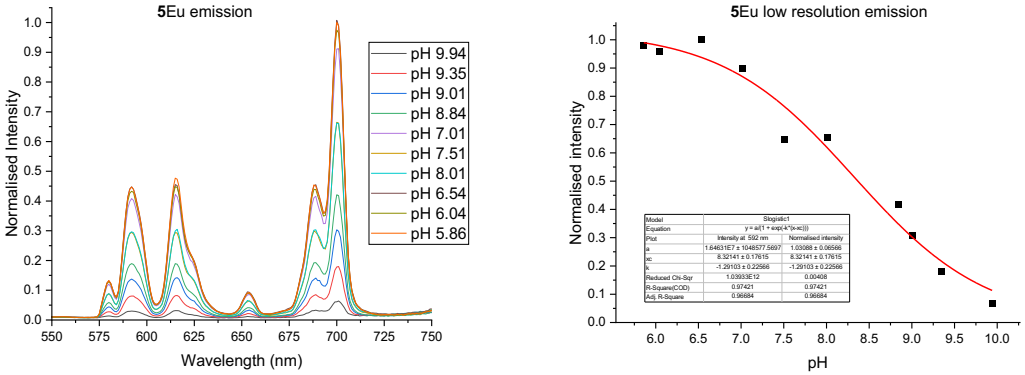


Figure 2.10 : low-resolution emission spectrum of 5Eu (λ_{exc}: 241 nm) and the intensity of emission of $^5D_0 \rightarrow {}^7F_1$ transition (λ_{em}: 592 nm) plotted against pH.

5Dy

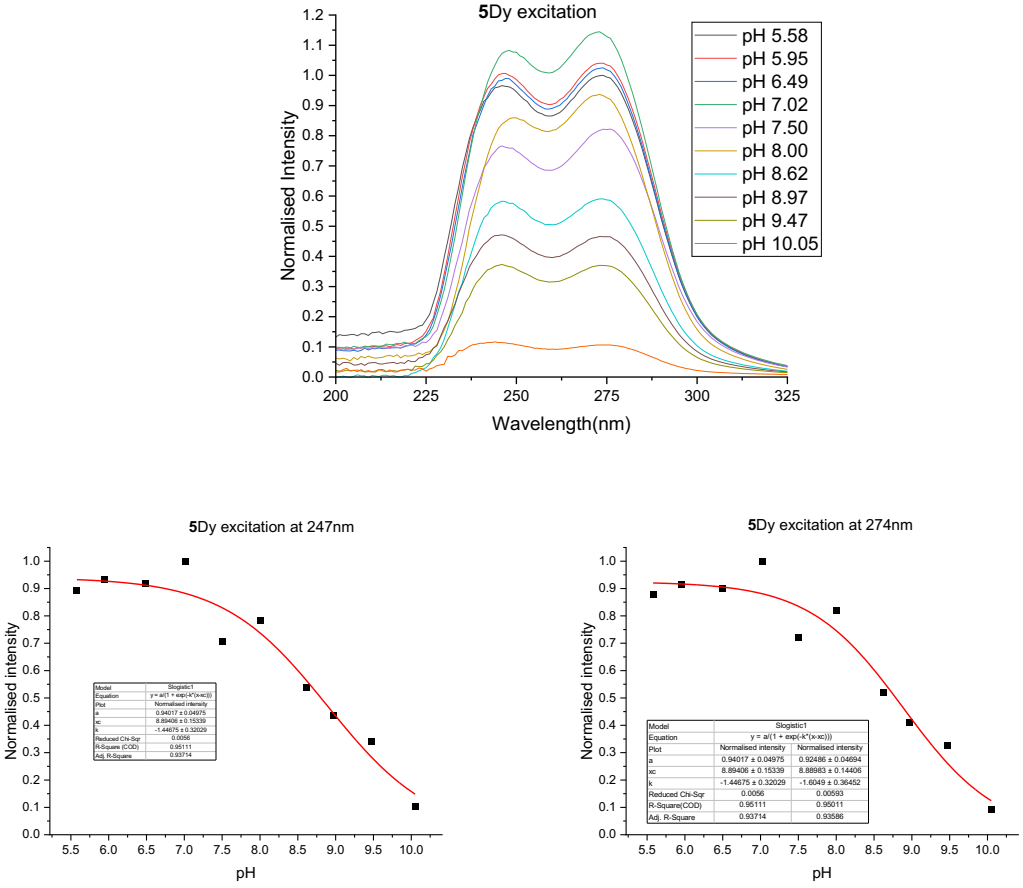


Figure 2.11 : excitation spectrum of the $^7F_{9/2} \rightarrow {}^6H_{15/2}$ transition of 5Dy (λ_{em}: 483 nm).

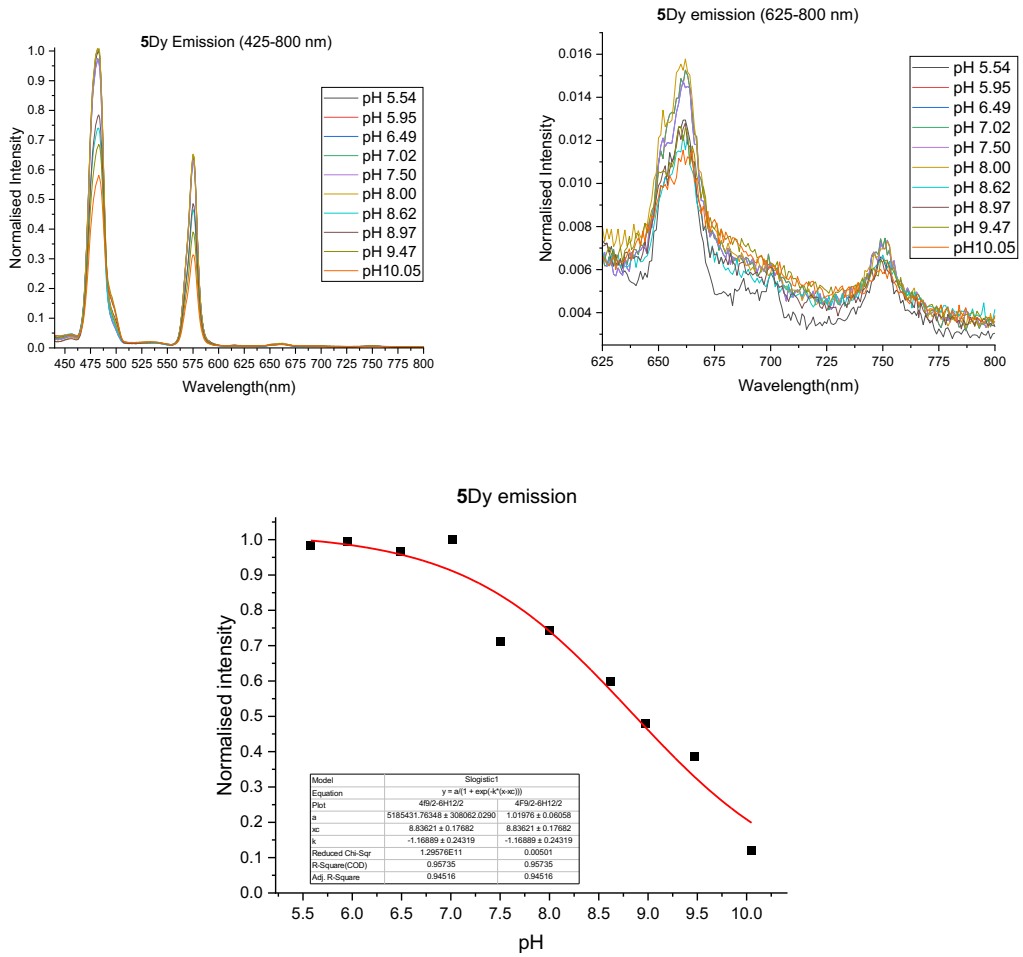


Figure 2.12 : emission spectrum of 5Dy (λ_{exc}: 241 nm) and the intensity of the $^{7}F_{9/2} \rightarrow {}^{6}H_{13/2}$ transition (λ_{em}: 575 nm) plotted against pH

5Sm

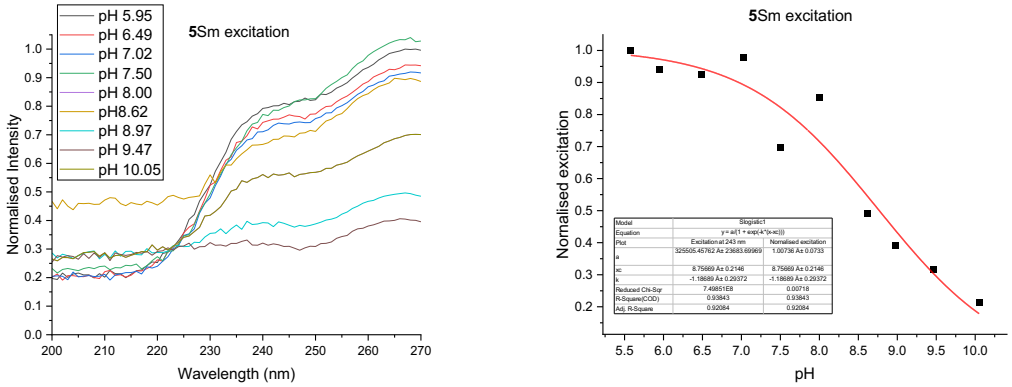


Figure 2.13 : excitation spectrum of the $^4G_{5/2} \rightarrow {}^4H_{7/2}$ transition (λ_{em}: 595 nm)) of 5Sm and the intensity of the peak at 243 nm plotted against pH.

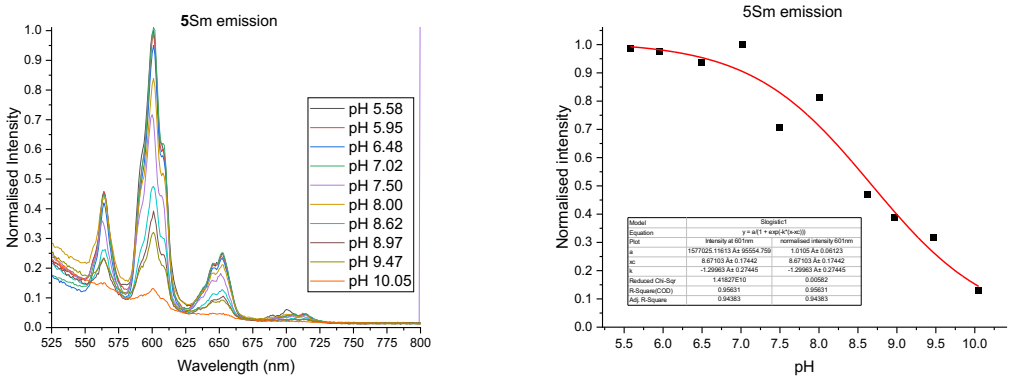


Figure 2.14 : emission spectrum of 5Sm (λ_{exc}: 243 nm) and the intensity of the $^4G_{5/2} \rightarrow {}^4H_{5/2}$ transition (λ_{em}: 595 nm) plotted against pH.

Dy-DO3A-3-acetylpyridine vs Eu-DO3A-3-acetylpyridine vs Sm-DO3A-3-acetylpyridine

The pKas of these complexes varied between the ones obtained from the excitation spectra and those from emission spectra but this difference is not statistically significant.

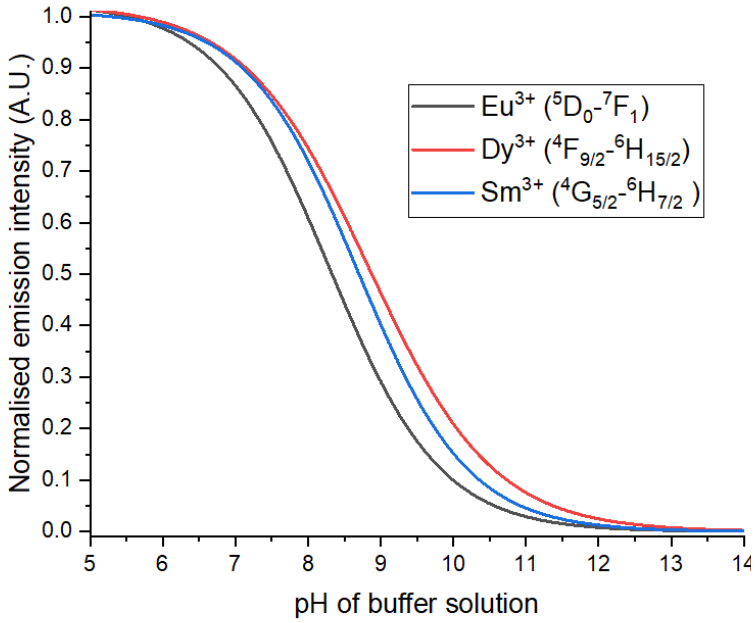


*Figure 2.15: simulated curves of the normalised intensity of the emission spectra of **5**Eu, **5**Dy and **5**Sm.*

There is a statistically significant difference between the pKas of **5**Dy, **5**Sm and **5**Eu as shown by Table 2.2.

Table 2.2: Summary of the pKa data obtained by fitting a logistic function to the plots in figures 2.7, 2.8 and 2.9.

Complex (resolution)	pKa			|ΔpKa|	
	Excitation (243 nm)	Emission	UV-Vis absorbance	Excitation	Emission
5Eu (low) (high)	8.44±0.05	8.32±0.05 8.38±0.05		Eu-Sm (0.32) Eu-Dy (0.45) Sm-Dy (0.13)	Eu-Sm (0.35) Eu-Dy (0.51) Sm-Dy (0.16)
5Sm	8.76±0.05	8.67±0.05			
5Dy	8.89±0.05	8.83±0.05	9.68±0.05		

Characterisation of the conjugate base and analyses of NMR Spectra (NMR/Crystal Field analysis)

All NMR spectra for the complexes presented here were recorded in deuterium oxide. The pH was increased by addition of 1M and 0.1M NaOD solution.

Identification of Conjugate base (Y-DO3A-3-acetylpyridine)

HNMR

Y-DO3A-3-acetylpyridine (**5Y**) was dissolved in neutral D_20 to obtain a solution of pD 5.42 to give the spectrum shown in Figure 2.16. The spectra shows that the positions of the chemical shifts of this NMR are consistent with the formula of **5Y** but integration did not add up to the expected number (26 instead of 28 protons); we believe this is due to the ketone's alpha carbon protons being labile and therefore in exchange with those in the D_2O solvent. The sample was measured again in a solution of pD 13.87 as this was beyond the endpoint of the luminescence titration (see Figure 2.16). The chemical shifts of **5Y** in acid and in base differ. The shifts of the aromatic protons of **5Y** in acid (9.18-7.63ppm) are downfield in relation to those of the complex under basic conditions (8.70-7.41ppm). This may suggest that the complex in acid has a deactivating (i.e. electron withdrawing) group which the complex under basic conditions does not possess, this suggests that **5Y**'s ketone is not present under basic conditions. The shifts belonging to cyclen ring and arms (4.00-2.00 ppm) are sharp under acidic conditions and broad under basic conditions. This suggests that the protons in these positions are in faster exchange (i.e. between axial and equatorial positions) under basic conditions.

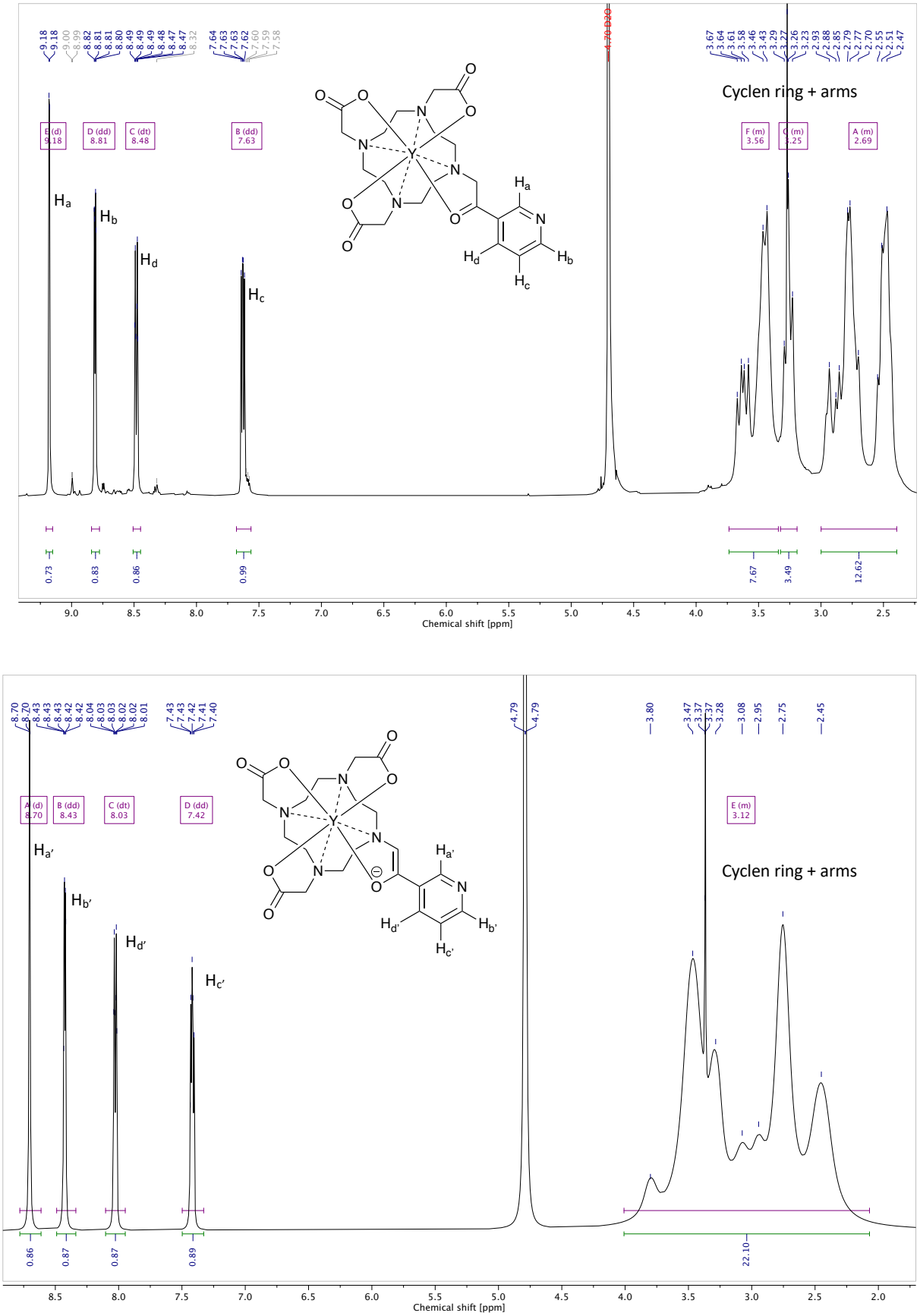


*Figure 2.16 : HNMR spectra of **5**Y in deuterium oxide at pD 5.42 (top) and pD 13.87 (bottom).*

CNMR

The DEPTQ spectra of this complex was also recorded under these conditions were combined to give Figure 2.16.

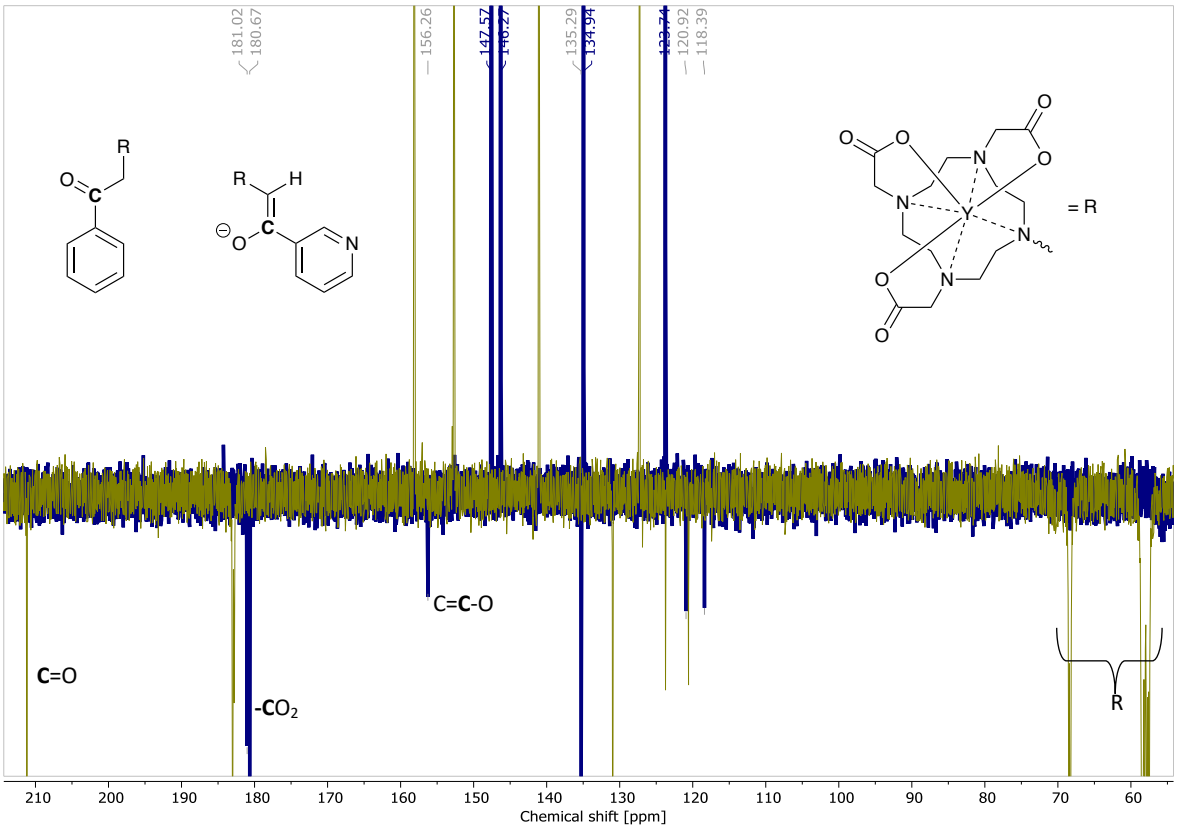


*Figure 2.17 DEPTQ spectra of **5**Y in deuterium oxide solution of pD 5.42 (gold) and pD 13.87 (blue).*

The broadening of both the HNMR spectrum and the disappearance of the CNMR shifts related to the cyclen ring carbons (58.5- 57.5 ppm - R peaks) and cyclen 'arms' (68.5 ppm - R peaks) suggests that basic conditions result in greater exchange between these positions. This suggests increased repulsion between the ligating positions, which suggests the presence of a negatively charged ion in the equatorial position of the complex under basic conditions. This, in conjunction with the presence of a peak at 156 ppm (=**C**-O peak) and the loss of the shift at 211 ppm (**C**=O peak) under basic conditions, suggests the loss of a ketone and the presence of an enol. This corresponds with what is shown in Figure 2.18.

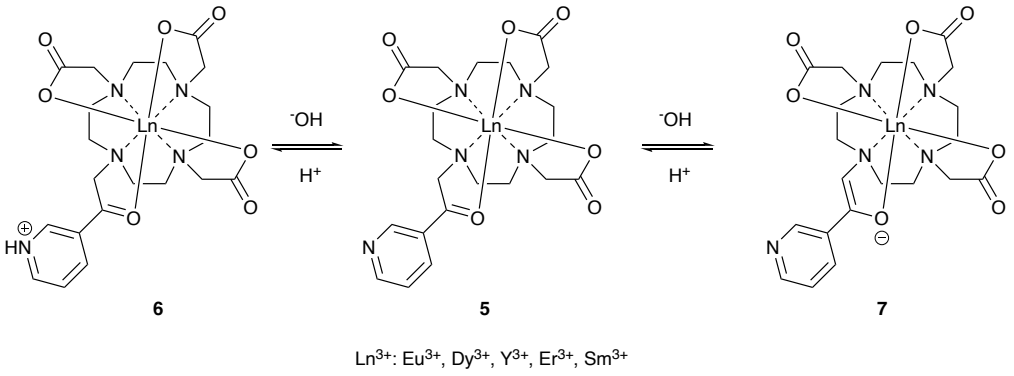


*Figure 2.18 : conjugate acid/base pairs formed by **5**Ln under acidic (**6**), neutral (**5**) and basic (**7**) conditions.*

Analysis of paramagnetic HNMR spectra

Eu-DO3A-3-acetylpyridine

The NMR spectrum of this species in pD 3.01 corresponds with that of a prolate species(see Figure 2.19) as the most shifted peak has a positive chemical shift (35.06 ppm) and follows the pattern predicted from crystal structures of DOTA (the parent species of these complexes) and Bleaney's theory.[35] This may seem surprising at first, the crystal field parameters for **5Eu** show that the spatial electronic distribution of the $^7F_1$ energy state of europium in this complex is oblate (B_0^2= +520 cm^{-1}) while that of [Eu(DOTA)$^-$] is prolate.[36,37] According to Bleaney theory, the chemical shifts of **5Eu a**re those of a species with prolate anisotropy. This is because Bleaney predicts the pseudocontact contribution depending on a proton's position relative to the molecular axis of highest symmetry[38,39] in the case of [LnDOTA]$^-$ this is a C4 symmetric axis which crosses the planes formed by the COO_2^- and N ligands. In these C1 symmetric complexes, there is no such axis, therefore the axis of highest symmetry could conceivably lie anywhere within the complex, including parallel to the COO_2^- and N planes.

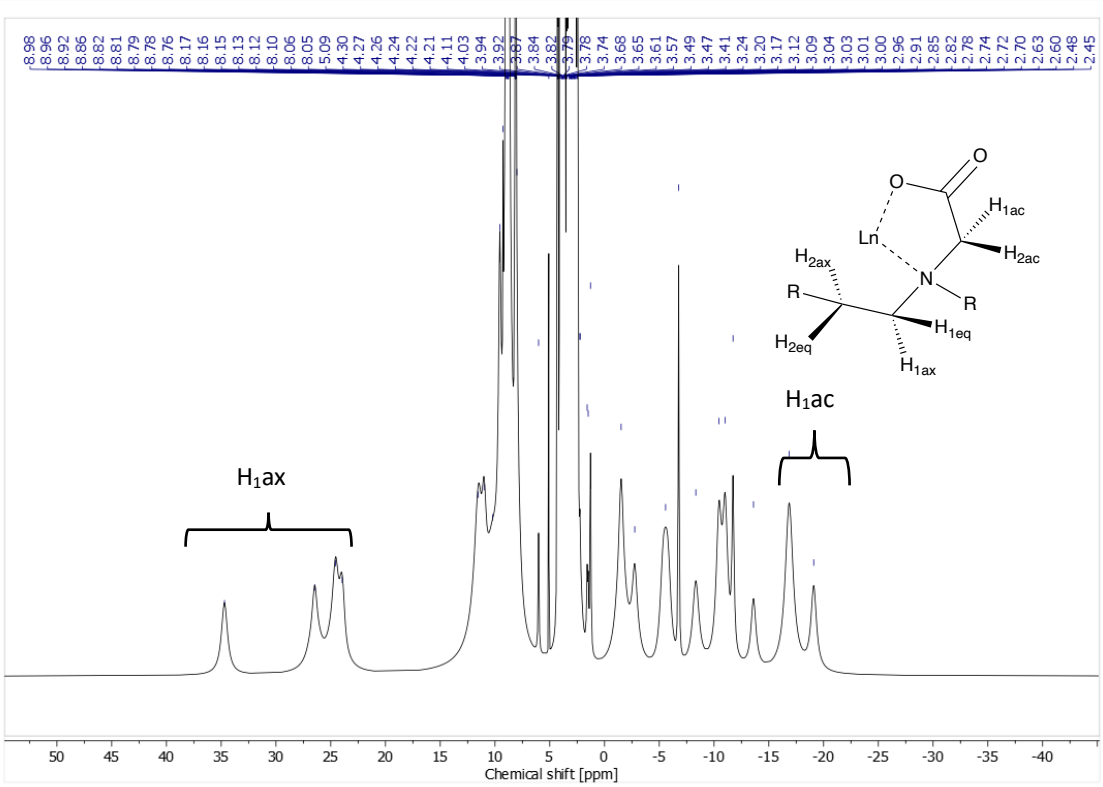


*Figure 2.19 : HNMR spectrum of **5**Eu in deuterium oxide solution of pD 3.01.*

The crystal field/stark splitting observed in the high-resolution emission spectrum of Eu-DO3A-3-acetylpyridine (Figure 2.20) by direct excitation and 'antenna' excitation was analysed at pH 3.1 and pH 13.9. These gave values of B_0^2=+520 cm^{-1} and B_2^2=-88 cm^{-1} (see experimental for calculation) under acidic conditions and a value of B_0^2= -570 cm^{-1}.

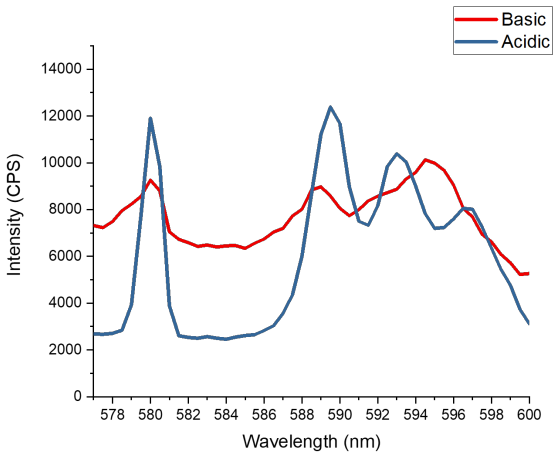


*Figure 2.20 : High resolution direct excitation spectra of **5**Eu in aqueous solution of pH 3.1 and pH13.9.*

These values suggest that the crystal field is inverted by the changes in the ligand environment. This inversion is observed in complexes used to quantify fluoride concentration by the binding of the halide ion in the axial position.[40,41] Although the inversion seen here is from a positive crystal field parameter

to a negative crystal field, this suggests that an anion is being ligated by the lanthanide ion at an equatorial position. Phosphorescent decay data shows no appreciable change in hydration number (q = 1.09 in acid and q = 1.345in base) which suggest an enol is formed at the alpha carbon of the chromophore (7) rather than the substitution of the chromophore ligand by a hydroxide ion. This would explain the decrease in fluorescent emission with increase in pH as the enol prevents the efficient transfer of electrons between the chromophore and the lanthanide.

The NMR spectrum of this complex was recorded at pD 10.87. The NMR spectrum of this complex was recorded at pD 10.87 (Figure 2.21).

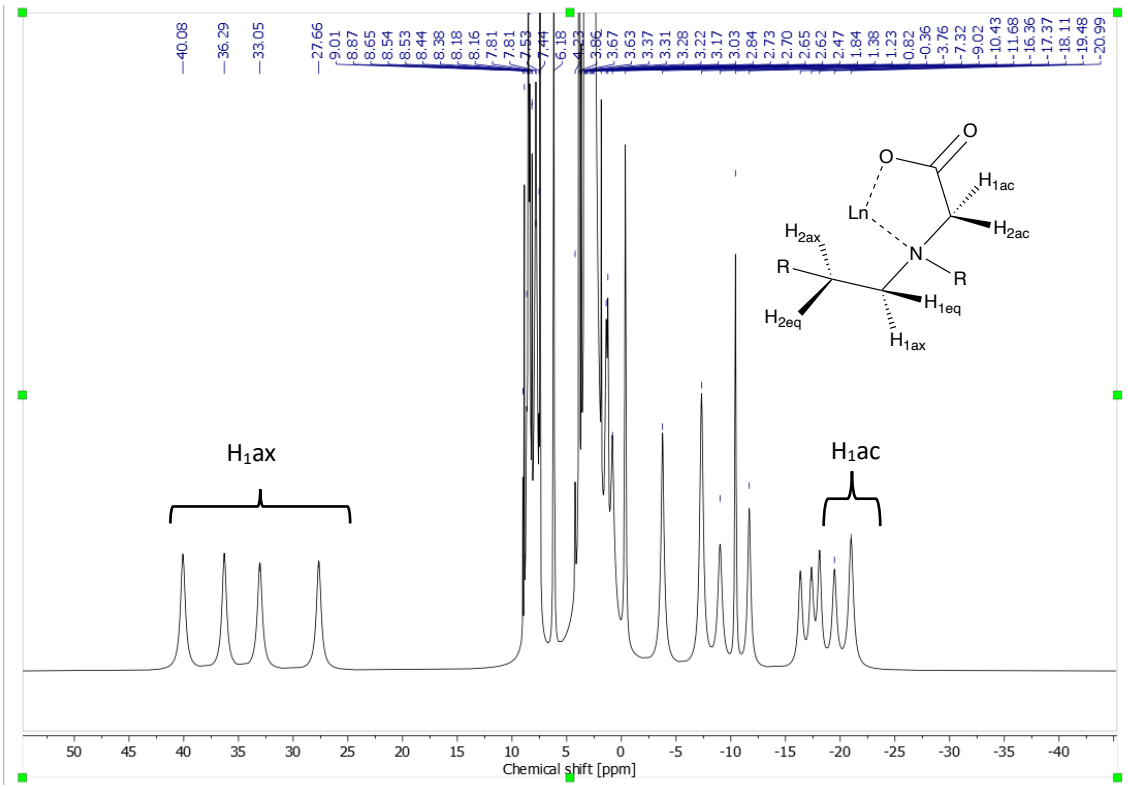


*Figure 2.21 : HNMR spectrum of **5**Eu in deuterium oxide solution of pD 10.87.*

This caused the shifts to spread outwards as shown by the highest and lowest shifted peaks in the pD 3.01 (34.7 ppm and -19.1 ppm) and pD 10.87 spectra (40.08 ppm and -20.99 ppm), and to cause the distributions of the shifts to change. The outer peaks have shifted by a

larger amount than that predicted by the $\frac{B^2_{0(basic)}}{B^2_{0(acidic)}}$ ratio (-1.096) which are -20.0 ppm and 38.0 ppm. Although this difference is small, it suggests that the positions of the protons in relation to the principal magnetic axis have changed (see Figure 2.22 for comparison of the stacked spectra).

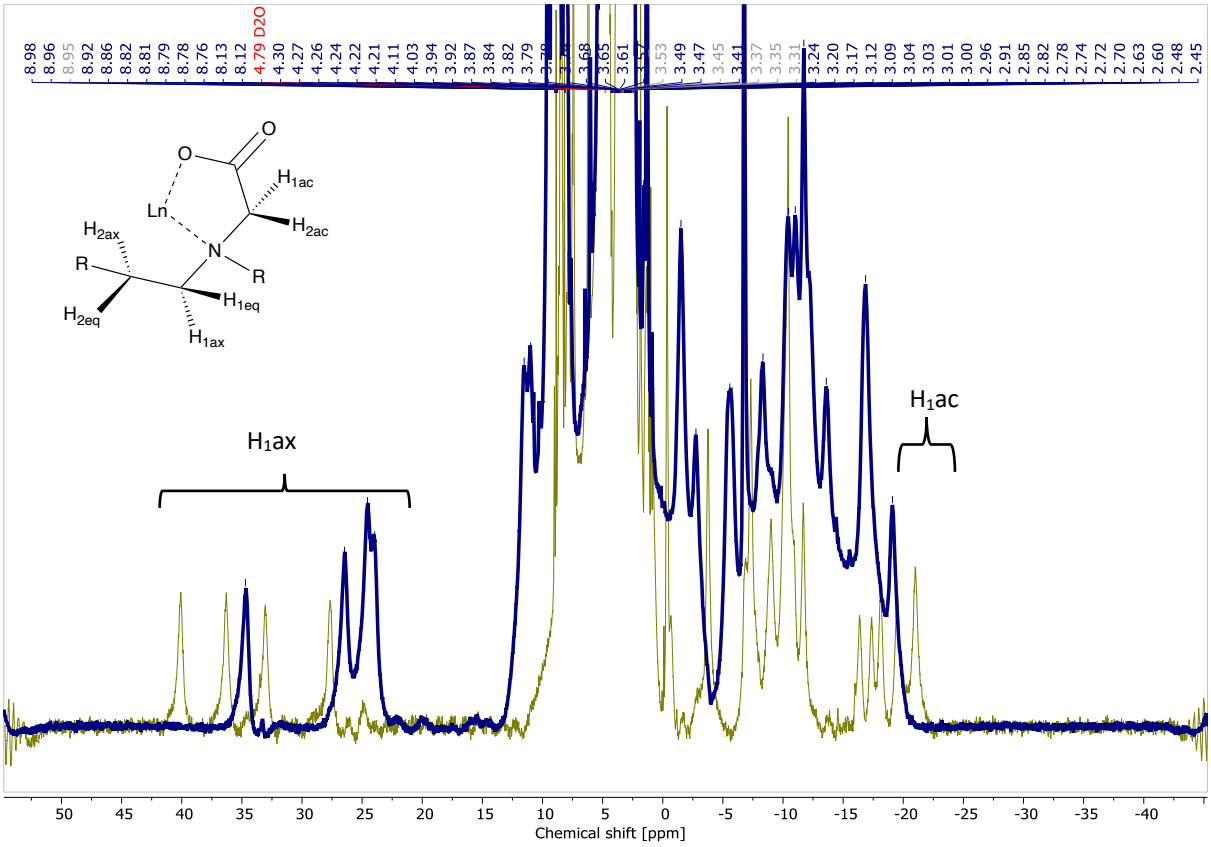


Figure 2.22 : HNMR spectra of 5Eu in deuterium oxide solution of pD 3.01(blue) and pD 10.87(gold).

Dy-DO3A-3-acetylpyridine

The NMR spectrum of this complex was recorded at pD 4.92 and pD 12.38. Under acidic conditions the most shifted peak is at +461 ppm. Under basic conditions the most shifted peak is at -526 ppm. This suggests that the crystal field has been inverted as seen in Figure 2.23, although given the weakness of this peak it is possible that these peaks belong to a minor isomer of **5**Dy**.**

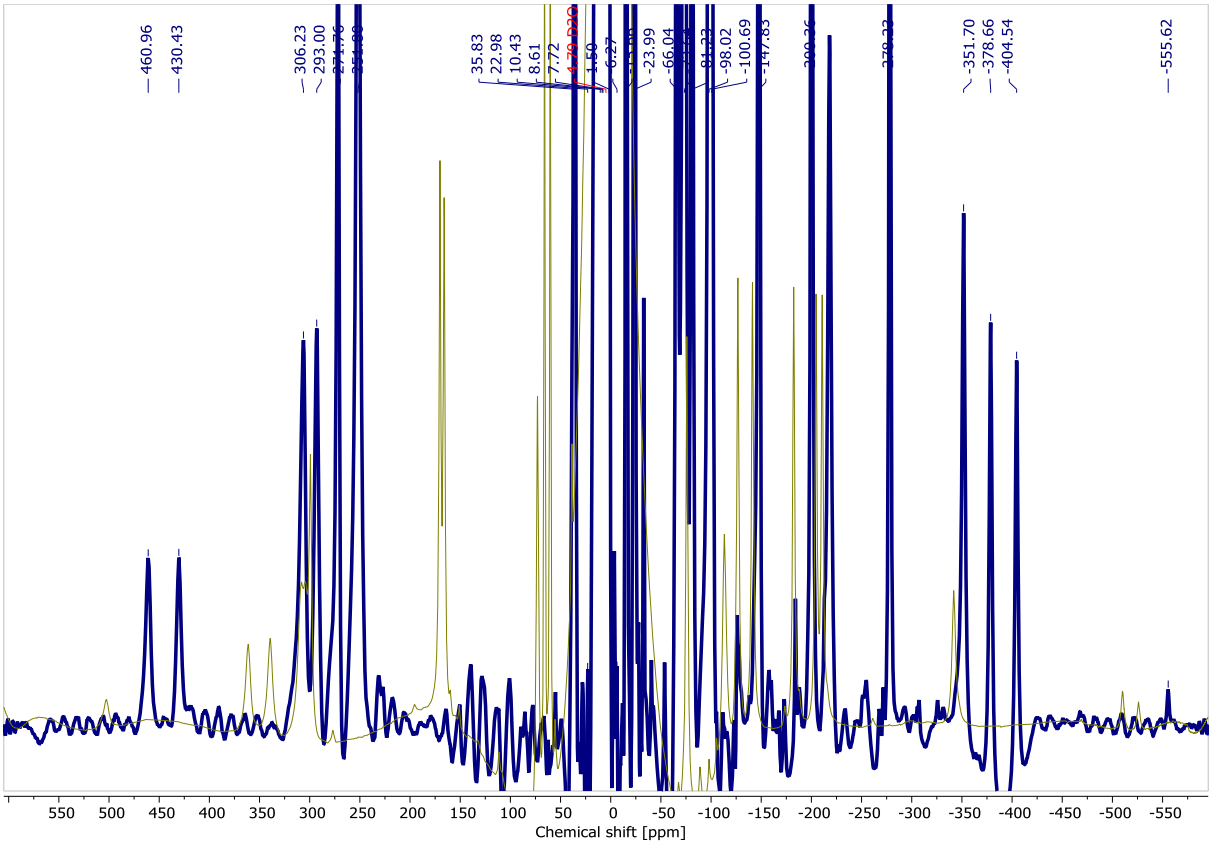


*Figure 2.23 : HNMR spectra of **5**Dy at pD4.92(blue) and pD 12.38(gold).*

Er-DO3A-3-acetylpyridine

The NMR spectra of this complex were recorded at pD 4.04 and pD 13.71 to give Figure 2.24. These spectra mimic those seen in the spectra of Eu-DO3A-3-acetylpyridine but with a greater pseudocontact shift contribution caused by the Bleaney constant of the Er^{3+} ion (+58.8) when compared to Eu^{3+} (-4.5).

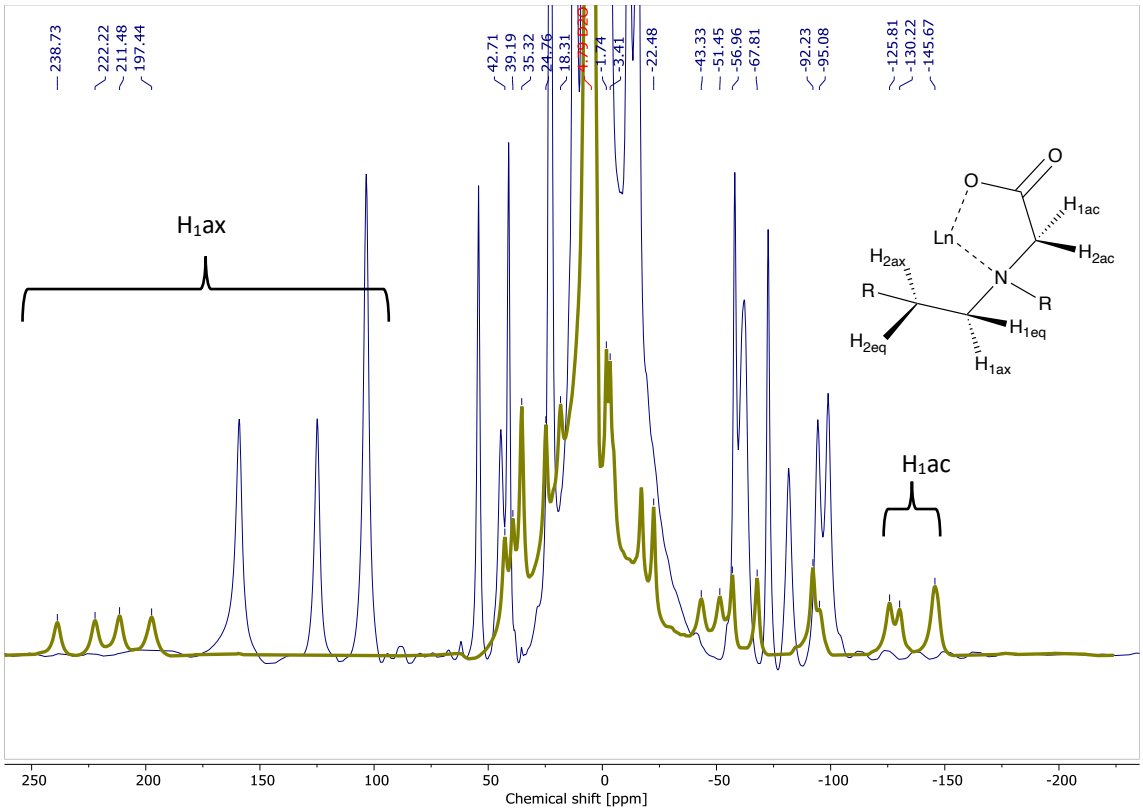


*Figure 2.24 : HNMR spectra of **5**Er in deuterium oxide solution of pD 4.04(blue) and pD 13.71(gold).*

Given the large changes in the positions of the shifts between pD 4 to pD 14 across this series of complexes we may conclude that these would be suitable as paraSHIFT probes for the monitoring of the physiological pH environment, if a reporting group such as methyl were added to the 'arms' of the DO3A part of the molecule.

Conclusion

The Eu^{3+}, Dy^{3+}, Y^{3+}, Er^{3+}, Sm^{3+}, Gd^{3+} and Nd^{3+} analogues of **5** were synthesised and characterised with NMR, mass spectrometry, IR and HPLC-MS. The pKa of the Eu^{3+}, Dy^{3+} and Sm^{3+} analogues were evaluated by means of luminescent pH titrations. These titrations showed that these probes have 2 sensitivity ranges; one is between pH 6-10 and the other is pH <3.5. The more basic range could be useful for measuring extracellular pH.

An NMR titration was carried out on the Eu^{3+}, Dy^{3+}, Y^{3+} and Er^{3+} analogues to assess the usefulness of theses complexes as NMR/MRI probes and attempt to identify the conjugate base under basic conditions. These showed significant changes in the position of their chemical shifts in acidic and basic conditions. This suggests that these probes may be of use as paraSHIFT NMR pH probes.

From the NMR and luminescence high resolution emission spectra, we can conclude that the pH response of these probes is caused by the formation of an enol.

In conclusion, the probes described in this chapter are suitable to monitor pH in the range of pH6-10. This range coincides with the pH range of a number of physiological environments.

References

1 R. J. Myers, *J Chem Educ*, 2010, **87**, 30–32.

2 W. Aoi and Y. Marunaka, *Biomed Res Int*, 2014, **2014**, 1–8.

3 J. L. Wike-Hooley, J. Haveman and H. S. Reinhold, *Radiotherapy and Oncology*, 1984, **2**, 343–366.

4 S.-H. Kuo, C.-J. Shen, C.-F. Shen and C.-M. Cheng, *Diagnostics*, 2020, **10**, 107.

5 G. H. Gao, Y. Li and D. S. Lee, *Journal of Controlled Release*, 2013, **169**, 180–184.

6 A. I. Hashim, X. Zhang, J. W. Wojtkowiak, G. V. Martinez and R. J. Gillies, *NMR Biomed*, 2011, **24**, 582–591.

7 J. Mania-Pramanik, S. C. Kerkar, P. B. Mehta, S. Potdar and V. S. Salvi, *J Clin Lab Anal*, 2008, **22**, 375–379.

8 Centre for disease control (CDC), Bacterial Vaginosis, https://www.cdc.gov/std/treatment-guidelines/bv.htm, (accessed 6 January 2023).

9 D. A. Zygun, L. A. Steiner, A. J. Johnston, P. J. Hutchinson, P. G. Al-Rawi, D. Chatfield, P. J. Kirkpatrick, D. K. Menon and A. K. Gupta, *Neurosurgery*, 2004, **55**, 877–882.

10 I. Timofeev, J. Nortje, P. G. Al-Rawi, P. J. Hutchinson and A. K. Gupta, *Journal of Cerebral Blood Flow & Metabolism*, 2013, **33**, 422–427.

11 Y. Shang, *Br J Anaesth*, 2016, **117**, el_14017.

12 T. R. Arnett, *Arch Biochem Biophys*, 2010, **503**, 103–109.

13 J. S. Lewis, J. A. Lee, J. C. E. Underwood, A. L. Harris and C. E. Lewis, *J Leukoc Biol*, 1999, **66**, 889–900.

14 N. Raghunand, R. A. Gatenby and R. J. Gillies, *Br J Radiol*, 2003, **76**, S11–S22.

15 S. D. Navaneethan, J. Shao, J. Buysse and D. A. Bushinsky, *Clinical Journal of the American Society of Nephrology*, 2019, **14**, 1011–1020.

16 D. C. Dugdale, Metabolic acidosis, https://www.pennmedicine.org/for-patients-and-visitors/patient-information/conditions-treated-a-to-z/metabolic-acidosis, (accessed 26 September 2024).

17 S. Vepraskas, H. Toth and M. Weisgerber, in *Nelson Pediatric Symptom-Based Diagnosis*, eds. R. M. Kliegman, P. S. Lye, B. J. Bordini, H. Toth and D. Basel, Elsevier, 2018, pp. 831–850.

18 McNaught A. and Wilkinson A., *The IUPAC Compendium of Chemical Terminology*, International Union of Pure and Applied Chemistry (IUPAC), Research Triangle Park, NC, 2019.

19 E. Martin and J. Law, 'Alkalosis.' Concise Medical Dictionary (2020): Concise Medical Dictionary, https://www-oxfordreference-com.ezproxy-prd.bodleian.ox.ac.uk/display/10.1093/acref/9780198836612.001.0001/acref-9780198836612-e-290?rskey=yBJ0jL&result=324, (accessed 5 July 2023).

20 M. Emmett, *Clinical Journal of the American Society of Nephrology*, 2020, **15**, 1848–1856.

21 K. Mæhle, B. Haug, H. Flaatten and E. W. Nielsen, *Crit Care*, 2014, **18**, 420.

22 M. C. Heffern, L. M. Matosziuk and T. J. Meade, *Chem Rev*, 2014, **114**, 4496–4539.

23 M. P. Lowe, D. Parker, O. Reany, S. Aime, M. Botta, G. Castellano, E. Gianolio and R. Pagliarin, *J Am Chem Soc*, 2001, **123**, 7601–7609.

24 M. P. Lowe and D. Parker, *Chemical Communications*, 2000, 707–708.

25 M. A. Caldwell, C. R. Brue, T. J. Whittemore and T. J. Meade, *RSC Adv*, 2020, **10**, 8994–8999.

26 Y. Wu, T. C. Soesbe, G. E. Kiefer, P. Zhao and A. D. Sherry, *J Am Chem Soc*, 2010, **132**, 14002–14003.

27 W. D. Horrocks and D. R. Sudnick, *Acc Chem Res*, 1981, **14**, 384–392.

28 K. Binnemans, *Coord Chem Rev*, 2015, **295**, 1–45.

29 R. M. Supkowski and W. DeW. Horrocks, *Inorganica Chim Acta*, 2002, **340**, 44–48.

30 A. Beeby, I. M. Clarkson, R. S. Dickins, S. Faulkner, D. Parker, L. Royle, A. S. de Sousa, J. A. G. Williams and M. Woods, *Journal of the Chemical Society, Perkin Transactions 2*, 1999, 493–504.

31 C. M. Metzler, R. Viswanath and D. E. Metzler, *Journal of Biological Chemistry*, 1991, **266**, 9374–9381.

32 A. N. Victor Talrose, A. A. Yermakov, A. A. Usov, A. N. Goncharova, N. A. Leskin, N. V. Messineva and M. V. E. Trusova, NIST Ethanone, 1-(3-pyridinyl)-, https://webbook.nist.gov/cgi/cbook.cgi?ID=C350038&Mask=400, (accessed 9 February 2024).

33 C. Spangler and M. Schäferling, *Lanthanide Luminescence chemical sensors*, Springer Berlin Heidelberg, Berlin, Heidelberg, 2011, vol. 7.

34 F. S. Richardson, *Chem Rev*, 1982, **82**, 541–552.

35 S. Aime, M. Botta and G. Ermondi, *Inorg Chem*, 1992, **31**, 4291–4299.

36 R. S. Dickins, D. Parker, J. I. Bruce and D. J. Tozer, *Dalton Transactions*, 2003, 1264–1271.

37 M. Woods, S. Aime, M. Botta, J. A. K. Howard, J. M. Moloney, M. Navet, D. Parker, M. Port and O. Rousseaux, *J Am Chem Soc*, 2000, **122**, 9781–9792.

38 A. M. Funk, K.-L. N. A. Finney, P. Harvey, A. M. Kenwright, E. R. Neil, N. J. Rogers, P. K. Senanayake and D. Parker, *Chem Sci*, 2015, **6**, 1655–1662.

39 B. Bleaney, *Journal of Magnetic Resonance (1969)*, 1972, **8**, 91–100.

40 O. A. Blackburn, A. M. Kenwright, P. D. Beer and S. Faulkner, *Dalton Transactions*, 2015, **44**, 19509–19517.

41 O. A. Blackburn, A. M. Kenwright, A. R. Jupp, J. M. Goicoechea, P. D. Beer and S. Faulkner, *Chemistry - A European Journal*, 2016, **22**, 8929–8936.

Chapter 3: On redox probes

Introduction

Physiological redox

In biological systems redox homeostasis must be maintained for cellular tissue to survive.[1] Reactive oxygen species were considered to have solely detrimental effect on the physiological redox environment, but these are now known to have signalling funtions.[1] The line between these two settings is not clear-cut.[1]

Multiple sclerosis and redox

Multiple sclerosis (MS) is an autoimmune demyelinating disease which affects the central nervous system.[2–4] It is also the most common neurological condition in young adults.[2–4] A possible cause for this disease is infection by the Epstein-Barr virus.[4,5] Symptoms of this disease include loss of motricity, spasticity, pain, anxiety and depression.[3] The pathogenesis of MS involves B-cells and T-cells causing the demyelination and neuroinflammation and consequently, the neurodegeneration associated with MS.[2,4,6] The diagnostic tools used to identify this condition include MRi and lumbar punctures.[4] The MacDonald criteria is used to diagnose MS.[4] These criteria require dissemination of lesions in time and space to diagnose MS by MRi.[4] Dissemination is observed by comparing MRi scans which are done periodically on the patient.[4]

The blood, cerebrospinal fluid and brain tissue samples obtained from post-mortem samples of MS patients show that the redox environment of these fluids/tissues is affected by this condition.[3] Possible biomarkers for MS include reactive nitrogen and reactive oxygen species.[3] The concentrations of these species and different enzymes change with progression of the condition.[3]

Azo dyes

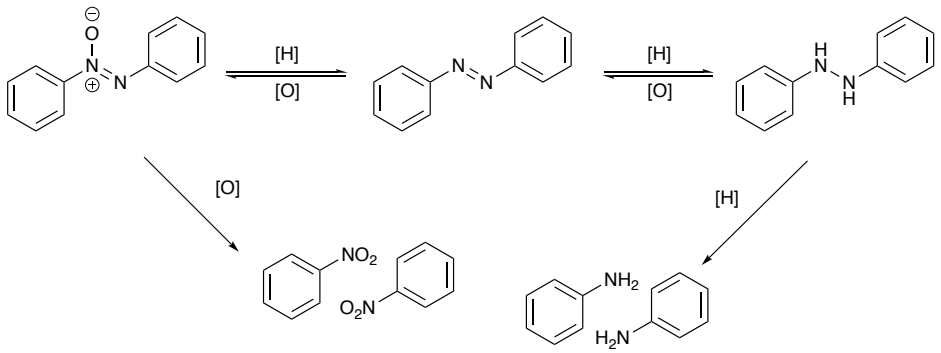
Azo dyes are coloured compounds which contain the R-N=N-R functional group.[7] These compounds are commonly used as dyes and pigments in clothing. The degradation some azo dyes result in aromatic amines which are carcinogenic compounds as well as being harmful to the environment.[8,9] This has caused the use of many of this type of azo dyes as pigments to be banned in the European Union.[9]

Synthesis of azo dyes

There are a number of ways of synthesising azo dyes. These include azo coupling and the Baeyer-Mills reaction. Azo coupling reactions require the formation of a diazonium ion from an aromatic amine. This then reacts via an electrophilic aromatic substitution mechanism to form an azo functional group. The Baeyer-Mills reaction involves the formation of an aromatic nitroso compound which then reacts via a nucleophilic addition with an aromatic amine to give the desired azo compound.[10]

Redox behaviour of azo dyes

Azo dyes are very varied in their redox behaviour, with the ability to both be oxidised and reduced to various compounds (see scheme 3.1).



Scheme 3.1 : Redox products of azo compounds

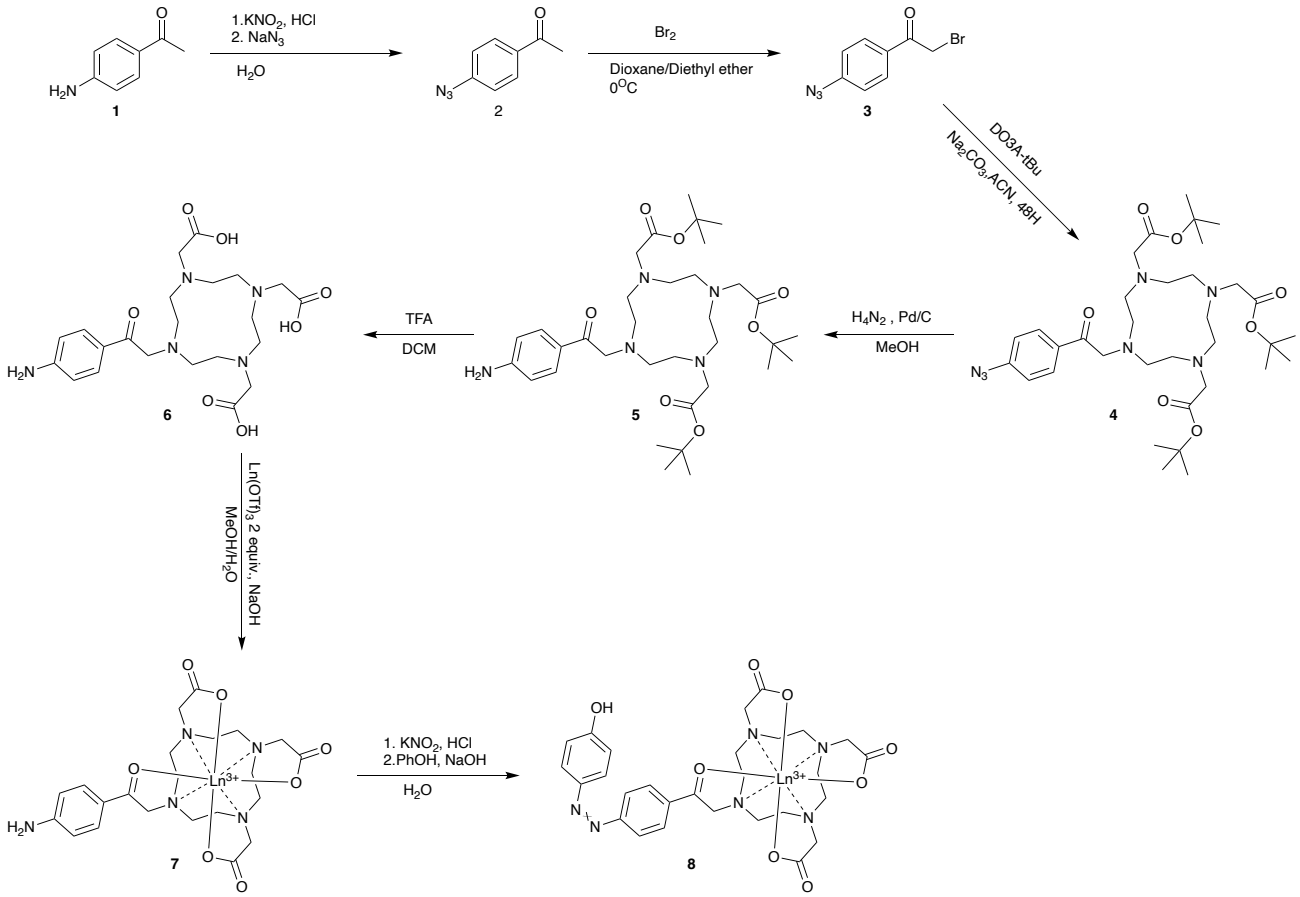
These redox products are formed under various conditions. Cyclic voltammetry measurements show that azo dyes have 4 different redox potentials each related to the production of different products.[11]

Aim

The aim of this synthesis is to produce a redox sensitive lanthanide probe with the ability to measure both hypoxic and hyperoxic environments. This is to be achieved with an azo dye as the redox sensitive group. The proposed synthetic target (**8**) fits this description.

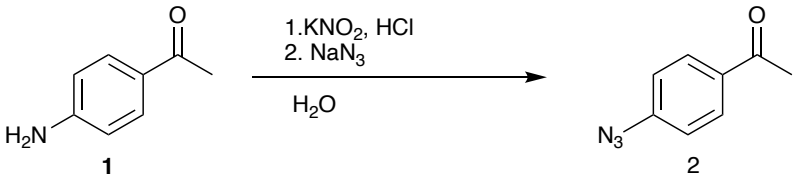
Synthesis

Initially, this synthesis was attempted by alkylating bromoacetyl para-azophenol. The bromination of the acetyl azophenol at the alpha carbon was found to be impractical due to azo-hydrazo tautomerism causing the enol required for the bromination to form between the ipso and carbonyl carbons in preference to the carbonyl and alpha carbon. This led to mostly unreacted starting material. A different synthetic route was carried out where the azo dye was to be formed at the end of the synthesis. The initial part of this second synthetic route (steps 2 and 3) had been carried out before by Tropiano & Faulkner.[12] The final reaction produced novel compounds (as far as a search on Reaxys and Scifinder could show). The overall yield for the synthesis up and including step 5 was 32%.



*Scheme 3.5 : Synthetic plan of the target molecule (**8**)*

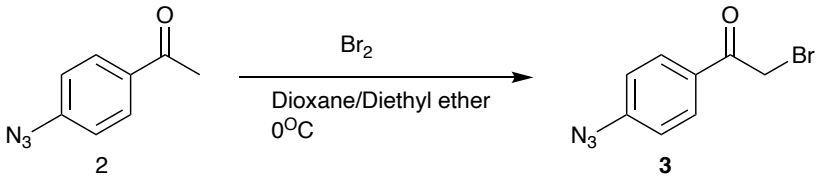
Azidation of 4'aminoacetophenone



Scheme 3.6 : Azidation of 4'aminoacetophenone

This first step of the synthesis was the substitution of an amino group via an azidation reaction. This resulted in the desired azide in good yield (78%). This reaction proceeded via the formation of a diazonium species which then reacts with an azide ion via a SN_{ar} mechanism to give the desired 4-azido acetophenone. This was done to protect the amine group from alkylation by the bromoketone produced in the next step.

Bromination of 4'-azidoacetophenone



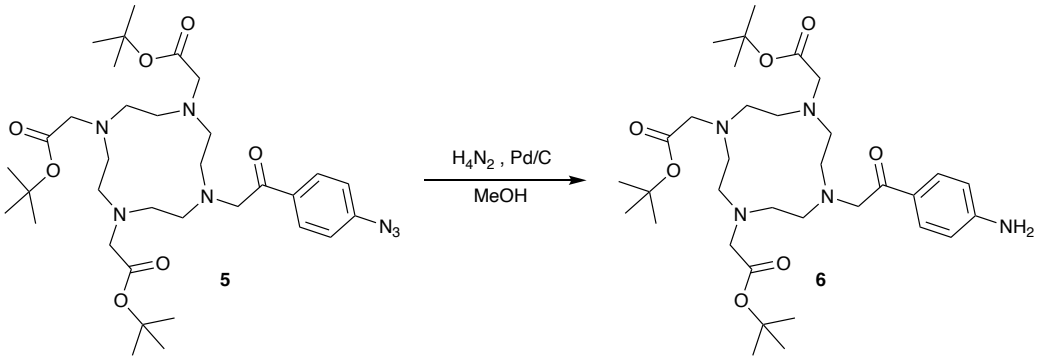
Scheme 3.7 : Bromination of 4'azidoacetophenone

This bromination step proceeded via the mechanism shown in scheme 3.4, albeit more successfully than in the previous synthetic attempt producing the monobrominated (**3**) and dibrominated 4'azidoacetophenone in 73% and 5% yields respectively.

Alkylation 1-(4-azidophenyl)-2-bromoethan-1-one

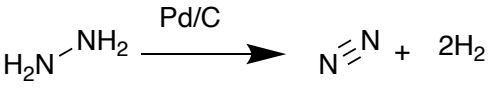
This alkylation proceeded via an SN_2 mechanism over 2 days. In contrast to the similar reactions shown in Chapter 2: On pH probes, it proceeded without much difficulty and with good yield (72%).

Reduction of the azido group



Scheme 3.8 : Reduction of azide to amine by hydrazine and palladium on carbon.

The azido functional group was reduced via a hydrogenation reaction involving hydrazine and palladium on carbon.[13] In this reaction, palladium on carbon causes the hydrazine to decompose as shown in Scheme 3.9.[13]

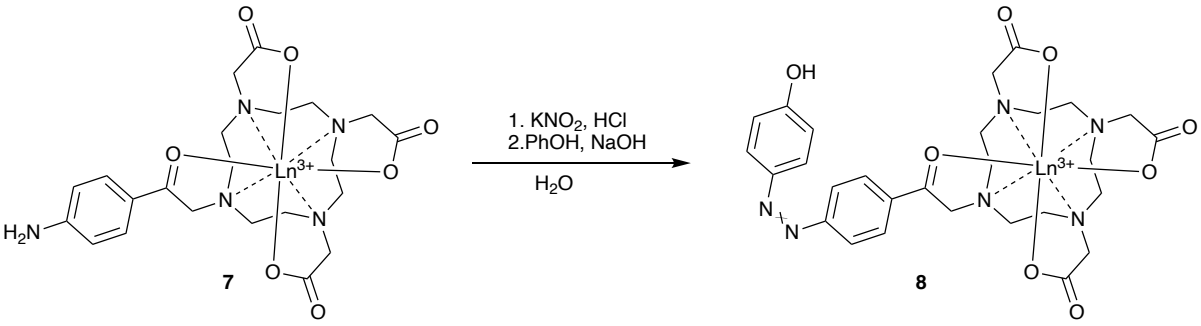


Scheme 3.9 : Decomposition of hydrazine by palladium on carbon.

The hydrogen produced by the decomposition then reacts with thiazide to generate an amine in a very good yield (82%). The purification of the product of this reaction involved filtration though a pad of celite. This resulted in the desired product with some slight contamination by hydrazine. The product was not purified as it was deemed easier to remove the hydrazine by dialysis after deprotection.

This method was selected after two different methods were tested. These were a Staudinger reaction and reduction by ammonium chloride and zinc. The first reaction was not selected due to the difficulty removing the phosphine oxide. The second condition was successful in reducing the azido group but had a lower yield than the reduction by hydrazine.

Formation of the azo dye



*Scheme 3.10 : Azo coupling of **7**.*

The syntheses of the Pr and Lu analogues (**8**) was completed by a standard azo coupling reaction. Mass spectrometry sample of crude products of these reactions were characterised by high resolution mass spectrometry (HRMS), these measurements showed the presence of the synthetic target. A crude NMR of the Lu analogue (**8Lu**) was taken. This showed the presence of multiple shifts in the aromatic region, some of which were produced by protons on phenol, the possible principal impurity. The phenol impurity was removed from the crude sample by preparative HPLC (Figure 3.1).

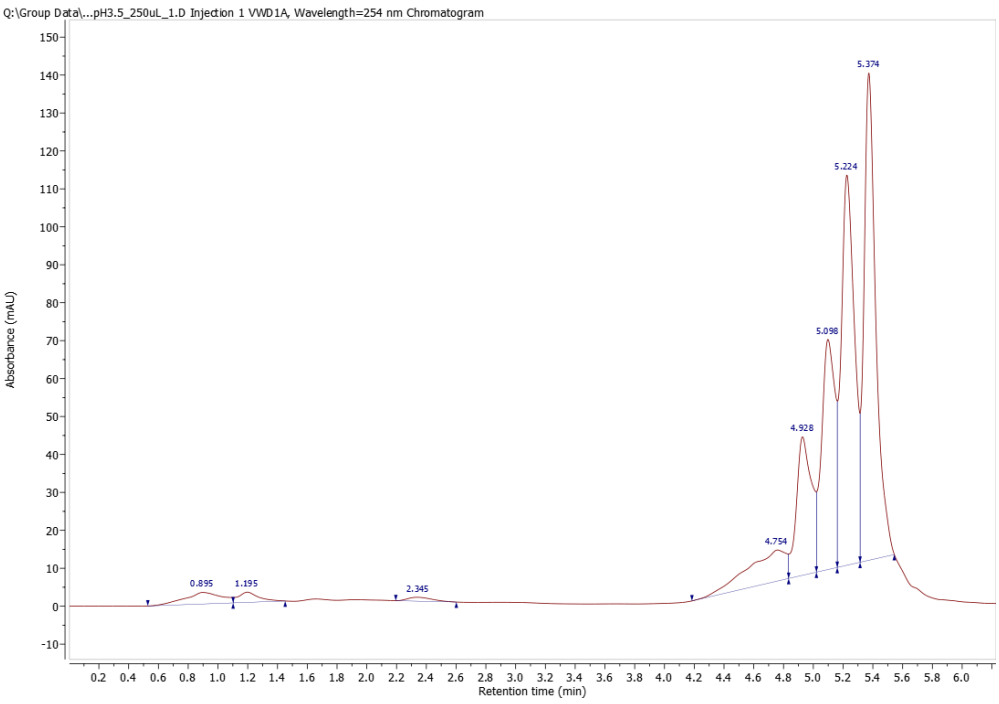
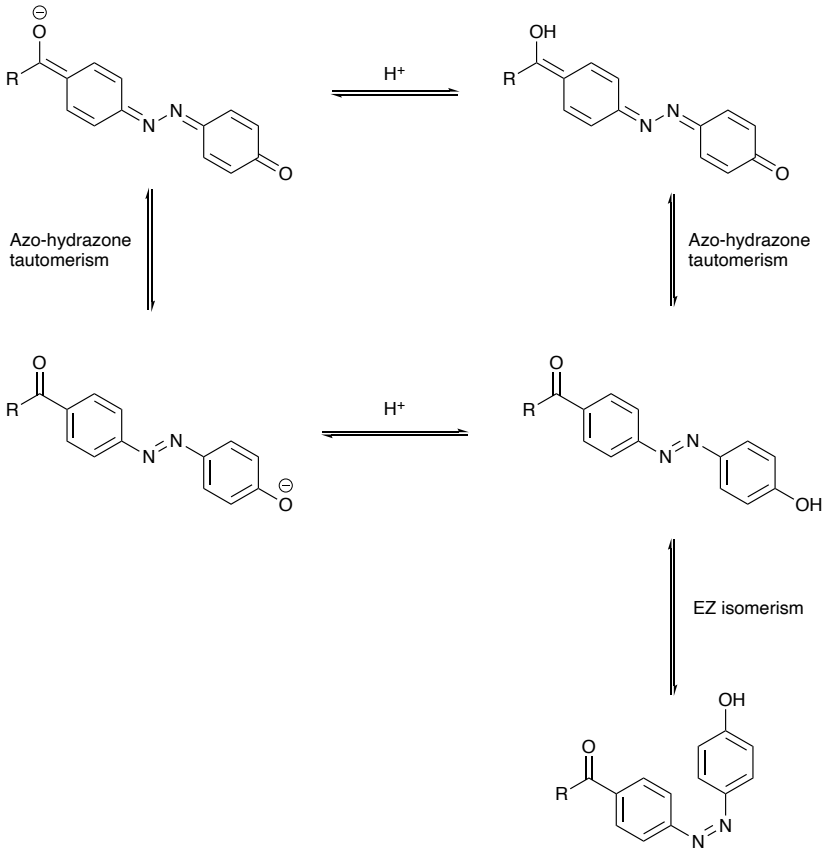


*Figure 3.1 : HPLC trace of the crude **8Lu** sample.*

The chromatograph showed three sets of peaks: two small peaks and a large envelope of peaks. The fractions from large envelope of peaks were collected and dried to give 18 mg of **7Lu** (35% yield). Although the envelope may suggest that the compound is very impure, this was not the case as the azo dye functional group forms many different isomers, tautomers and acid-base pairs each of which may have a different retention factor (Scheme 3.11).



Scheme 3.11 : the possible different acid-base pairs, tautomers and isomers of the azo dye complex **8**. R is a Ln^{3+} complexed by a DO3A type ligand.

The total yield (from **4** to **8**)for the synthesis was 21%, giving an average yield per step of 73%.

An NMR of the product purified by HPLC was recorded (see Figure 3.2). This showed shifts in the aromatic range which correspond with those expected for a diazo compound. The shifts between 2.50 and 4.00 ppm correspond to the DO3A fragment.

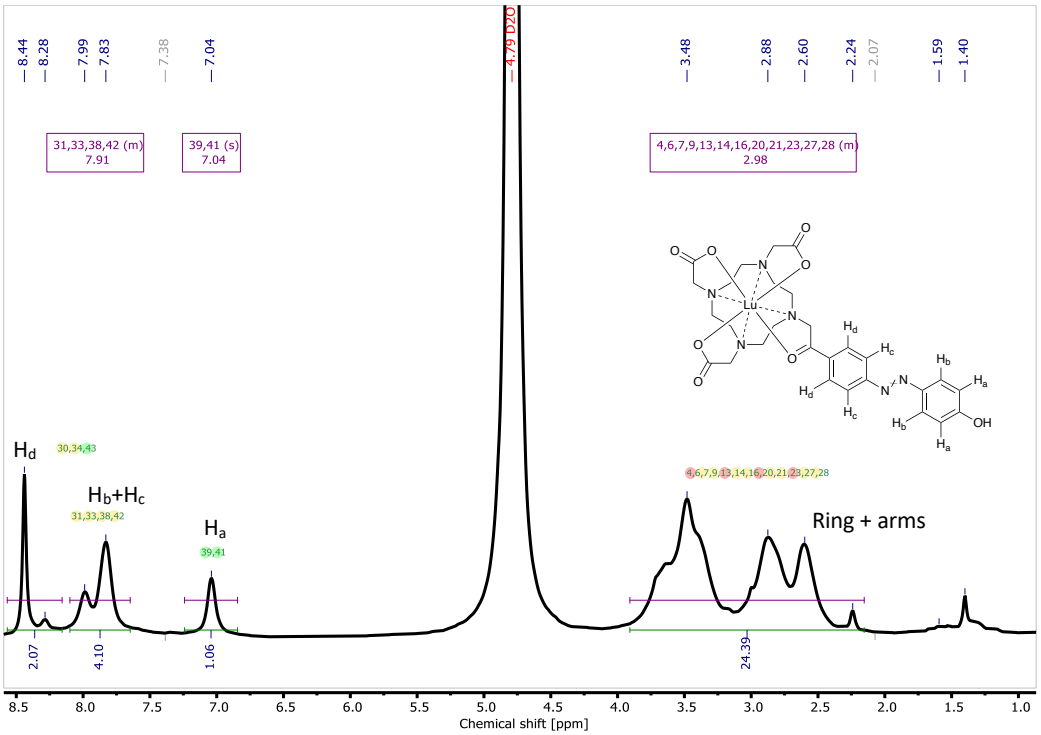


*Figure 3.2 : HNMR of **8Lu** in D_2O.*

The praseodymium analogue of **8** was also synthesised following the same process. High resolution mass spectrometry confirmed the success of the synthesis and the NMR was recorded. (see Figure 3.3) The yield from **4** to **8Pr** was 25%.

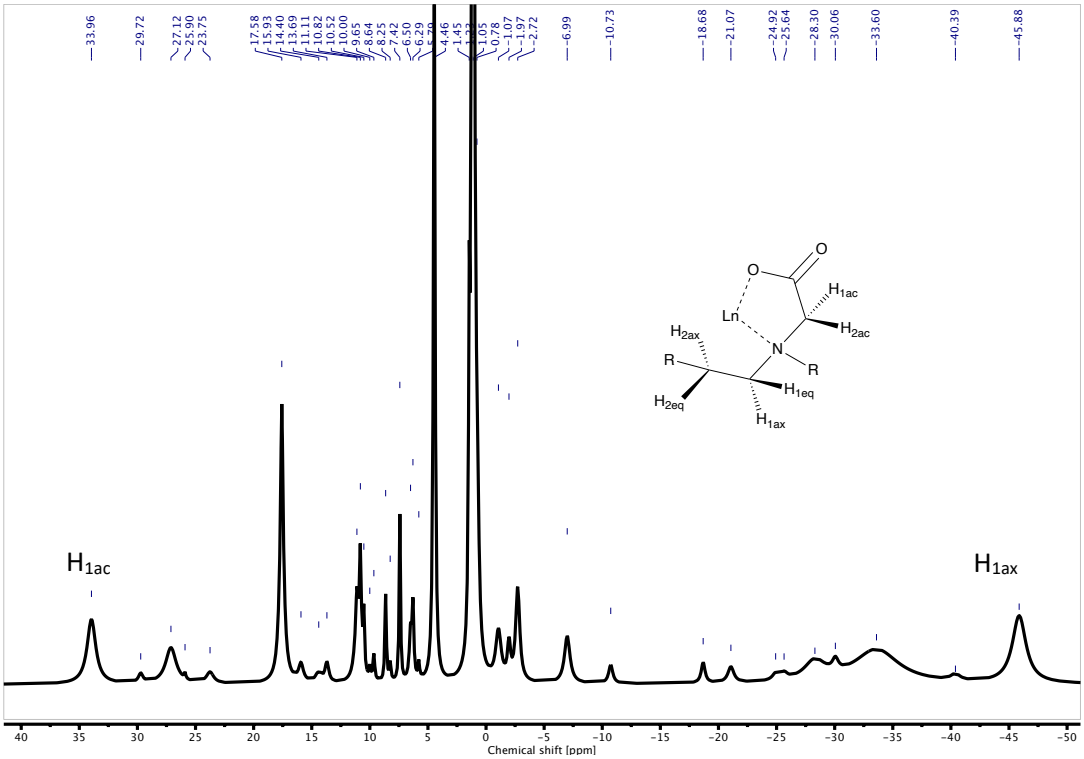


*Figure 3.3: HNMR of **8Pr** in DMSO-D_6. Peaks assigned areonly those which could be confidently assigned.*

Conclusion

The synthesis of a redox sensitive probe was successful, and the synthetic problems encountered over the course of the synthesis were overcome to produce the praseodymium and lutetium analogues of the synthetic target. A yield of 21% was recorded for the synthesis of **8Lu** and 25% for **8Pr** from **4** to **8**. All of the steps of this synthesis, except for the final reaction had a good, very good or almost quantitative yield. This synthetic route could be used to synthesise water-soluble azo based redox probes.

References

1 M. C. Zimmerman and A. J. Case, *Redox Biol*, 2019, **27**, 101267.

2 K. Ohl, K. Tenbrock and M. Kipp, *Exp Neurol*, 2016, **277**, 58–67.

3 M. Tanaka and L. Vécsei, *Biomedicines*, 2020, **8**, 406.

4 R. Dobson and G. Giovannoni, *Eur J Neurol*, 2019, **26**, 27–40.

5 S. S. Soldan and P. M. Lieberman, *Nat Rev Microbiol*, 2023, **21**, 51–64.

6 J. M. Frischer, S. D. Weigand, Y. Guo, N. Kale, J. E. Parisi, I. Pirko, J. Mandrekar, S. Bramow, I. Metz, W. Brück, H. Lassmann and C. F. Lucchinetti, *Ann Neurol*, 2015, **78**, 710–721.

7 E. of E. Britannica, azo dye, https://www.britannica.com/science/azo-dye., (accessed 8 August 2023).

8 S. H. Hashemi and M. Kaykhaii, in *Emerging Freshwater Pollutants*, eds. T. Dalu and N. T. Tavengwa, Elsevier, 2022, pp. 267–287.

9 C. Senaldi, P. Piccinini, E. Buriova and Institute for Health and Consumer Protection., *European survey on the presence of banned azodyes in textiles*, Publications Office, 2008.

10 R. J. Tombari, J. R. Tuck, N. Yardeny, P. W. Gingrich, D. J. Tantillo and D. E. Olson, *Org Biomol Chem*, 2021, **19**, 7575–7580.

11 A. Zille, P. Ramalho, T. Tzanov, R. Millward, V. Aires, M. H. Cardoso, M. T. Ramalho, G. M. Gubitz and A. Cavaco-Paulo, *Biotechnol Prog*, 2004, **20**, 1588–1592.

12 M. Tropiano and S. Faulkner, *Chem. Commun.*, 2014, **50**, 4696–4698.

13 A. Furst, R. C. Berlo and S. Hooton, *Chem Rev*, 1965, **65**, 51–68.

Chapter 4: On CF parameters

Introduction

CF parameters

According to perturbation theory one may describe the effect of a crystal field on an ion as a separate Hamiltonian operator acting on the wavefunction of the metal centre.[1] Figure 4.1 shows how this can be described.

$$H = H_{free\ ion} + H_{crystal\ field}$$

$$H_{crystal\ field} = \sum_{i=0}^{n} \sum_{k=0}^{\infty} \sum_{q=-k}^{k} B_q^k C_q^k(i)$$

Figure 4.1 : H is the total Hamiltonian operator, i is the nth electron, n is the number of electrons, k is the rank of the operator, q is a component, $C_q^k(i)$ are tensor operators and B_q^k are crystal field parameters.[1,2]

The number of parameters related to a particular metal centre depends on the symmetry around the metal centre,[1,2] ranging from one for I_h symmetric complexes to twenty-seven for C_1 symmetric complexes.[1,2] It should be noted that these parameters describe the perturbation across all the f-orbitals rather than a particular orbital.

In the case of a lanthanide ion in an I_h ligand field, the orbitals split as shown in Figure 4.2. The value of ΔI_h is equal to 14Dq (differential quanta) and depends solely on B_0^6 as shown by Equation 4.1.

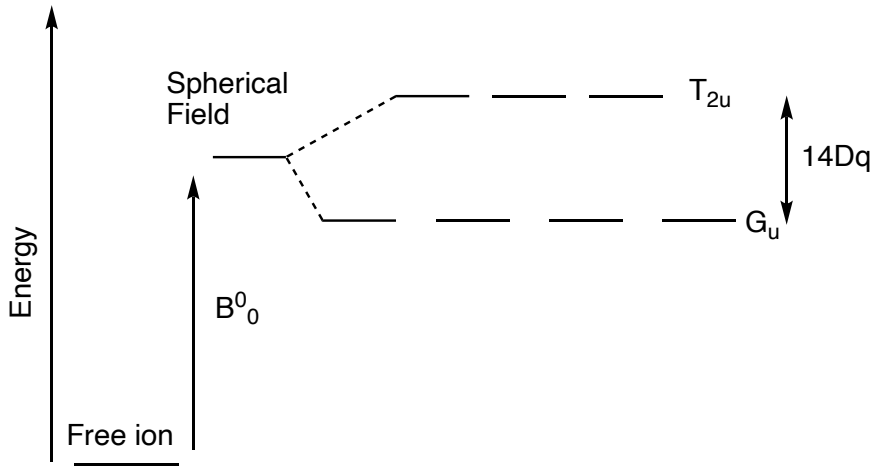


Figure 4.2 : the splitting of f-orbitals in an icosahedral crystal field as rationalized by M. Suta, F. Cimpoesu and W. Urland.[3]

We should be aware that Δ values refer to the largest split in the crystal field which in the case of lanthanides in an icosahedral crystal field is the only split orbital energy.

Equation 4.1 : Dependency of ΔI_h on B_0^6 as rationalised by M. Suta, F. Cimpoesu and W. Urland.[3]

$$14\mathrm{Dq} = \frac{175}{429}\mathrm{B}_0^6$$

Lanthanides in an Elpasolite structure (K_2NaAlF_6, the lanthanide substitutes Al) are forced to occupy sites of octahedral symmetry. This crystal field causes the orbitals to split in energy twice into 3 sets with irreducible representations of A_{2u}, T_{1u} and T_{2u} as shown if Figure 4.3.

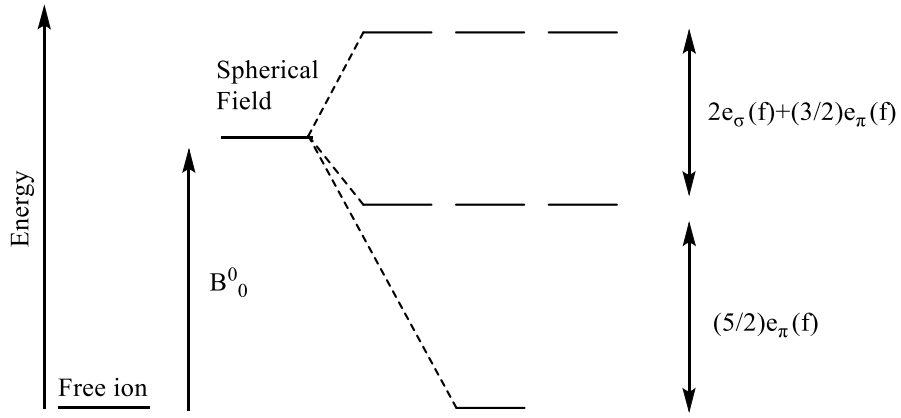


Figure 4.3 : the splitting of f-orbitals in an octahedral crystal field. Where B_0^0 is the spherical crystal field parameter, e_σ is the perturbation caused by a sigma interaction and e_π is the perturbation caused by a pi interaction.[3]

All other point groups are subgroups of either the O_h or the I_h point groups. Therefore, all coordination environments can be treated as distortions of one of these point groups as shown by Figure 4.4.

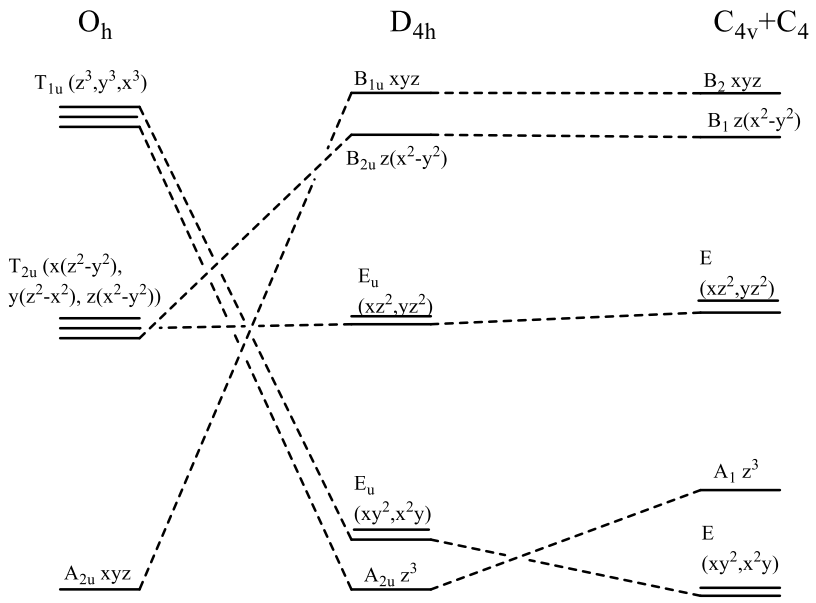


Figure 4.4 :: 'Descent of symmetry' showing the change in f-orbital splitting from Oh symmetry to C_4.

Current CF-LF theories

There are several theories pertaining to the crystal/ligand field of lanthanide complexes. The 3 main ones are the point charge electrostatic model (PCEM), angular overlap model (AOM) and simple overlap model (SOM).[4]

PCEM

The PCEM model considers that all of the interactions between the electrons of the metal ion and the ligating ions/atoms' electrons as additive quantities.[2] The main pitfall of this theory is that it considers that all interactions are electrostatic in nature and that covalent interactions are non-existent.[2] This model gives rise to equation 4.2. This allows for the crystal field parameters to be estimated from crystallographic data and in the case of

parameters of with non-zero quotients to be assigned a value through a combination of symmetric arguments and the formulae obtained by the PCEM.

Equation 4.2 : relationship between the second, fourth, and sixth order zeroth quotient crystal field parameters and the position of the ligating ions/atoms along a z crystallographic axis. Where: Z is the effective nuclear charge of the ligand (equal to 1 if ligating species has no charge), p the number of axial ligands, m the number of ligands at the base of the metal centre and n the number of equatorial Ligands, R is the distance between a ligand and the ion, $<r^2>$ is the expectation value and θ is the angle from the z crystallographic axis which the ligating species is on.

$$B_0^2 = Ze^2 \frac{< r^2 >}{R^3}\left[p - \frac{n}{2} + m(3\cos^2\theta - 1)\right]$$

$$B_0^4 = Ze^2 \frac{< r^4 >}{R^5}\left[p + \frac{3n}{8} + \frac{m}{4}(35\cos^4\theta - 30\cos^2\theta + 3)\right]$$

$$B_0^6 = Ze^2 \frac{< r^6 >}{R^7}\left[p - \frac{5n}{16} + \frac{m}{8}(231\cos^6\theta - 315\cos^4\theta + 105\cos^2\theta - 5)\right]$$

This model assumes all ligating ions are identical except for their formal charge. This assumption is not wholly valid as the values predicted by this model are not usually close to the values of the phenomenological parameters.[4] This is because differences in polarizability and the possibility of orbital overlap are not accounted for in this model.

AOM

This model considers that there is some weak overlap between the orbitals of the ligand set and the f-orbitals.[4] Using the method described in M. Suta, F. Cimpoesu and W. Urland, *Coord. Chem. Rev.*, 2021, **441**, 213981. We can rationalise that the crystal field around a lanthanide ion in $[LnDOTA(H_2O)]^-$ (C_4 symmetry in solution) to be as shown by Figure 4.5.

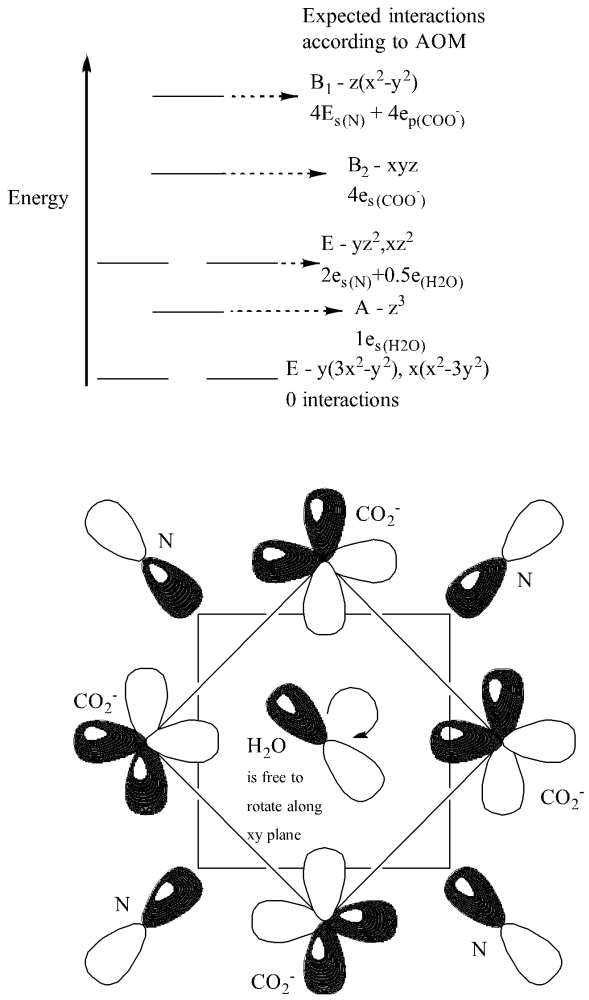


Figure 4.5 : ligand field splitting and possible f orbital-ligand interactions in [LnDOTA(H_2O)]$^-$ in aqueous solution. For ease of interpretation, we have not displayed the sigma interaction of the H_2O molecule. The view of the interactions is from the perspective from the z axis, the x and y axes are found on the diagonals formed between the p orbitals of the N atoms.

Figure 4.5 shows the expected interactions of the f orbitals in [Eu(DOTA)(H_2O)]$^-$. This method considers that there are four possible types of overlaps between the f orbitals and ligating orbitals. These are: sigma, pi, delta, and phi interactions.

SOM

This model considers that the crystal field interacting with the 4f electrons is not completely symmetric and that the point charges causing the perturbation are found somewhere halfway between the ligands and the metal centre.[4] SOM crystal field parameters are

calculated by using the values obtained by the AOM model and applying a correction factor as shown in Equations 4.3 and 4.4.

Equation 4.3 : relationship between SOM crystal field parameters and AOM crystal field parameters. p is proportional to the overlap between metal and ligands and β is a correction factor.

$$B_q^k(SOM) = p(2\beta)^{k+1}B_q^k(AOM)$$

Equation 4.4 : calculation of the correction factor. P_L is another correction factor describing the position of the region of charge, R_0 is the shortest metal-ligand distance and R_L the distance of the bond being considered.

$$\beta = \frac{1}{1 \pm P_L} \quad P_L = 0.05\left(\frac{R_0}{R_L}\right)^{3.5}$$

Lanthanide anisotropy and parametrisation

The energy levels of lanthanides are split by the crystal field. The parametrization of these spectra can be obtained by the Stevens method.[5] This method uses operator equivalents to obtain values for the crystal field parameters by substituting coordinated generated by spherical harmonics with total angular momentum ($J_{x,y,z}$) vector operators.[5,6] These operator equivalents describe the character of the spherical harmonics which describe the m_j states of a particular manifold.[6] The Stevens second rank, zeroth quotient and second rank, zeroth quotient operators define the electronic distribution along the ion's z axis an xy plane (See Equation 4.5).[6,7]

Equation 4.5 : second rank Stevens operator equivalents where J_z is the total angular momentum vector in the z direction.

$$O_0^2 = 3{J_z}^2 - J(J+1), if\ J = 1\ then\ O_0^2 = 1, -2$$

$$O_2^2 = \frac{1}{2}\left({J_+}^2 - {J_-}^2\right), m_j = J_{\pm 1}, if\ m_j = \pm 1\ then\ O_2^2 = 1, -1$$

These operators are then multiplied by so called Stevens coefficients to give the second rank multiple moments of the m_J state in question (Equation 4.5).[6] The stevens coefficients are specific to each manifold of each lanthanide.[5,6]

The sign of the second rank zeroth quotient multiple moment of the m_J state describes whether the electronic distribution of a particular m_J state is oblate or prolate.[6] If positive, distribution is prolate and if negative it is oblate (see Figure 4.6).[6]

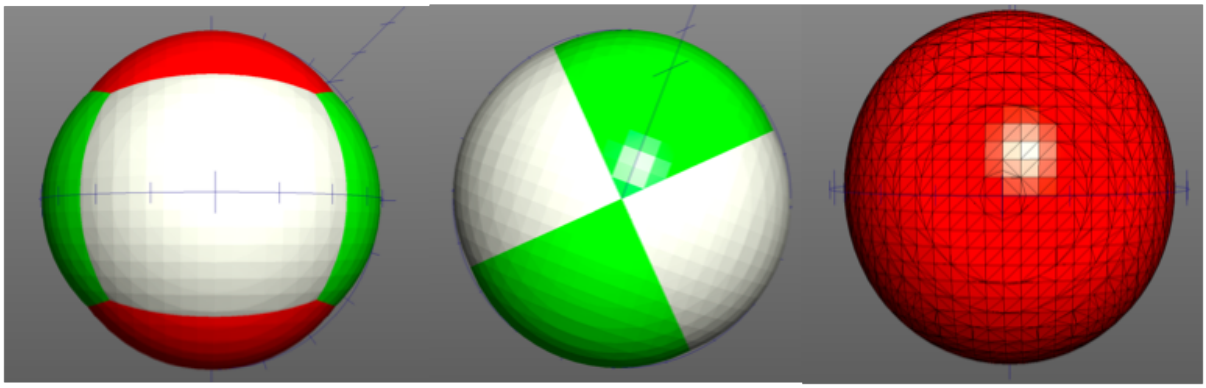


Figure 4.6 : electronic distribution of the $^7F_1$ manifold modelled using tesseral harmonics (left). Electronic distribution of the m_J=±1 components viewed from z axis (total quadrupole moment=-0.1, oblate anisotropy) (centre). Electronic distribution of the m_J= 0 component viewed from xy plane (total quadrupole moment=0.2, prolate anisotropy)

By using the spherical harmonics Y_0^0, Y_0^2, Y_0^4 and Y_0^6, we can plot the electronic distribution of m_j state.[8] Figure 4.6 shows the electronic distributions of the manifold components of the $^7F_1$ energy level of europium by the method presented by Sievers.[8] This manifold is described only by zeroth and second order spherical harmonics. For energy levels with J>3/2 the manifold components are described the electronic distribution by the addition of higher quotient spherical harmonics (see Figure 4.7).[8]

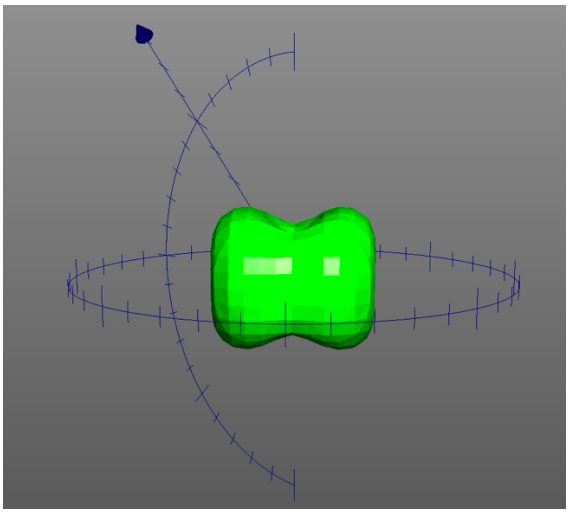


Figure 4.7 : Electronic distribution of $^7F_2$ m_J=±2 manifold component as described by the Sievers method.[8]

The perturbation by the crystal field affecting each manifold is quantified by Stevens parameters.[5,6]

These parameters can be estimated in several ways. These include by fluorescence spectra, EPR and NMR.

From fluorescence spectra

We may parametrise the fluorescent emission spectra by the use of the Stevens parametrization method.[5,6] This is done by identifying the barycentre of each manifold, assigning the appropriate m_J value to each stark level. The energy difference between each stark level and the barycentre is the sum of all the products of the multipole quotients and the Stevens parameters,[5,6] Equation 4.6 shows how this is done for the $^7F_1$ manifold of Eu^{3+} and Tb^{3+}.

Equation 4.6: parametrization of the $^7F_1$ manifold by the Stevens parametrization (left) and Wybourne (right).[5,9,10] *Where $\Delta_{mj=0}$ is the perturbation of the m_j=0 state from barycentre (in cm^{-1}), $\Delta_{mj=\pm1}$ is the perturbation of the m_j=±1 states from barycentre(in cm^{-1}), α is the Stevens parameter (0.2 for the $^7F_1$ manifold).*[5,6]

$$\Delta_{mJ=0,\pm1} = A_0^2 O_0^2 + A_2^2 O_2^2 \qquad \Delta_{mJ=0,\pm1} = B_0^2 \mathrm{C}_0^2 + B_2^2 \mathrm{C}_2^2$$

$$\Delta_{mJ=0} = -2\alpha A_0^2 \qquad \Delta_{mJ=0} = -\frac{2}{10} B_0^2$$

$$\Delta_{mJ=\pm1} = \alpha A_0^2 \pm \frac{1}{2}\alpha A_2^2 \qquad \Delta_{mJ=\pm1} = \frac{1}{10} B_0^2 \pm \frac{\sqrt{6}}{5} B_2^2$$

Stevens parameters have now been largely replaced by Wybourne parameters (B_x^x).[9–11] These can be easily obtained by multiplying Stevens parameters by the factor in which these multiplied in the original Bleaney Theory paper.[7,10] Table 4.1 shows the Stevens-Wybourne equivalents of the even rank and quotient parameters used to describe orthorhombic crystal fields.[10,12]

Table 4.1 : Stevens-Wybourne parameter equivalents for parameters of even rank and even quotient.[10,12]

		Parameter rank		
		k=2	k=4	k=6
Parameter quotient	0	$B_0^2 = 2A_0^2 < r^2 >$	$B_0^4 = 8A_0^4 < r^4 >$	$B_0^6 = 16A_0^6 < r^6 >$
	2	$B_2^2 = \frac{2}{\sqrt{6}} A_2^2 < r^2 >$	$B_2^4 = \frac{4}{\sqrt{10}} A_2^4 < r^4 >$	$B_2^6 = \frac{16}{\sqrt{105}} A_2^6 < r^6 >$
	4		$B_4^4 = \frac{8}{\sqrt{70}} A_4^4 < r^4 >$	$B_4^6 = \frac{16}{3\sqrt{14}} A_4^6 < r^6 >$
	6			$B_6^6 = \frac{16}{\sqrt{231}} A_6^6 < r^6 >$

Bleaney theory

Bleaney's theory is the name given to a theory which describes the effect magnetic anisotropy has on the NMR spectra of paramagnetic complexes of lanthanides.[7] This theory links the pseudocontact shift of the NMR signal of a proton in a lanthanide complex to the position of said proton with respect to the magnetic z and xy axes of the complex and the B_0^2 and B_2^2 parameters as shown in Equation 4.7.[7,13]

Equation 4.7 : Bleaney Theory formula (in CGS units). Where X_{ax} is the axiality, X_{rh} is the rhombicity of the magnetic susceptibility, X_{xx}, X_{yy} and X_{zz} are the magnetic susceptibility tensors in the X, y, and z axes, r is the distance between the proton in question and the metal centre responsible for the shift, φ is the angle along the xy axis on which the proton is located, θ is the angle along the z axis on which the proton is found, C_j is the Bleaney factor and μ_b is the Bohr magnetron.[7,13–15] Crystal field parameter values in these formulae must be in ergs.

$$\partial = X_{ax}\frac{3cos^2\theta - 1}{r^3} + \frac{3}{2}X_{rh}\frac{sin^2\varphi cos^2\theta}{r^3},$$

$$X_{ax} = \frac{{\mu_b}^2 C_j B_0^2}{60(kT)^2} = X_{zz} - X_{av}, X_{rh} = \frac{3}{2} \times \frac{{\mu_b}^2 C_j B_2^2}{60(kT)^2} = X_{xx} - Xyy$$

This equation has been further expanded to take into account the effect of other second rank parameters[16] as shown in Equation 4.8 and to consider the effect of higher order crystal field parameters.[17] Taking into consideration the higher order CF parameters leads to an estimation of the shifts from a structure to be within a 20% margin of error.[17]

Equation 4.8 : Bleaney theory expanded to include X_{xy}, X_{xz} and X_{yz} magnetic susceptibility tensors.[16]

$$\partial^{pc} = X_{ax}\frac{3cos^2\theta - 1}{r^3} + \frac{3}{2}X_{rh}\frac{cos(2\varphi)sin^2\theta}{r^3} + X_{xy}\frac{(sin^2\theta sin\,(2\varphi))}{r^3}$$

$$+ X_{xz}\frac{(sin\,(2\theta)cos\varphi)}{r^3} + +X_{yz}\frac{(sin^2\theta sin\varphi)}{r^3}$$

Correlation of between pKa and B_0^2

Inspired by the correlation between pKa and the luminescence intensity of hypersensitive transitions[18] as shown in Henrie, et al., 1976, we decided to consider whether such a correlation exists between ligand pKa and B_0^2. pKa could be considered a parameter which represents a measurement of the stability of the ligating mode of the ligand. The pKa data for the complexes examined in Figure 4.8 was obtained from SciFinder and was predicted by their Advanced Chemistry Development (ACD/Labs) Software V11.02 (© 1994-2021 ACD/Labs). This gave data for individual functional groups in a molecule. For the purposes of determining the presence of a correlation between pKa and B_0^2, the mean pKa was calculated for the entire ligand and for the full set of non-cyclen ligands. The axial crystal field parameter (B_0^2) data was obtained from references 13 ,14, 19, 20, and 21 (see data in Appendix I: Crystal field parameters and pKa values for the ligands used to propose a correlation between the CF parameters and pKa). All of these have been measured in aqueous solution at room temperature except for cycEuphenLa and cycEuphen which were measured as a solid at 10K (Ref.19). Data from europium complexes was exclusively used as the B_0^2 parameter can be conveniently obtained from the $^5D_0 \rightarrow {}^7F_1$ transition[2,22] and as so most luminescence measurements of B_0^2 are obtained in this way.

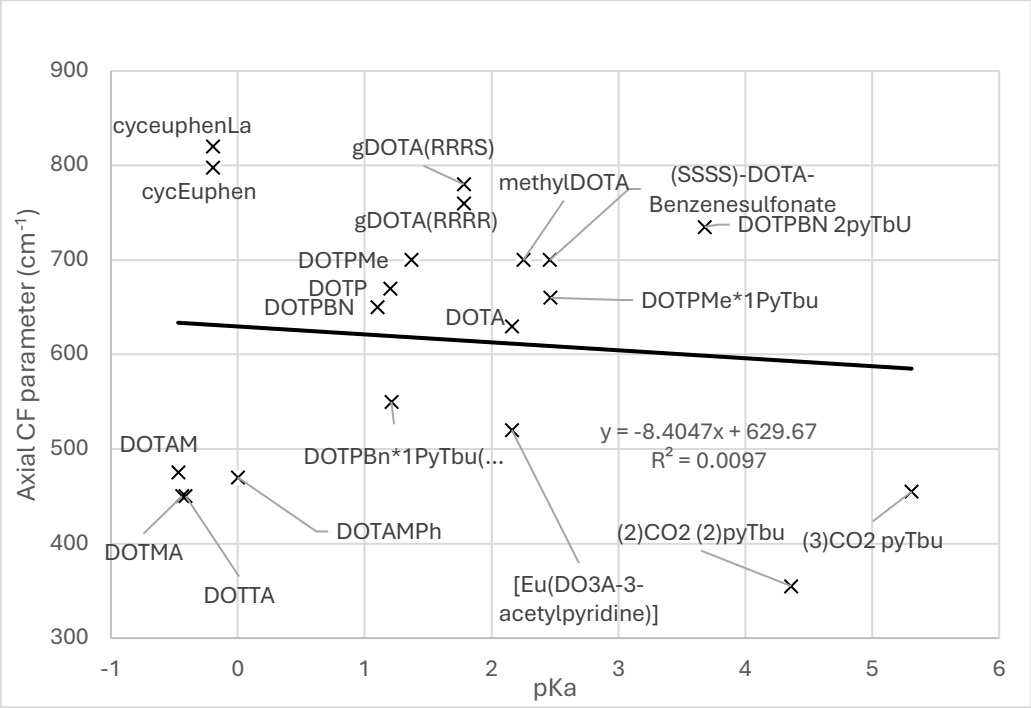


Figure 4.8 : correlation of the average pKa of the top ligand set (non-cyclen) and the absolute value of the axial crystal field parameter for all complexes collected from references 13, 14, 19, 20, *and* 21.

Initially, Figure 4.8 above was obtained. It did not show any correlation. To confirm whether this was due to two opposing trends caused by different symmetric environments, these data points were separated by symmetry point group. Leading to two sets of data; one for C_4 symmetric complexes and another C_1 complexes. It should be noted that the there is a difference in the coordination environment of phosphate-based ligands and carbonyl ligands, the former adopting a TSAP conformation and the latter a CSAP conformation. It should be also noted that the magnitude of B_0^2 for a complex in the TSAP form is usually at around 55% of the same complex in the CSAP form.[20]

One main failing for the following correlations presented in the following sections is the lack of data available for analysis. It should also be noted that the choice of solvent can have an effect of the B_0^2 parameter due to axial ligand effects and the solvent´s effect on the pKa of the ligating functional groups.

C4

The separation of C_4 complexes from Figure 4.8 produced Figure 4.9. This shows a very strong correlation (having a Pearson's correlation coefficient of 0.90) and a strong coefficient of determination (r^2=0.82) between the pKa of the top set of ligands and the magnitude of the B_0^2 crystal field parameter. It should be kept in mind that the sample size used was of 11 complexes; for a more accurate trend to assess the usefulness of pKa as a predictor, a larger sample size is needed. It should be noted that all the ligating atoms/ions in the top ligand set are oxygen based.

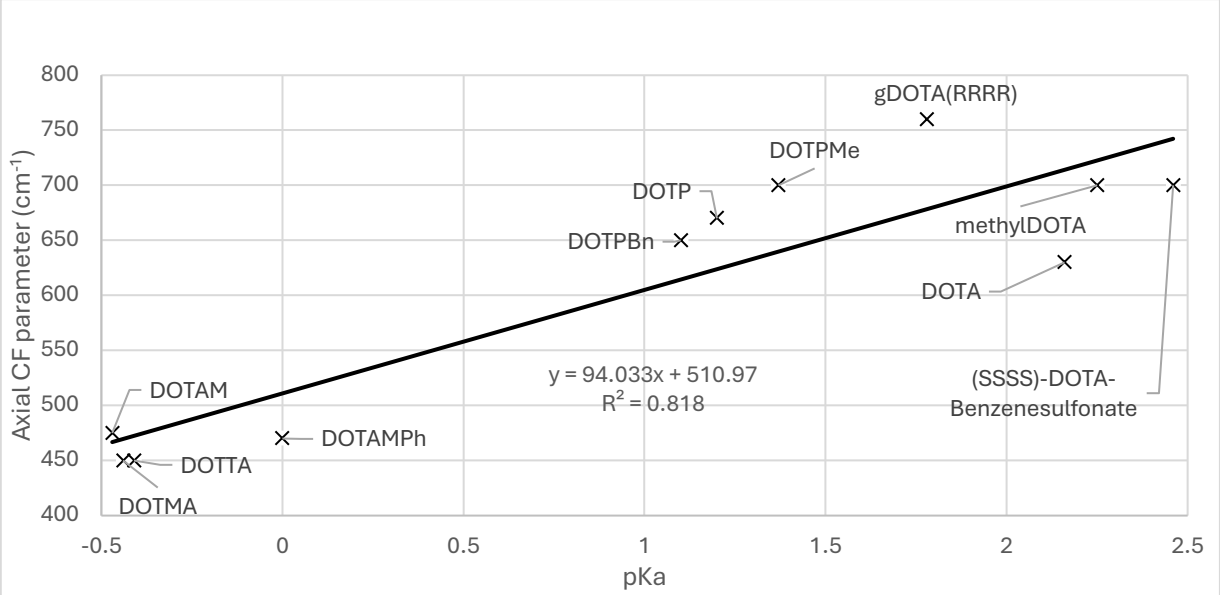


Figure 4.9 : correlation of the average pKa of the top ligand set (non-cyclen) and the absolute value of the axial crystal field parameter for C4 symmetric complexes collected from references 14, 19, 23, 20, *and* 21.

Analysis of the difference between values predicted by the trendline and actual values gave a maximum 12% difference between the real and predicted values an average difference of 6%. This would suggest that these correlations might be suitable for determining B_0^2, although it should be considered that the available data was limited to 11 C_4 symmetric complexes and that the data presented comes from ligands with a ligand set of $N_4O_{4/5}$.

We may conclude that the size of the B_0^2 parameter decreases in the order CO_2^->PO_3^- >C(O)NR_2. Further data analysis of similar complex data could lead to a new spectrochemical series for the lanthanides or confirmation that the spectrochemical series applies to lanthanide ions. B_0^2 might not be the most suitable parameter to correlate with pKa as it only describes an axial component of the crystal field. The ligand field strength (N_v) might be a more suitable as it considers all the CF parameters.

Effect of the lanthanide ion on the crystal field strength

The N_v (crystal field strength) parameter is a measure of the sum of all the crystal field parameters. It is given by Equation 4.9.

$$N_v = \left[\sum \frac{4\pi}{2k+1}\left(B_q^k\right)^2\right]^{1/2}$$

Equation 4.9 : where k is the rank, q is the quotient and B is a crystal field parameter.[20]

For lanthanide doped crystals, the crystal field strength decreases with ionic radius.[24] The reason for this is that the radial integral of the crystal field parameter becomes smaller as the radius becomes smaller. This overcomes the increase in the lattice sum parameter, which leads to an overall decrease in crystal field strength. [24] From Eu^{3+} to Yb^{3+}, N_v decreases by 25%.[24]

Axial donors

Axial donors can have large effects on the B_0^2 parameter. This has been linked to the ligand polarizability. Highly polarisable axial ligands cause the B_0^2 parameter in Eu^{3+} to become more negative[20] and therefore the electronic distribution in the ion to become more prolate. Hard ligands such as fluoride cause the B_0^2 to become more positive in Eu^{3+}. [20]

Maximum values of B_0^2

We must consider the maximum reasonable value of the B_0^2 parameter as this could give an idea of what would be the axial/oblate limit of the anisotropy of an ion. From first principles, this value should be infinity as no electronic distribution could ever be completely oblate or prolate. We could consider the maximum value at which 'purely' crystal field parameters are applicable to be the maximum. This could be considered as a low crystal field limit or a B_0^2 beyond which we could assume that the coupling model has changed from LS coupling to JJ coupling.

As a test case we will consider the Eu^{3+} ion. The lowest energy levels are $^7F_0$ (0 cm^{-1}), $^7F_1$ (379 cm^{-1}) and $^7F_2$ (1043 cm^{-1}).47 We will consider the case of the $^7F_0$ and $^7F_1$ overlapping as only the $^7F_1$ manifold is affected by the crystal field. Each $^7F_1$ manifold component is affected differently as shown in Equation 4.6; this means that there is a positive and a negative limit to the crystal field. To calculate these values, we calculated which values of B_0^2 cause the m_J = 0 and m_J = ±1 to overlap with the $^7F_0$ energy level. These values are -1895 cm^{-1} and +3790 cm^{-1}. Although these values are large, they do not seem unreasonable as the binding of fluoride by europium may give values of B_0^2 in the high hundreds of wavenumbers.[10,13,25] From reference [13] we see that one of the complexes in the paper has B_0^2=-700 cm^{-1} this would suggest that the crystal field experienced by the Eu^{3+} is not as weak as we might usually consider, as this value is within 37% of the maximum value of B_0^2 . A value greater than of maximum value of B_0^2 would imply overlap between manifolds and therefore a strong ligand field.

Aim

The aim of this chapter is to assign solution structures to the $[Ln^{3+}(DTtBuMA)]^{3+}$ complexes received from Miss Amy-Grace Berger and Dr. Adam Sedgwick and to test the suitability of using average lanthanide-proton distances from crystals is of any merit for obtaining solution structures instead of relaxivity measurements. These were synthesized as part of a larger project on paraSHIFT probes. All crystal structures presented in this chapter were obtained by Mr. Eric Yang (see Appendix II: Crystallographic data).

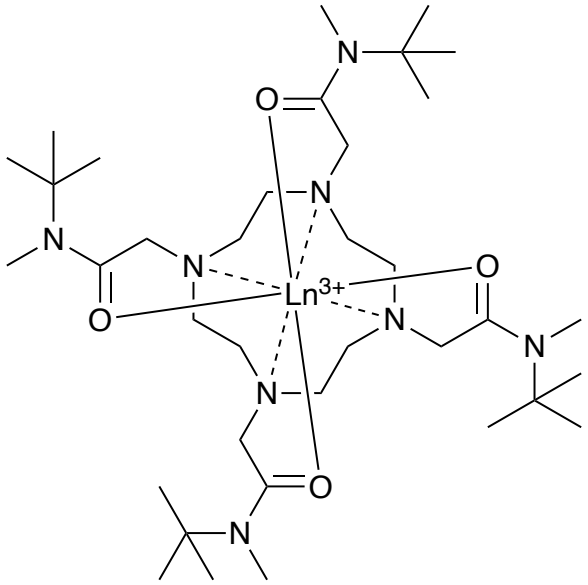


Figure 4.10 : structure of the $[Ln(DTtBuMA)]^{3+}$ ion. No axial water molecule shown.

Results and discussion

Analysis of luminescence spectra

The fluorescence spectra of $[Eu(DTtBuMA)]^{3+}$ and $[Tb(DTtBuMA)]^{3+}$ were recorded in H_20. The high-resolution spectrum of $[Eu(DTtBuMA)]^{3+}$ was used to calculate the B_0^2 for the Eu^{3+} ion in this ligand system (see Figure 4.11). This gave a value of B_0^2=-283 cm^{-1}.

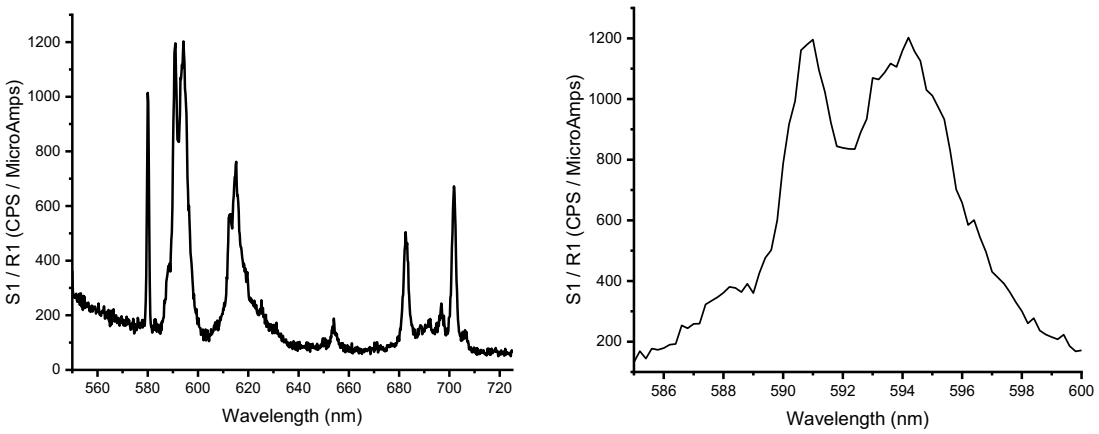


Figure 4.11: direct excitation spectrum of {Eu(DTtBuMA)]$^{3+}$ λ_{ex}: 395 nm). $^5D_1 \rightarrow {}^7F_1$ transition expanded .

The phosphorescencent decay in D_2O and H_2O of both $[Eu(DTtBuMA)]^{3+}$ and $[Tb(DTtBuMA)]^{3+}$ were recorded to use the Horrocks equation (see Equation 2.1). The results of this gave a hydration number of 1 (q = 0.86) for the europium analogue and 0 for the terbium analogue (q = 0.46). This suggests that the Tb analogue has a TSAP geometry and that the Eu analogue has a CSAP or CTSAP geometry.

Calculation of solution structure from NMR

Diamagnetic NMR

The NMR spectra of the La, Lu and Y analogues were recorded. These showed differences in chemical shifts and ^2J coupling (geminal coupling) of the La analogue and the Lu and Y analogues as shown in Table 4.2. This suggests that the lighter lanthanides adopt a different geometry than the heavier lanthanides.

Table 4.2 : chemical shifts and geminal J coupling for the Lu, Y and Y analogues. All coupling values assumed negative as based on a CH_2 species.

Arm		
Analogue	Shift	^2J (Hz)
Lu	4.13ppm and 3.93ppm	-17.0
Y	4.08ppm and 3.79ppm	-17.0
La	3.97ppm and 3.72ppm	Broad
Axial ring protons		
Lu	3.50ppm and 3.03ppm	-13.9
Y	3.45ppm and 3.03ppm	-13.9
La	3.56ppm and 3.02ppm	Broad
Equatorial ring protons		
Lu	2.96-2.80ppm	unmeasurable
Y	2.80ppm and 2.71ppm	-13.4
La	2.61ppm	Broad

The geminal couplings observed in the Lu and Y analogues are larger than those observed in the La analogue. This suggests that either the protons in the Lu and Y analogues a have larger H-C-H bond angles as they have a more negative ^2J coupling.[26] This is a sign that the Ln-O-C-C-N-Ln rings formed in the Lu and Y analogues are smaller than those formed in the La analogue.[26] Although the peaks in the La analogue's NMR spectrum are broader, this could be the result of fast exchange between the protons in this analogue.

Paramagnetic NMR

The NMR spectra of the paramagnetic complexes were recorded in D_2O. The spectra belonging to the Er and Eu analogues (see Figures 4.3 and 4.6), showed a shift pattern

suggestive of prolate anisotropy (as confirmed by the fluorescence data for the Eu analogue).

[Eu(DTtBuMA)] $^{3+}$

The NMR of the Eu analogue shows the presence of both a CSAP and a TSAP (or CTSAP) isomer. This is confirmed by the presence of 8 major peaks which by their positions between 20 ppm and -10 ppm suggest that they belong to a TSAP type isomer and a smaller partial set of shifts between -40ppm and -20ppm which belong to a CSAP/SAP isomer.

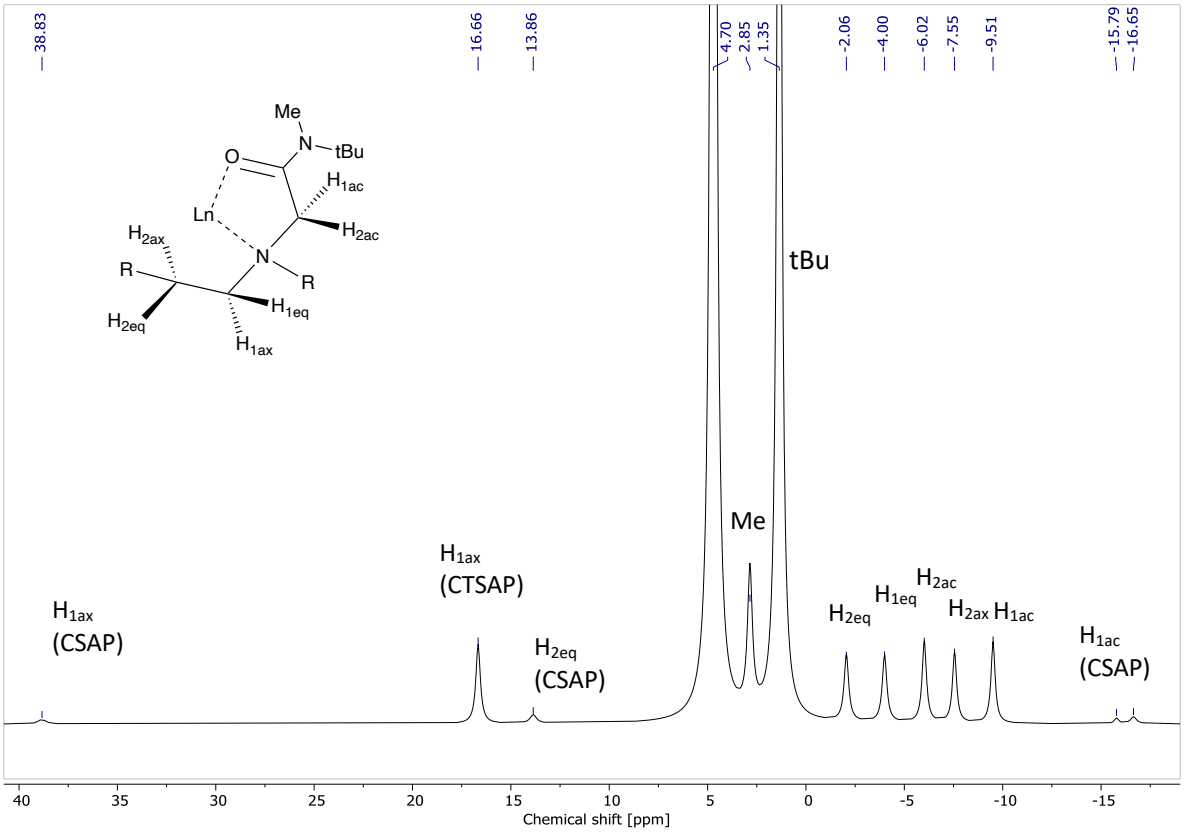


Figure 4.3. NMR Spectrum of [Eu(DTtBuMA)]$^{3+}$ in D_2O. All peaks unless specified belong to CTSAP isomer.

We can rationalize this by the fact that CSAP isomers have B_0^2 parameters which are twice the size of those observed in TSAP isomers of the same complex.110 Given that from the phosphorescent decay data the hydration number for the europium analogue is q = 0.86 we may conclude that this complex is adopting a CTSAP geometry in preference to a CSAP geometry in aqueous solution.

The chemical shifts of the europium analogue were used to obtain a solution structure for this ion by using Bleaney theory. From the high-resolution fluorescence spectrum, we obtained a value of -283 cm^{-1} for B_0^2. This is equal to a value of 2142 $Å^3$ ppm for the axial magnetic susceptibility tensor (X_{ax}) at 298K. If we use the simplest version of the Bleaney formula for magnetic anisotropy, (see Bleaney theory section) we can obtain the partial spherical coordinates for the positions of the of the protons in the structure relative to the principal magnetic axis. In the case of complexes of higher symmetry than C_1 this axis is the same as the highest order proper rotation axis. For the DTtBuMA complexes, this is a C_4 axis. Calculations gave the positions shown in Figure 4.4.

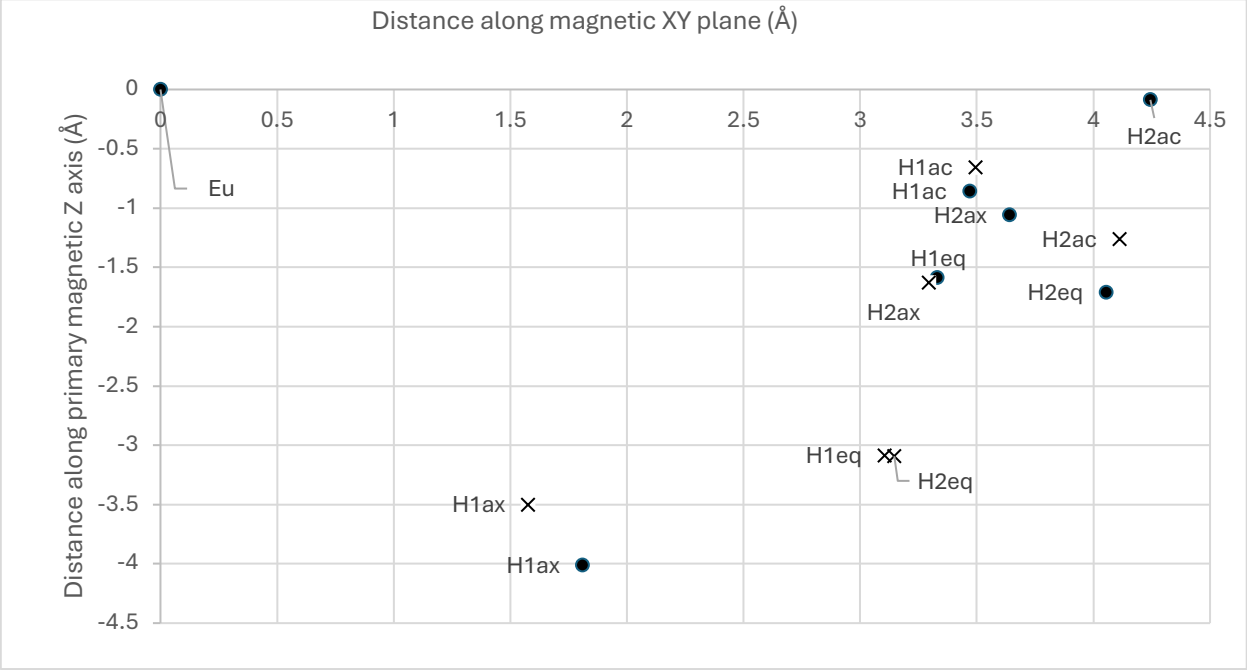


Figure 4.4 : Positions of the protons in the ion along the z axis (magnetic axis) with distances of each point from Eu proportional to those from the $[Eu(DTtBuMA)]^{3+}(OTf)_3$ crystal (dots) and from NMR (crosses).

As we can see in Figure 4.4, the angular values obtained by Bleaney theory match up relatively well with those observed in the crystal structures, albeit the positions in the solution structure seem more compressed. This could be due to the fact that this is a snapshot of a structure in solution which includes significant contributions from molecular

vibrations and the fact that the proton positions from the crystal are uncertain, due to the fact that these are assigned from electron densities between the proton in question and the atom to which it is bonded.

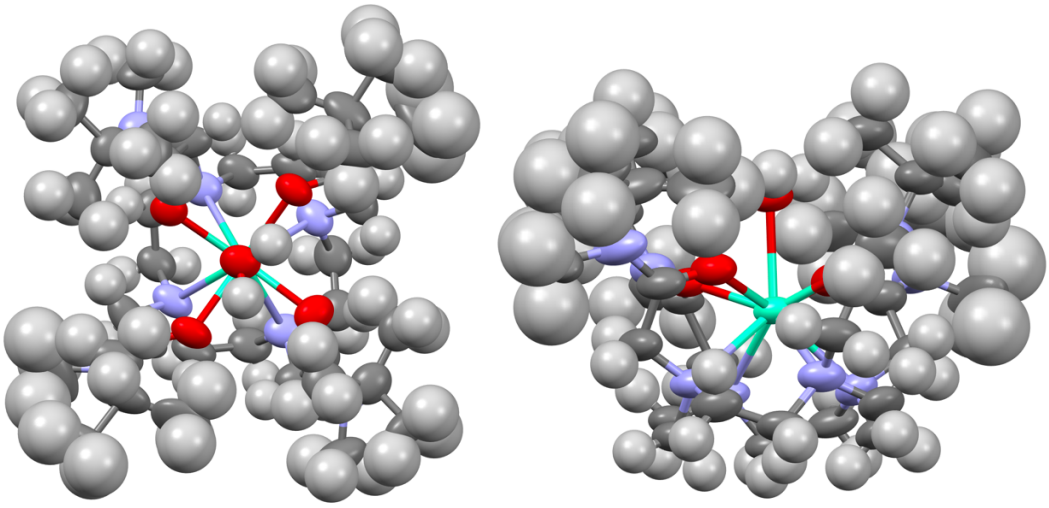


Figure 4.5 : Crystal structure of [Eu(DTtBuMA)]$^{3+}$ion as seen from the molecular xy plane (left) and the principal magnetic axis (right).

To obtain the solution structures angles in relation to the C_4 axis, distances between lanthanide and proton were obtained by averaging values obtained from crystals of DOTA-based complexes of europium in the CCDC database (CCDC identifiers: 1484639, 158148, 220683, 2070879 and 158150). The reason for doing this was to test whether or not this was a valid replacement for distances obtained via T_1 relaxation measurements, as, when obtaining the averages, we found that the average had an error of <5%. In general, this method gave reasonable values for the angles between the principal magnetic axis (see figure). From the NMR and luminescence data we may conclude that the Eu analogue adopts a CTSAP conformation in solution as a major isomer and a CSAP conformation as a minor isomer.

[Er(DTtBuMA)] $^{3+}$

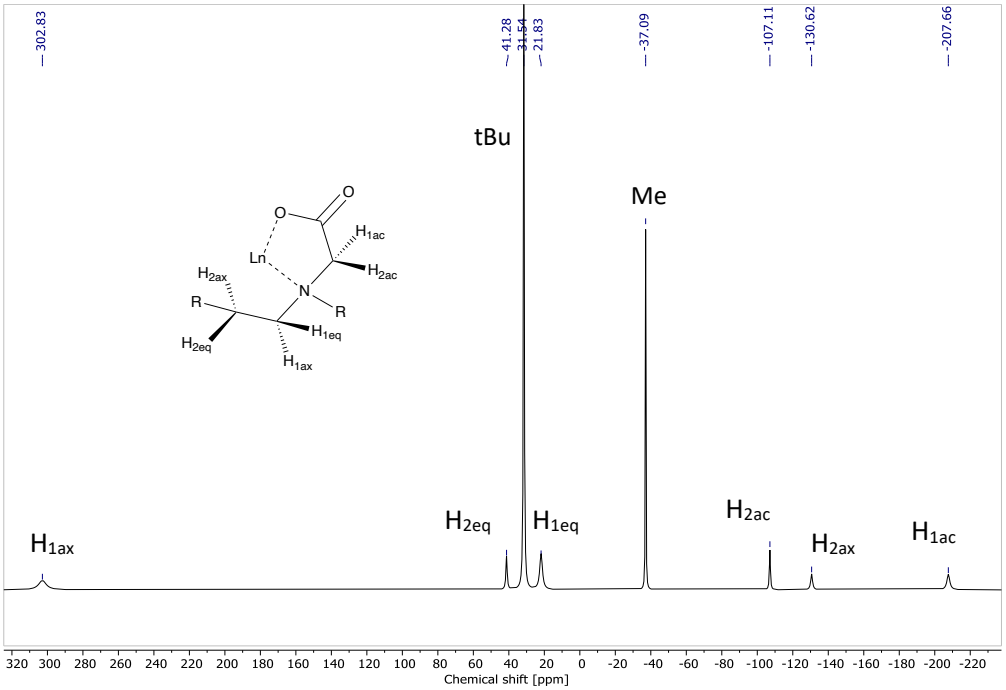


Figure 4.6 : NMR spectrum of [Er(DTtBuMA)] $^{3+}$ion in D_2O.

The fact that the shift pattern of the Er analogue does not look similar to that of the Eu analogue suggests that the heavier lanthanide analogues and lighter lanthanide analogues are not iso-structural. When comparing the Eu analogue's crystal structure and the Er crystal structure we see that the Er analogue has no axial water molecule and is in the TSAP conformation (Figure 4.7).

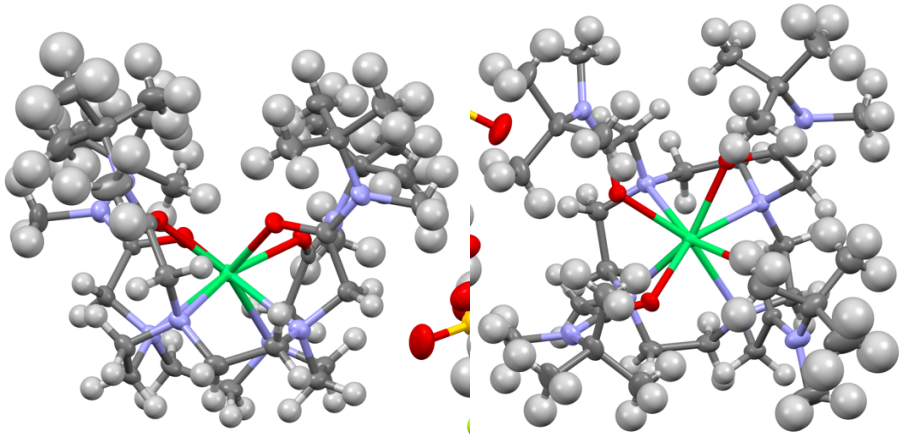


Figure 4.7 : Crystal structure of [Er(DTtBuMA)] $^{3+}$ ion as seen from the molecular xy plane (right) and the principal magnetic axis (right).

Conclusions

From the NMR data and luminescence data obtained for these complexes we may conclude that these complexes are not isostructural across the lanthanide series. We have also seen how for the Eu analogue it was possible to obtain a reasonable solution structure for in aqueous solution and that distance measurements from crystals may be used for obtaining angular values for the positions of protons in the solution structure of these complexes.

References

1 K. Binnemans, *Coord Chem Rev*, 2015, **295**, 1–45.

2 C. Görller-Walrand and K. Binnemans, in *Handbook on the physics and chemistry of the rare earths*, eds. K. A. Gschneidr and L. Eyring, Elsevier Science B.V., 1996, pp. 121–283.

3 M. Suta, F. Cimpoesu and W. Urland, *Coord Chem Rev*, 2021, **441**, 213981.

4 A. De Bettencourt-Dias, *Luminescence of Lanthanide Ions in Coordination Compounds and Nanomaterials*, John Wiley & Sons Ltd, 2014, vol. 9781119950.

5 K. W. H. Stevens, *Proceedings of the Physical Society. Section A*, 1952, **65**, 209–215.

6 R. Skomski, P. Manchanda and A. Kashyap, in *Handbook of Magnetism and Magnetic Materials*, Springer International Publishing, 2021, pp. 1–83.

7 B. Bleaney, *Journal of Magnetic Resonance (1969)*, 1972, **8**, 91–100.

8 J. Sievers, *Zeitschrift für Physik B Condensed Matter*, 1982, **45**, 289–296.

9 D. Parker, E. A. Suturina, I. Kuprov and N. F. Chilton, *Acc Chem Res*, 2020, **53**, 1520–1534.

10 C. Görller-Walrand and K. Binnemans, *Handbook on the physics and chemistry of the rare earths*, 1996, 121–283.

11 Z.-Y. Yang and Q. Wei, *Physica B Condens Matter*, 2005, **370**, 137–145.

12 D. J. Newman and B. Ng, Eds., *Crystal Field Handbook*, Cambridge University Press, 2000.

13 A. M. Funk, K.-L. N. A. Finney, P. Harvey, A. M. Kenwright, E. R. Neil, N. J. Rogers, P. K. Senanayake and D. Parker, *Chem Sci*, 2015, **6**, 1655–1662.

14 A. C. Harnden, E. A. Suturina, A. S. Batsanov, P. K. Senanayake, M. A. Fox, K. Mason, M. Vonci, E. J. L. McInnes, N. F. Chilton and D. Parker, *Angewandte Chemie International Edition*, 2019, **58**, 10290–10294.

15 E. Terazzi, J. P. Rivera, N. Ouali and C. Piguet, *Magnetic Resonance in Chemistry*, 2006, **44**, 539–552.

16 C. Piguet and C. F. G. C. Geraldes, in *Handbook on the physics and Chemistry of Rare Earths*, 2003, vol. 3, pp. 353–463.

17 B. R. McGarvey, *Journal of Magnetic Resonance (1969)*, 1979, **33**, 445–455.

18 D. E. Henrie, R. L. Fellows and G. R. Choppin, *Coord Chem Rev*, 1976, **18**, 199–224.

19 G. Bao, Z. Liu, Y. Luo, K.-L. Wong and P. A. Tanner, *Dalton Transactions*, 2019, **48**, 4314–4323.

20 R. S. Dickins, D. Parker, J. I. Bruce and D. J. Tozer, *Dalton Transactions*, 2003, 1264–1271.

21 D. Parker, E. A. Suturina, I. Kuprov and N. F. Chilton, *Acc Chem Res*, 2020, **53**, 1520–1534.

22 L. B. Zinner, J. R. Matos and A. B. Nascimento, *Inorganica Chim Acta*, 1988, **141**, 305–308.

23 A. M. Funk, K.-L. N. A. Finney, P. Harvey, A. M. Kenwright, E. R. Neil, N. J. Rogers, P. Kanthi Senanayake and D. Parker, *Chem Sci*, 2015, **6**, 1655–1662.

24 E. Antic-Fidancev, J. H ls and M. Lastusaari, *Journal of Physics: Condensed Matter*, 2003, **15**, 863–876.

25 O. A. Blackburn, A. M. Kenwright, A. R. Jupp, J. M. Goicoechea, P. D. Beer and S. Faulkner, *Chemistry - A European Journal*, 2016, **22**, 8929–8936.

26 M. Balci, in *Basic 1H- and 13C-NMR Spectroscopy*, ed. M. Balci, Elsevier, 2005, pp. 87–133.

Chapter 5: Conclusion

The original aim of this work was to produce pH and redox responsive lanthanide probes. Due to the COVID-19 pandemic, lockdown time was spent becoming more familiar with the more physicochemical aspects of lanthanide complexes due to a personal interest in the magnetic anisotropy of lanthanide complexes. This led to the inclusion of chapter 4: On crystal field parameters.

Chapter 2 describes the work carried out to achieve the synthesis of a pH probe. This work was successful in producing a series of probes with a 3-acetylpyridinyl chromophore. These showed pH sensitivity across two ranges <pH3.5 and pH6-pH10. The higher pH range was thoroughly characterised by UV-Vis, luminescent titrations and NMR titrations. The data of obtained from these techniques allowed us *to* identify the conjugate acid-base pairs of these probes, finding that the acidic form *to be* the complex with a protonated pyridine arm and the basic for being an enol. Analogues of these probes with methylated alpha carbons might be of use as paraSHIFT pH probes (1). As future work, we might suggest that one of the alpha carbons in the molecule is ^{13}C labelled (2) and DNP-NMR is used to test the usefulness of the*se* probes as bimodal probes as pH probes and hyperpolarised MRI probes or to use hyperpolarised shifts to make the probes ratiometric (Figure 5.1).

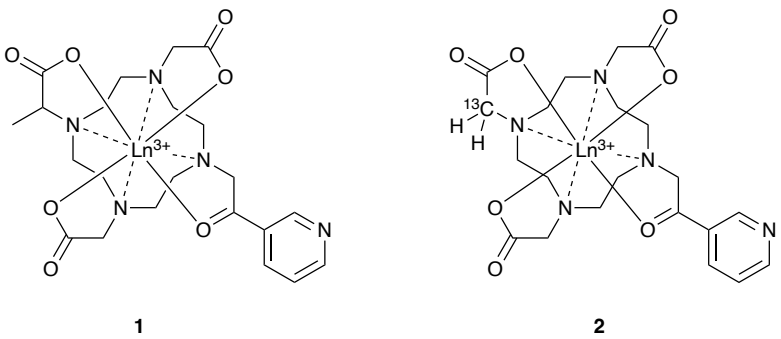


Figure 5.1: proposed probes for future work.

Chapter 3 presents the synthesis of an azo dye based redox probe. This work was successful in synthesising simple azo dye probes in a high overall yield of 21%-25%. This work only provides a starting point for other researchers to produce simple water-soluble azo dye based redox probes.

The introduction to Chapter 4 is the collection of several months of reviewing literature and coming to a better understanding of crystal field theory as applied to lanthanides. The understanding obtained during the literature review was then applied to obtaining possible solution structures for a series of paraSHIFT probes. This was successful for the Eu^{3+} analogue as crystal field parameters were easily obtained for this complex, but due to the complexes not being isostructural the values for the CF parameters were not transferrable between analogues. We hope the work presented on this chapter may lead to a better understanding of the CF of lanthanides complexes and the possibility of designing their magnetic properties.

This thesis describes lanthanide probes in two ways: how their ligands interact with their local chemical environment and how this affects the complexes' crystal field. We believe that the work presented in this thesis may lead to other lanthanide probes and to the ability to design the crystal field and therefore the magnetic properties of lanthanide complexes.

Experimental

General procedures

Commercially sourced solvents and reagents were used without purification. All reagents obtained commercially were of laboratory grade and obtained from standard commercial sources, these being Merck, Fischer Scientific and Fluorochem. Silica gel for column chromatography was purchased from Merck (Geduran®, pore size 60 Å, 230-400 mesh, 40-63 µm).

Float-A-Lyzer® G2 dialysis tubes (500 MWCO) equipped with regenerated cellulose were purchased from Spectrum and used to purify the lanthanide complexes. The dialysis tubes were activated by 10 % ethanol or isopropanol solution in deionised water followed by deionised water before being used. The corresponding complexes were dissolved in deionised water and transferred into the dialysis tube. The dialysis tube was placed in a 5 L-beaker filled with deionised water. The dialyses ran for 18-48 hours under stirring and the deionised water was replaced with fresh deionised water at least twice. Dialyses were left to stir until level of water in tube did not change overnight.

NMR spectroscopy: NMR spectra were recorded at 298 K unless otherwise stated.

600 MHz 1H-NMR and 151 MHz 13C-NMR were obtained using a Bruker NEO 600 with broadband helium cryoprobe equipped with a 14 T magnet. 500 MHz 1H-NMR, 126 MHz 13C-NMR were recorded on a Bruker Avance III NMR equipped with a 11.75 T magnet. 400 MHz 1H-NMR and 101 MHz 13CNMR were obtained using a Bruker Avance III HD nanobay 400 NMR equipped with a 9.4 T magnet.

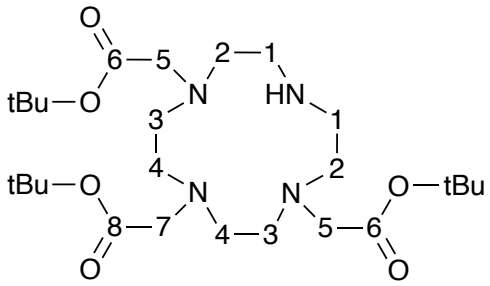
All coupling constants are quoted in Hz with all chemical shifts quoted in parts per million (ppm) and referenced to the residual solvent peak. Abbreviations when quoting NMR data are as follows: singlet (s), doublet (d), triplet (t), quartet (q), doublet of doublets (dd), triplet of doublets(td), doublet of triplets (dt) and multiplet (m). Assignments to the structure of the compound described seen as the last number before the closing bracket.

Luminescence spectroscopy: HORIBA Jobin Yvon FluoroLog3-12 fluorimeter (Hamamatsu R928 detector and a double-grating emission monochromator) was used to acquire the luminescence spectra operated under FluorEssence software. The standard conditions for acquiring emission and excitation spectra are room temperature and steady-stated mode unless otherwise stated. HORIBA Jobin Yvon FluoroLog3 fluorimeter system equipped with a Xenon flash lamp was used to acquire emission lifetimes. Luminescence lifetimes were obtained by tail fit for Eu(III) complexes using Origin software.

pH probes

DO3A-tBu[1]

1,4,7,10-Tetraazacyclododecane (2.00 g, 11.62 mmol, 1 equiv.) and $NaHCO_3$ (2.928 g, 34.88 mmol, 3 equiv.) were dissolved in MeCN (60 mL) under N_2. Tert-butyl bromoacetate (5.15 mL, 6.8 g, 34.88 mmol, 3 equiv.) was added dropwise. The reaction was stirred for 48h. The solvent was concentrated under reduced pressure to yield an off yellow solid. This was crystallised from boiling toluene to yield DO3A-tBu·HBr as a white solid (2.3025 g, 3.87 mmol, 33%)



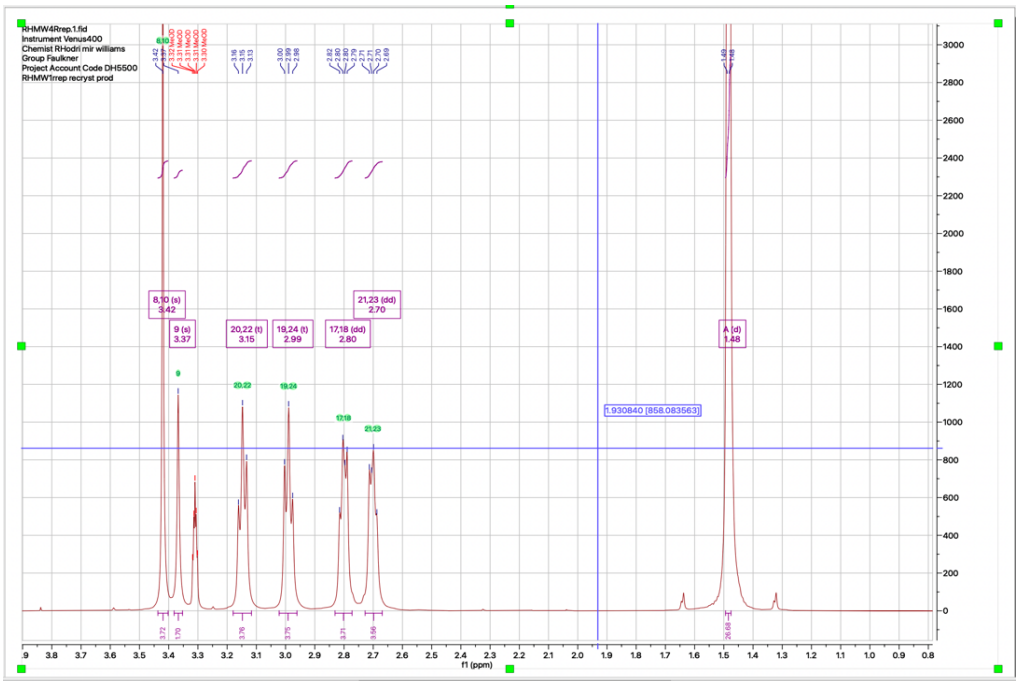
Chemical Formula: $C_{26}H_{50}N_4O_6$

Exact Mass: 514.37 Da

Molecular Weight: 514.71 Da

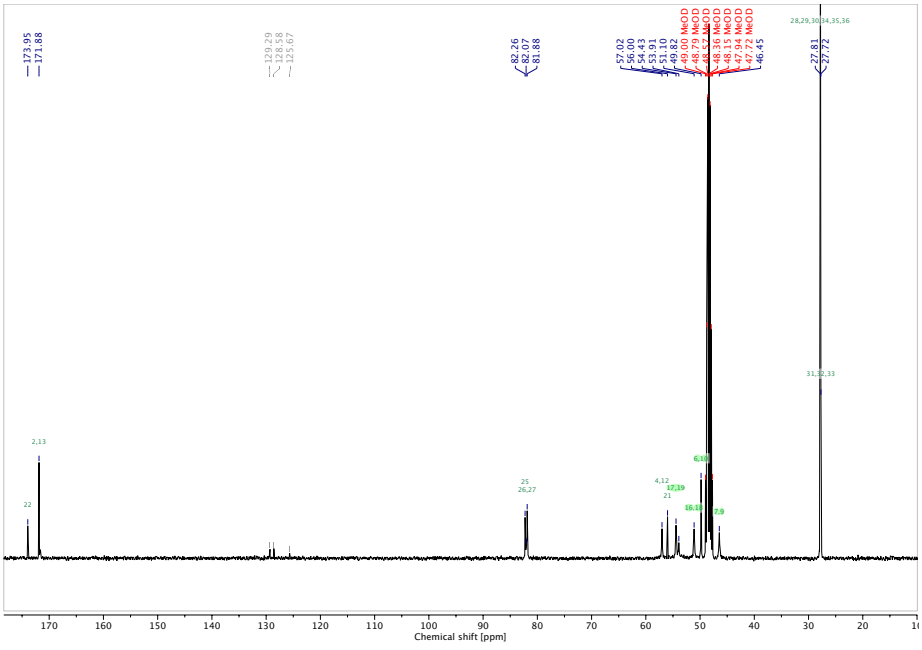
HNMR

δ_H (400 MHz, MeOD) 3.43(4 H, s, 5), 3.38(2 H, s,7), 3.15(4 H, s, 1), 3.01(4 H, s, 2), 2.81(4 H, s, 3), 2.77 – 2.63(4 H, s, 4), 1.56 – 1.39 (27 H, m, tBu).



CNMR

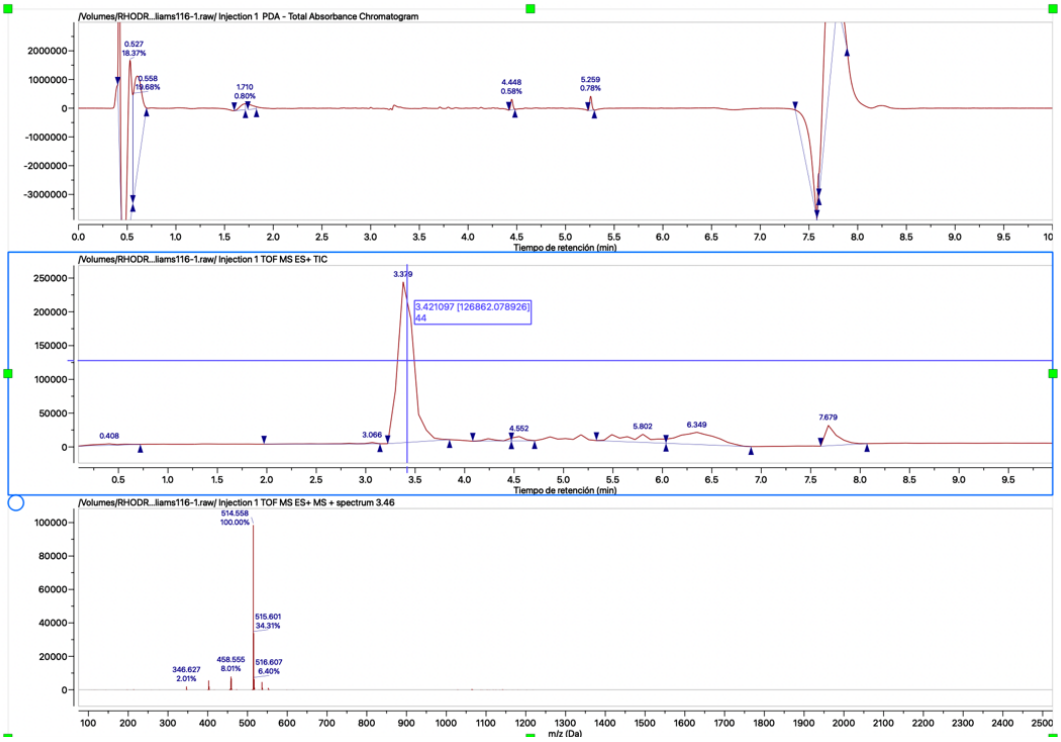
δ_C (101 MHz, MeOD) 174.0 (22), 171.9 (2, 13), 82.3 (25), 82.1, 81.9 (26, 27), 57.0 (4, 12), 56.0 (21), 54.4, 53.9, 51.1, 49.8, 46.5, 27.8, 27.7 (31, 32, 33).



Mass Spectrometry

Predicted: $[M-H]^+$ m/z: 514.37 (100.0%), 515.38 (28.9%), 516.38 (5.3%), 515.37 (1.5%)

HPLC-ESI: $[M-H]^+$ = 514.536 Da, 3.329 min

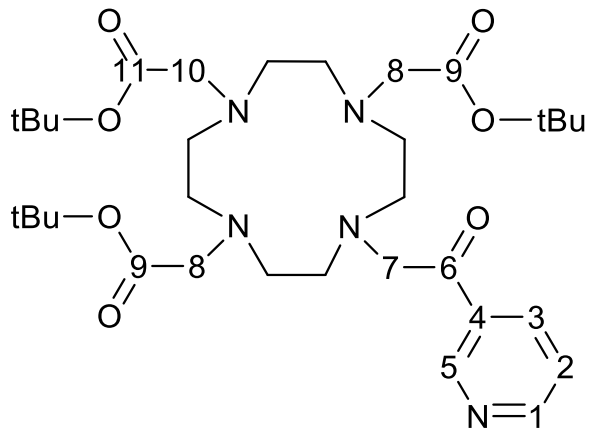


DO3A-tBu-3-acetylpyridine (first synthesis)

2-Bromo-3'-acetylpyridine hydrobromide (0.68 g, 2.41 mmol), tBu-DO3A (1.13 g, 1.94 mmol) and Cs_2CO_3 (0.79 g, 2.42 mmol) were dissolved in acetonitrile (20 ml) under nitrogen at 0 ^oC. The reaction was stirred for 1h in an ice bath. The reaction was stirred for 24H in total (TLC confirmed reaction had finished 9:1 DCM/EtOH). The solvent was evaporated. Full deprotection was carried out (see DO3A acetylpyridine 1 first synthesis).

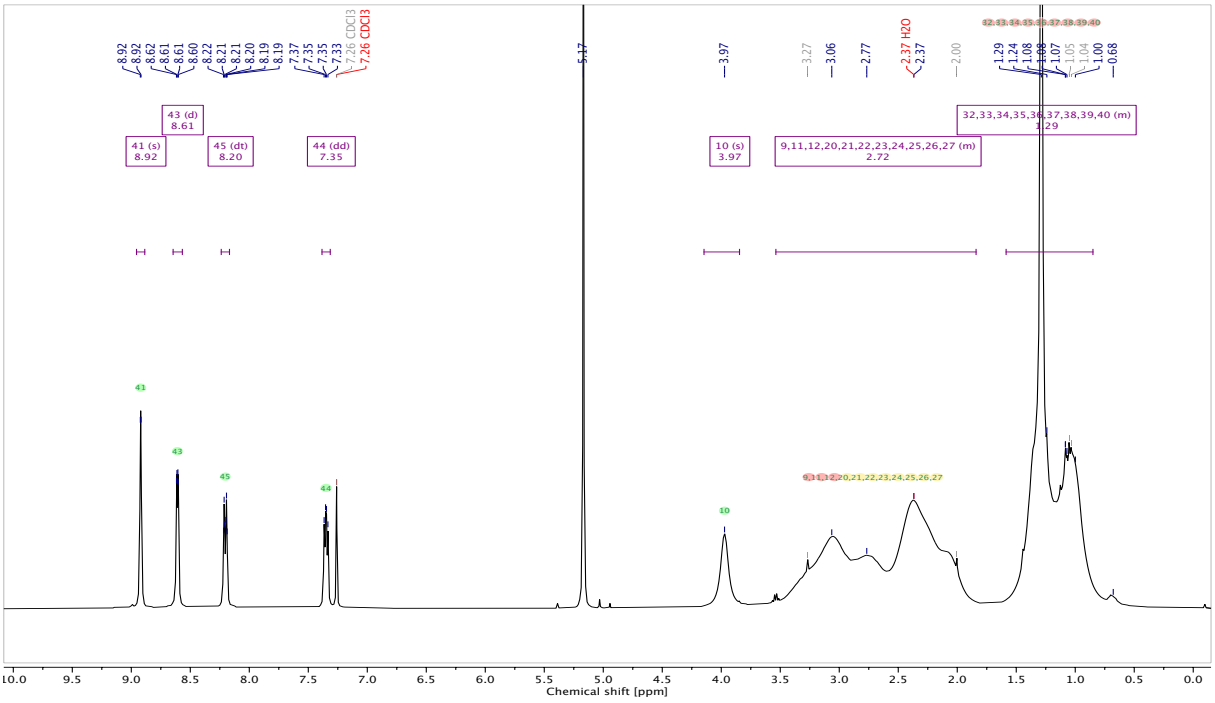
DO3A-tBu-3-acetylpyridine

tBu-DO3A (500 mg, 0.84 mmol, 1 equiv.), K_2CO_3 (462.5 mg, 3.35 mmol, 4 equiv.) and 2-Bromo-3'-acetylpyridine hydrobromide (300 mg, 1.05 mmol, 1.25 equiv.) were put into a 50 mL rbf and dissolved in dry MeCN (37.5 mL) left to stir under an argon atmosphere left for 24h until HPLC-MS and TLC confirmed that all the triester had been consumed. The reaction mixture was filtered. The filtrate was concentrated under reduced pressure to give the crude product. The crude product was purified by column chromatography (Neutral alumina, Trichloromethane: Methanol 100:0>99:1>98:2>97:3>95:5) to give the product (322 mg, 0.51 mmol, 61 %) This was carried forward to deprotection after a confirmatory NMR which showed that the product was present with large amounts of solvent.



HNMR

δ_H (400 MHz, $CDCl_3$) 8.92 (1 H, s, 5), 8.61 (1 H, d, *J* 4.3, 1), 8.20 (1 H, dt, *J* 8.1, 2.1, 3), 7.35 (1 H, dd, *J* 8.0, 4.9, 2), 3.97 (2 H, s,7), 3.54 – 1.84 (22 H, m, ring, 8, 10), 1.59 – 0.85 (27 H, m, tBu).

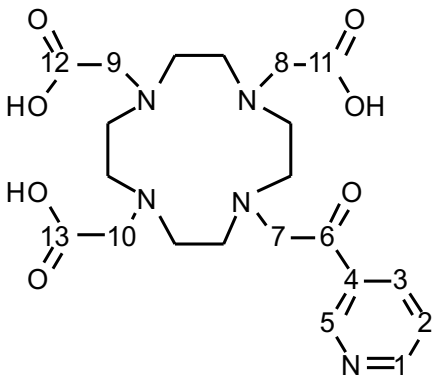


DO3A-3-acetylpyridine first synthesis

DO3A-tBu-3-acetylpyridine (impure) (~1 g, 1.58 mmol), was dissolved in TFA (5 ml) and DCM (5 ml) and stirred for 12 hours, the solvent was concentrated in vacuo. This was followed by the addition and concentration of methanol (10 ml) and diethyl ether (3 x 20 ml) yielding a brown solid (0.5 g) to achieve digestion. The solid was then dissolved in 95:5 H_2O : ACN and purified by HPLC (Sunfire column, Standard H_2O(1%TFA)/MeCN gradient). The solvent was then removed to yield a yellow solid (70 mg, 0.11 mmol, 7.6 % across alkylation and deprotection steps)

DO3A-3-acetylpyridine second synthesis

DO3A-tBu-3-acetylpyridine (291 mg, 0.46 mmol, 1 equiv., not dry), was dissolved in TFA (10 ml) and DCM (10 ml) and stirred overnight, the solvent was concentrated in vacuo. This was followed by the addition of methanol and diethyl ether to achieve digestion. The mixture was then centrifuged after each dilution and the solid removed and digested a further two times to yield DO3A-3-acetylpyridine (123.9 mg, 0.26 mmol, 57%) as a yellow solid.



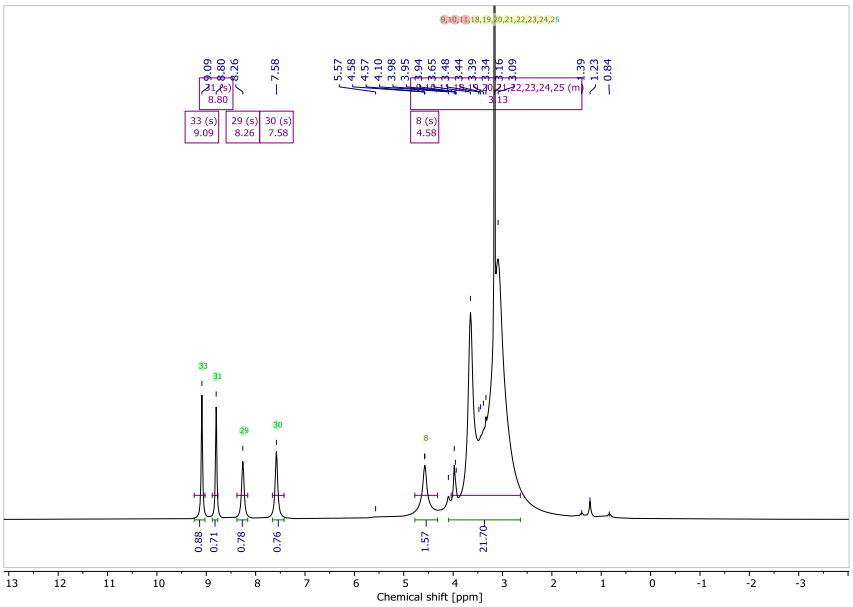
Chemical Formula: $C_{21}H_{31}N_5O_7$

Exact Mass: 465.22 Da

Molecular Weight: 465.51 Da

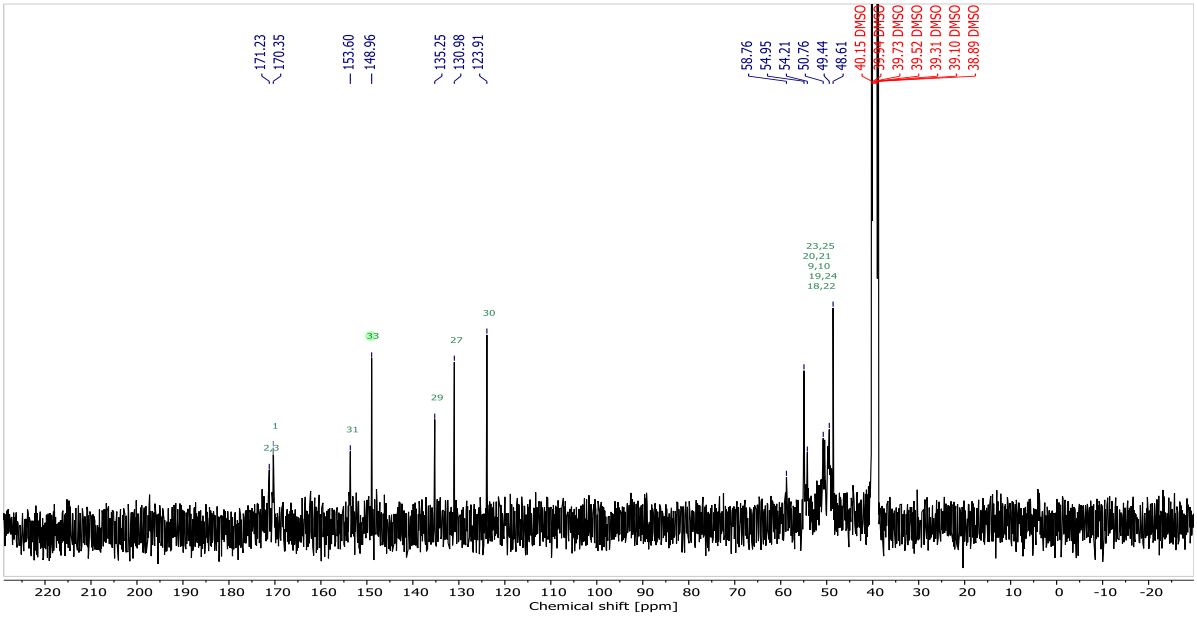
HNMR

δ H (400 MHz, DMSO) 9.24 – 9.03 (1 H, s, 5), 8.88 – 8.77 (1 H, s, 1), 8.38 – 8.16 (1 H, s, 3), 7.66 – 7.42 (1 H, s, 2), 4.78 – 4.32 (2 H, s, 7), 4.04 – 2.64 (22 H, m, 8, 9, 10, cyclen ring).



CNMR

δ_C (101 MHz, DMSO) 171.2(10,11), 170.4(9), 153.6(1), 149.0(5), 135.3(3), 131.0(4), 123.9(2), 58.8(7), 55.0(cyclen ring, 8,9,10), 54.2(cyclen ring, 8,9,10) , 50.8(cyclen ring, 8,9,10) , 49.4(cyclen ring, 8,9,10), 48.6(cyclen ring, 8,9,10).

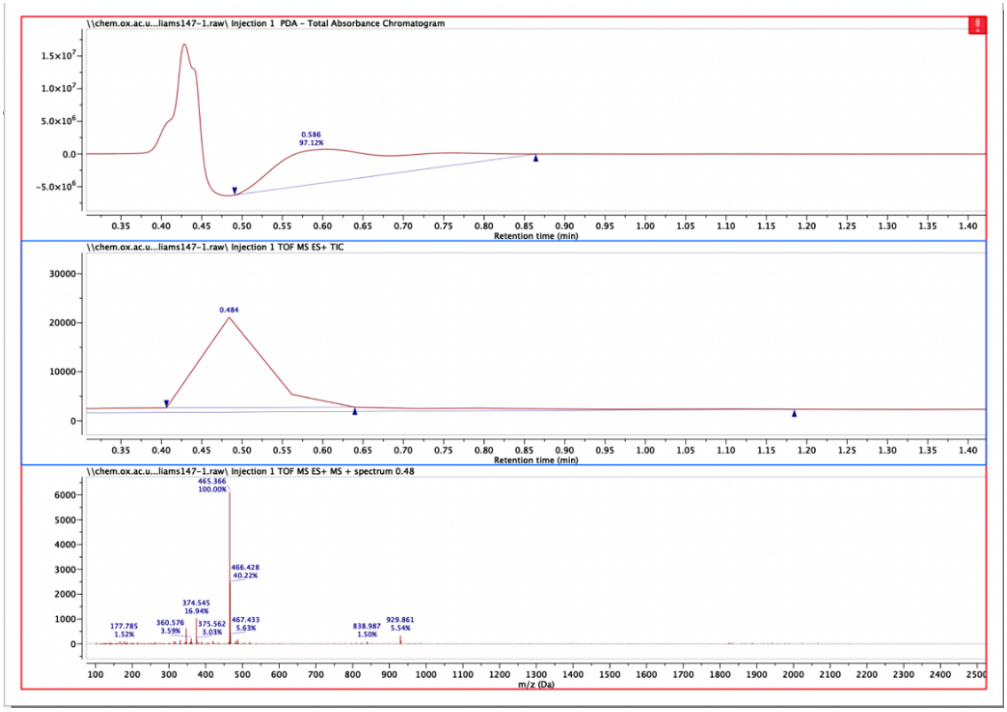


Mass Spectrometry

HPLC-LRMS-ESI

Predicted: m/z: 465.22 (100.0%), 466.23 (23.3%), 467.23 (4.0%), 466.22 (1.8%)

Observed: $[M-H]^+$ = 465.435 Da, (0.586 min, 97%)



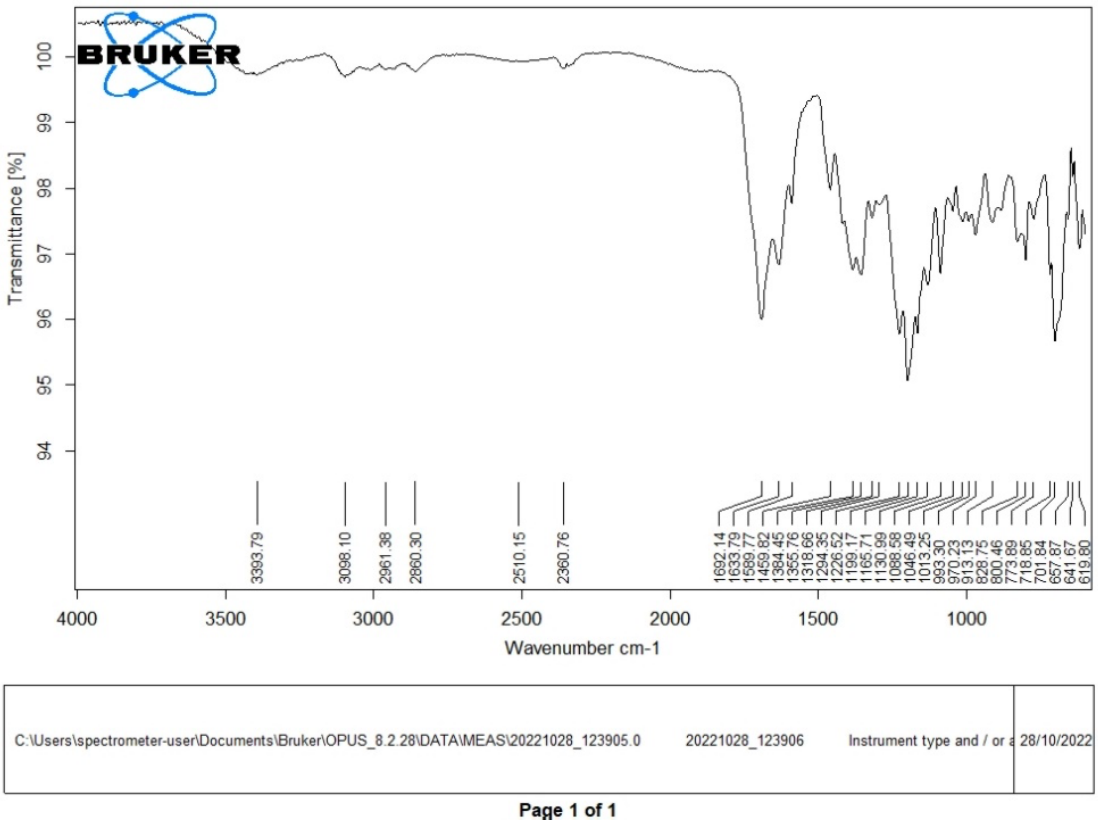
HRMS-ESI

Predicted: $[M-H]^+$ = 466.2296 Da, $[M-Na]^+$ = 488.2116 Da

Observed: $[M-H]^+$ = 466.2305 Da, $[M-Na]^+$ = 488.2128 Da

IR

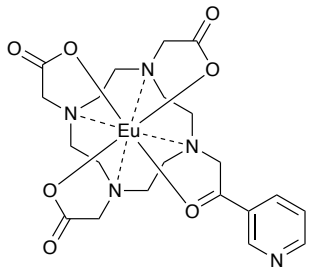
IR(cm^{-1}): 3394(w), 3098(w), 2961(w), 2860(w), 2510(w), 2361(w), 1691(vs), 1634(s), 1590(m), 1460(m), 1384(s) 1319(s), 1294(m), 1227(vs), 1199(vs), 1166(vs), 1131(vs), 1089(s), 1047(m), 1013(m), 993(m), 970(s), 913(m), 829(s), 801(s), 774(m),719 (s), 702(vs), 658(m), 642(s), 620(s).



General method for complexation (first syntheses)

Ligand (1 equiv.) and metal triflate (1.5 equiv.) was dissolved in 1:1 MeOH/H_2O (2 mL). The mixture was stirred at 40 ^oC for 3 days, adding over this period NaOH (1 M, 3 equiv.) to control pH, which was kept between 5-7. The product was then dialysed to yield the desired complex as a yellow solid.

Eu-DO3A-3-Acetylpyridine (first synthesis)



Yield: 43 mg

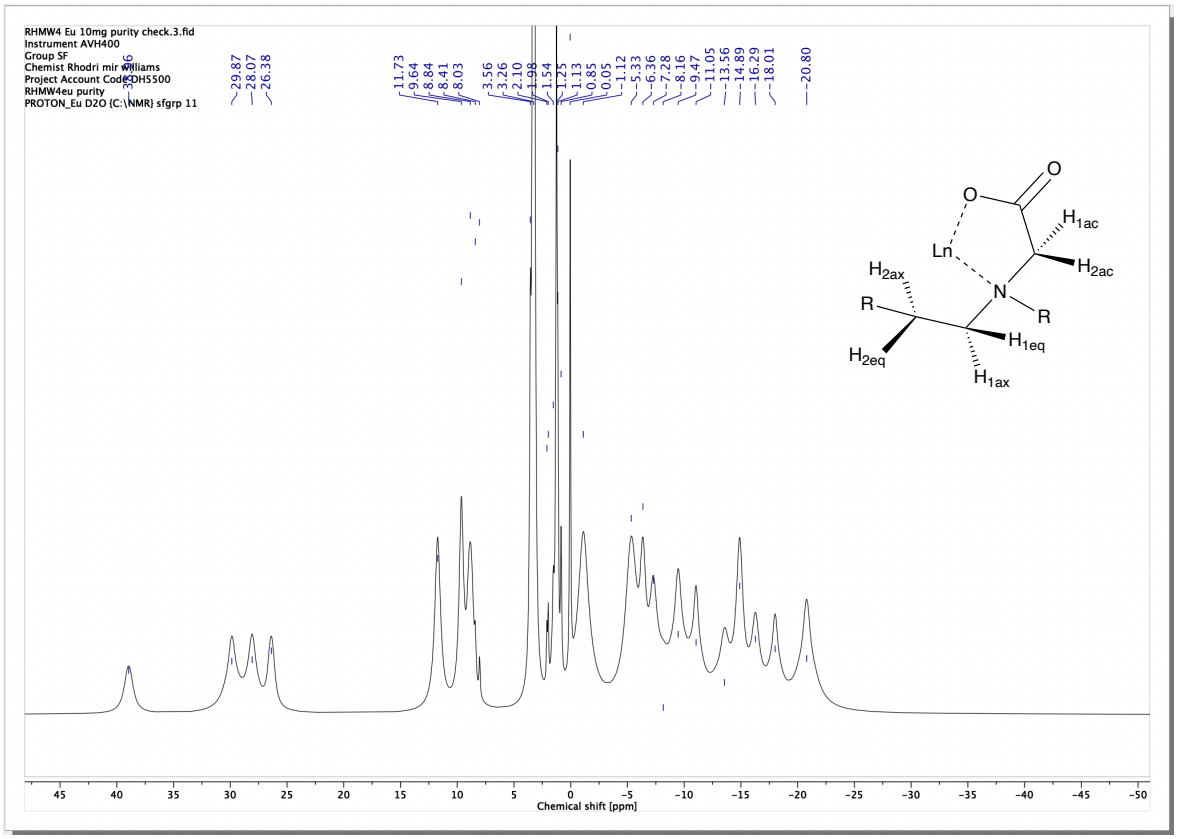
Chemical Formula: $C_{21}H_{28}N_5O_7Eu$

Exact Mass: 615.12 Da

Molecular Weight: 614.45 Da

HNMR

δ_H (400 MHz, D_2O) 38.96 (H_1ax), 29.87(H_1ax), 28.07(H_1ax), 26.38(H_1ax), 11.73,9.64, 8.84, 8.41, 8.03, -1.12, -5.33, -6.36,-7.28, -8.16, -9.47, -11.05, -13.56, -14.89, -16.29, -18.01, -20.80(H_1ac). Only partial assignation.



Mass Spectrometry

HPLC-MS: $[M-H]^+$- 615.402 Da 95.47%

HRMS, ESI:

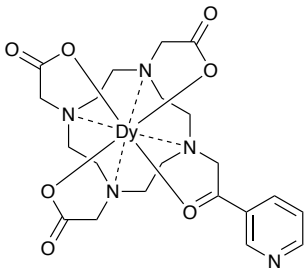
Predicted: $[M-H]^+$ = 616.1278 Da

Observed: $[M-H]^+$ = 616.1273 Da

UV-Vis

244 nm, 272 nm

Dy-DO3A-3-Acetylpyridine (first synthesis)



Yield: 83.9 mg (crude) – max 27 mg

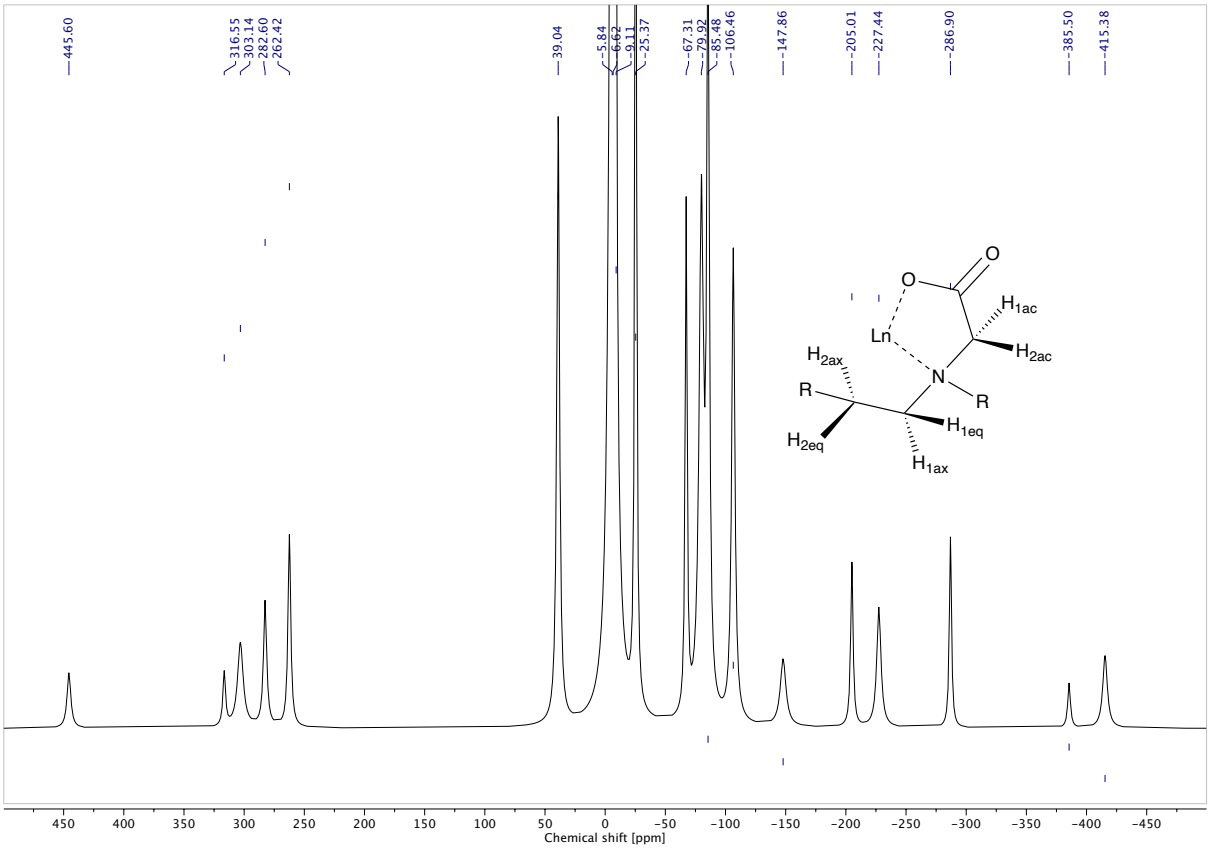
Chemical Formula: $C_{21}H_{28}N_5O_7Dy$

Exact Mass: 626.13 Da

Molecular Weight: 624.98 Da

HNMR

δ_H (400 MHz, D_2O) 445.60(H_1ax), 316.55, 303.14, 282.60, 262.42, 39.04, -5.84, -6.62, -9.11, -25.37, -67.31, -79.92, -85.48, -106.46, -147.86, -205.01, -227.44, -286.90, -385.50(H_1ac), -415.38 (H_1ac). tentative assignation



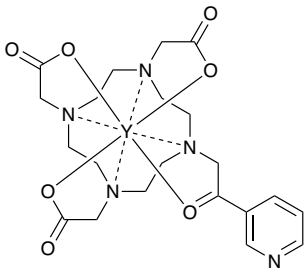
Mass Spectrometry

HRMS, ESI:

Predicted: $[M-H]^+$ = 627.1153 Da, $[M-Na]^+$ = 649.1173 Da

Observed: $[M-H]^+$ = 627.1358 Da, $[M-Na]^+$ = 649.1164 Da

Y-DO3A-3-Acetylpyridine (first synthesis)



Chemical Formula: $C_{21}H_{28}N_5O_7Y$

Exact Mass: 551.10 Da

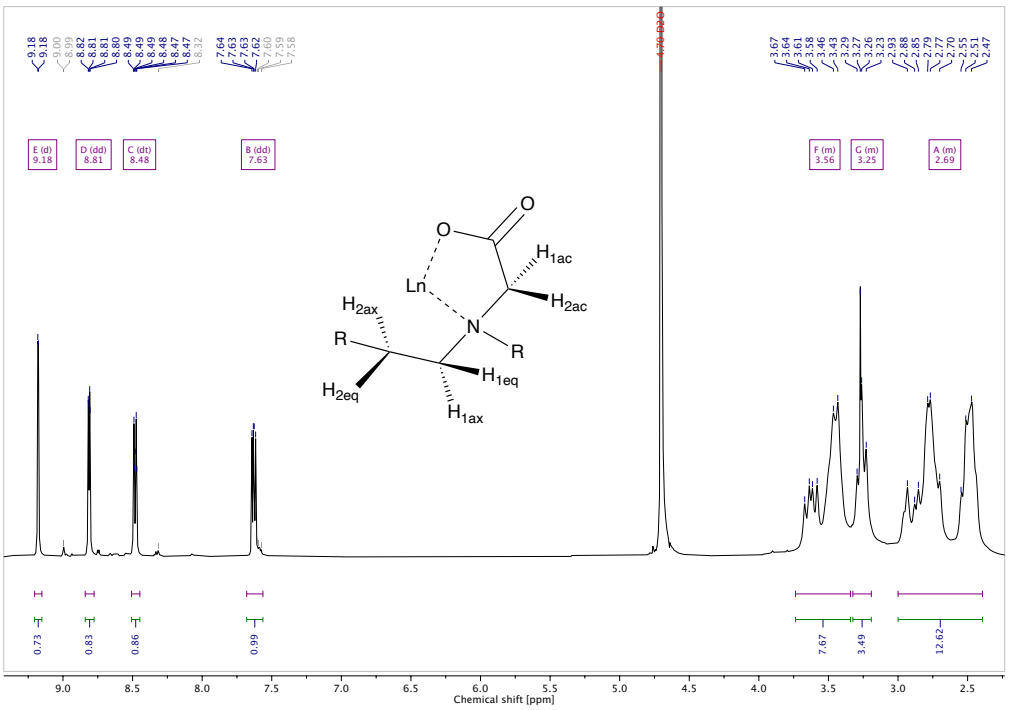
Molecular Weight: 551.39 Da

Yield: 91.7 mg (crude) – max 23 mg wet

HNMR

In Acid (pD 5.42)

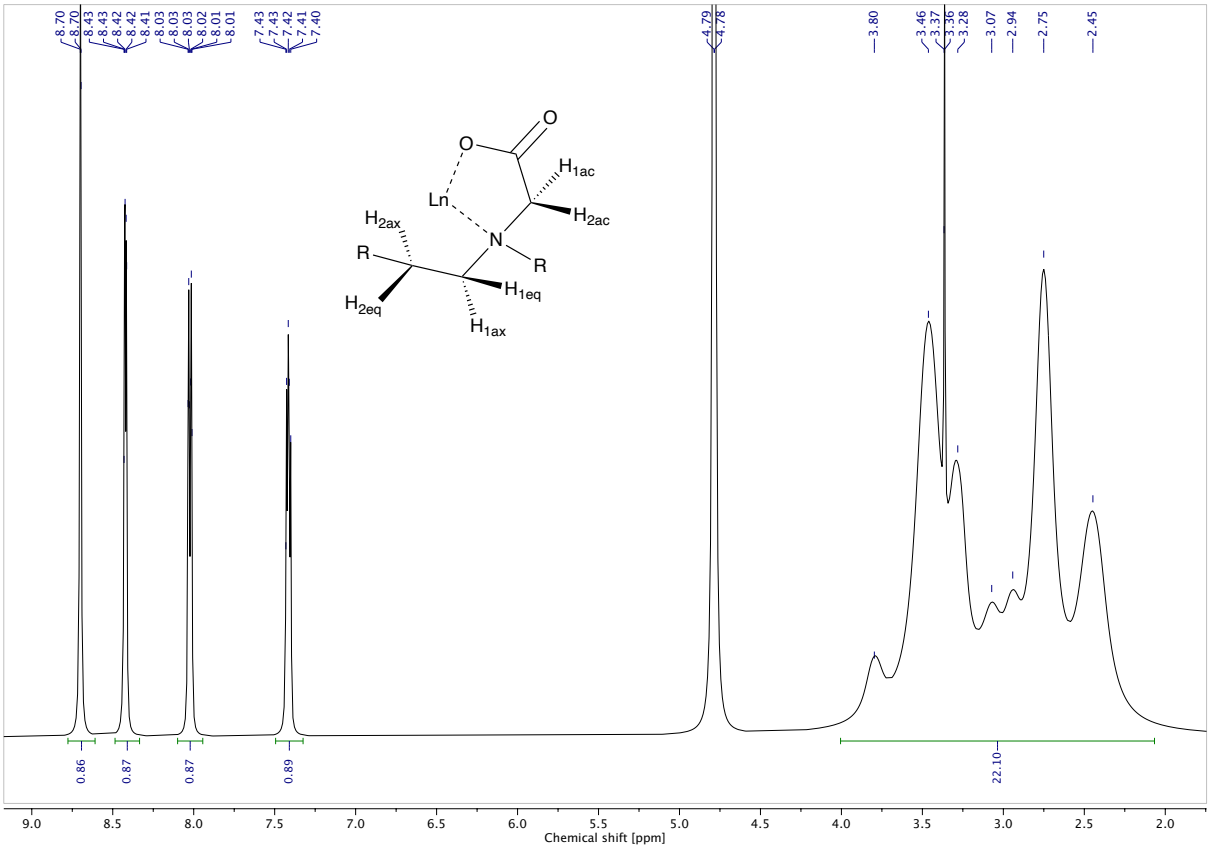
δ_H (500 MHz, D_2O) 9.18 (1 H, d, *J* 2.3, H-Ar), 8.81 (1 H, dd, *J* 5.0, 1.6, H-Ar), 8.48 (1 H, dt, *J* 8.1, 1.9, H-Ar), 7.63 (1 H, dd, *J* 8.1, 5.0, H-Ar), 3.74 – 3.34 (8 H, m, arm protons), 3.32 – 3.19 (4 H, m, ring), 3.00 – 2.39 (12 H, m, ring).



In base (pD 10.14)

δ_H (500 MHz, D_2O) 8.70 (1 H, d, *J* 2.2,H-Ar), 8.42 (1 H, dd, *J* 4.5, 1.3, H-Ar), 8.02 (1 H, dt, *J*

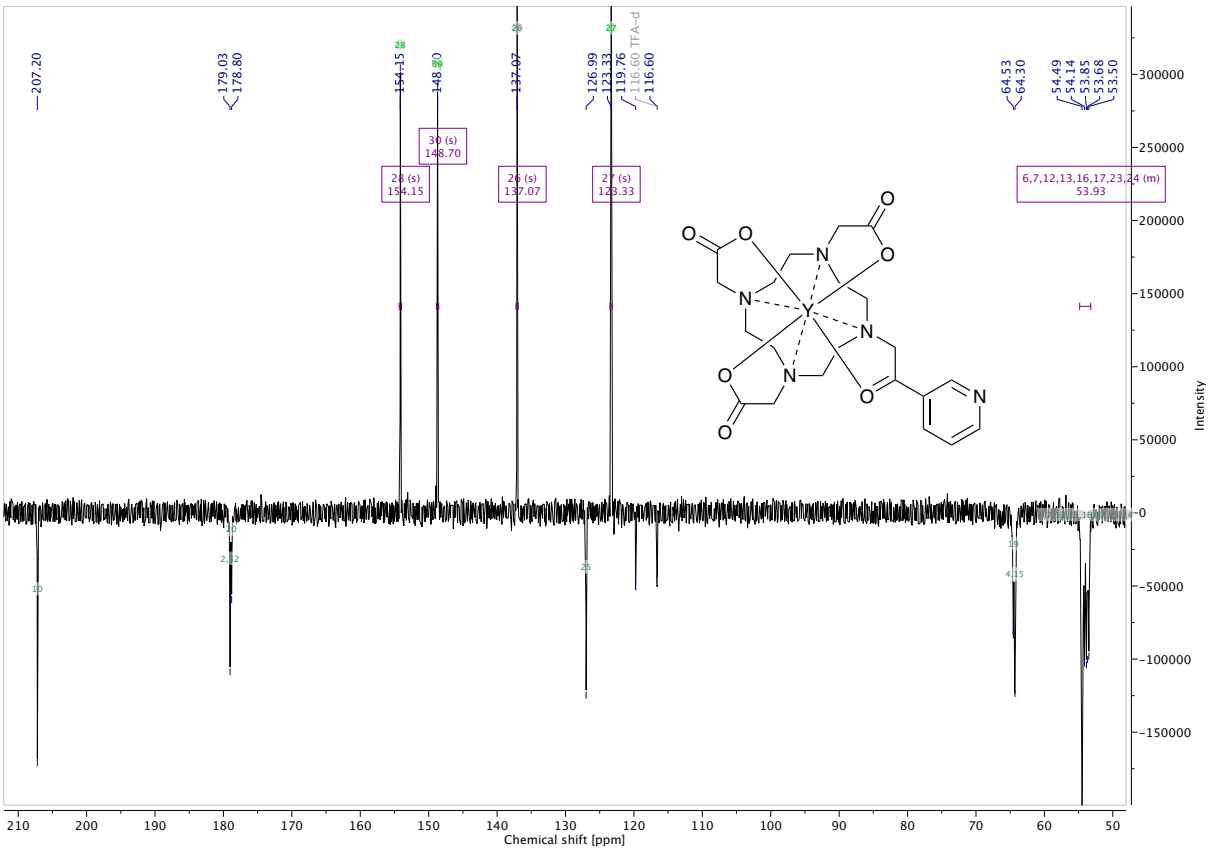
7.9, 2.0, H-Ar), 7.41 (1 H, dd, *J* 8.0, 4.9, H-Ar), 4.01 – 2.07 (22 H, m, ring and arm protons).



CNMR

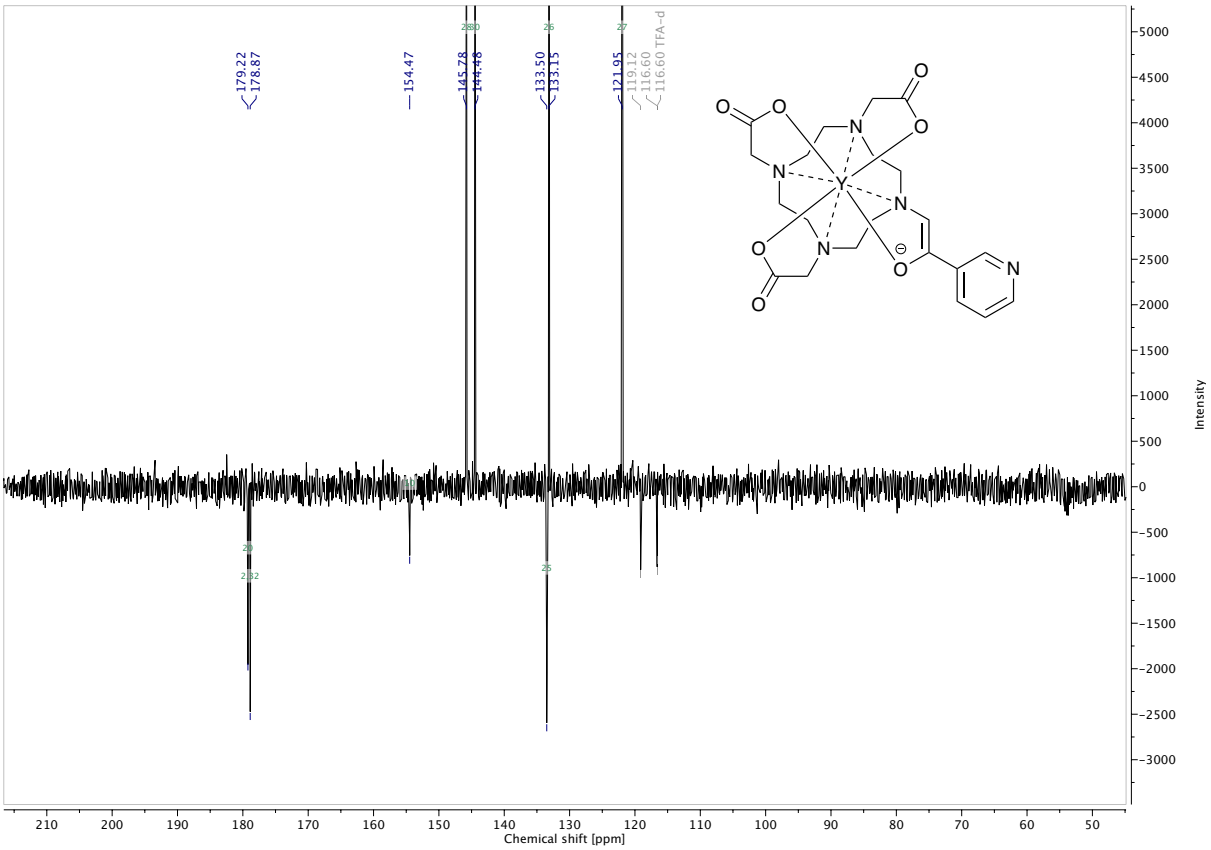
In Acid (pD5.42)

δ $_C$ (101 MHz, H_2O) 211.2(**C**O(py)), 183.0(**C**O_2), 182.8(**C**O_2), 158.1(N**C**H-Ar), 152.7(N**C**H-Ar), 141.1(N**C**H-Ar), 131.0(**C**-Ar), 127.3(**C**H-Ar), 68.5(**C**-CO(py)), 68.3(**C**-CO_2), 58.5(ring), 58.1(ring), 57.8(ring), 57.7(ring), 57.5(ring).



In base (pD 10.14)

δ $_C$ (126 MHz, D_2O) 179.2(R**C**O_2), 178.9(R**C**O_2), 154.5(C=**C**O(py)), 145.8(N-**C**H-Ar), 144.5(**C**H-Ar), 133.5(**C**-Ar), 133.1(**C**H-Ar), 121.9(**C**H-Ar), 116.6 (TFA reference).



Mass Spectrometry

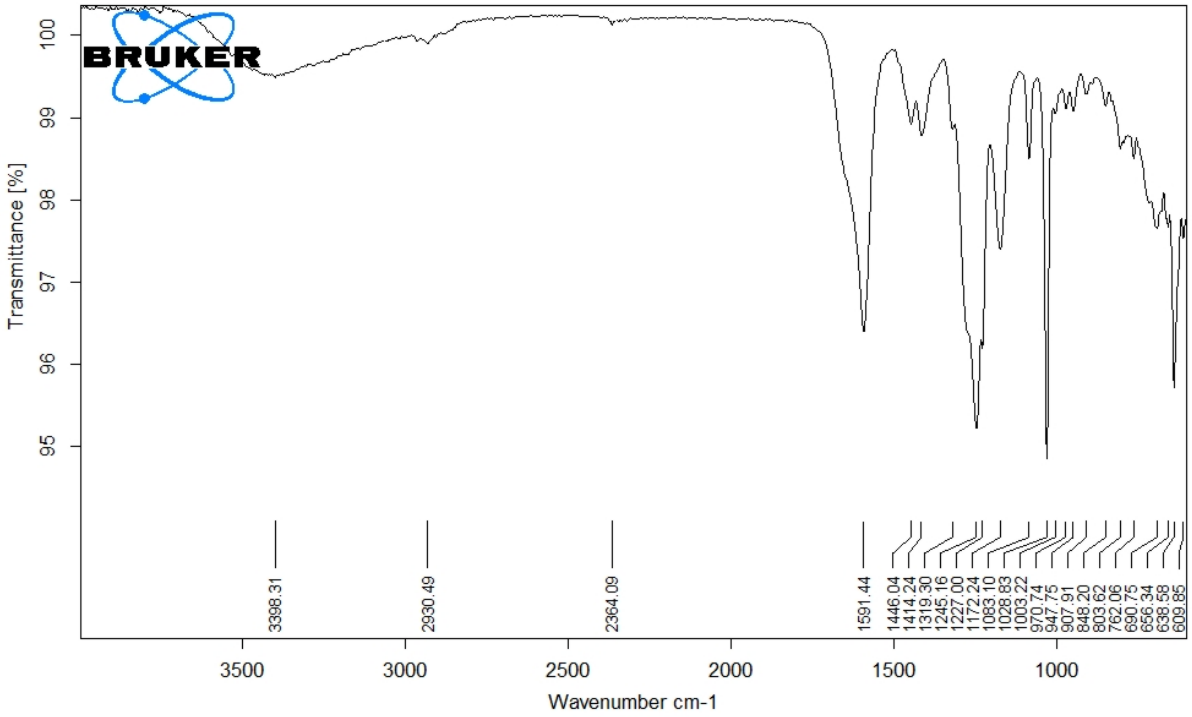
HRMS, ESI:

Predicted: $[M-H]^+$ = 522.1120 Da, $[M-Na]^+$ = 574.0940 Da

Observed: $[M-H]^+$ = 522.1100 Da, $[M-Na]^+$ = 574.0916 Da

IR

IR (cm^{-1}): 3398(w), 2930(w), 2364(w), 1591(s), 1446w), 1414(m), 1245(s), 1172(m), 1083(m), 1029(vs), 971(w), 948(w), 804(w), 762(m), 691(m), 656(m), 639(vs), 610(m).

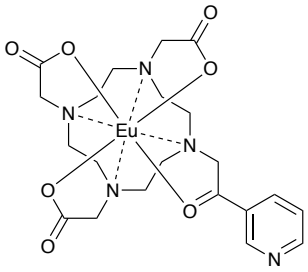


C:\Users\spectrometer-user\Documents\Bruker\OPUS_8.2.28\DATA\MEAS\20221028_131127.0	20221028_131127	Instrument type and / or a	28/10/2022

General complexation method (second syntheses)

Ligand (1 equiv.) and lanthanide chloride or triflate (1 equiv.) was dissolved in MeOH (100 mL per mole). The mixture was stirred at reflux for 2 days, adding over this period NaOH (1 M, 3 equiv.) to control pH, which was kept between 3-7. The product was then concentrated and dialysed to yield the desired complex as a yellow solid.

Eu-DO3A-3-Acetylpyridine (second synthesis)



Yield: 53.9 mg

Chemical Formula: $C_{21}H_{28}N_5O_7Eu$

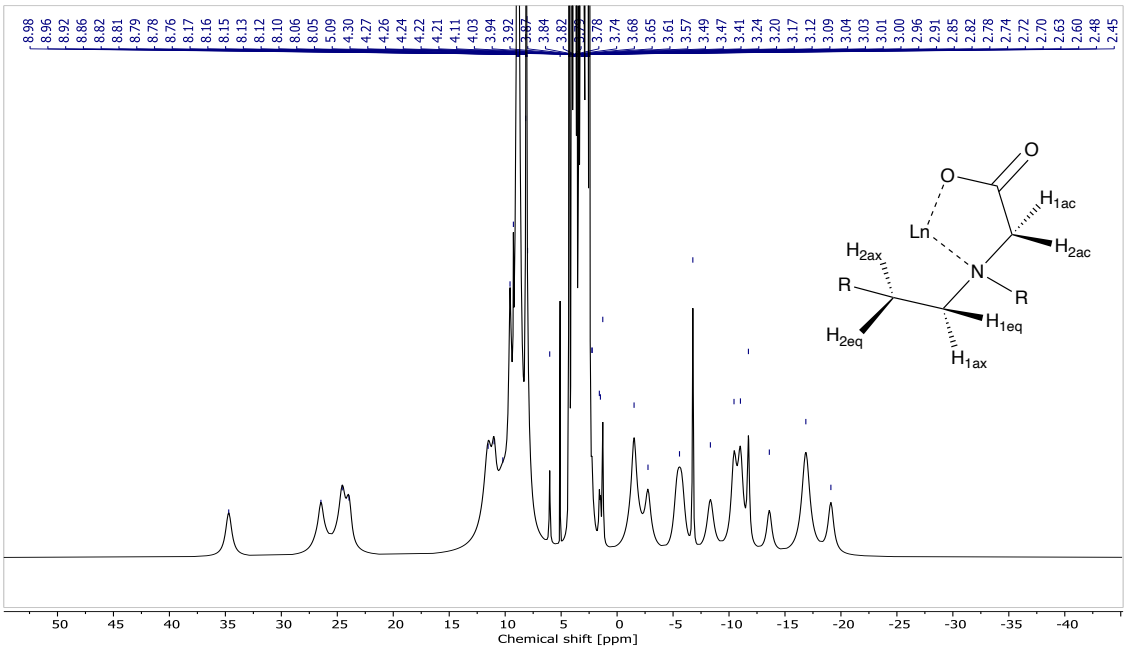
Exact Mass: 615.12 Da

Molecular Weight: 614.45 Da

HNMR

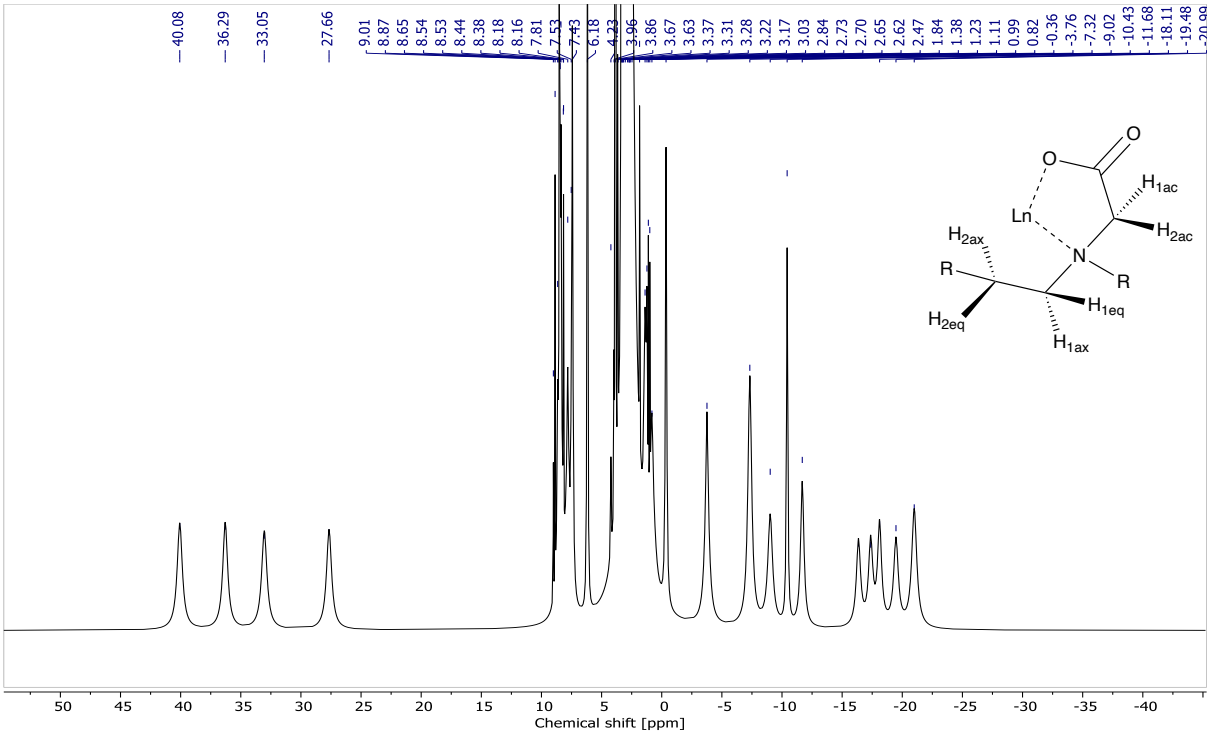
In Acid (pD3.1)

δ_H (500 MHz, D_2O) 34.70 (H_1ax), 26.46, 24.56, 23.95, 11.53, 10.99, 10.21, 9.57, 9.27, 8.98, 8.96, 8.92, 8.86, 8.82, 8.81, 8.79, 8.78, 8.76, 8.17, 8.16, 8.15, 8.13, 8.12, 8.10, 8.06, 8.05, 8.00, 6.02, 5.09, 4.30, 4.27, 4.26, 4.24, 4.22, 4.21, 4.11, 4.03, 3.94, 3.92, 3.87, 3.84, 3.82, 3.79, 3.78, 3.74, 3.68, 3.65, 3.61, 3.57, 3.49, 3.47, 3.41, 3.24, 3.20, 3.17, 3.12, 3.09, 3.04, 3.03, 3.01, 3.00, 2.96, 2.91, 2.85, 2.82, 2.78, 2.74, 2.72, 2.70, 2.63, 2.60, 2.48, 2.45, 2.24, 2.24, 1.59, 1.49, 1.28, -1.52, -2.76, -5.58, -6.77, -8.34, -10.45, -11.02, -11.73, -13.60, -16.86, -19.10 (H_1ac).



In base (pD10.87)

δ_H (500 MHz, D_2O) 40.08 (H_1ax), 36.29, 33.05, 27.66, 9.01, 8.87, 8.65, 8.54, 8.53, 8.44, 8.38, 8.18, 8.16, 7.81, 7.53, 7.43, 6.18, 4.23, 3.96, 3.86, 3.67, 3.63, 3.37, 3.31, 3.28, 3.22, 3.17, 3.03, 2.84, 2.73, 2.70, 2.65, 2.62, 2.47, 1.84, 1.38, 1.23, 1.11, 0.99, 0.82, -0.36, -3.76, -7.32, -9.02, -10.43, -11.68, -16.36, -17.37, -18.11, -19.48, -20.99 (H_1ac).



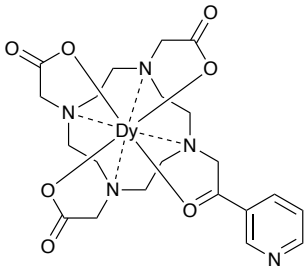
Mass Spectrometry

HRMS, ESI:

Predicted: $[M-H]^+$ = 616.1274 Da

Observed: $[M-H]^+$ = 616.1285 Da

Dy-DO3A-3-Acetylpyridine (second synthesis)



Yield: 34.9 mg (wet) from 0.0539 mmol starting material

Chemical Formula: $C_{21}H_{28}DyN_5O_7$

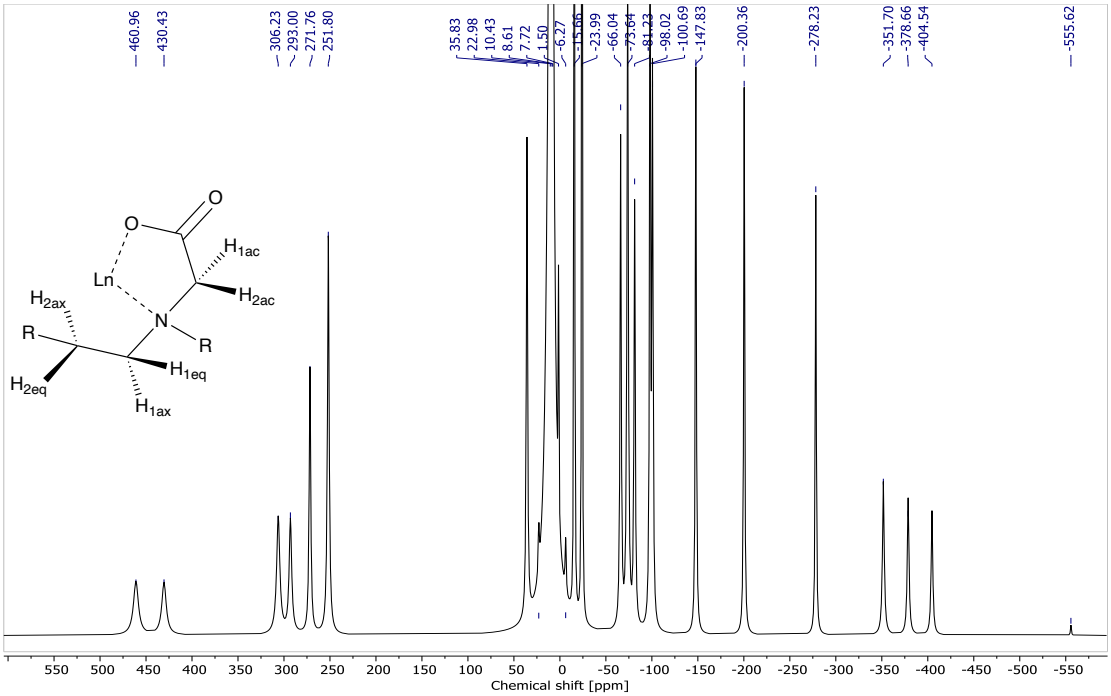
Exact Mass: 626.13 Da

Molecular Weight: 624.98 Da

HNMR

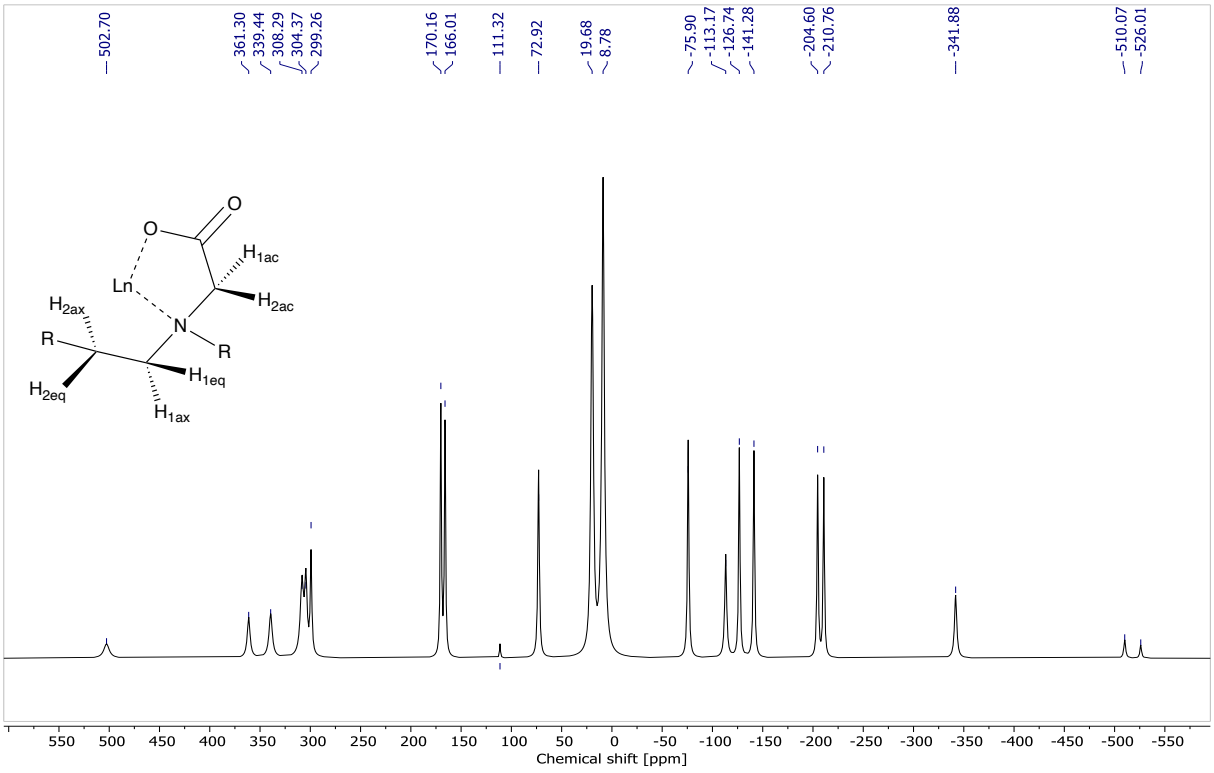
In acid (pD4.92)

δ_H (500 MHz, D_2O) 460.96(H_1ac), 430.43, 306.23, 293.00, 271.76, 251.80, 35.83, 22.98, 10.43, 8.61, 7.72, 1.50, -6.27, -15.66, -23.99, -66.04, -73.64, -81.23, -98.02, -100.69, -147.83, -200.36, -278.23, -351.70, -378.66, -404.54, -555.62(H_1ax).



In base (pD12.38)

δ_H (500 MHz, D_2O) 502.70((H_1ac), 361.30, 339.44, 308.29, 304.37, 299.26, 170.16, 166.01, 111.32, 72.92, 19.68, 8.78, -75.90, -113.17, -126.74, -141.28, -204.60, -210.76, -341.88, -510.07, -526.01(H_1ax).



Mass Spectrometry

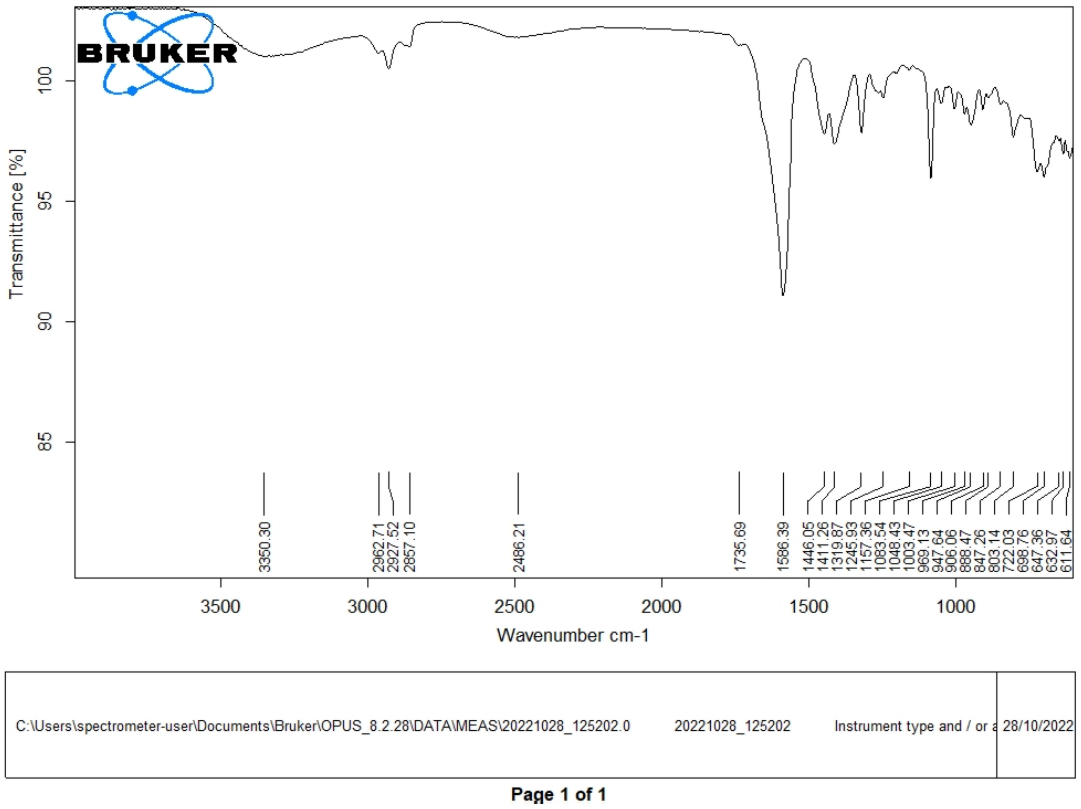
HRMS, ESI:

Predicted: $[M-H]^+$ = 627.1340 Da

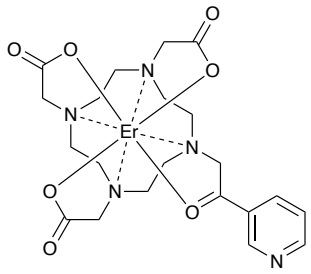
Observed: $[M-H]^+$ = 627.1353 Da

IR

IR (cm^{-1}): 3350(w), 2963(w), 2928(w), 2857(w), 2486(w, Ar), 1586(vs), 1446(m), 1411(m), 1320(m), 1157(s), 1084(m), 1048(m), 1003(m), 969(m), 988(m), 948(m), 803(m), 722(s), 699(s), 647(s), 633(s), 612(s).



Er-DO3A-3-Acetylpyridine



Yield: 36.2 mg from 0.0539 mmol of starting material

Chemical Formula: $C_{21}H_{28}N_5O_7Er$

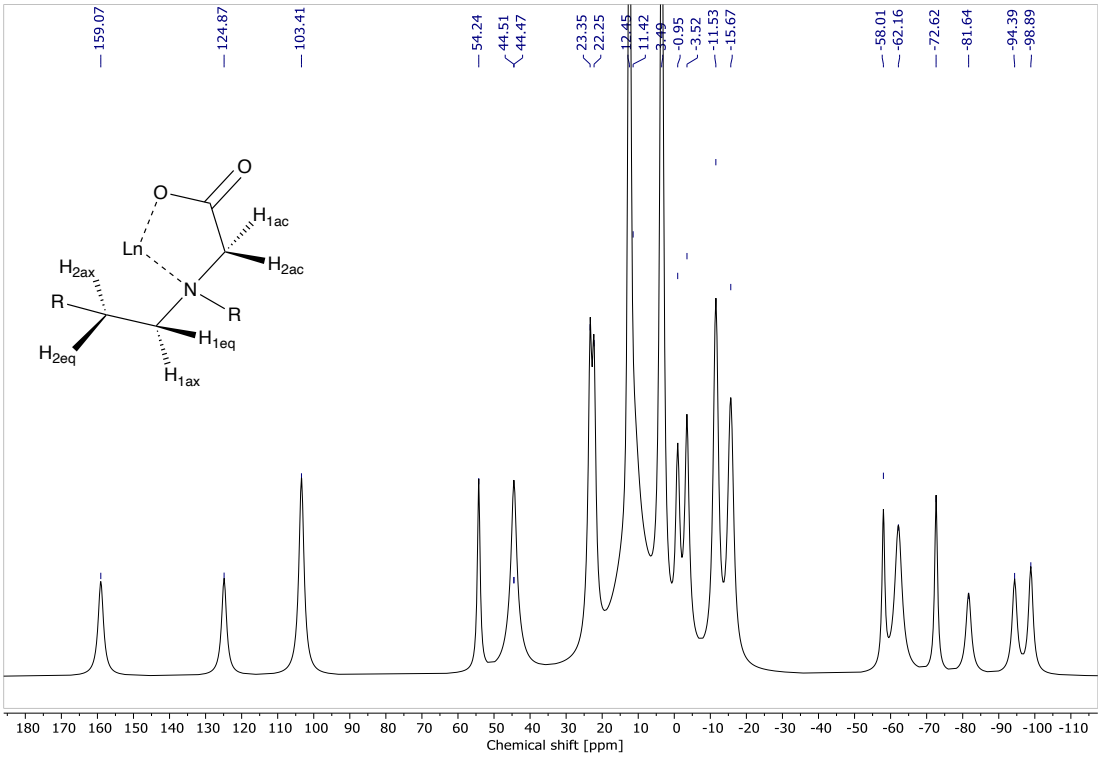
Exact Mass: 628.13 Da

Molecular Weight: 629.74 Da

HNMR

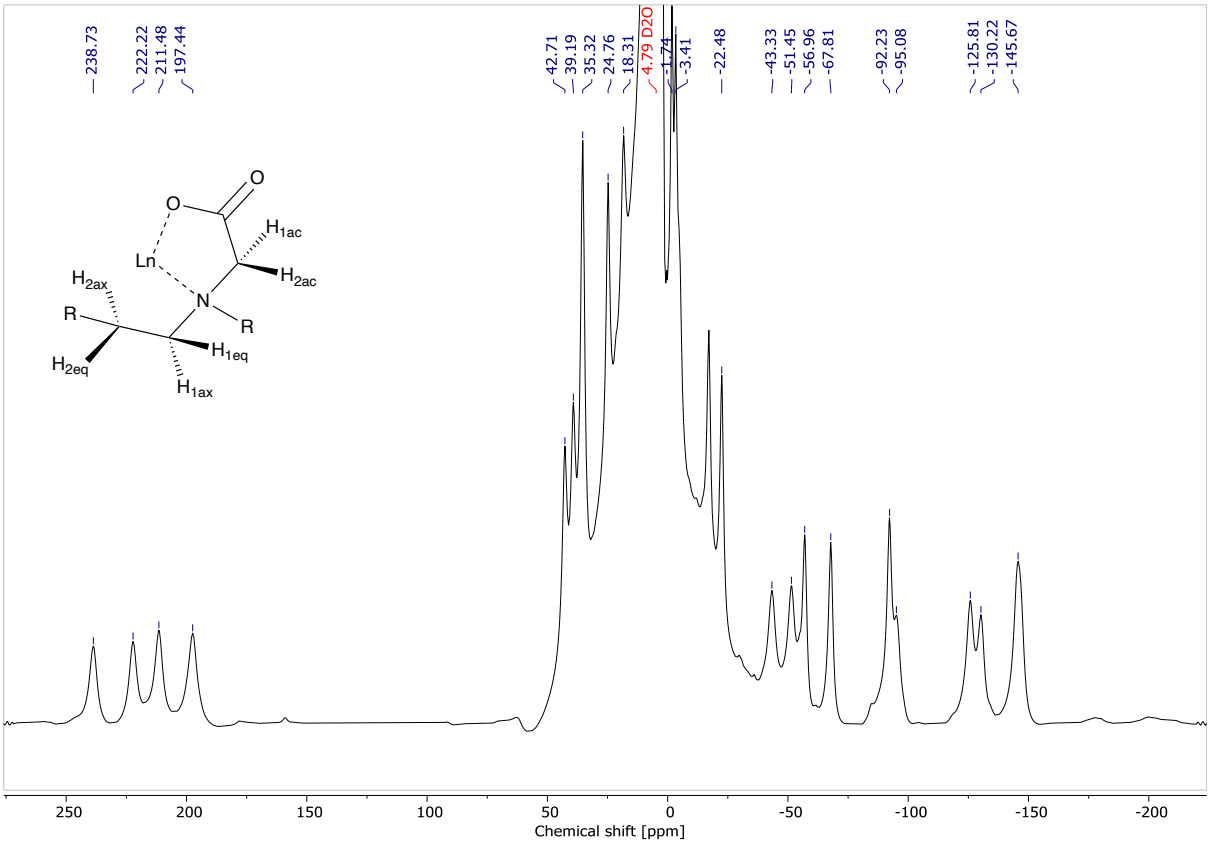
In acid (pD4.04)

δ_H (500 MHz, D_2O) 159.07 (H_1ax), 124.87, 103.41, 54.24, 44.51, 44.47, 23.35, 22.25, 12.45, 11.42, 3.49, -0.95, -3.52, -11.53, -15.67, -58.01, -62.16, -72.62, -81.64, -94.39, -98.89 (H_1ac).



In base (pD13.71)

δ_H (500 MHz, D_2O) 238.73 (H_1ax), 222.22, 211.48, 197.44, 42.71, 39.19, 35.32, 24.76, 18.31, 4.79, -1.74, -3.41, -22.48, -43.33, -51.45, -56.96, -67.81, -92.23, -95.08, -125.81, -130.22, -145.67 (H_1ac).



Mass Spectrometry

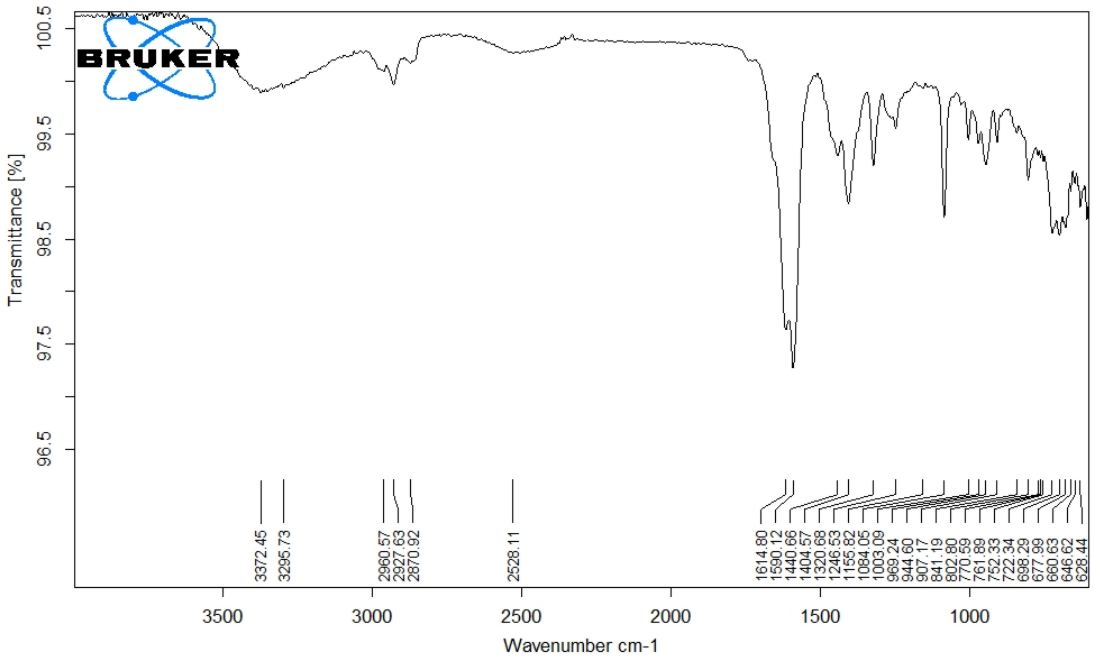
HRMS, ESI:

Predicted: $[M-H]^+$ = 629.1365 Da, $[M-Na]^+$ = 651.1184 Da

Observed: $[M-H]^+$ = 629.1395 Da, $[M-Na]^+$ = 651.1158 Da

IR

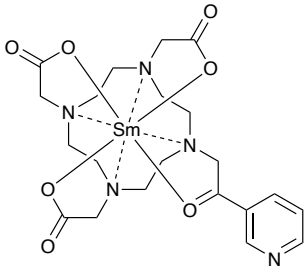
IR (cm^{-1}): 3382(w), 2961(w), 2928(w), 2871(w), 2528(w), 1614(s), 1590(s), 1441(m), 1405(s), 1321(s), 1247(m), 1003(s), 969(m), 945(m), 907(m), 841(m), 803(s), 771(s), 761(s), 752(s), 722(s), 698 (s), 678(s), 661(s), 647(s), 628(s).



C:\Users\spectrometer-user\Documents\Bruker\OPUS_8.2.28\DATA\MEAS\20221028_130010.0	20221028_130010	Instrument type and / or a	28/10/2022

Page 1 of 1

Sm-DO3A-3-Acetylpyridine



Yield: 35.7 mg from 0.0539 mmol starting material

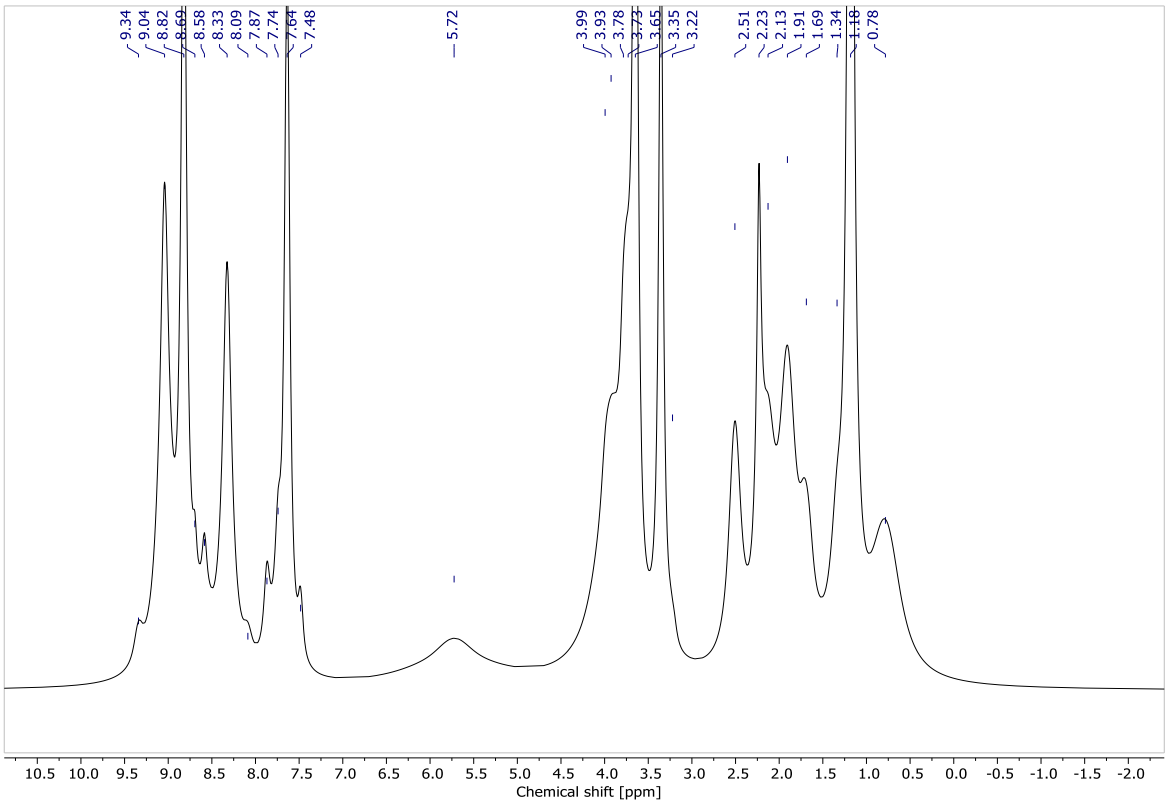
Chemical Formula: $C_{21}H_{28}N_5O_7Sm$

Exact Mass: 614.12 Da

Molecular Weight: 612.84 Da

HNMR

δ_H (400 MHz, D_2O) 9.34, 9.04, 8.82, 8.69, 8.58, 8.33, 8.09, 7.87, 7.74, 7.64, 7.48, 5.72, 3.99, 3.93, 3.78, 3.73, 3.65, 3.35, 3.22, 2.51, 2.23, 2.13, 1.91, 1.69, 1.34, 1.18, 0.78. Unassignable due to small lanthanide induced shift.



Mass Spectrometry

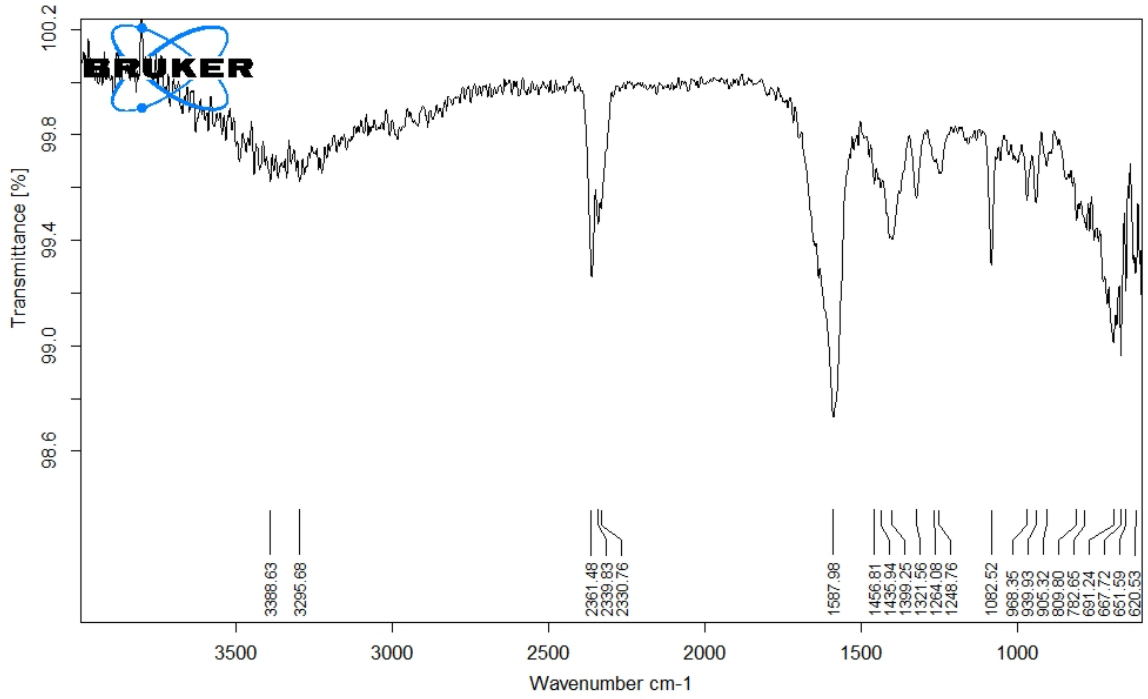
HRMS, ESI:

Predicted: $[M-H]^+$ = 615.1259 Da

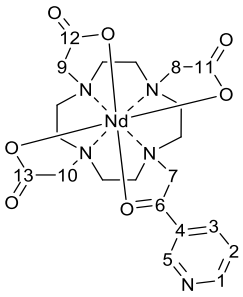
Observed: $[M-H]^+$ = 615.1285 Da

IR

IR (cm^{-1}): 2362(s), 2340(m), 1588(vs), 1399(m), 1322(m), 1249(w), 1083(m), 968(m), 940(m), 905(w), 810(w), 691(s), 667(s), 651(s), 621(m).



Nd-DO3A-3-Acetylpyridine



Yield: 26 mg from 0.0539 mmol starting material.

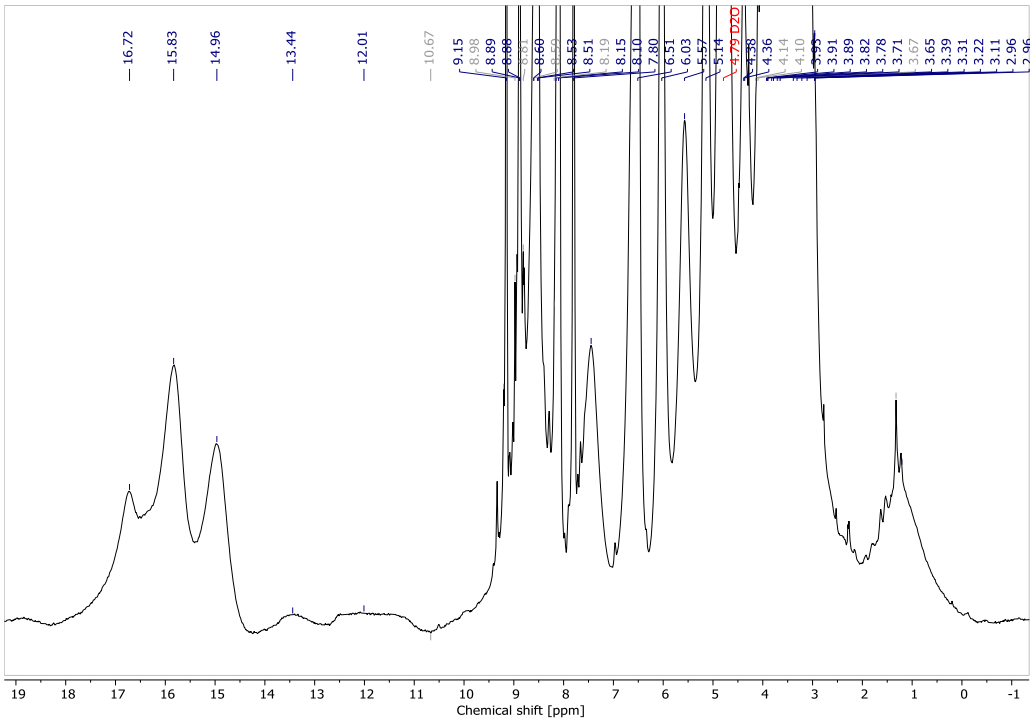
Chemical Formula: $C_{21}H_{28}N_5NdO_7$

Exact Mass: 604.11 Da

Molecular Weight: 606.73 Da

HNMR

δ_H (400 MHz, $CDCl_3$) 16.78, 15.86, 14.98, 11.28, 9.16, 8.89, 8.62, 8.55, 8.09, 7.82, 7.44, 6.50, 5.98, 5.54, 5.12, 4.37, 4.12, 3.91, 3.78, 3.70, 3.55, 3.38, 3.19, 1.29, -2.77, -3.71, -6.07, -10.29.



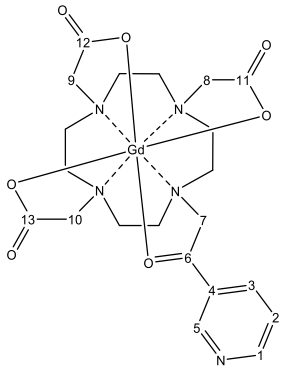
Mass Spectrometry

HRMS ESI:

Predicted : $[M-H]^+$ = 605.1139 Da

Observed: $[M-H]^+$ = 605.1131 Da

Gd-DO3A-3-Acetylpyridine



Yield: 47.7 mg from 0.0539 mmol starting material

Chemical Formula: $C_{21}H_{28}GdN_5O_7$

Exact Mass: 620.12 Da

Molecular Weight: 619.73 Da

Mass Spectrometry

HRMS ESI:

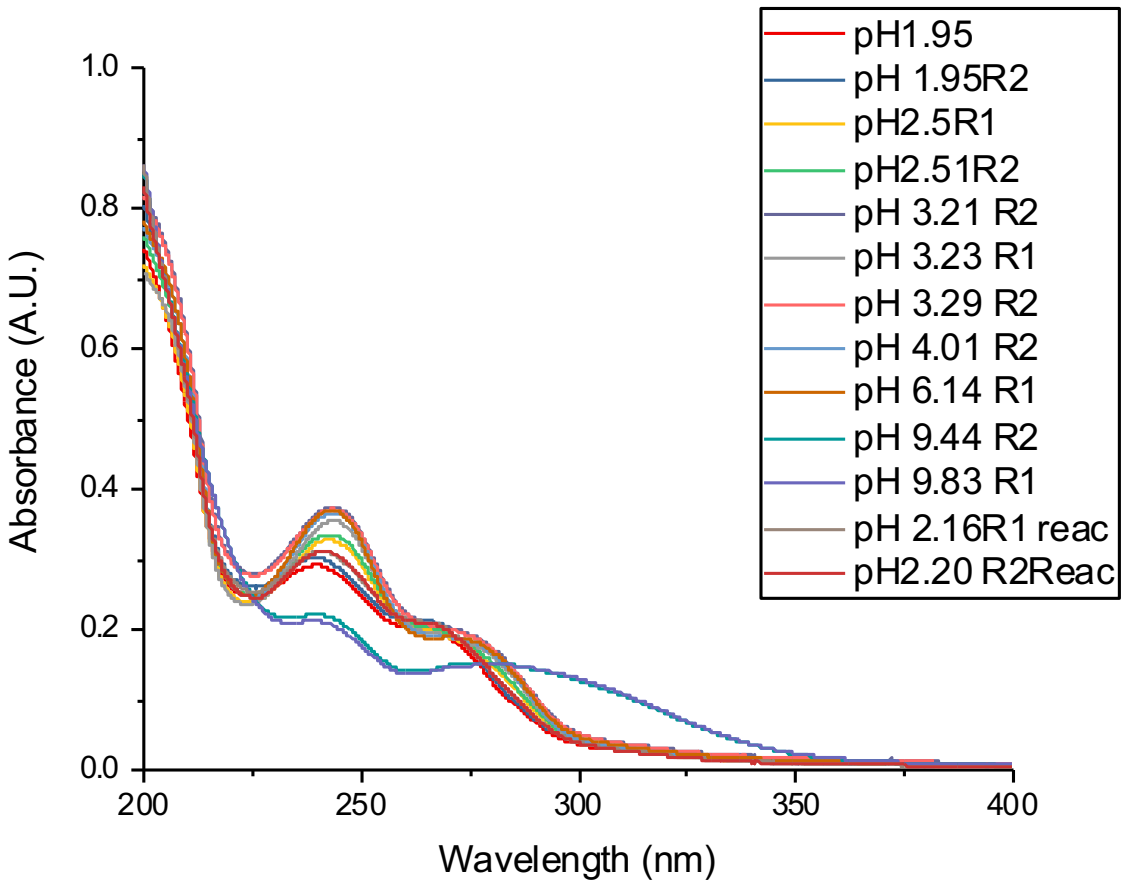
Predicted : $[M-H]^+$ = 621.1303 Da

Observed: $[M-H]^+$= 621.1313 Da

Rough titration data

Eu-Unbuffered

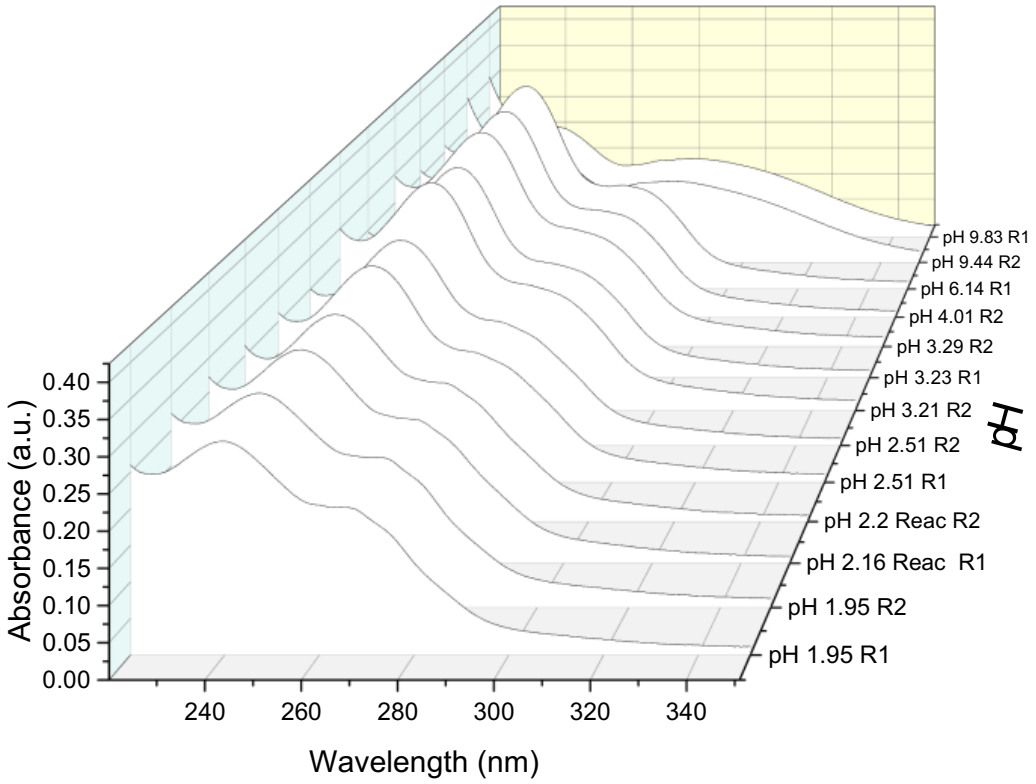
UV/Vis



At pH 1.95-3.5 Maxima at 241 nm and 265 nm

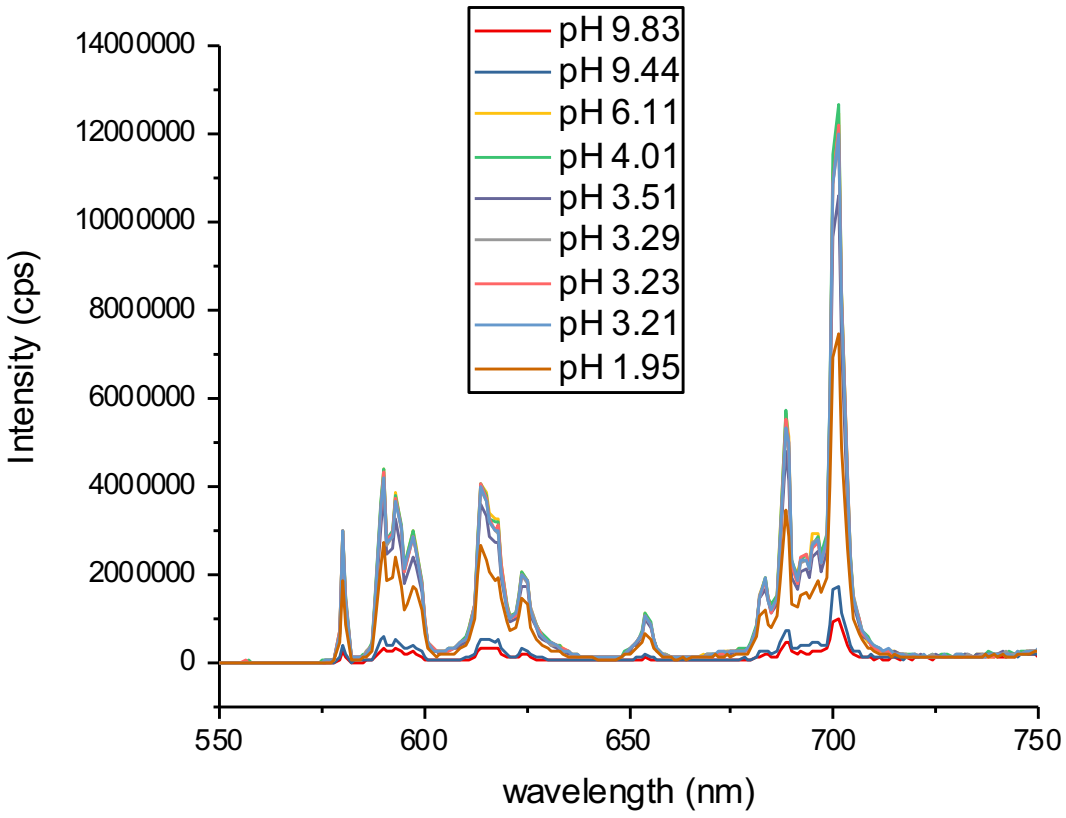
At pH 3.5-6 Maxima at 241 nm and 275 nm

At pH 9+ Maxima at 241 nm and 285 nm

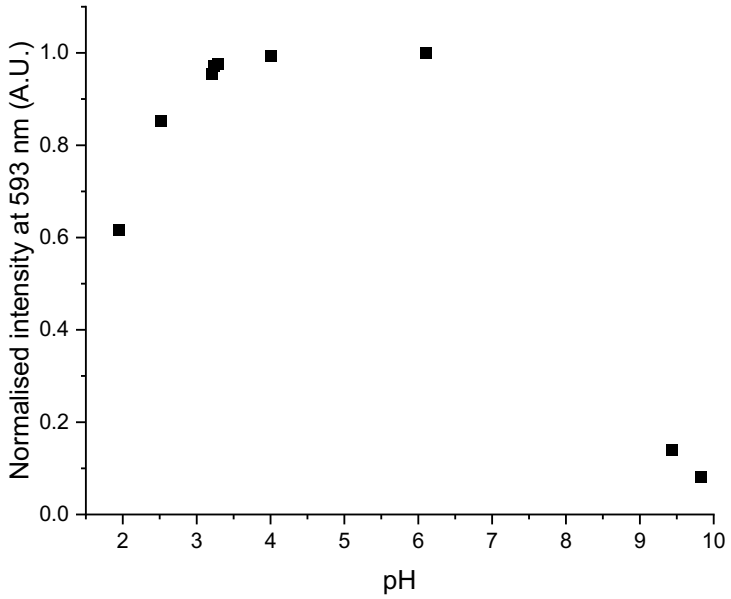

Absorbance (a.u.)
0.40
0.35
0.30
0.25
0.20
0.15
0.10
0.05
0.00
240
260
280
300
320
340
Wavelength (nm)
pH 9.83 R1
pH 9.44 R2
pH 6.14 R1
pH 4.01 R2
pH 3.29 R2
pH 3.23 R1
pH 3.21 R2
pH 2.51 R2
pH 2.51 R1
pH 2.2 Reac R2
pH 2.16 Reac R1
pH 1.95 R2
pH 1.95 R1
pH

Fluorescence data

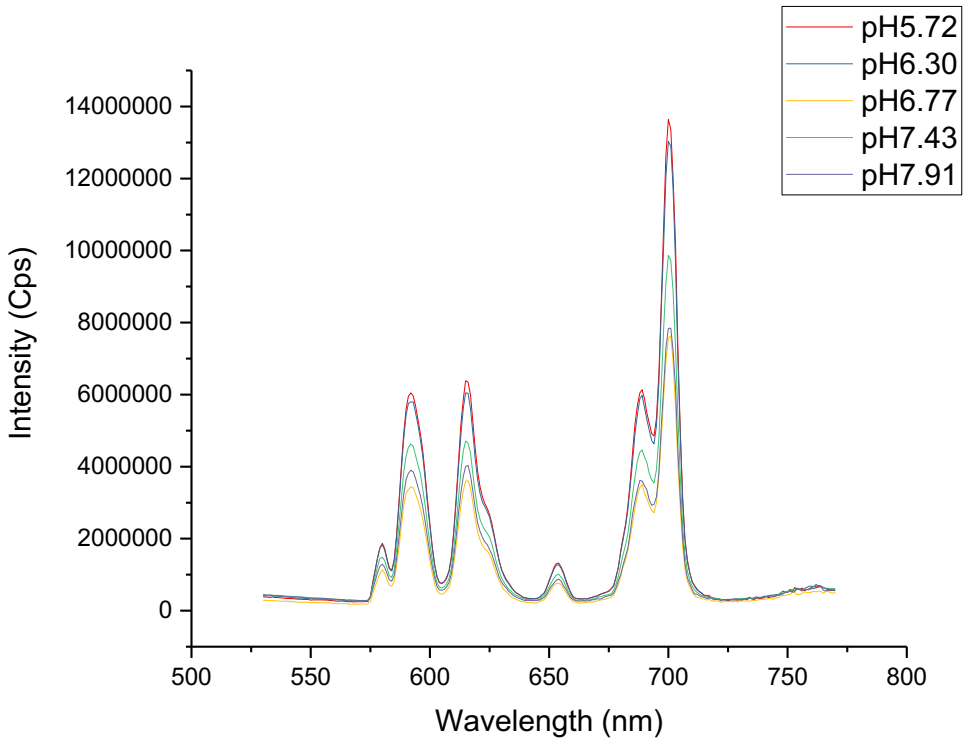
High Resolution



Intensity vs pH for high resolution $^5D_0$-$^7F_1$ transition



Eu-Phosphate buffer titration



CF Analysis

The position of the peaks remained invariant throughout all the titrations for the samples which are emitting by indirect excitation.

Transition $^5D_0 \rightarrow {}^7F_?$ (Barycentre cm^{-1})	Wavelength (nm)	Wavenumber (cm^{-1})	Mj
$^7F_0$	580	17241	0
$^7F_1$ (16845)	590	16949	±1
	593	16863	±1
	597	16722	0
$^7F_2$ (16124)	614	16260	0
	619	16181	±1
	624	1600	±2
$^7F_3$	654	15267	-
$^7F_4$	683	14614	0
	688	15534	±1
	693	14430	±2
	696	14367	±3
	701	14264	±4

Crystal Field Parameters

B_0^2 = +520 cm^{-1}

B_2^2 = -176 cm^{-1}

Derivation of CF parameters from data using Stevens' parametrisation

In order to parametrize spectra, we must first identify the components of each m_J manifold. The splitting of the terms follows the magnitudes described in K W H Stevens 1952 *Proc. Phys. Soc. A* **65** 209.[2]

For $^7F_1$ a=1/5, multiplication factor (F)= 1

$3(J_z)^2$- J(J+1) values

M_j=0 value is equal to -2

M_j=1 value is equal to 1

$^7F_1$ Split between Mj = 0 and 1 (Δ) is equal to 1*3*0.2 = 3/5

When converting to the Wybourne formalism divide by 2

Therefore $\Delta = \frac{3}{10} B_0^2$

$3(J_z)^2$- J(J+1) values when multiplied by (a) give an operator equivalent of the electronic distribution. The sign of this value gives a description of the nature of the electronic distribution of that manifold component. Negative gives a prolate distribution and positive gives an oblate distribution.

For B_2^2 the difference in energy between the M_j = ±1 states (λ).

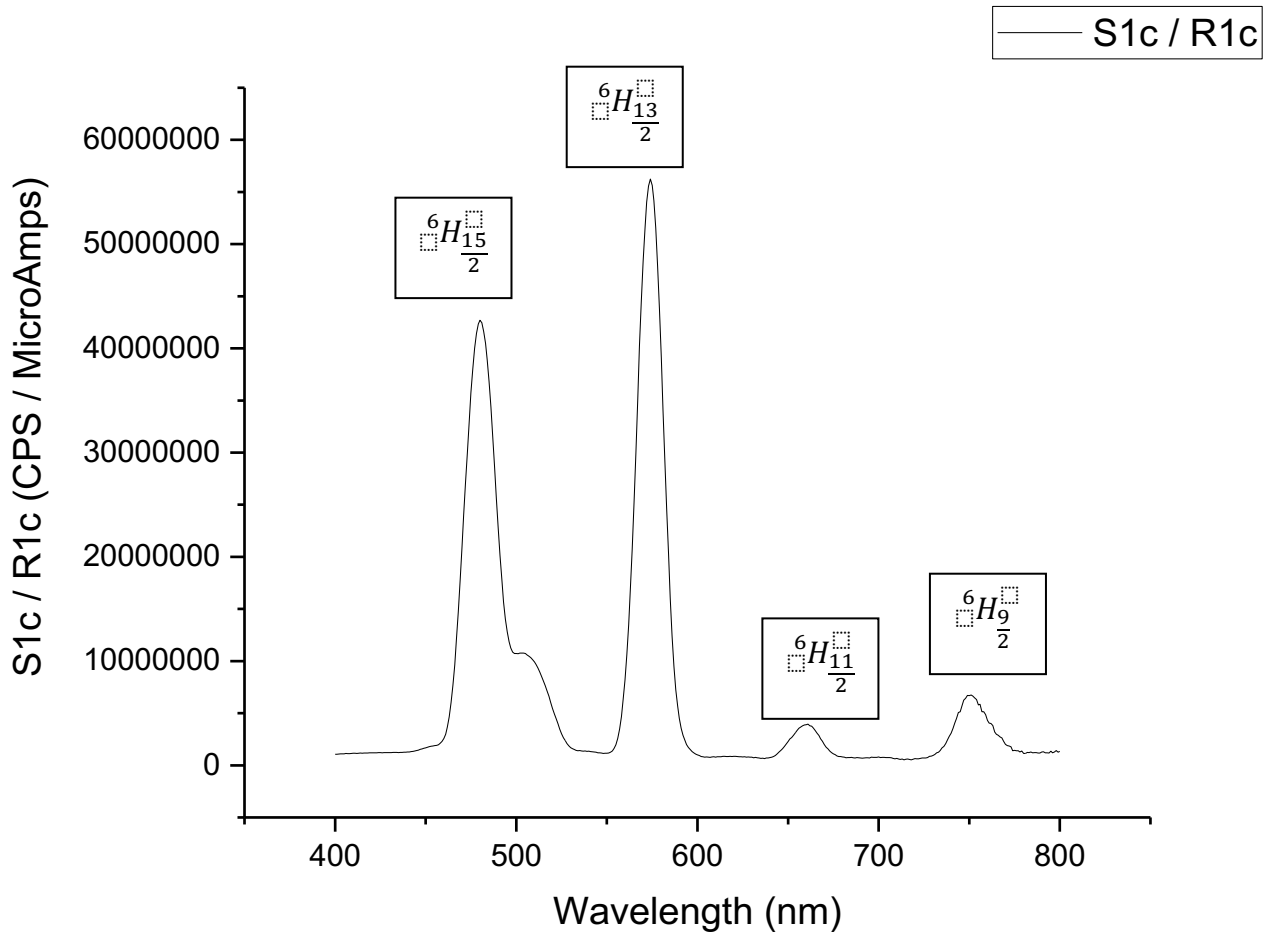
$$\lambda = \frac{\sqrt{6}}{5} B_2^2$$

Dy-DO3A-3-acetylpyridine data

Fluorescence

In D_2O

$^4F_{9/2}\rightarrow$



MES, CHES, HEPES Titration

Excitation spectra

5Eu

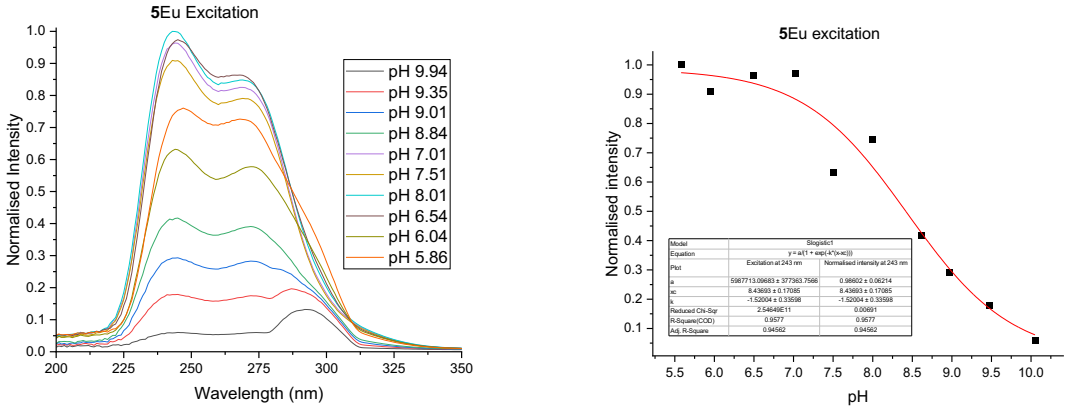


*Figure 1: excitation spectrum of the $^5D_0 \rightarrow {}^7F_1$ transition of **5**Eu. The intensity of the peak at 243nm was plotted against the pH of the solution. Normalised with intensity at 243 nm. The blanking of the data did not remove completely the shoulder caused by scattering (592nm/2). This makes the peak at 273 nm unusable as this affects the intensity of this peak.*

5Dy

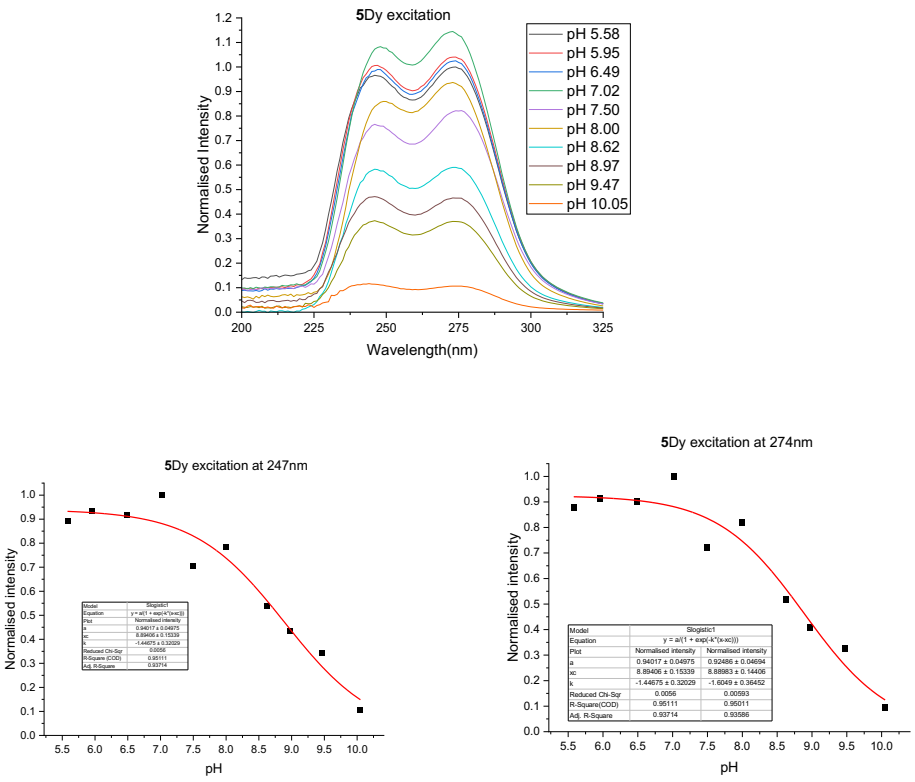


*Figure 2: excitation spectrum of the $^7F_{9/2} \rightarrow {}^6H_{15/2}$ transition (483 nm) of **5**Dy. Normalised with intensity at 275nm The intensity of both peaks (247 nm and 275nm) was plotted against the pH of the buffer solution as both of these peaks were effectively blanked. This gave the same pKa for both excitation wavelengths within the margin of error.*

5Sm

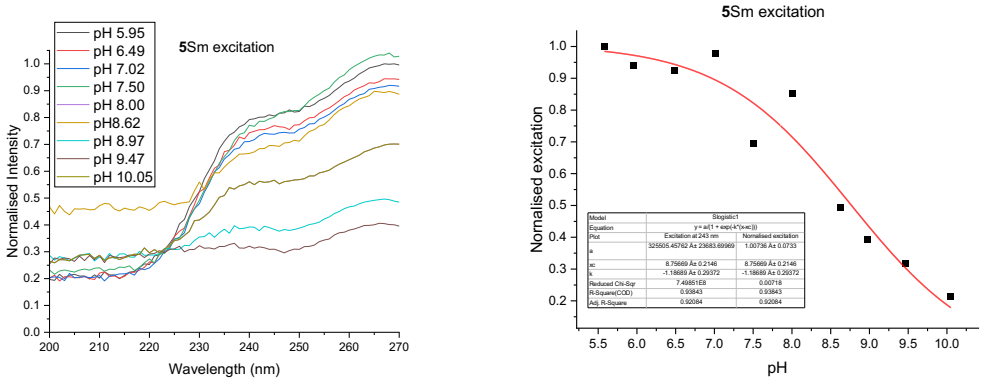


*Figure 3: excitation spectrum of the $^4G_{5/2} \rightarrow {}^4H_{7/2}$ transition (595nm) of **5**Sm. Normalised with intensity at 265 nm. Due to issues blanking this data the peak at 273 nm was unusable as it led to inverted peaks, therefore the intensity of the peak at 243 nm was plotted against pH.*

Emission spectra

5Eu

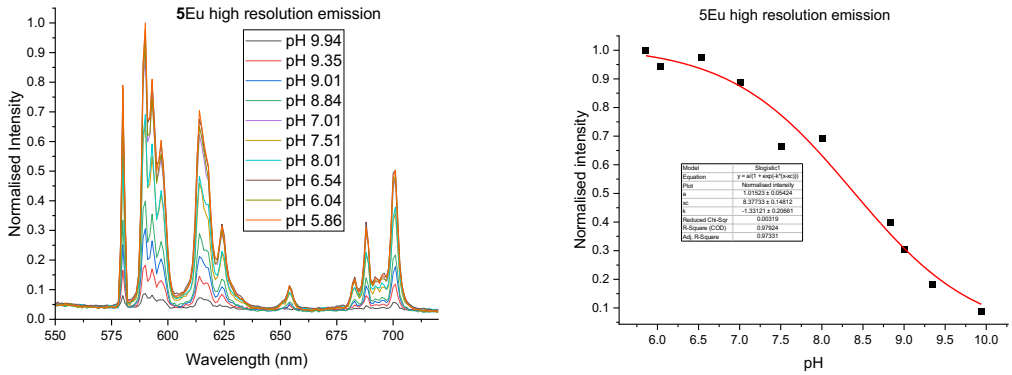


*Figure 4: high resolution emission spectrum of **5**Eu. Normalised with intensity at 592 nm. The intensity of the $^5D_0 \rightarrow {}^7F_1$ transition at 590 nm was plotted against pH.*

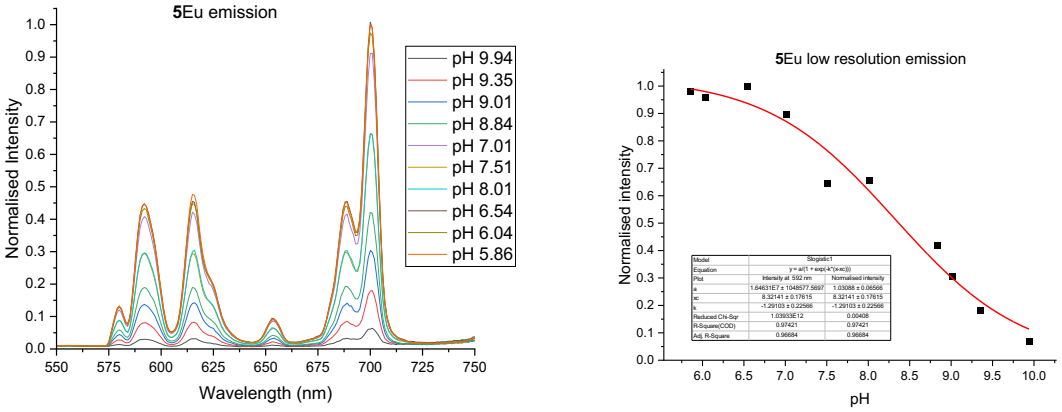


*Figure 5: low resolution emission spectrum of **5**Eu. Normalised with intensity at 700 nm. The intensity of the $^5D_0 \rightarrow {}^7F_1$ transition at 592 nm was plotted against pH. This was used to obtain a pKa value for the complex.*

5Dy

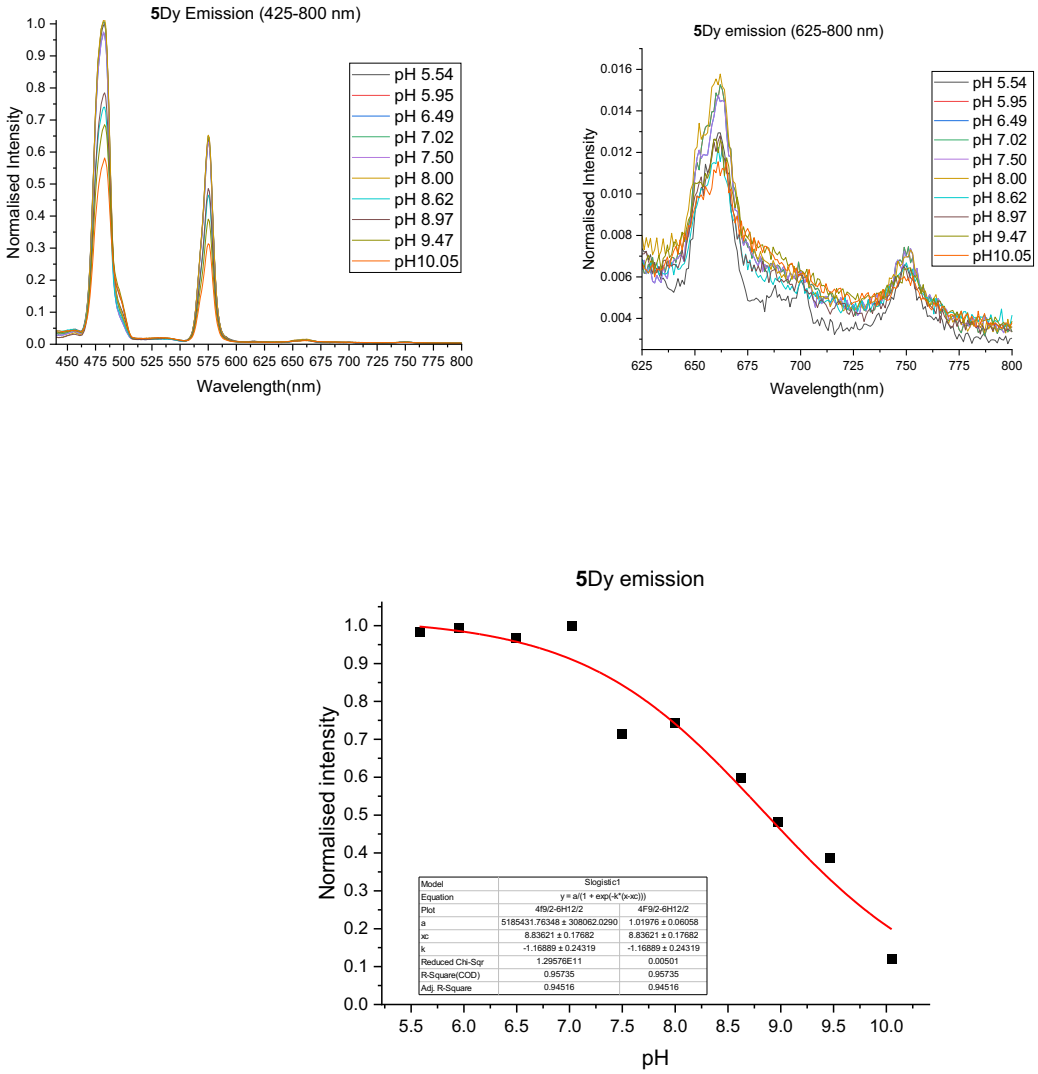


*Figure 6: emission spectrum of **5**Dy. Normalised with intensity at 475 nm. The intensity of $^{7}F_{9/2} \rightarrow {}^{6}H_{13/2}$ transition (575 nm) was plotted against pH*

5Sm

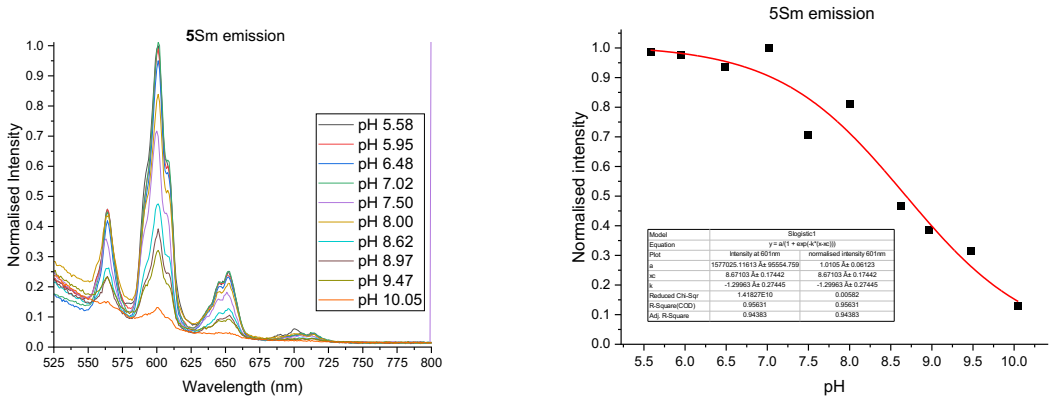
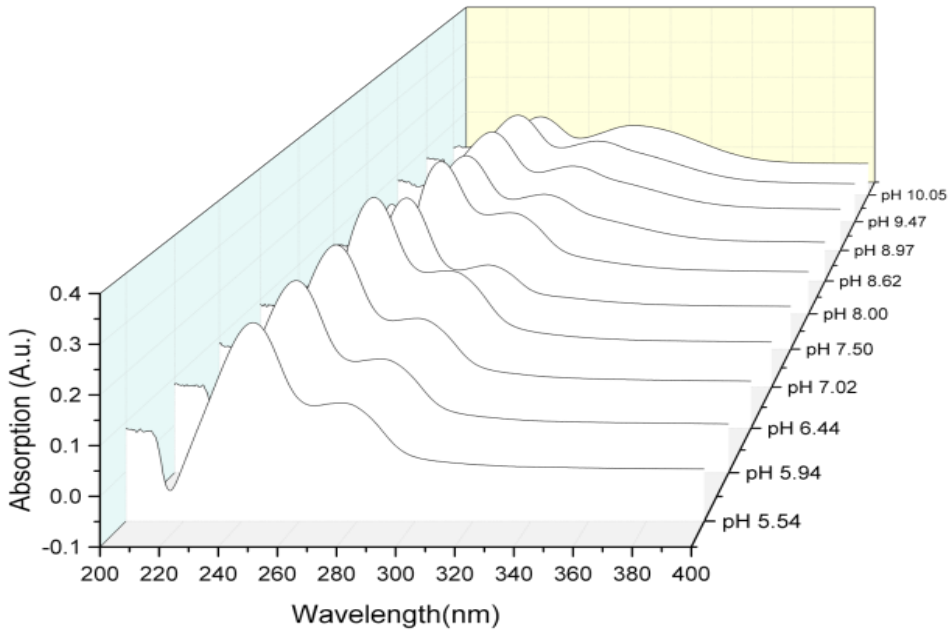


*Figure 7: emission spectrum of **5**Sm. Excitation wavelength 243 nm. Normalised with intensity at 595 nm. The intensity of the $^4G_{5/2} \rightarrow {}^4H_{5/2}$ transition (595 nm).*

UV-Vis spectrum of **5**Dy



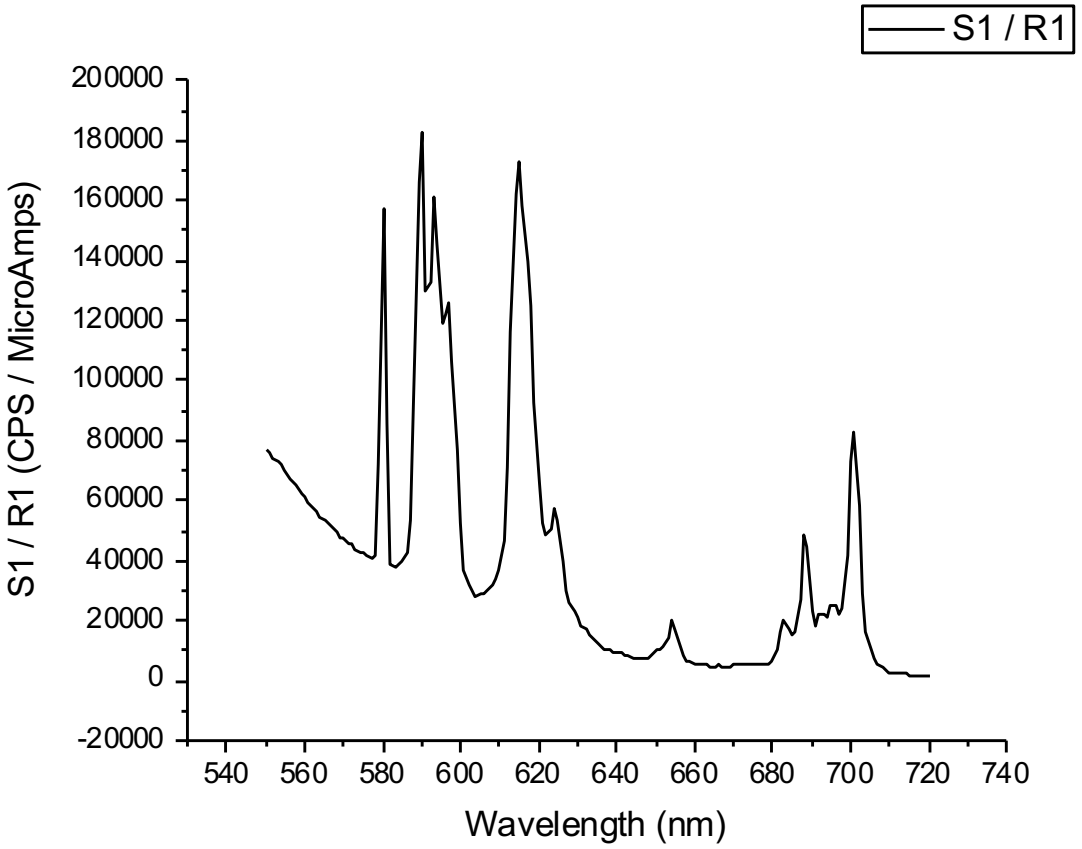
pH of buffer	*Maximum 1 (nm)*	*Abs. 1 (A.U.)*	*Maximum 2 (nm)*	*Abs. 2 (A.U.)*
5.54	243.2	0.3005	274.4	0.1384
5.94	243.8	0.3045	274.4	0.1396
6.44	244.2	0.3023	274.8	0.1410
7.02	244.4	0.3329	273.0	0.1656
7.50	243.8	0.2582	277.0	0.0996
8.00	245.2	0.2744	274.0	0.1488
8.62	243.2	0.2120	277.2	0.1211
8.97	242.8	0.2124	278.2	0.1224
9.47	243.0	0.1903	280.0	0.1201
10.05	242.0	0.1198	289.0	0.0954

Direct Excitation

$Eu^{3+}\,{}^5L_2 \leftarrow {}^7F_{0\text{-}4}$ - 395nm

pH 5.74

Peak positions same as in antenna excitation.

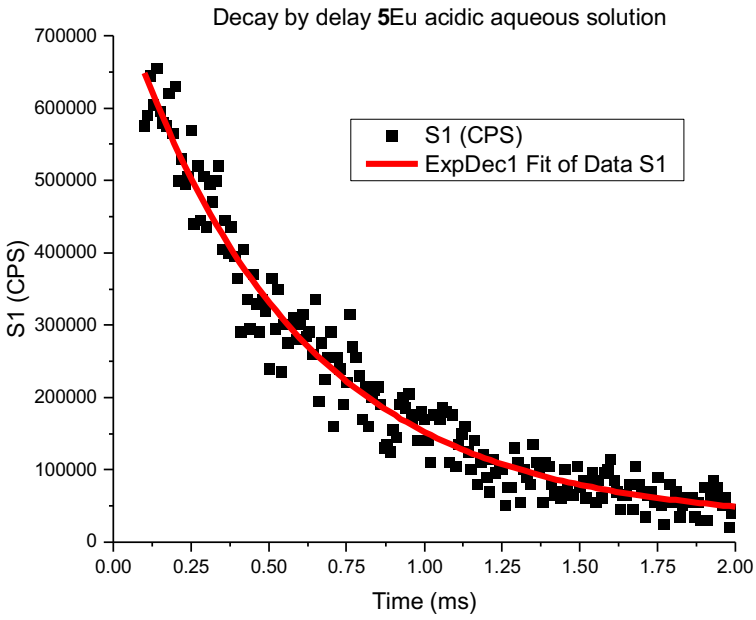


Phosphorescent decay

H_2O

		Value	Standard Error
S1	y0	28350.61191	7216.10938
S1	A1	742541.84098	12351.10311
S1	t1	**0.55898**	0.02324

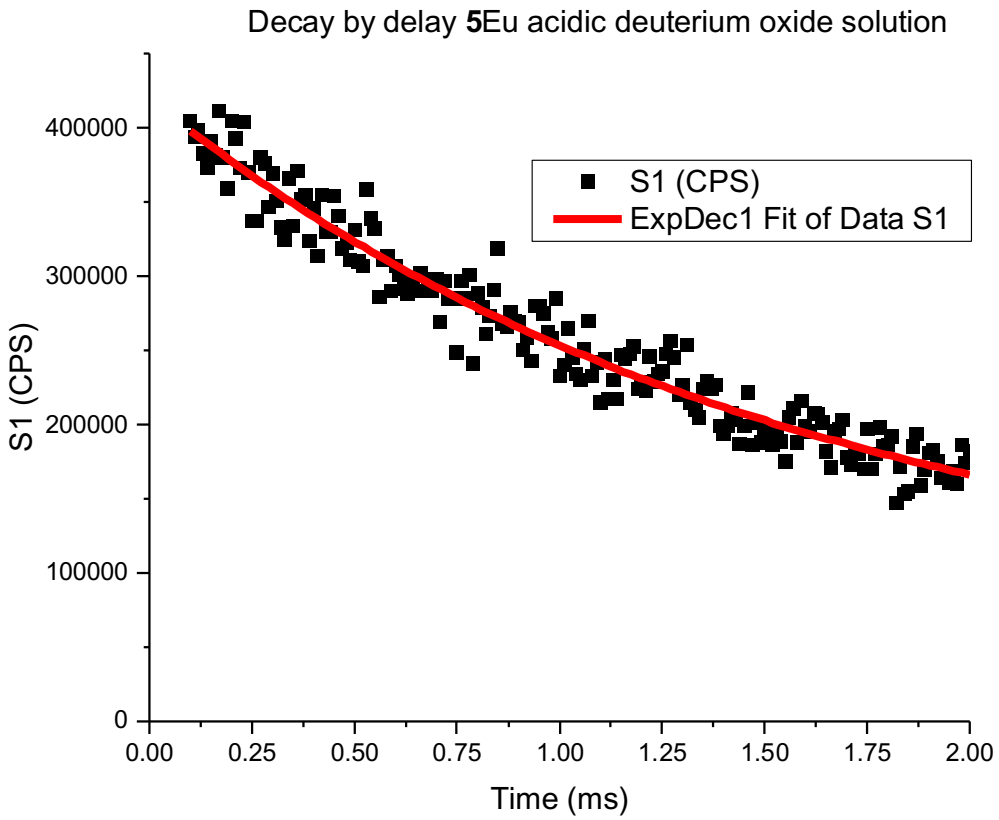
Half-life = 0.55898±0.02324 ms



D_2O

		Value	Standard Error
S1	y0	70876.73396	20143.35141
S1	A1	349288.44092	16868.58176
S1	t1	**1.53963**	0.16663

Half-life = 1.53963±0.16663 ms

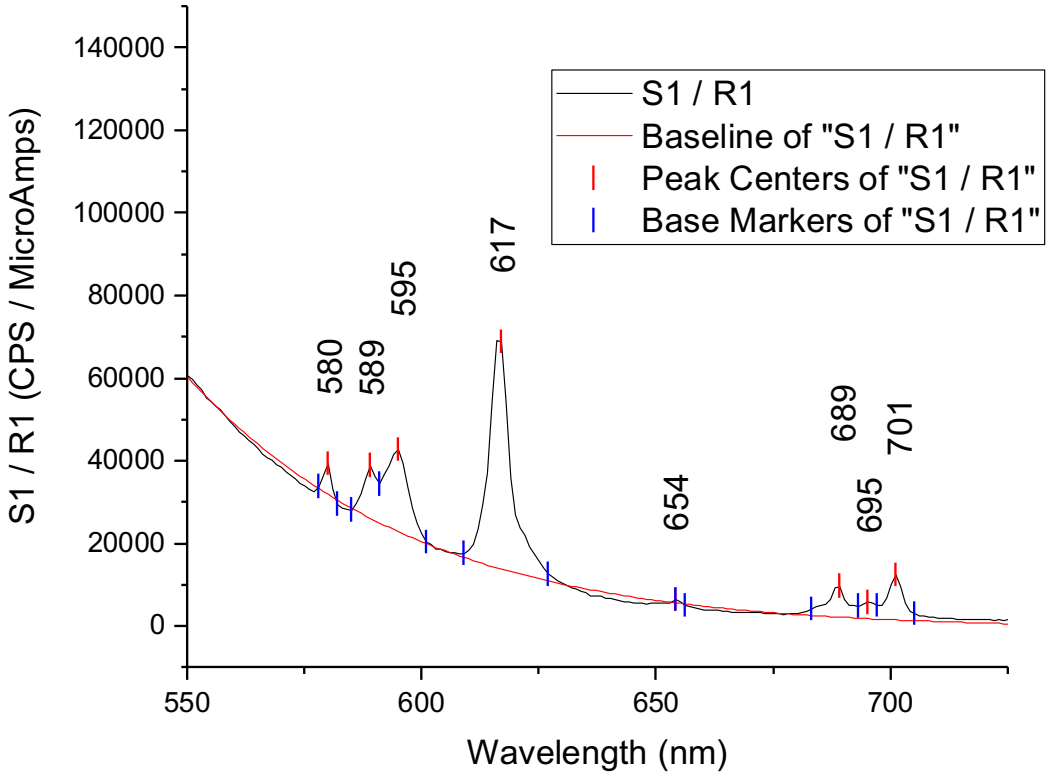


Hydration number q = 1.09

Equation used[3] :

$$q = 1.2\left(\frac{1}{t_{H_20}} - \frac{1}{t_{D_20}} - 0.25\right)$$

pH 13.93

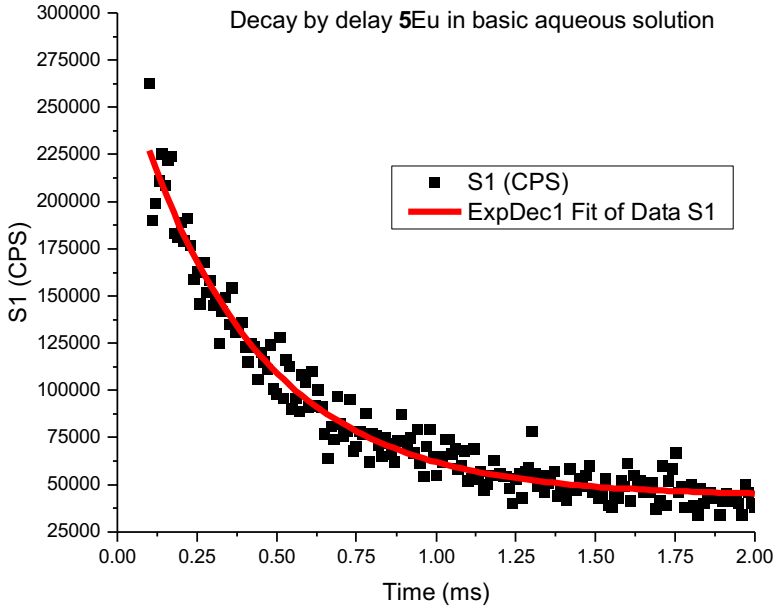


Transition $^5D_0\rightarrow$	Wavelength (nm)	Wavenumber (cm^{-1})	M_j
$^7F_0$	580	17,241	0
$^7F_1$	589	16,978	0
	595	16,807	±1
$^7F_2$	617	16,207	-
$^7F_3$	654	15,291	-
$^7F_4$	689	14,514	-
	695	14,388	-
	701	14,265	-

B_0^2 = -570 cm^{-1}

Phosphorescent decay

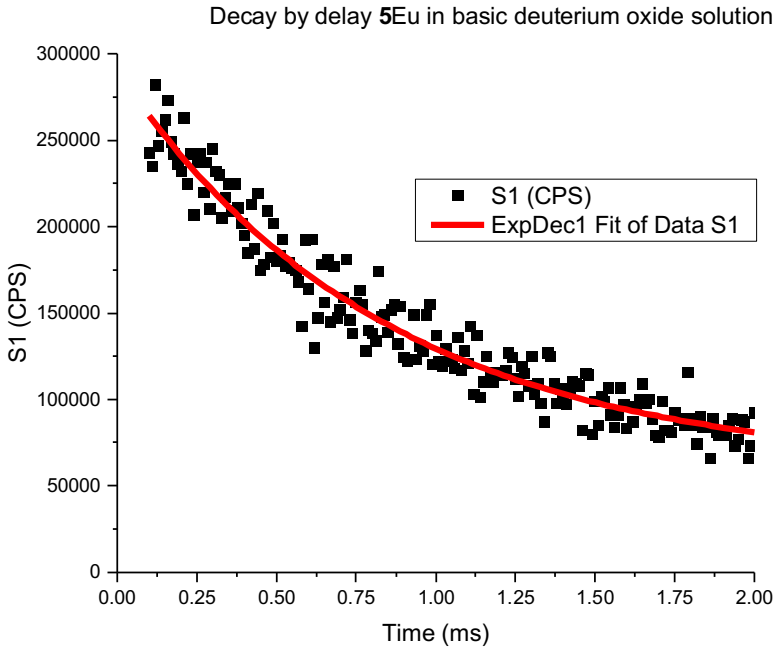
H_2O



		Value	Standard Error
S1	y0	43911.94614	1352.96845
S1	A1	236862.47367	5068.97413
S1	t1	**0.38841**	0.01379

Half-life = 0.38841±0.01379 ms

D_2O



		Value	Standard Error
S1	y0	60330.46416	5202.64598
S1	A1	229998.60309	4153.82595
S1	t1	**0.83231**	0.05517

Half-life = 0.83231±0.05517 ms

Hydration number q = 1.348

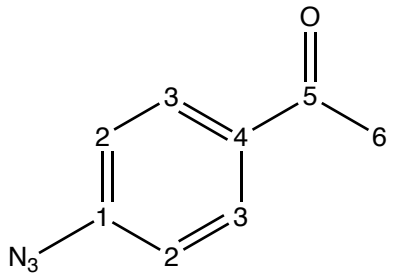
Equation used:[3]

$$q = 1.2\left(\frac{1}{t_{H_20}} - \frac{1}{t_{D_20}} - 0.25\right)$$

Redox

Synthesis of 4’azidoacetophenone[4]

The 4'-aminoacetophenone (37 mmol, 5 g, 1.0 equiv.) was dissolved in aq. HCl (23.31 mL, 6 M) and the solution was cooled to -5 °C. An aq. solution of potassium nitrite (3.78 g, 44.4 mmol, 1.2 equiv.) in water (12.95 mL) was then added slowly and the mixture was stirred for 15 min. The reaction temperature was not allowed to rise above -1 °C. An aq. solution of NaN_3 (2.89 g, 44.4 mmol, 1.2 equiv.) in water (12.95 mL) was added and stirring was continued for 15 min at rt. The resultant precipitate was filtered, washed Synthesis of 2-Bromo-1-(4'-azidophenyl)ethanone with water and dried to give 4'-azidoacetophenone (4.19 g, 26 mmol, 70%).



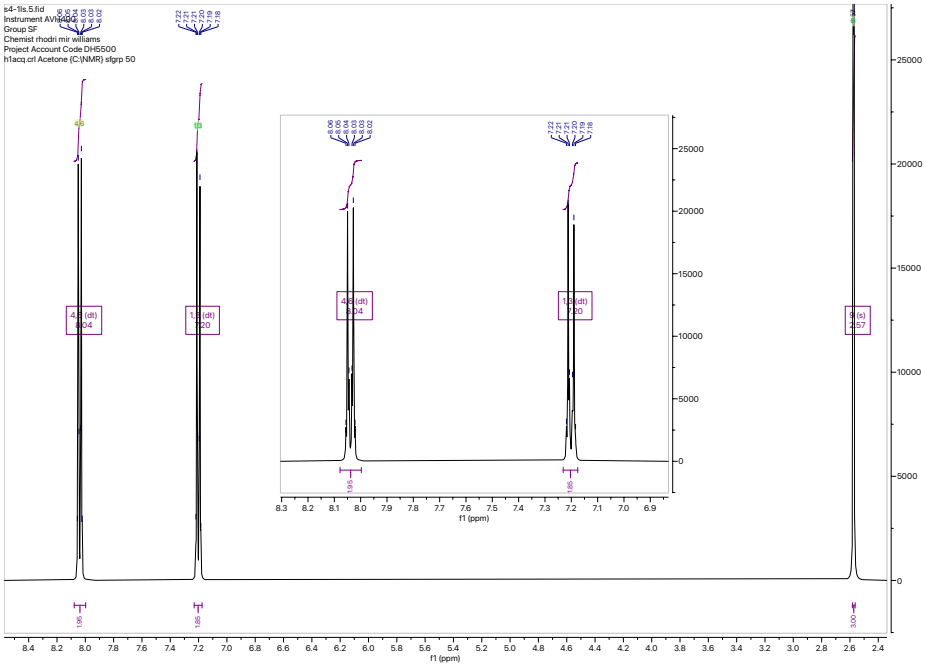
Chemical Formula: $C_8H_7N_3O$

Exact Mass: 161.06 Da

Molecular Weight: 161.16 Da

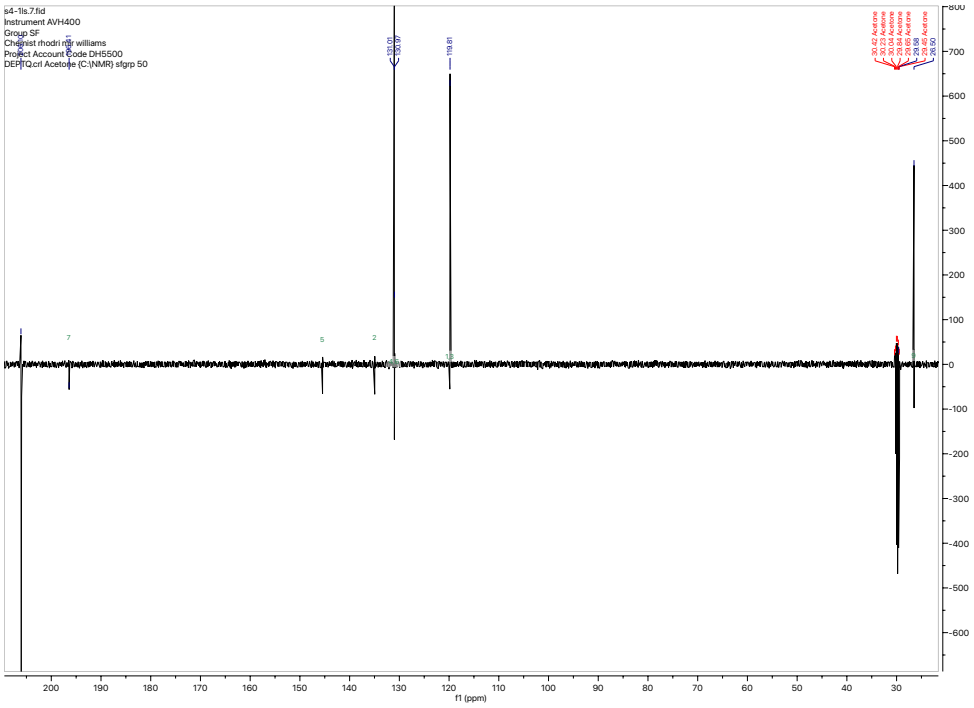
NMR

δ_H (400 MHz, Acetone-d6) 8.04 (dt, J = 8.8, 2.6 Hz, 2H, 2), 7.20 (dt, J = 8.8, 2.0 Hz, 2H, 3), 2.57 (s, 3H, 6).



CNMR

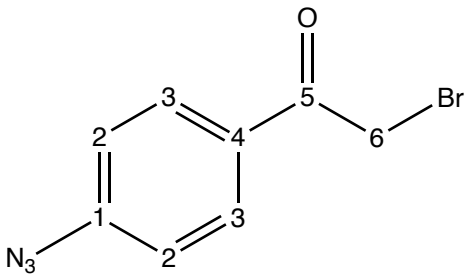
13C NMR (101 MHz, Acetone-d6) δ 196.5(5), 145.5(1), 135.0(5), 131.1(3), 119.9(2), 26.6(6).



Bromination of 4'azidoacetophenone[5]

4'-azidoacetophenone (3.48g, 21.576 mmol, 1 equiv.) was dissolved in Et_2O (10.4 mL) and dioxane (5.77 mL) and this mixture was cooled down with an ice bath. At this point Br_2 (0.91 mL, 3.45 g, 21.58 mmol, 1 equiv.) was added dropwise with a syringe. The reaction was left stirring for 1.5 hours while the ice bath was kept bellow 0 °C. TLC (Petroleum Ether:CH_2Cl_2 9:1) after 1.5 hours showed full consumption of the starting material. The reaction was stopped by the addition of water, and then was extracted with Et_2O. The combined organic phase was dried over MgSO4, filtered, and concentrated under reduced pressure. The crude product (4.68 g) was dry loaded onto a silica gel column (H:15cm, Ø: 5cm, Pentane: Et_2O= 9:1). 30 fractions were collected this gave the dibrominated (0.34g, 1.2 mmol, 5%) and monobromated (3.763 g, 15.68 mmol, 72%).

Monobrominated



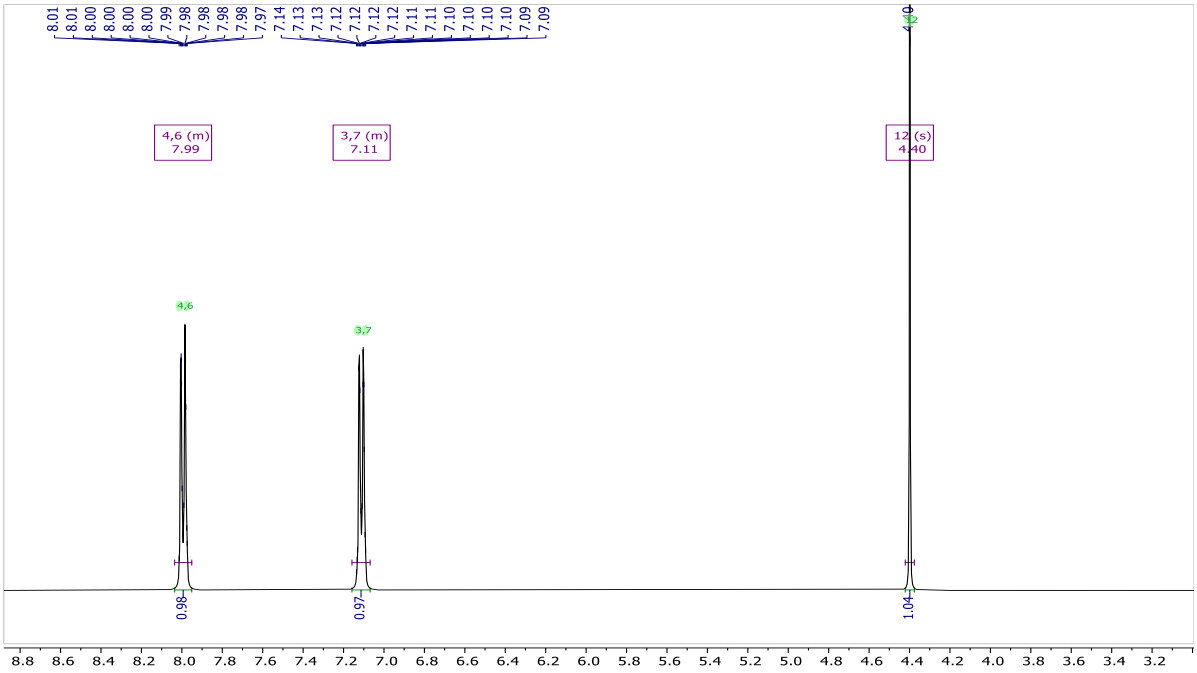
Chemical Formula: $C_8H_6BrN_3O$

Exact Mass: 238.97 Da

Molecular Weight: 240.06 Da

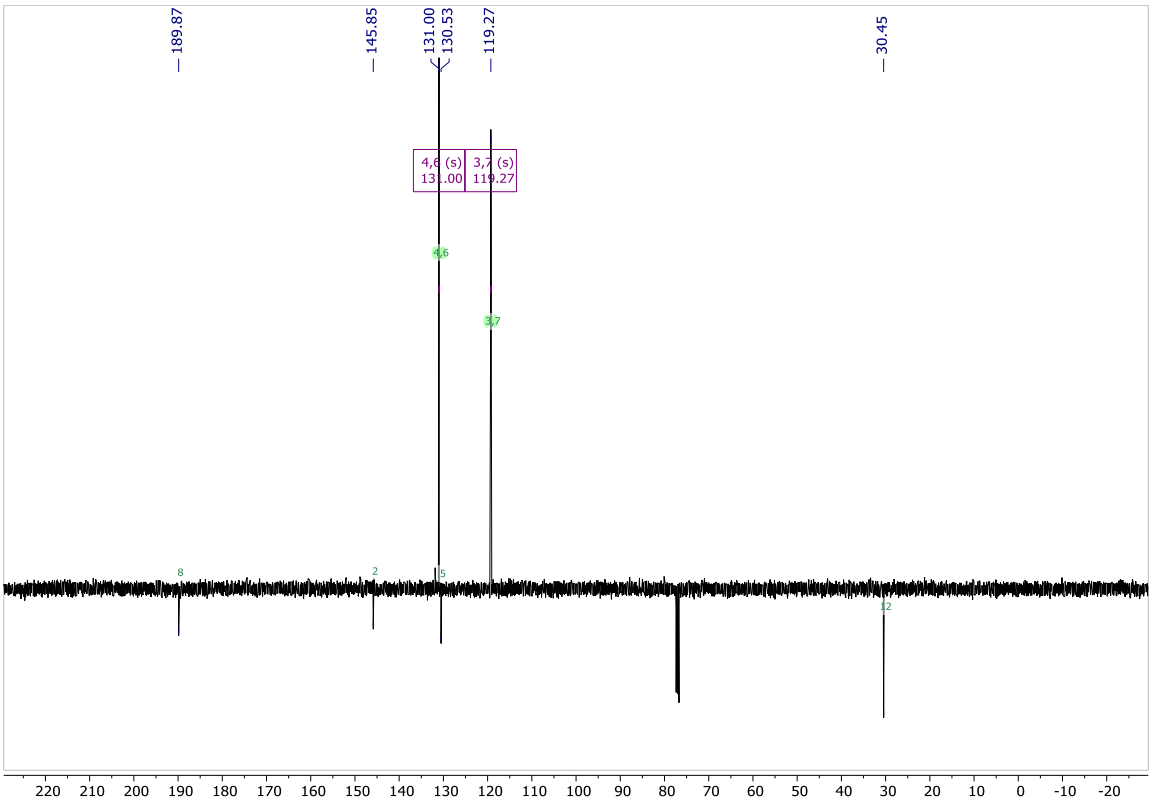
HNMR

δ_H (400 MHz, $CDCl_3$) δ 8.04 – 7.95 (m, 2H, 3), 7.16 – 7.07 (m, 2H,2), 4.40 (s, 2H, 6).



CNMR

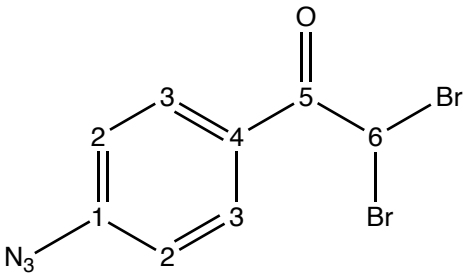
δ_c (101 MHz, $CDCl_3$) δ 189.9 (5), 145.9(1), 131.0(5), 130.5(3), 119.3(2), 30.5(6).



Mass spectrometry

[M+H]: 284.82 Da (HPLC purity: 98%)

Dibrominated



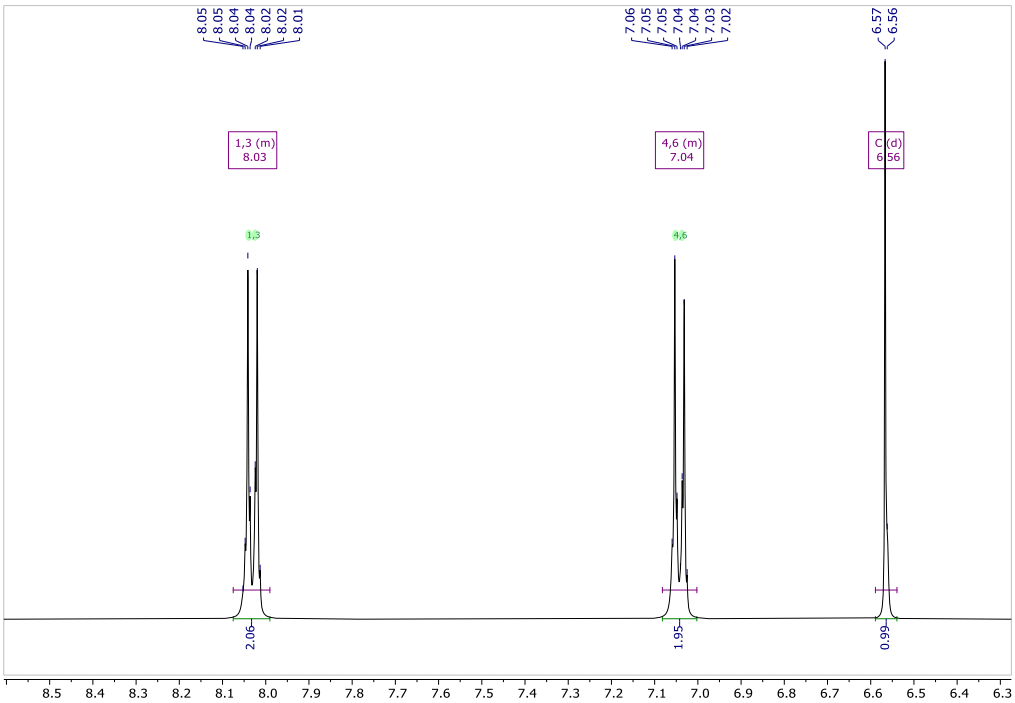
Chemical Formula: $C_8H_5Br_2N_3O$

Exact Mass: 316.88 Da

Molecular Weight: 318.96 Da

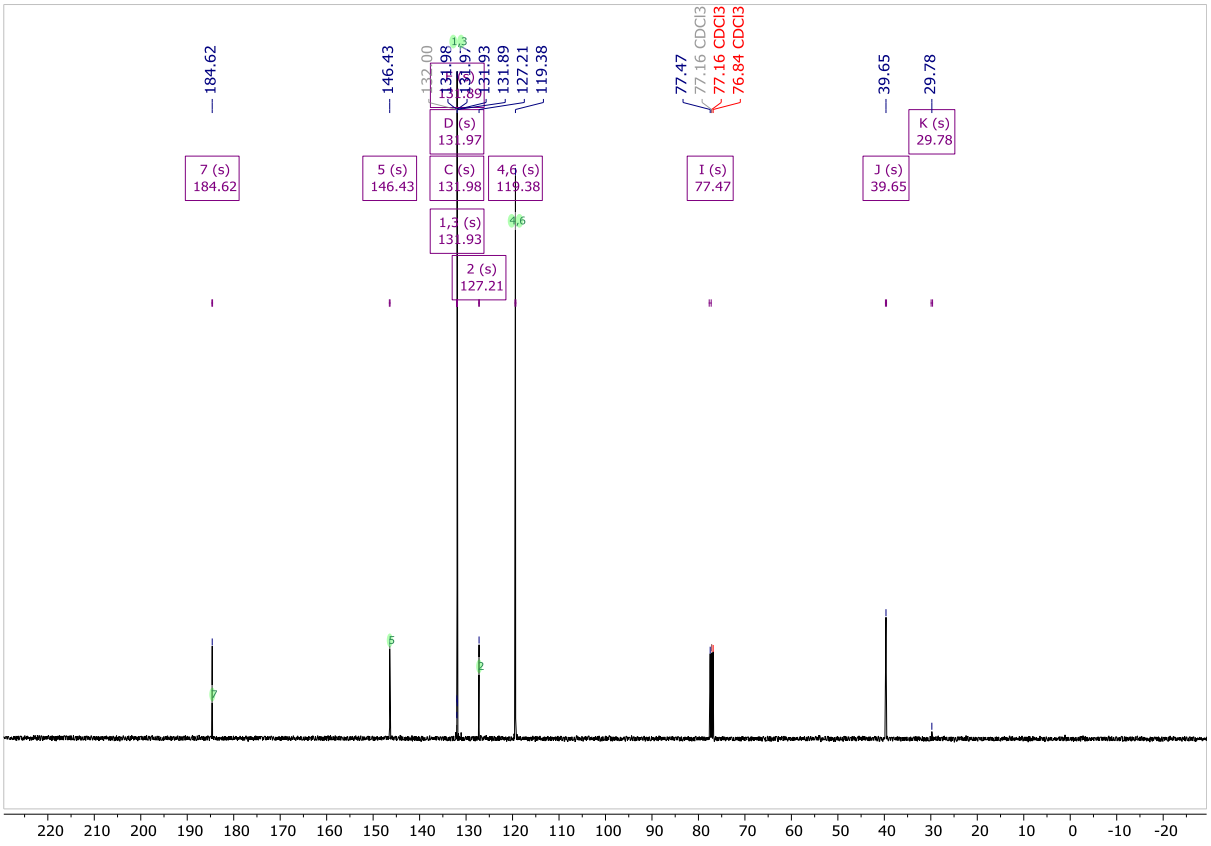
HNMR

δ_H NMR (400 MHz, $CDCl_3$) 8.08 – 7.99 (m, 2H, 3)), 7.08 – 7.00 (m, 2H, 2), 6.56 (d, J = 1.9 Hz, 1H, 6))



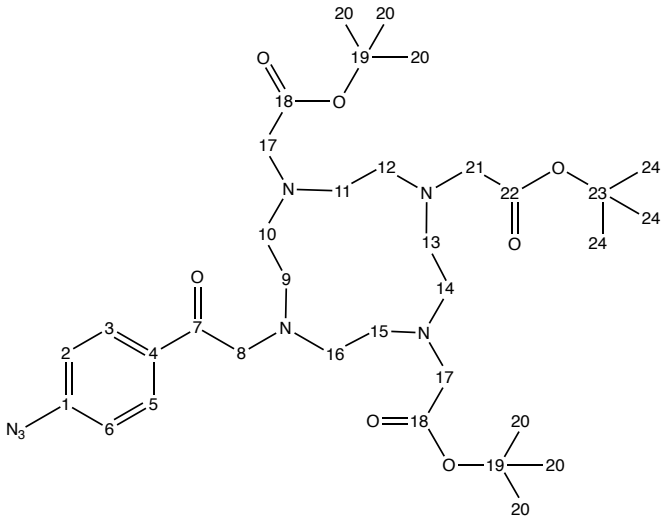
CNMR

δ_c NMR (101 MHz, $CDCl_3$) δ 184.6(5), 146.4(1), 131.9(3), 127.2(4), 119.4(2), 39.7(6).



Synthesis of DO3A-tBu-1-(4’-azidophenylethanone)[5]

tBu-DO3A (1.00 g, 1.94 mmol, 1 equiv.) and Na_2CO_3(0.89 g, 8.39 mmol, 4.3 equiv.), 2-bromo-4'-azidoacetophenone (0.51g, 2.1 mmol, 1.1 equiv.) were put into a 50 mL RBF and dissolved in dry CH_3CN (27 mL) and left to stir under an argon atmosphere. TLC showed full reaction after 48 h. The reaction mixture was filtered. The filtrate was concentrated under reduced pressure to give the crude product. The reaction mixture was purified twice by column chromatography. The first column (CH_2Cl_2/MeOH 1:0>95:5>8:2, 30 fractions) yielded the pure product which when concentrated gave an orange foam (0.5609 g) and 2 fractions of crude product. These were then purified further by a second column (CH_2Cl_2/MeOH 95:5>9:1>8:2), this yielded 11 fractions which gave an orange foam (0.4539 g) when concentrated and one impure fraction which was not further purified. The orange foam was the desired product (1.02 g, 1.47 mmol, 76 %).



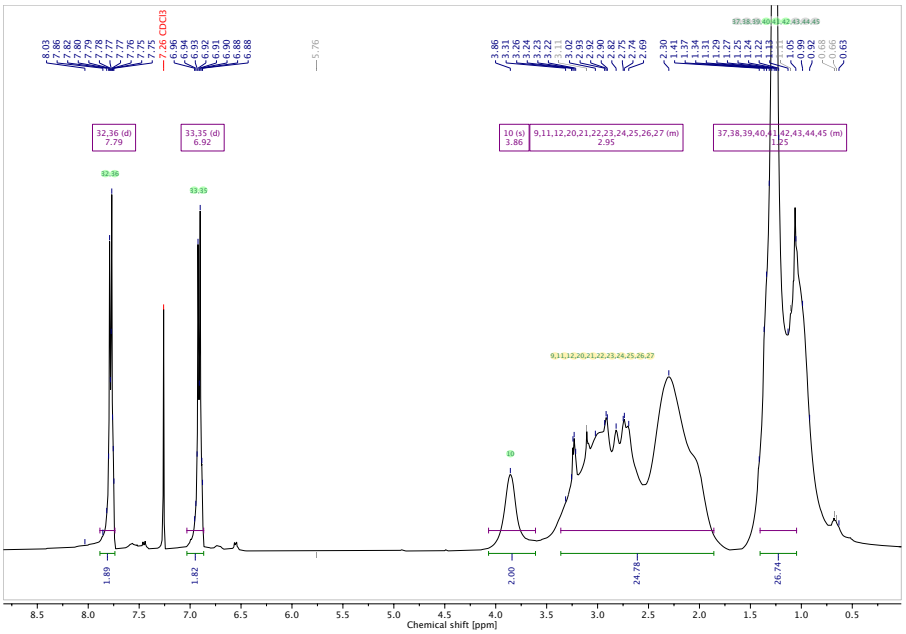
Chemical Formula: $C_{34}H_{55}N_7O_7$

Exact Mass: 673.42 Da

Molecular Weight: 673.86 Da

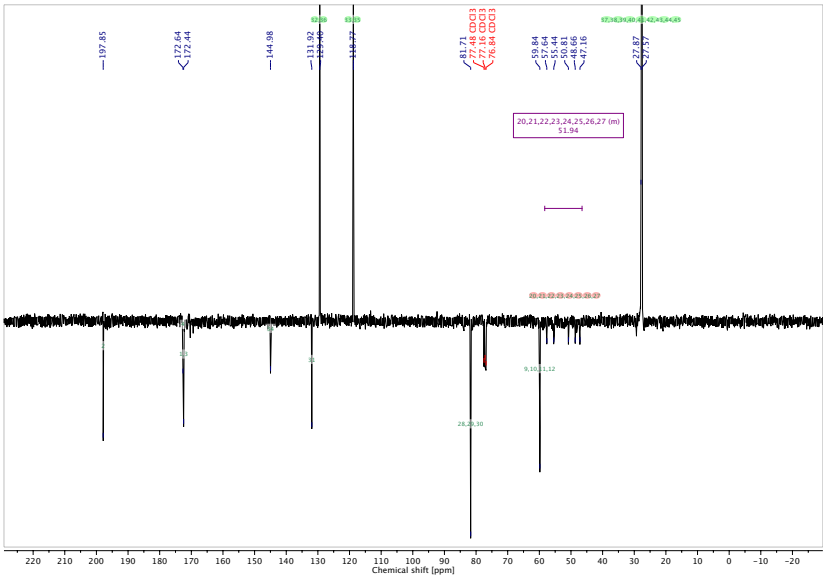
HNMR

δ_H NMR (400 MHz, $CDCl_3$) 7.91 – 7.85 (m, 2H, 3,5), 7.05 – 6.99 (m, 2H, 2,6), 3.97 (s, 2H, 8), 3.64 – 3.00 (m, 6H 17, 22), 2.98 – 1.83 (m, 16H, 9,10,11,12,13,14,15,16), 1.39 (s, 27H, 20,24).



CNMR

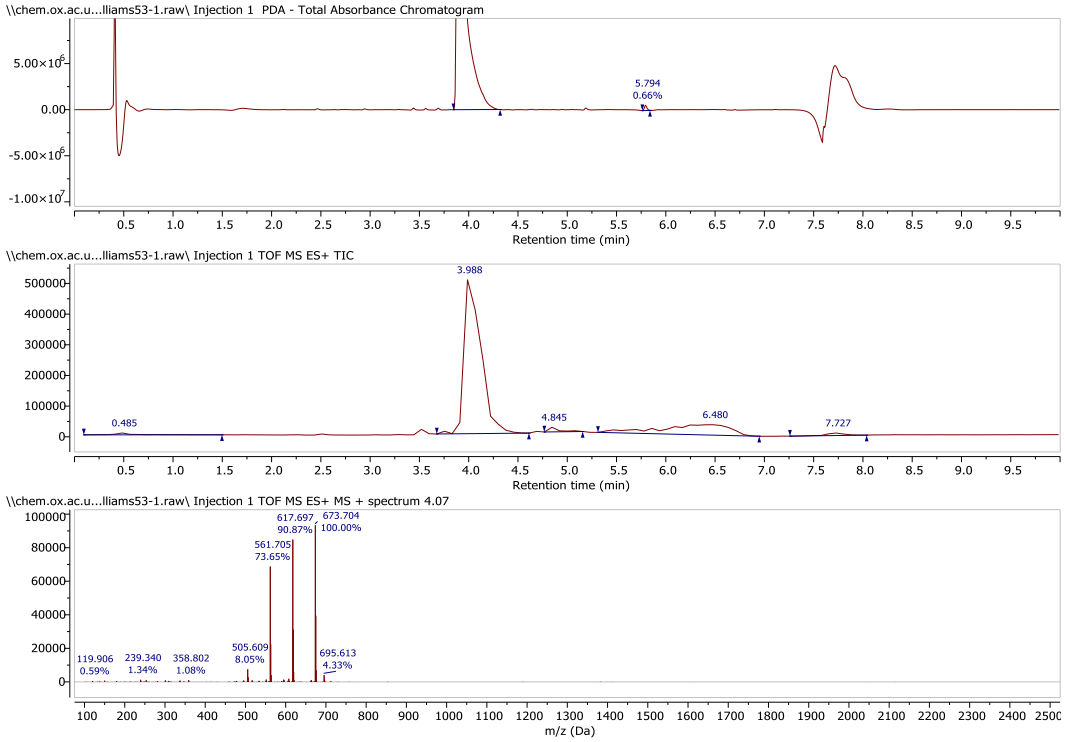
δ c (101 MHz, CDCl3) δ 198.20 (7), 173.07 (22), 172.81 (18), 145.40 (31), 132.30 (4), 129.69 (3,5), 119.07 (2,6), 81.96 (19), 81.93 (23), 60.23 (8), 55.85 (21), 55.62 (17), 53.45 (9,10,11,12,13,14,15,16), 27.91 (20), 27.83 (24).



HPLC-MS

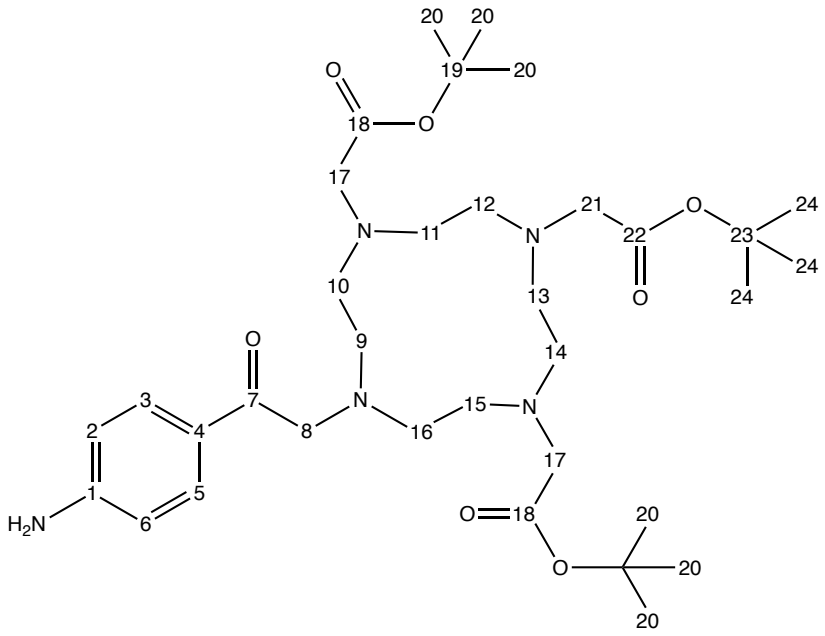
Predicted: $[M+H]^+$ = 674.42 Da

LRMS: $[M+H]^+$ = 673.729 Da (99%, RT=3.988min)



Synthesis of DO3A-tBu-4'-aminoacetophenone[6]

DO3A-tBu-1-(4'-azidophenylethanone) (595 mg, 0.86 mmol, 1equiv.) was dissolved in MeOH (25 mL). Pd/C (30 mg) and hydrazine hydrochloride 50-60% (0.085 mL, 87.68 mg, 1.37 mmol,1.76 equiv.) was added. The mixture was refluxed until the reaction was complete (1H 20min), checked by HPLC-MS). The mixture was the filtered through a pad of celite and the filtrate was then evaporated to give an oil. This was then analysed by NMR and mass spectrometry. The oil was the desired amine (465 mg,0.70 mmol, 82%) with some slight hydrazine contamination.



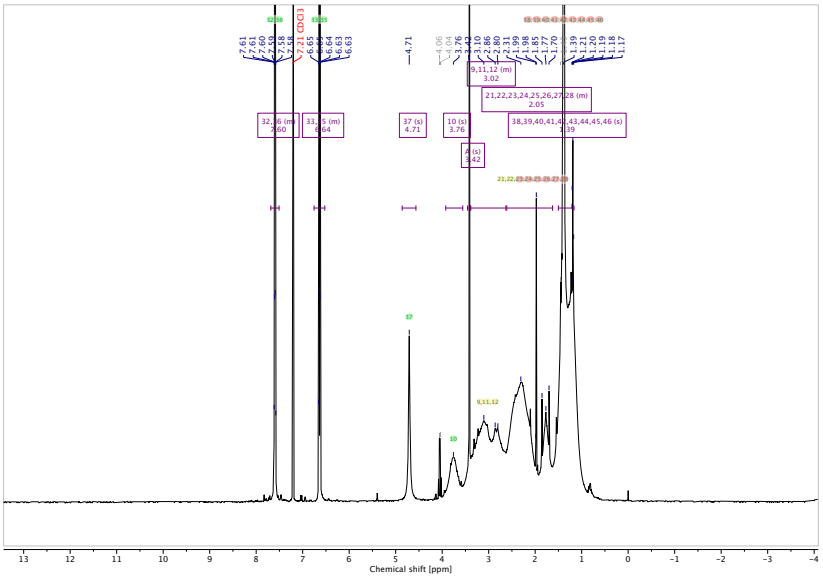
Chemical Formula: $C_{34}H_{57}N_5O_7$

Exact Mass: 647.43 Da

Molecular Weight: 647.86 Da

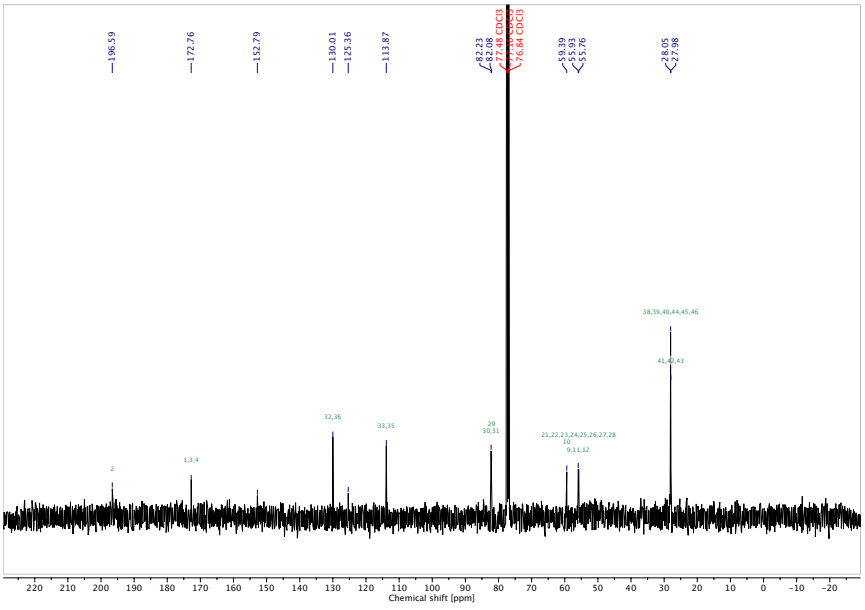
HNMR

δ H 1H NMR (400 MHz, CDCl3) δ 7.68 – 7.51 (m, 2H,3,5), 6.75 – 6.53 (m, 2H,2,6), 4.71 (s, 2H, amine), 3.76 (s, 2H,8), 3.42 (s, 1H, hydrazine impurity), 3.39 – 2.63 (m, 6H,17,21), 2.61 – 1.63 (m, 16H, 9,10,11,12,13,14,15,16), 1.39 (s, 27H, 20,24).



CNMR

δ $_c$ (101 MHz, $CDCl_3$) δ 196.6 (7), 172.8(18,22,22), 152.8(1), 130.0(3,5), 125.4(4), 113.9(2,6), 82.2(19), 82.1(23), 59.4(8), 55.9(17,21), 55.8(9,10,11,12,13,14,15,16), 28.1(20), 28.0(24).

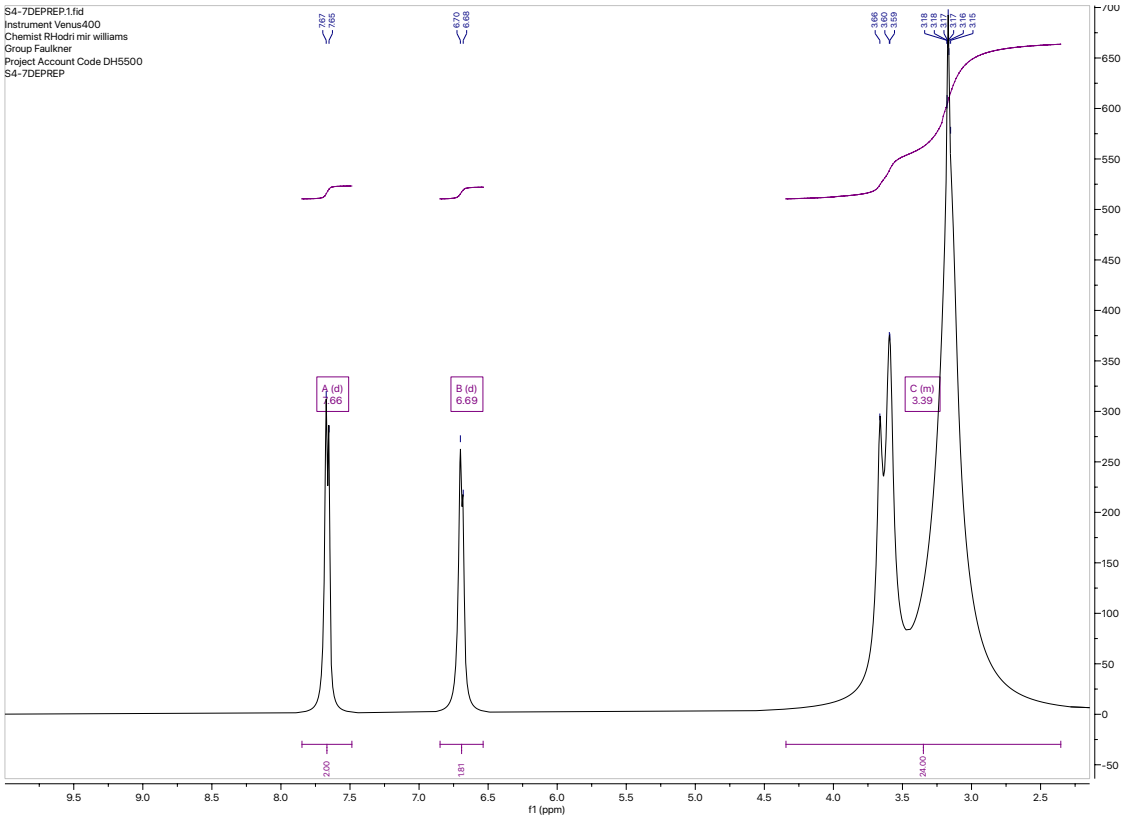


Synthesis of DO3A-4'-aminoacetophenone[6]

TFA (0.5ml) was added dropwise to a solution of DO3A-tBu-4'-aminoacetophenone (10 mg, 0.0154 mmol) in CH_2Cl_2 (0.5 ml). The reaction was stirred at RT for 48 h, the solvents were removed under reduced pressure and the product was obtained quantitatively (7 mg, 0.015 mmol, 97%) from methanol by trituration with diethyl ether.

HNMR

^{1}H NMR (400 MHz, D_2O) δ 7.66 (d, *J* = 8.1 Hz, 2H, 3,5), 6.69 (d, *J* = 8.3 Hz, 2H, 2,6), 3.66– 2.95 (m, 24H,8, 9,10,11,13,14,15,16,17,21).



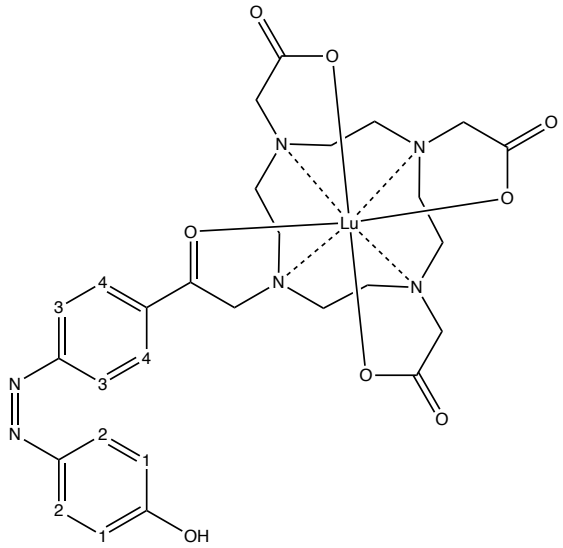
Synthesis of [LuDO3A-4'-aminoacetophenone]

Lutetium trifluoromethanesulfonate (45 mg, 0.072 mmol, 1.1 equiv.) and DO3A-4'-aminoacetophenone (31 mg, 0.011mmol, 1 equiv.) were dissolved in 1:1 MeOH/H20 (1mL)

and stirred at 60 °C for 2 days. The pH was controlled and kept between 3-5. The crude reaction product was then carried forward to diazotization.

Synthesis of [Lu(4-((4-hydroxyphenyl diazenyl)phenyl)-2-oxoethyl-DO3A]

[LuDO3A-4'-aminoacetophenone] reaction mixture (max. 0.072 mmol) mix was dissolved in HCl (0.1M, 1 mL) and cooled to 0 °C. KNO_2 (6 mg, 0.114 mmol, 1.6 equiv.) was added and the mixture was stirred for 10 minutes. To this mixture phenol (7 mg, 0.124 mmol, 1.7 equiv.) was added followed by NaOH (1M, 0.1mL + 0.1M, 0.01mL). The reaction was left to stir for 20 minutes. The pH was then corrected to be around above 7 by adding HCl (0.1 M, 0.01mL + 0.000001M, 0.1 mL). The reaction mixture was then concentrated in vacuo. This yielded the crude desired product (54 mg). This was then purified by HPLC. The fractions were concentrated to give the pure product as a red-orange water-soluble solid (18.3 mg, 0.025 mmol, 35%)



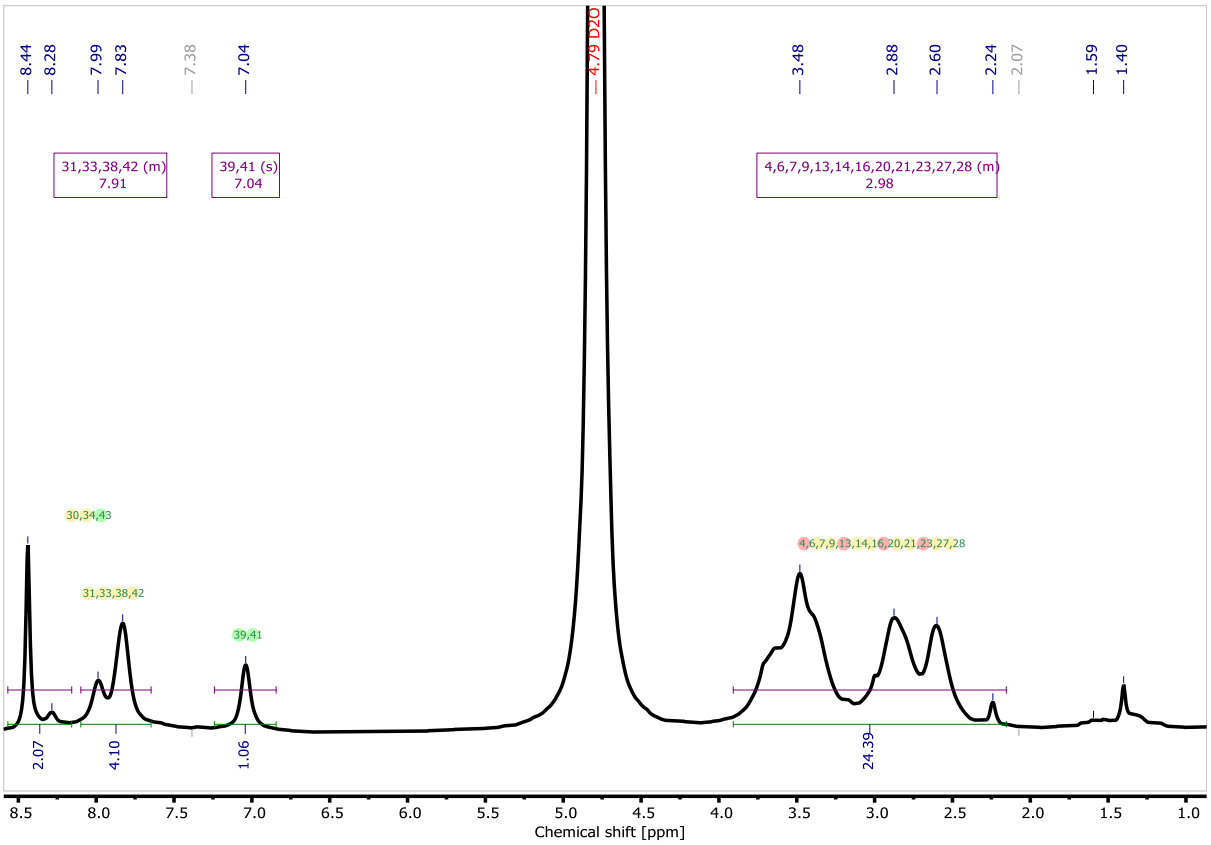
Chemical Formula: $C_{28}H_{33}N_6O_8Lu$

Exact Mass: 756.18 Da

Molecular Weight: 756.57 Da

HNMR

δ_H (400 MHz, D_2O) 8.57 – 8.16 (2 H, m, 4), 8.10 – 7.65 (4 H, m,2,3), 7.04 (2 H, s, 1), 3.91 – 2.15 (24 H, m, ring and arm).



HRMS

Predicted: $[M-H]^-$ = 755.1695 Da

Observed: $[M-H]^-$ =755.1597 Da

HPLC Data

HPLC was ran by Dr. Daniel Kovacs.

Conditions:

Stoptime

Stoptime Mode: As Pump/Injector

Posttime

Posttime Mode: Off

Peak Detection Settings

Peak Triggers

Used	Peak Detector	Used Signal
No	G7114A:DEACX23759	A (mAU)
No		A
No		A
No		A

Peak Detection Mode	Up Slope	Down Slope	Threshold
	mAU/s	mAU/s	mAU
Threshold	1.00	2.00	5.550
Threshold	5.00	5.00	5.000
Threshold	5.00	5.00	5.000
Threshold	5.00	5.00	5.000

Upper Threshold	Limit Peak Duration
mAU	

2000.000 Use Max Peak Duration

2000.000 No Timeout

2000.000 No Timeout

2000.000 No Timeout

Max. Peak Duration

s

30.000

Maximum Fill Volume

Maximum Fill Volume Mode: as configured

Collection Behavior

Collection Mode: Enabled

End of Fraction Delay Settings

Is End of Fraction Delayed: No

Trigger Combinations

Combination: AND condition

Delay Settings

Delay Settings

Peak Trigger Delay Mode

---

1 As calibrated

2 As calibrated

3 As calibrated

4 As calibrated

Timetable

Time Function Parameter

5.27 Change Fraction Mo. Time-based, collecting a number of fract

ions 1

6.60 Change Fraction Mo. Off

Instrument Curves

Store Delay Sensor: No

==========

Column(s)

==========

Column Description : ZORBAX PrepHT Original C18 USP L1 Cartridge , 21.2 x 250mm

Serial# : USAIZ01101

Product# : 877952-102

Batch# : ZBX2173002

Diameter : 21.2 mm

Length : 250.0 mm

Particle size : 7.0 µm

Void volume : 65.0 %

Maximum Pressure : 350.0 bar

Maximum pH : 8.0

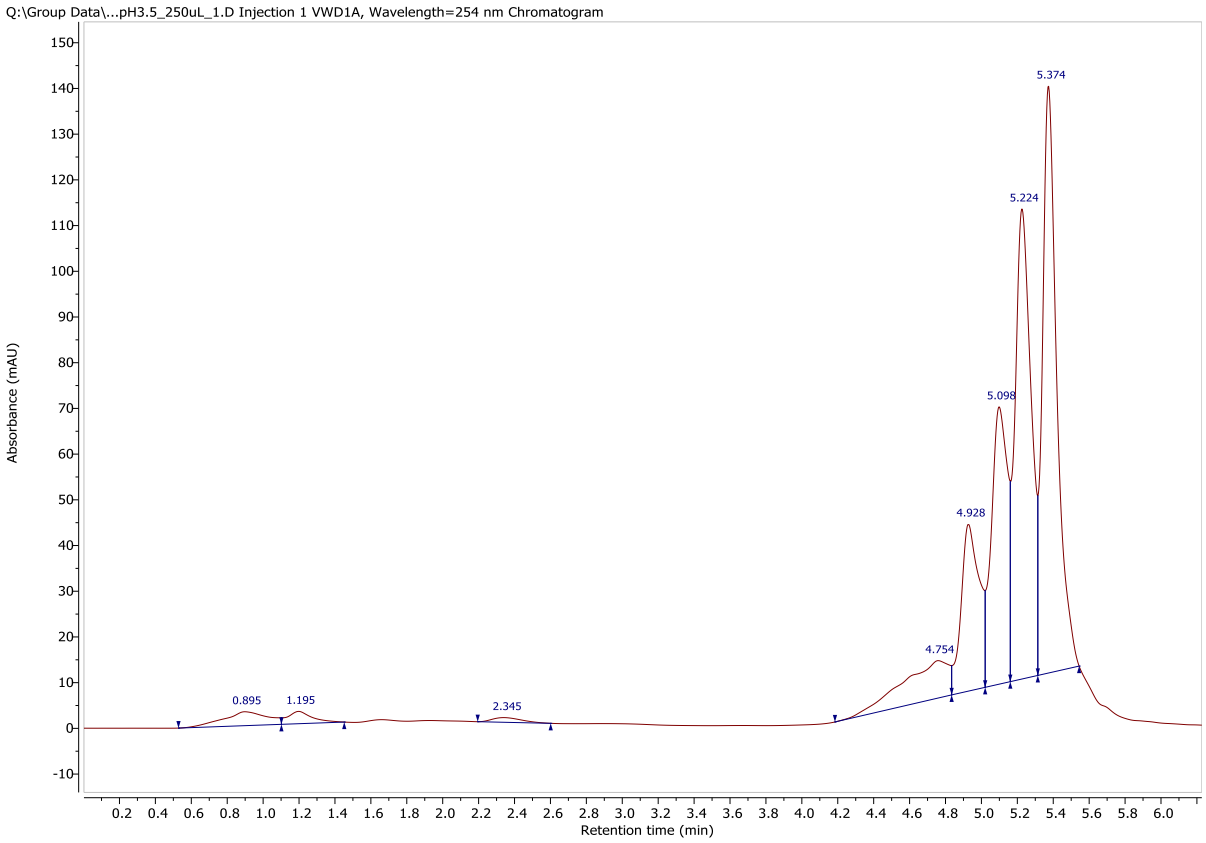
Minimum pH : 2.0

Maximum Temperature: 60.0 °C

Comment : ZORBAX PrepHT Original C18 USP L1 Cartridge , 21.2 x 250mm : ZORBAX C18 USP L1

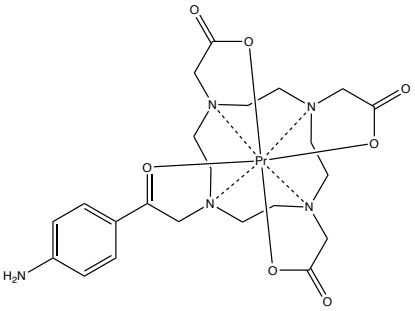
70Å 300 m2/g 60 °C 2.0 - 8.0 Yes/No 20%

HPLC Trace



Synthesis of [PrDO3A-4'-aminoacetophenone]]

Praseodymium trifluoromethanesulfonate (92 mg, 0.156 mmol, 1.5 equiv.) and DO3A-4'-aminoacetophenone (50 mg, 0.104 mmol, 1 equiv.) were dissolved in 1:1 MeOH/H_20 (1 mL) and stirred at 60 °C for 2 days. The pH was adjusted using 1 M NaOH solution and maintained between 3-5. The reaction was then carried forward for diazotization without further purification.



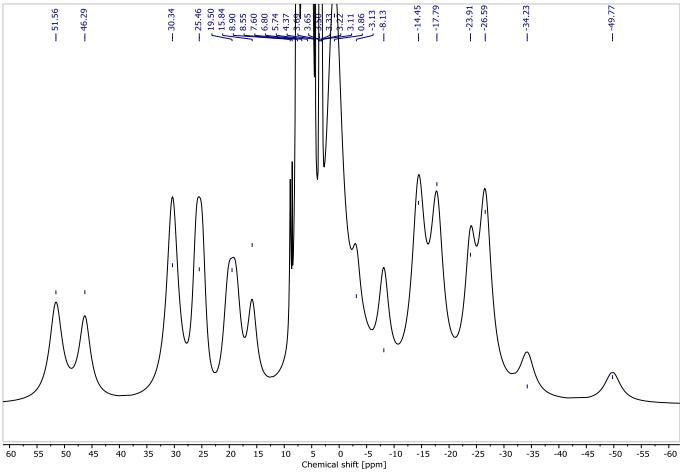
Chemical Formula: $C_{22}H_{30}N_5O_7Pr$

Exact Mass: 617.12 Da

Molecular Weight: 617.42 Da

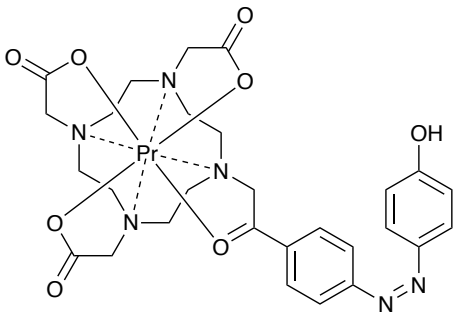
HNMR

δ_H (400 MHz, DMSO) 49.96, 44.75, 35.76, 28.33, 22.98, 17.08, 13.60, 6.58, 5.40, 4.53, 1.39, 1.23, 1.08, 0.84, 0.74, -1.25, -5.48, -10.53, -16.94, -20.47, -26.41, -29.66, -37.49, -41.90, -45.46, -53.49.



Synthesis of [Pr(4-((4-hydroxyphenyldiazenyl)phenyl)-2-oxoethyl-DO3A]

[PrDO3A-4'-aminoacetophenone] reaction mixture (max. 0.069 mmol) mix was dissolved in HCl (0.1M, 1 mL) and cooled to 0 °C. KNO_2 (12.4 mg, mmol, 2 equiv.) was added, and the mixture was stirred for 10 minutes. To this mixture phenol (22.1 mg, 0.234 mmol, 3.4 equiv.) was added followed by NaOH (1M, 0.1mL + 0.1M, 0.01mL). The reaction was left to stir for 50 minutes. The pH was then corrected to be around above 7 by adding HCl (0.1 M, 0.01mL + 0.000001M, 0.1 mL). The solvent was then removed, and the mixture re-dissolved in distilled water and dialysed overnight. This yielded the crude desired product (33.2 mg, 44% over from complexation) which was characterised by HRMS and NMR.



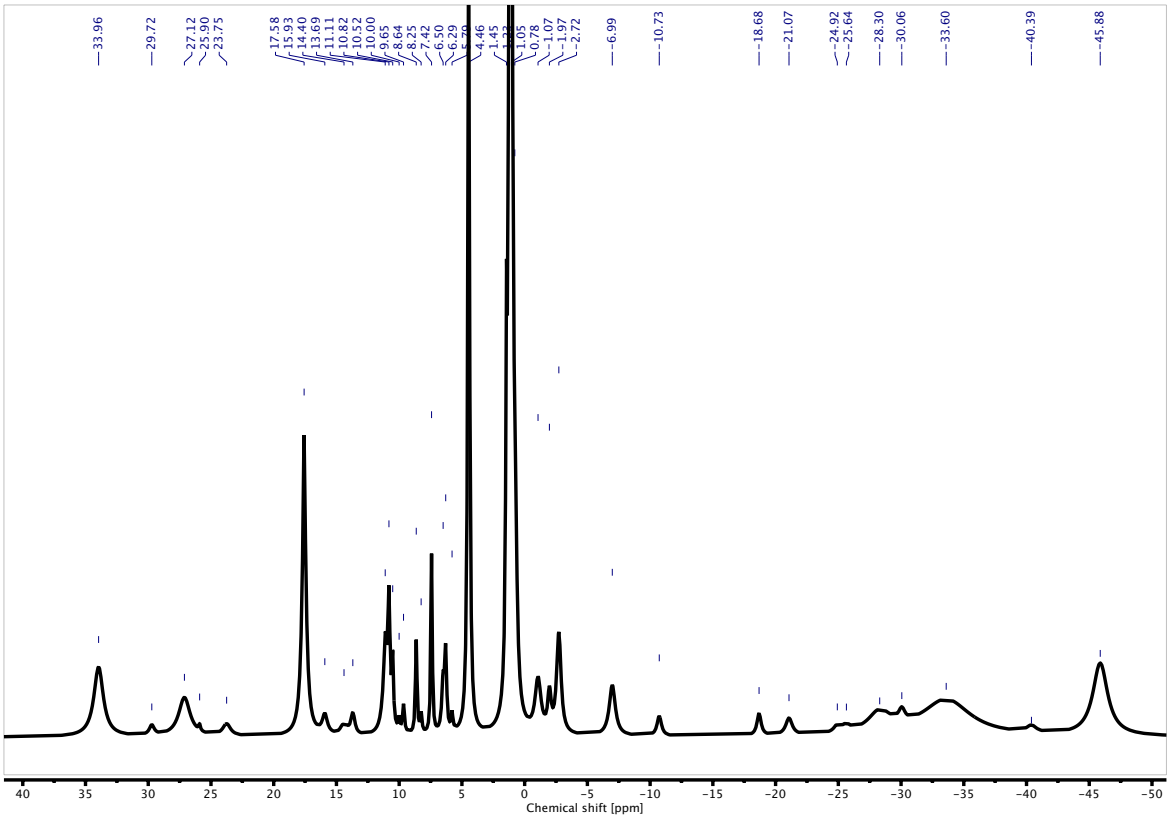
Chemical Formula: $C_{28}H_{33}N_6O_8Pr$

Exact Mass: 722.14 Da

Molecular Weight: 722.51 Da

NMR

δ_H (400 MHz, DMSO) 33.93, 27.09, 25.74, 23.76, 17.56, 15.91, 14.38, 13.68, 11.10, 10.80, 10.51, 9.99, 9.64, 8.63, 7.40, 7.23, 6.48, 6.28, 5.77, 4.86, 4.53, 4.44, 2.95, 1.44, 1.21, 1.04, 0.81, 0.70, -1.07, -1.98, -2.72, -18.07, -20.93, -28.30, -29.96, -33.47, -45.38.



HRMS

Predicted: $[M-H]^-$ = 721.1364 Da

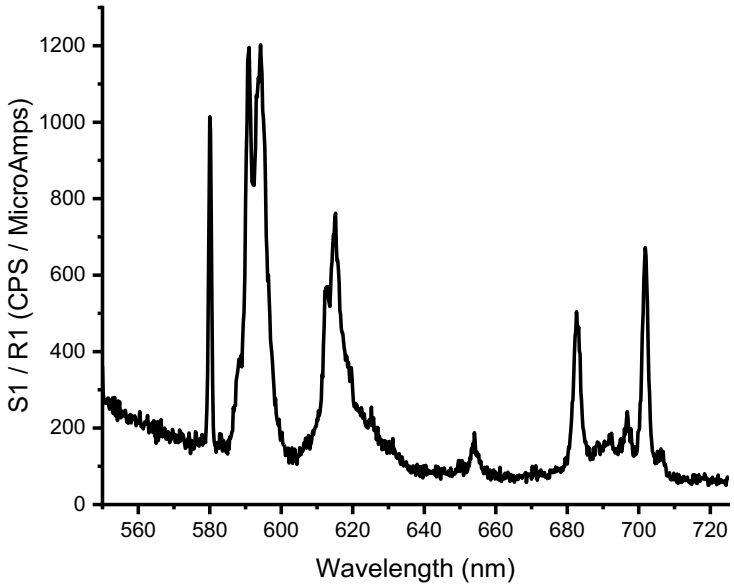
Observed: $[M-H]^-$ = 721.1392 Da

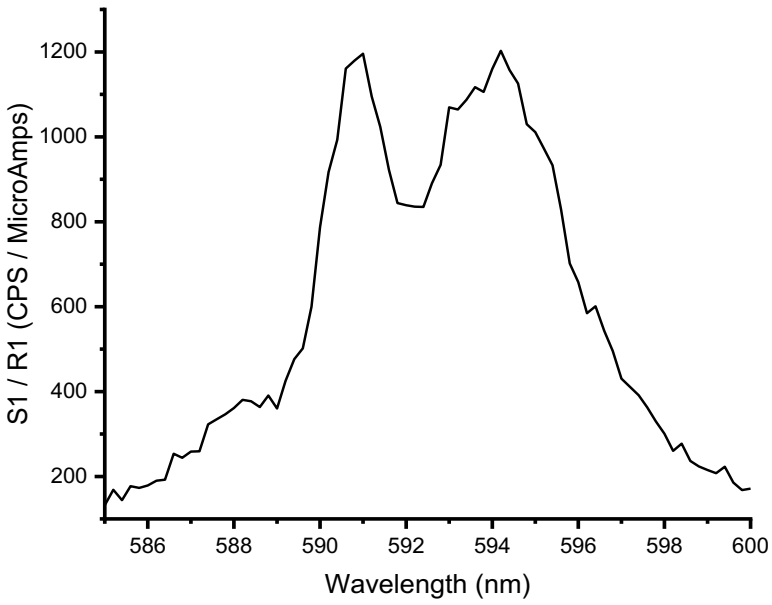
Complex review

Complex luminescence spectra were obtained by Amy-Grace Berger and the author as part of her part II thesis.

Fluorescence spectra

DOTTA-Eu





Excitation wavelength is 395nm

Crystal field analysis

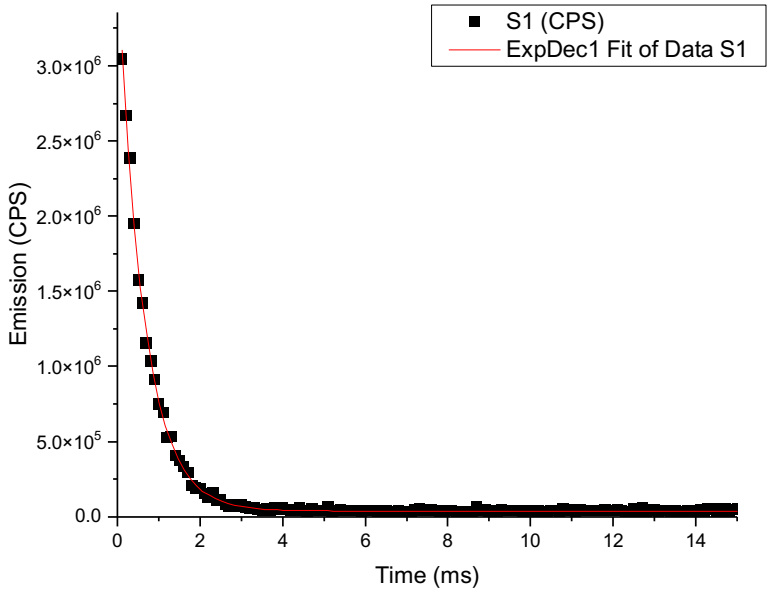
Peak $^5D_0$- $^7F_?$	m_J	Wavelength (nm)	Wavenumber (cm^{-1})
0	0	580	17241
1	0	591	16920
	1	594	16835

Rest of transitions are unassignable

Phosphorescencent decay

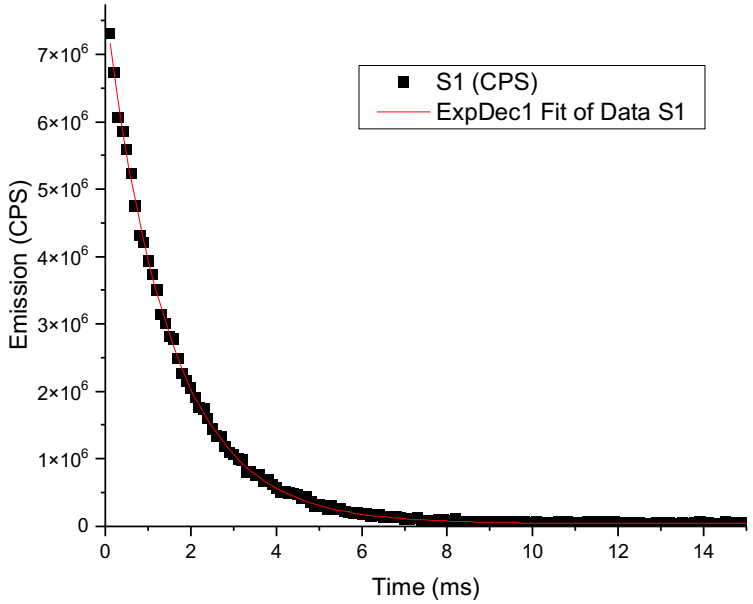
[Eu(DTtBuMA)]$^{3+}$

H_2O



	Value	Standard Error
y0	40360.61534	1591.59358
A1	3602769.88698	16913.83762
t1 (ms)	0.62223	0.00399

D_2O



	Value	Standard Error
y0	45724.62066	3911.70722
A1	7621397.48681	20646.06708
t1 (ms)	1.49033	0.00636

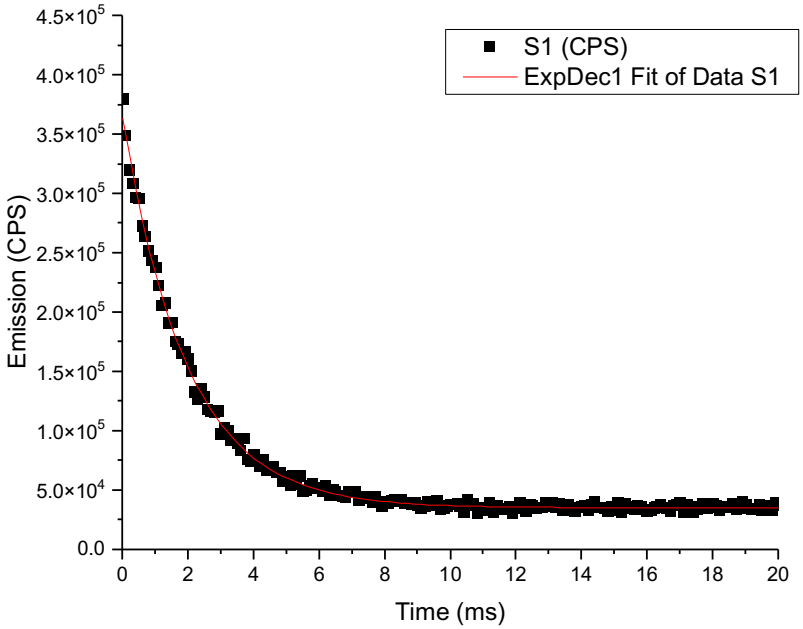
Hydration number, q = 0.82 ~ 1

Equation used[3] :

$$q = 1.2\left(\frac{1}{t_{H_20}} - \frac{1}{t_{D_20}} - 0.25\right)$$

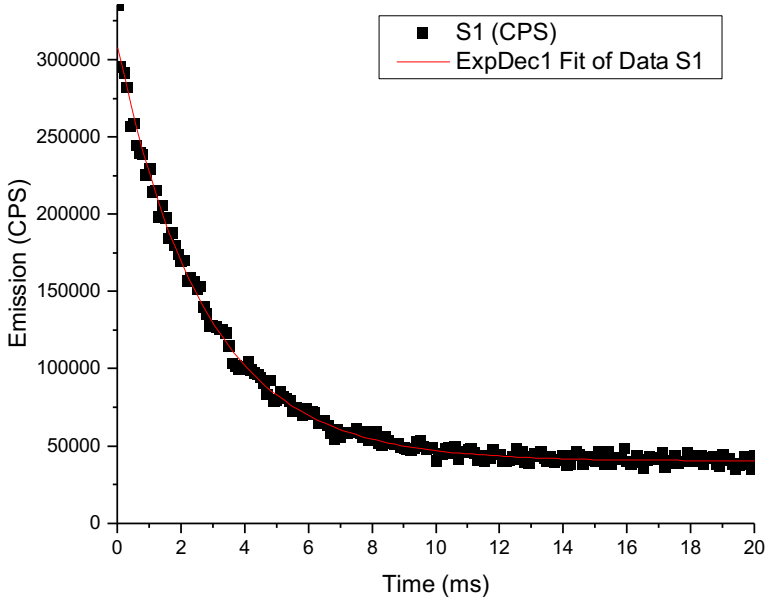
[Tb(DTtBuMA)]$^{3+}$

$\underline{H_2O}$



	Value	Standard Error
y0	35167.78177	309.42867
A1	330242.36257	1497.63034
t1 (ms)	1.94314	0.01458

D_2O



	Value	Standard Error
y0	40378.03579	417.75844
A1	268845.11495	1502.78967
t1 (ms)	2.72153	0.02737

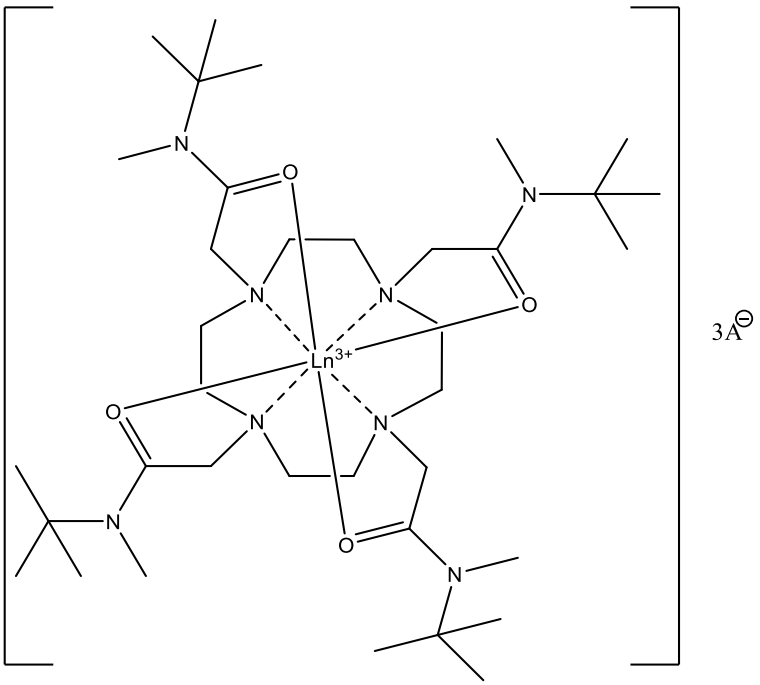
Hydration number, q = 0.4359 ~ 0

Equation used[7]:

$$q = 5\left(\frac{1}{t_{H_20}} - \frac{1}{t_{D_20}} - 0.06\right)$$

Complex NMR spectra and crystal structure

All complexes presented here have this general formula.



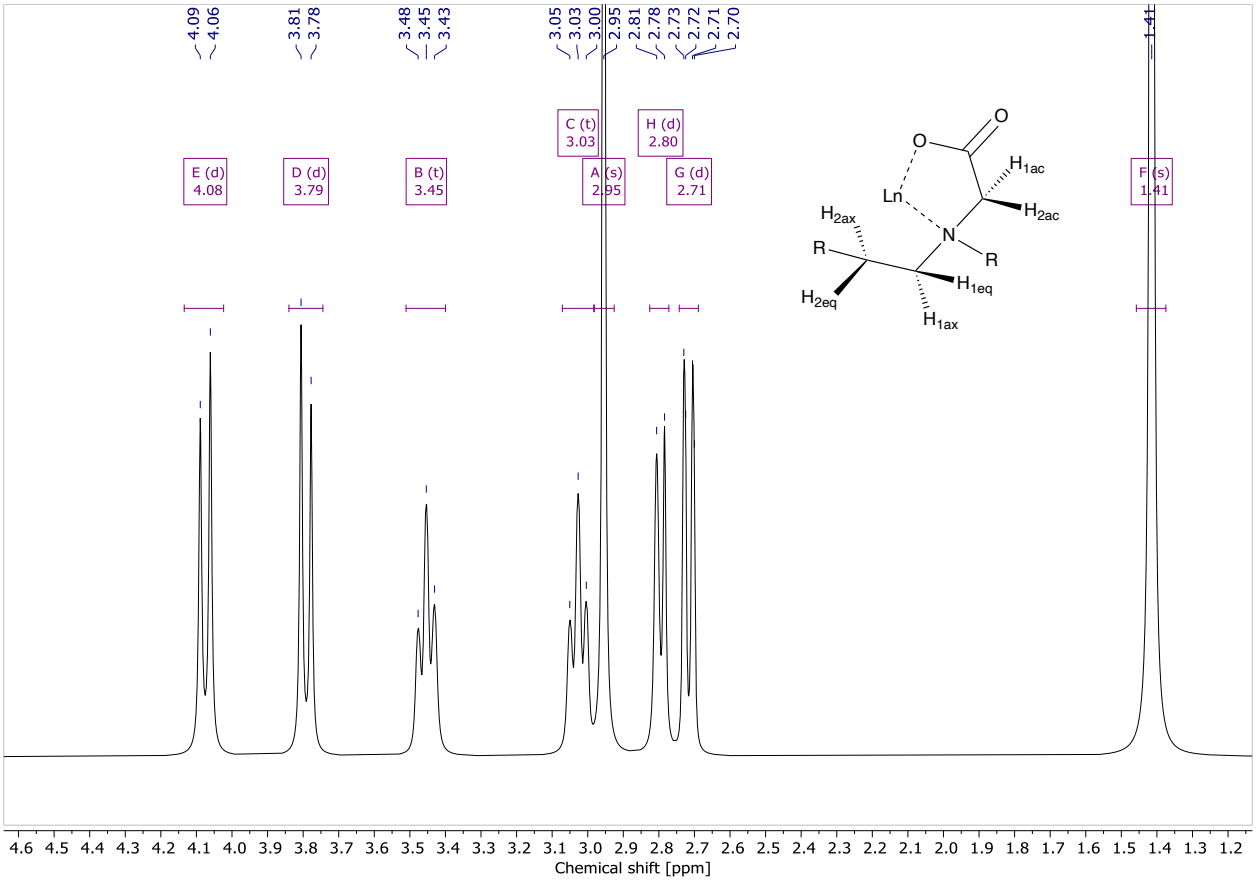
$[C_{36}H_{72}N_8O_4Ln]A_3$

A^- is any anion

[Y(DTtBuMA)]$^{3+}$

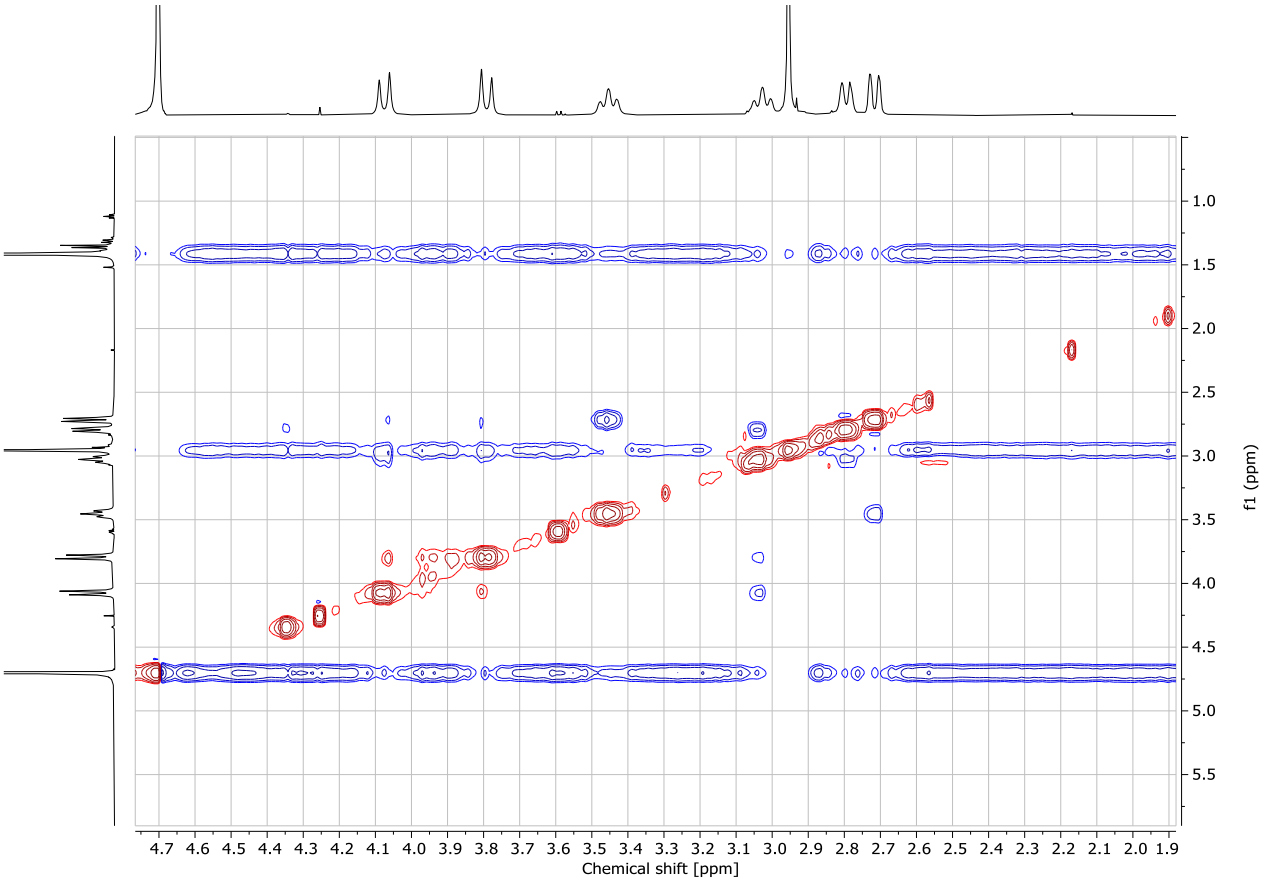
HNMR

δ_H (600 MHz, D_2O) 4.08 (4 H, d, *J* 17.0, H_1ac), 3.79 (4 H, d, *J* 17.0, H_2ac), 3.45 (4 H, t, *J* 13.9, H_1ax), 3.03 (4 H, t, *J* 13.9, H_2ax), 2.95 (12 H, s, Me), 2.80 (4 H, d, *J* 13.4, H_2eq), 2.71 (4 H, d, *J* 3.2, H_1eq), 1.41 (36 H, s, tBu).



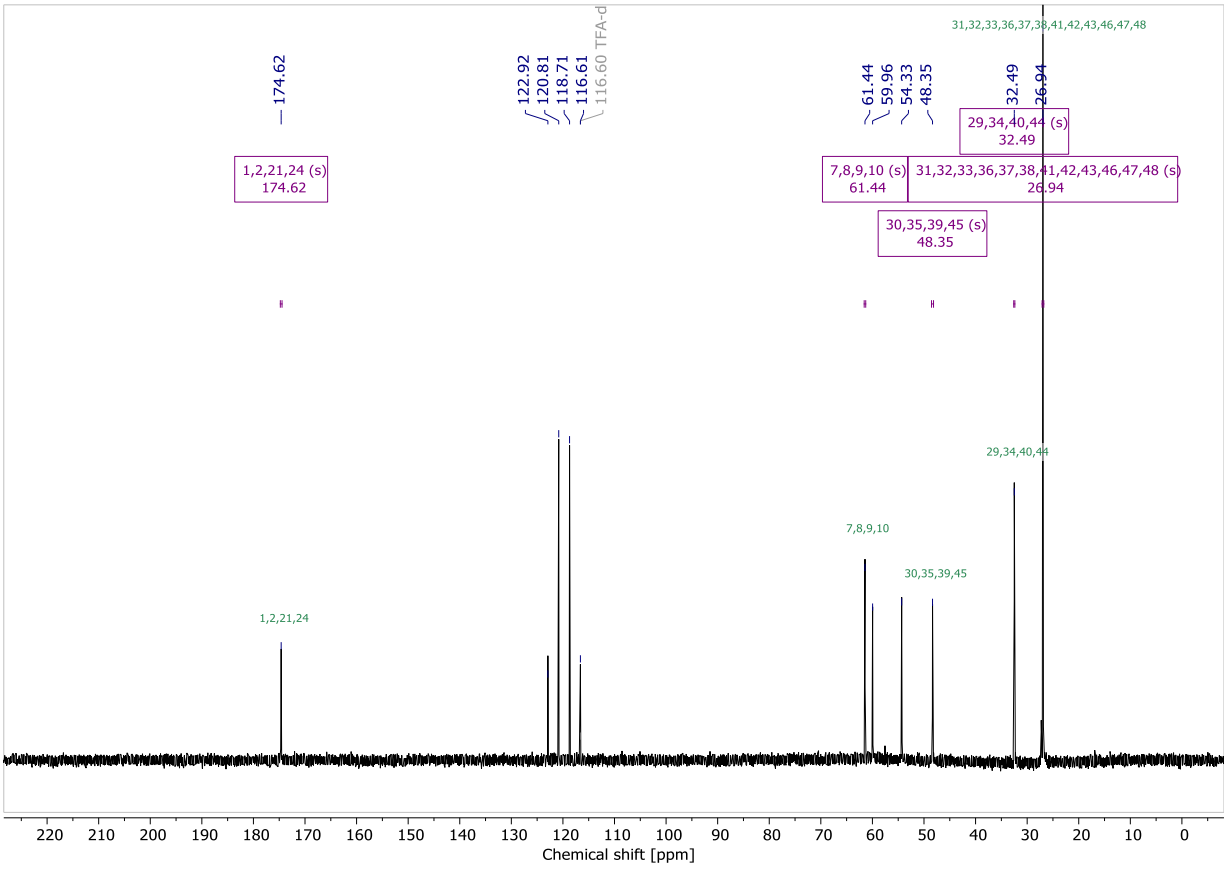
EXSY

$\delta_{H\text{-}H}$ ((600, 600) MHz, D_2O) (4.07 4.07), (4.06 3.81), (3.81 4.06), (3.79 3.79), (3.46 2.71), (3.46 3.46), (3.04 2.79), (3.03 3.79), (3.03 4.07), (2.80 2.79), (2.80 3.02), (2.71 4.07), (2.71 3.46), (2.71 3.79).



CNMR

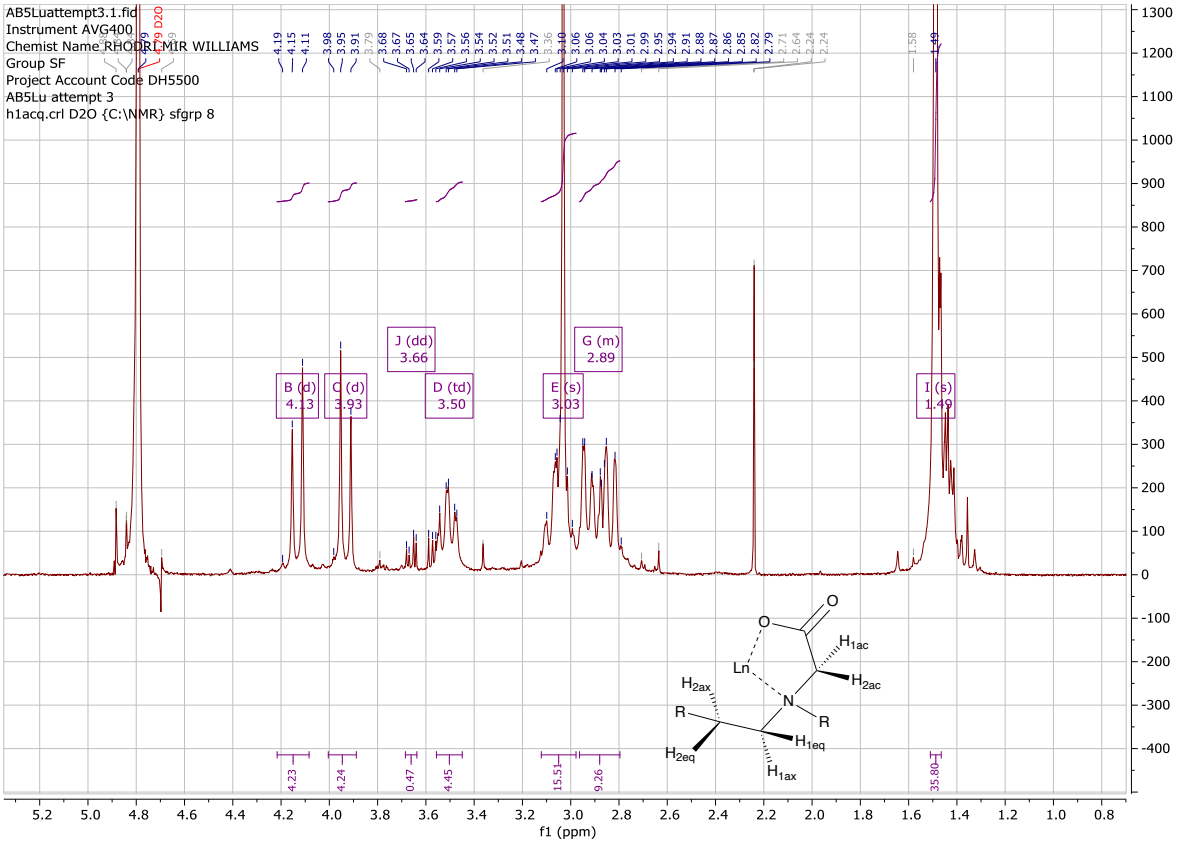
δ_C (151 MHz, D_2O) 174.6(**C**(O)N), 61.4(**C**H_2-arm), 60.0(**C**H_2 ring), 54.3(**C**H_2-ring), 48.4(**C**-tBu), 32.5(Me), 26.9(Me-tBu). (Shifts around 123-161 ppm belong to CF_3 part of triflate counter ion).



[Lu(DTtBuMA)]$^{3+}$

HNMR

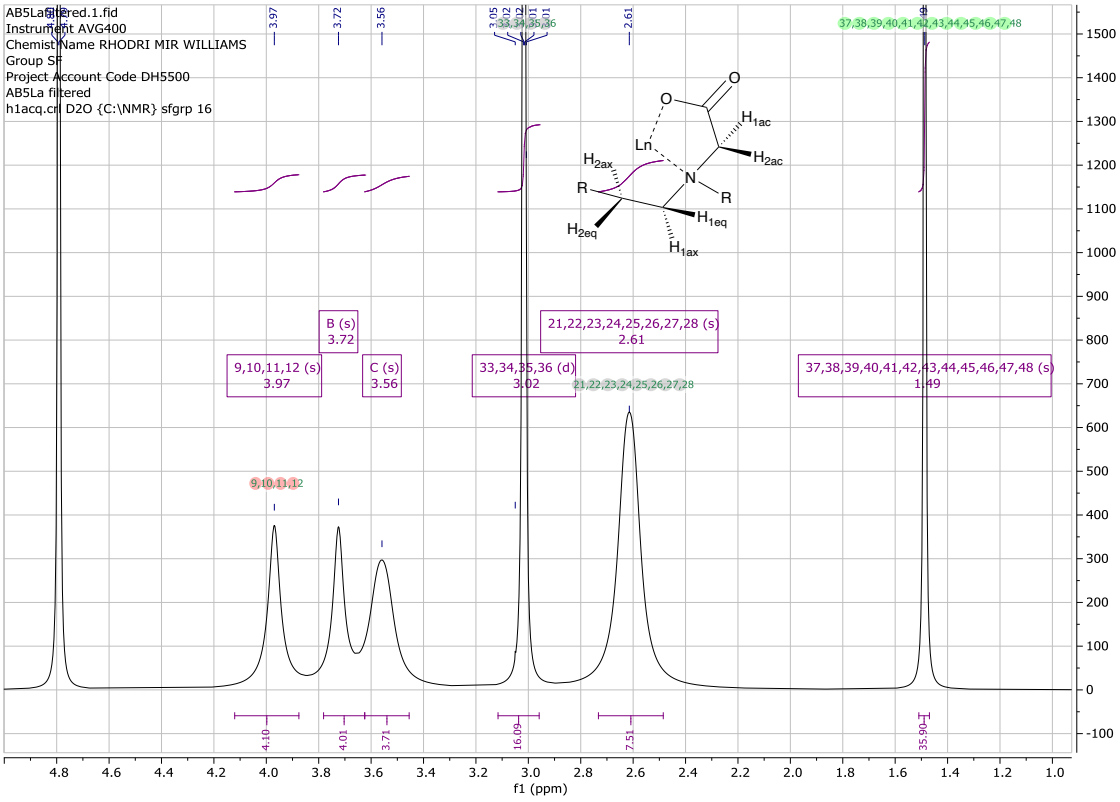
δ_H (400 MHz, D_2O) 4.13 (4 H, d, *J* 17.0, H_1ac), 3.93 (4 H, d, *J* 17.0, H_2ac), 3.66 (0 H, dd, *J* 11.7, 4.3, Minor isomer), 3.50 (4 H, td, *J* 13.9, 3.5, H_1ax), 3.03 (16 H, s, H_2ax and Me), 2.96 – 2.80 (9 H, m, Heq + minor isomer), 1.49 (36 H, s, tBu). Minor isomer may be TSAP due to smaller J coupling values of minor isomer. There is also some minor methanol and ethanol contamination.



$[La(DTtBuMA)]^{3+}$

HNMR

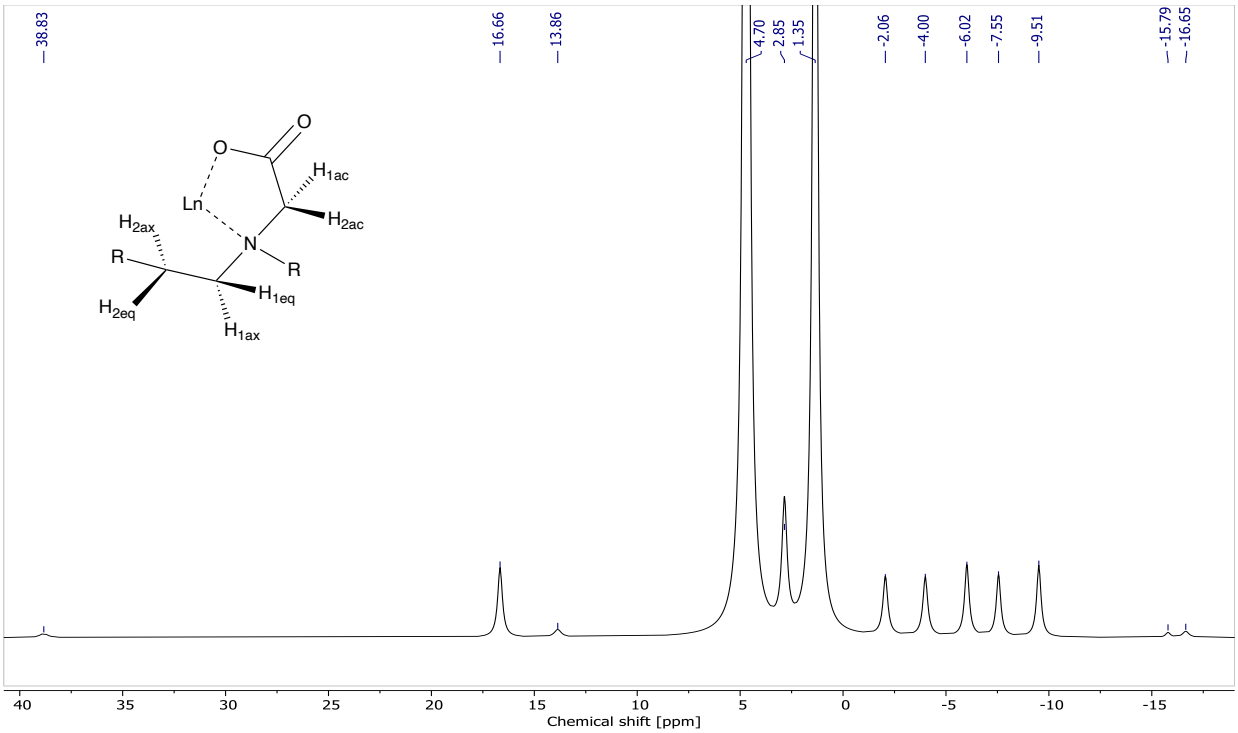
δ_H (400 MHz, D_2O) 3.97 (4 H, s, H_1ac), 3.72 (4 H, s, H_2ac), 3.56 (4 H, s, H_1ax), 3.02 (16 H, s, H_2ax and Me), 2.61 (8 H, s, Heq), 1.49 (36 H, s, tBu).



[Eu(DTtBuMA)]$^{3+}$

HNMR

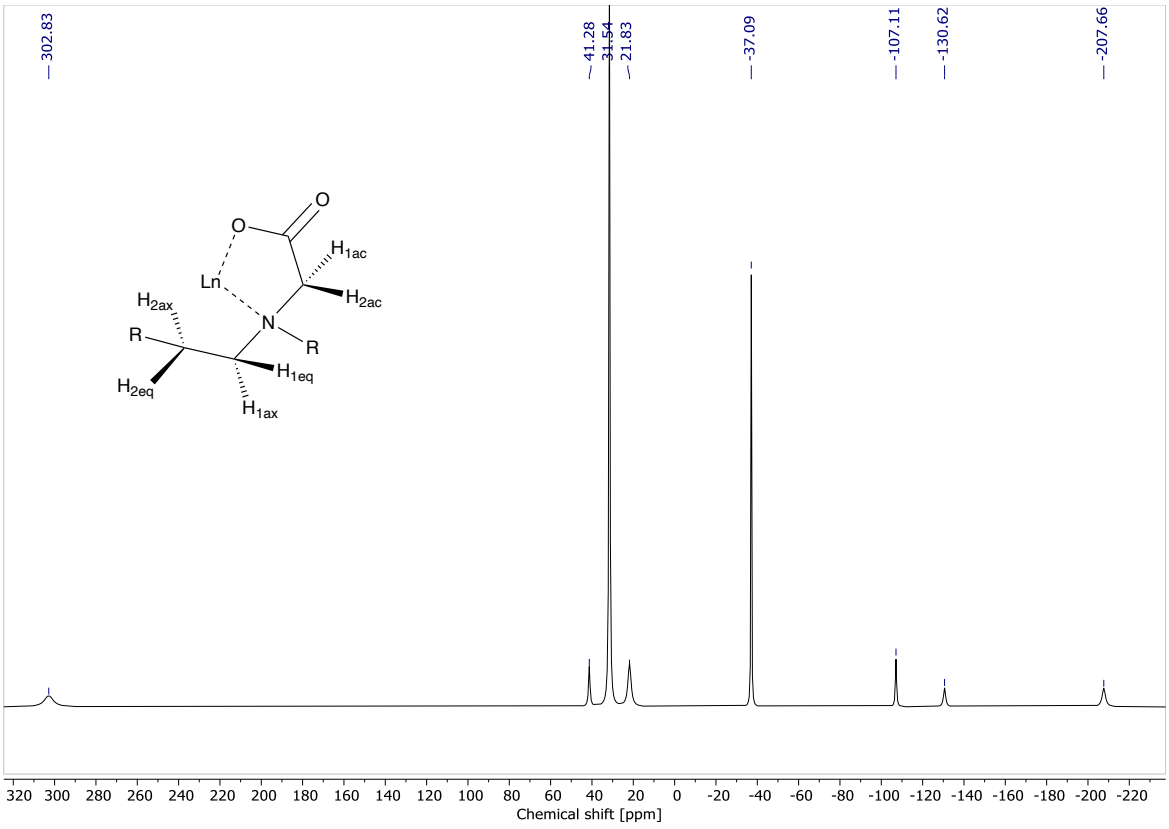
δ_H (400 MHz, D_2O) 38.83(H_1ax (CSAP)), 16.66(H_1ax, (TSAP)), 13.86(CSAP?), 4.70(H_2O), 2.85(Me), 1.35(tBu), -2.06(H_2eq, (TSAP)), -4.00(H_1eq, (TSAP)), -6.02(H_2ac, (TSAP)), -7.55(H_2ax, (TSAP)), -9.51 (H_1ac, (TSAP)), -15.79(CSAP), -16.65(CSAP).



[Er(DTtBuMA)]$^{3+}$

HNMR

δ_H (400 MHz, D_2O) 302.83(H_1ax), 41.28(H_2eq), 31.54(tBu), 21.83(H_1eq), -37.09(Me), -107.11(H_2ac), -130.62(H_2ax), -207.66(H_1ac).



References

1 F. Zamberlan, C. Lesbats, N. J. Rogers, J. L. Krupa, G. E. Pavlovskaya, N. R. Thomas, H. M. Faas and T. Meersmann, *ChemPhysChem*, 2015, **16**, 2294–2298.

2 K. W. H. Stevens, *Proceedings of the Physical Society. Section A*, 1952, **65**, 209–215.

3 A. Beeby, I. M. Clarkson, R. S. Dickins, S. Faulkner, D. Parker, L. Royle, A. S. de Sousa, J. A. G. Williams and M. Woods, *Journal of the Chemical Society, Perkin Transactions 2*, 1999, 493–504.

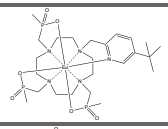
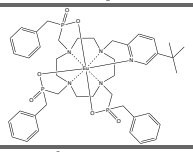
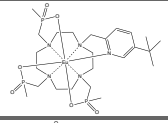
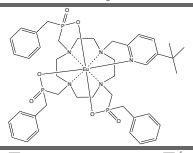
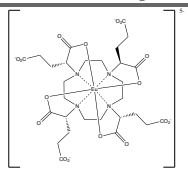
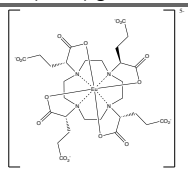
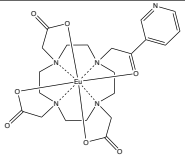
4 H. W. El-Shafey, R. M. Gomaa, S. M. El-Messery and F. E. Goda, *Bioorg Chem*, 2020, **101**, 103987.

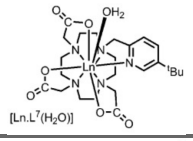
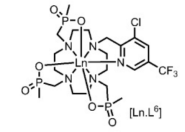
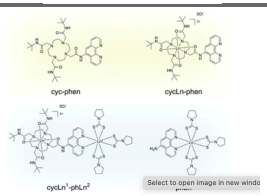
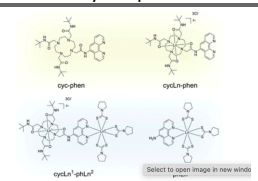
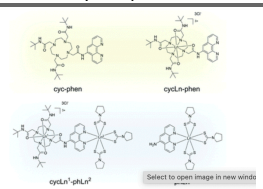
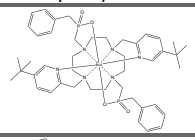
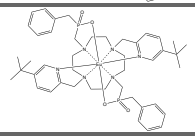
5 M. Tropiano and S. Faulkner, *Chem. Commun.*, 2014, **50**, 4696–4698.

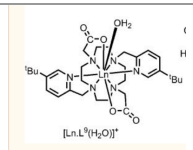
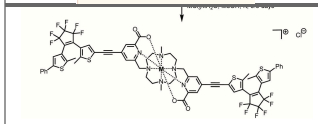
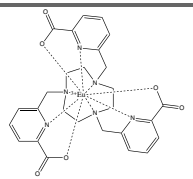
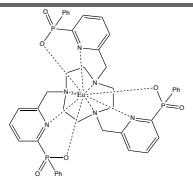
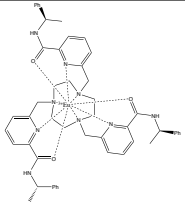
6 S. Mizukami, K. Tonai, M. Kaneko and K. Kikuchi, *J Am Chem Soc*, 2008, **130**, 14376–14377.

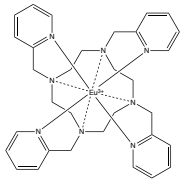
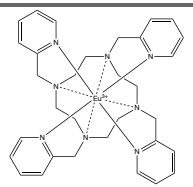
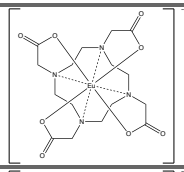
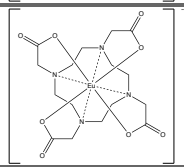
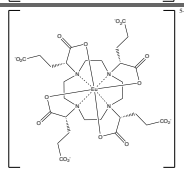
7 A. G. Cosby, G. Quevedo and E. Boros, *Inorg Chem*, 2019, **58**, 10611–10615.

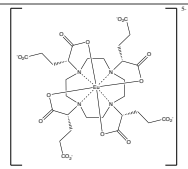
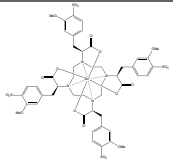
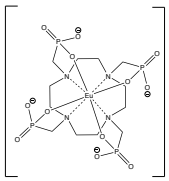
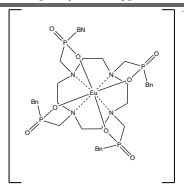
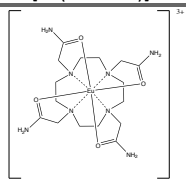
Appendix I: Crystal field parameters and pKa values for the ligands used to propose a correlation between the CF parameters and pKa.

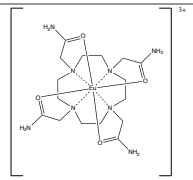
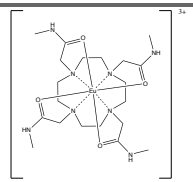
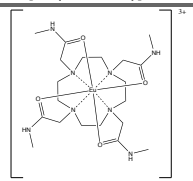
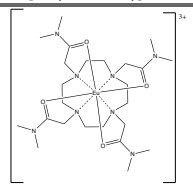
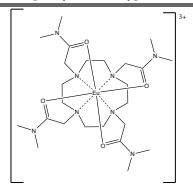
COMPLEX	B20 cm^{-1}	B22 cm^{-1}	Point Group	Prism	Coord No	Ligating atoms/ions	Base	Solvent	A^-/C^+ Counter ion	Charge	Reference	Name
	-660	-122	C_1	TSAP	8	$N(PO_4)_3$	N_4	H_2O	none	0	https://doi.org/10.1002/anie.201906031	DOTPMe*1PyTbu
	-650	-80	C_1	TSAP	8	$N(PO_4)_3$	N_4	H_2O	none	0	https://doi.org/10.1002/anie.201906031	DOTPBn*1PyTbu
	-596	-228	C_1	TSAP	8	$N(PO_4)_3$	N_4	MeOH	none	0	https://doi.org/10.1002/anie.201906031	DOTPMe*1PyTbu
	-703	-167	C_1	TSAP	8	$N(PO_4^{2-})_3$	N_4	MeOH	none	0	https://doi.org/10.1002/anie.201906031	DOTPBn*1PyTbu
 (RRRS)-gDOTA	-780	-	C_1	CSAP	9	$(CO_2^-)_4$	N_4	H_2O	?	5-	3B/10=split Dalton Trans., 2003, 1264–1271 https://doi.org/10.1039/B211939K	(RRRS)-gDOTA
 (RRRS)-gDOTA	-445	-	C_1	TSAP	8	$(CO_2^-)_4$	N_4	H_2O	?	5-	3B/10=split Dalton Trans., 2003, 1264–1271 https://doi.org/10.1039/B211939K	(RRRS)-gDOTA
 RHMW4Eu	-520	-175	C1	CSAP	9	$(CO_2)_3$(COPy)	N_4	H_2O	-	0	Chapter on pH probes	RHMW4Eu

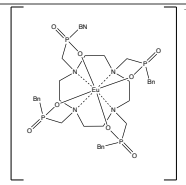
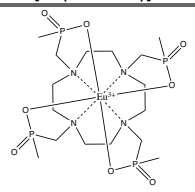
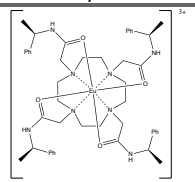
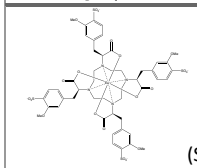
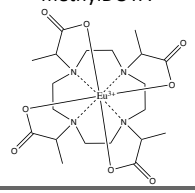
	-455	-	C_1	CSAP	9	$N_1(CO_2)_3$	N_4	H_2O	-	0	https://doi.org/10.1039/C4SC03429E	(3)CO2 pyTbu
	-550	-	C_1	TSAP ?	8	$N(PO_2)_3$	N_4	H_2O	-	0	https://doi.org/10.1039/C4SC03429E	DOTPBn*1PyTbu(CF3)
 CycEu-phen	-798	-136	C_1	CSAP ?	8?	CONtBu	N_4	10K solid	3+	-	Dalton Trans., 2019,48, 4314-4323 https://doi.org/10.1039/C9DT00533A	CycEu-phen
 CycEu-phenLa	-820	-102	C_1	CSAP ?	8?	CONtBu	N_4	10K solid	-	-	Dalton Trans., 2019,48, 4314-4323 https://doi.org/10.1039/C9DT00533A	CycEu-phenLa
 cycLa-phEu	-313	-4	C_1	CSAP ?	8?	$N_2(S_2)_3$	-	10K Solid	-	-	Dalton Trans., 2019,48, 4314-4323 https://doi.org/10.1039/C9DT00533A	cycLa-phEu
	+735	-220	C_2	TSAP	8	$N_2(PO_4)_2$	N_4	H_2O	PF_6	1+	https://doi.org/10.1002/anie.201906031	DOTPBN 2pyTbU
	+923	-153	C_2	TSAP	8	$N_2(PO_4^{2-})_2$	N_4	MeOH	PF_6^-	1+	https://doi.org/10.1002/anie.201906031	DOTPBN 2pyTbU

	**-355**	**-**	**C_2**	**CSAP**	**9**	**$N_2(CO_2)_2$**	**N_4**	**H_2O**	**?**	**1+**	**https://doi.org/10.1039/C4SC03429E**	(2)CO2 (2)pyTbu
 EuLoo Cl-	**478**	**-58**	**C_2**	**TSAP ?**	**8**	**$NpyCO_2^-$**	**N4**	**Immobilised in organic glass**	**Cl-**	**1+**	**Inorg. Chem. Front., 2020, 7, 2979–2989 https://doi.org/10.1039/D0QI00354A Calculated from Split data**	ceuloocl
Eu_2O_3 solid not a complex Not cubic	**-288**	**-695**	**C_2**	**-**	**2**	**$3(O^{2-})$**	**-**	**-**	**-**	**0**	**https://doi.org/10.1016/j.omx.2019.100028**	Not in graph Not cyclen based
 EuL1	**+75**	**-**	**C_3**	**TTP**	**9**	**$N_3(CO_2)_3$**	**N_3**	**H_20**	**-**	**0**	**https://doi.org/10.1039/C4SC03429E**	Not in graph Not cyclen based
 L2	**+110**	**-**	**C_3**	**TTP**	**9**	**$N_3(PO_2)_3$**	**N_3**	**H_20**	**-**	**0**	**https://doi.org/10.1039/C4SC03429E**	Not in graph Not cyclen based
 L3	**+235**	**-**	**C_3**	**TTP**	**9**	**$N_3(C(NR)O)_3$**	**N_3**	**H_20**	**-**	**3+**	**https://doi.org/10.1039/C4SC03429E**	Not in graph Not cyclen based

 tetrakis(2-pyridylmethyl)cyclen	**≈ 0**	**-**	**C_4**	**TSAP**	**8**	**N_4(py)**	**N_4**	**H_2O**	**$(CF_3SO_3)^-$**	**3+**	**https://doi.org/10.1002/chem.201601170**	Not in graph Not cyclen based
 tetrakis(2-pyridylmethyl)cyclen with F-	**+1130**	**-**	**C_4**	**TSAP CSAP ?**	**9**	**N_4(py)**	**N_4**	**H_2O**	**$(CF_3SO_3)^-$ Or F^- with NaF**	**3+**	**https://doi.org/10.1002/chem.201601170**	Not in graph Not cyclen based
	**-400**	**-**	**C_4**	**TSAP**	**8**	**$(CO_2^-)_4$**	**N_4**	**H_2O**	**?**	**1-**	**https://doi.org/10.1039/B211939K 3B/10=split**	DOTA
	**-630**	**-**	**C_4**	**CSAP**	**9**	**$(CO_2^-)_4$**	**N_4**	**H_2O**	**?**	**1-**	**https://doi.org/10.1039/B211939K 3B/10=split**	DOTA
 (RRRR)-gDOTA	**-760**	**-**	**C_4**	**CSAP**	**9**	**$(CO_2^-)_4$**	**N_4**	**H_2O**	**?**	**5-**	**https://doi.org/10.1039/B211939K 3B/10=split**	gDOTA(RRRR)

 (RRRR)-gDOTA	**-425**	**-**	**C_4**	**TSAP**	**8**	**$(CO_2^-)_4$**	**N_4**	**H_2O**	**?**	**5-**	**https://doi.org/10.1039/B211939K 3B/10=split**	gDOTA(RRRR)
 (SSSS)-DOTA-Benzenesulfonate	**-410**	**-**	**C_4**	**TSAP**	**8**	**$(CO_2^-)_4$**	**N_4**	**H_2O**	**?**	**5-**	**https://doi.org/10.1021/acs.accounts.0c00275**	(SSSS)-DOTA-Benzenesulfonate
 $[Eu(DOTP)]^{5-}$	**670**	**-**	**C_4**	**TSAP**	**8**	**$(PO_4^{2-})_4$**	**N_4**	**H_2O**	**?**	**5-**	**https://doi.org/10.1039/B211939K 3B/10=split**	DOTP
 $[Eu(DOTPBn)]^-$	**-650**	**0**	**C_4**	**TSAP**	**8**	**$(PO_2OBn)_4$**	**N_4**	**H_2O**	**?**	**1-**	**https://doi.org/10.1039/C4SC03429E**	DOTPBN
 $EuDOTAM^{3+}$	**-475**	**-**	**C_4**	**CSAP**	**9**	**$(CONH_2)_4$**	**N_4**	**H_2O**	**?**	**3+**	**https://doi.org/10.1039/B211939K https://doi.org/10.1021/acs.accounts.0c00275 3B/10=split**	DOTAM

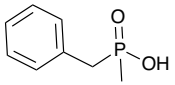
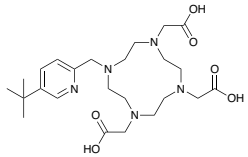
 $EuDOTAM^{3+}$	**-205**	**-**	**C_4**	**TSAP**	**8**	**$(CONH_2)_4$**	**N_4**	**H_2O**	**?**	**3+**	**https://doi.org/10.1039/B211939K** **https://doi.org/10.1021/acs.accounts.0c00275** **3B/10=split**	DOTAM
 $[Eu(DOTMA)]^{3+}$	**-450**	**-**	**C_4**	**CSAP**	**9**	**$(CONHMe)_4$**	**N_4**	**H_2O**	**?**	**3+**	**https://doi.org/10.1039/B211939K** **3B/10=split**	DOTMA
 $[Eu(DOTMA)]^{3+}$	**-200**	**-**	**C_4**	**TSAP**	**8**	**$(CONHMe)_4$**	**N_4**	**H_2O**	**?**	**3+**	**https://doi.org/10.1039/B211939K** **3B/10=split**	DOTMA
 $[Eu(DOTTA)]^{3+}$	**-450**	**-**	**C4**	**CSAP**	**9**	**$(CONMe_2)_4$**	**N_4**	**H_2O**	**?**	**3+**	**https://doi.org/10.1039/B211939K** **3B/10=split**	DOTTA
 $[Eu(DOTTA)]^{3+}$	**-185**	**-**	**C4**	**TSAP**	**8**	**$(CONMe_2)_4$**	**N_4**	**H_2O**	**?**	**3+**	**https://doi.org/10.1039/B211939K** **3B/10=split**	DOTTA

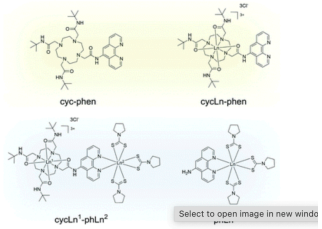
 [Eu(DOTPBn)]$^-$	**+920**	**-153**	**C_4**	**TSAP**	**8**	**$(PO_2OBn)_4$**	**N_4**	**MeOH**	**?**	**1-**	**https://doi.org/10.1039/C4SC03429E**	DOTPBN
 Methyl DOTP	**-700**	**-**	**C_4**	**TSAP**	**8**	**PO_2Me**	**N_4**	**H_2O**	**?**	**1-**	**https://doi.org/10.1039/C4SC03429E**	DOTPMe
 [Eu(DOTAMPh)]$^{3+}$	**-470**	**-**	**C_4**	**CSAP**	**9**	**(CONH(CH MePh)$_4$**	**N_4**	**H_2O**	**?**	**3+**	**https://doi.org/10.1039/B211939K 3B/10=split**	DOTAMPh
 (SSSS)-DOTA-Benzenesulfonate	**-700**	**-**	**C_4**	**CSAP**	**9**	**$(CO_2^-)_4$**	**N_4**	**H_2O**	**?**	**5-**	**https://doi.org/10.1021/acs.accounts.0c00275**	SSSS)-DOTA-Benzenesulfonate
methylDOTA 	-700	-	C_4	CSAP ?	9	CO_2^-	N_4	H_2O	?	1-	**https://doi.org/10.1039/C4SC03429E**	methylDOTA

Data for total pKa estimation

The values shown on this table were obtained for each functional group from prediction from SciFinder Advanced Chemistry Development (ACD/Labs) Software V11.02 (© 1994-2021 ACD/Labs)

Average pKa values were calculated by obtaining the mean values of the pKa of each individual ligating group for each complex.

Fragment	pKa
	2.63±0.50 In Bn DOTP(1.1±0.5) Cyclen(7.94±0.2)
	2.90±0.50 methylDOTP(1.37±0.50) cyclen(8.01±0.20)
PO3	2.27±0.50 In dotp (1.2±0.1) Cyclen(10.73±0.20)
CO2-	4.756 In DOTA(2.16±0.10) Cyclen(10.32±0.20)
DOTAM	C(O)**N** -0.47+-0.7 In ring 6.22±0.20
	CO2? 2.46±0.10 pyN(separate) 6.26±0.1 In ring 9.81±0.20
DOTMA	C(O)**N -0.44+-0.7** Cyclen 6.03±0.20

Fragment	pKa
DOTTA	C(O)**N** Cyclen 6.18±0.20
DOTAMPh (RRRR)	Cyclen (6.19±0.20) CON (0+-0.7)
gDOTA	COOH 1.78
1,4,7,10-tetra-kis(2-pyridylmethyl)-1,4,7,10-tetraaza-cyclododecane	Picoline(6.40) Cyclen(7.94±0.2)
MethylDOTA	Cyclen (10.45±0.2) COOH 2.25±0.1
 cyceu-phen	5.99+-0.2 cyc CONTbu -0.44±0.70 CONphen 0.53+-0.70

Appendix II: Crystallographic data

All data in this appendix was collected by Mr. Eric Yang. Tilt angles were calculated from crystal structures by Rhodri Mir Williams.

[Er(DTtBuMA)] $^{3+}$

Crystal Structure

Generated by CrystalMaker X for Windows (http://crystalmaker.com)
Coordinates for "esy_abser-metbu_mp"
Unit cell parameters:-
a = 14.97280; b = 13.09320; c = 15.43710 Å
alpha = 90.0000; beta = 97.1490; gamma = 90.0000 °

Listing of all 326 visible atoms:

		Fractional Coordinates			Orthogonal Coordinates [Å]		
Elmt	Label	x	y	z	xor	yor	zor
Er	Er1	0.266250	0.575910	0.252840	3.95552	7.54050	3.40700
Er	Er1	0.733750	0.075910	0.747160	10.90088	0.99390	10.16674
S	S1	0.144890	0.168710	0.009070	2.15254	2.20895	-0.12997
S	S1	0.855110	0.668710	0.990930	12.70386	8.75555	13.70370
S	S2	0.422390	0.617690	0.702910	6.27519	8.08754	10.06382
S	S2	0.577610	0.117690	0.297090	8.58120	1.54094	3.50991
S	S3	0.919220	0.737250	0.535120	13.65630	9.65296	6.54786
S	S3	0.080780	0.237250	0.464880	1.20010	3.10636	7.02588
O	O4	0.285500	0.741700	0.295000	4.24150	9.71123	4.02195
O	O4	0.714500	0.241700	0.705000	10.61490	3.16463	9.55178
O	O1	0.811100	0.158500	0.863500	12.05003	2.07527	11.81856
O	O1	0.188900	0.658500	0.136500	2.80637	8.62187	1.75517
O	O3	0.581800	0.084900	0.707320	8.64345	1.11161	9.83486
O	O3	0.418200	0.584900	0.292680	6.21295	7.65821	3.73887
O	O2	0.678600	0.000300	0.863200	10.08155	0.00393	12.06082
O	O2	0.321400	0.500300	0.136800	4.77485	6.55053	1.51291
F	F9	0.039100	0.177900	0.303400	0.58089	2.32928	4.61076
F	F9	0.960900	0.677900	0.696600	14.27551	8.87588	8.96298
F	F6	0.320500	0.761200	0.757400	4.76148	9.96654	11.09485
F	F6	0.679500	0.261200	0.242600	10.09492	3.41994	2.47888
F	F2	0.681000	0.678400	0.950800	10.11721	8.88243	13.40864
F	F2	0.319000	0.178400	0.049200	4.73919	2.33583	0.16509
F	F8	0.008400	0.579600	0.600900	0.12479	7.58882	9.26050
F	F8	0.991600	0.079600	0.399100	14.73161	1.04222	4.31323
N	N3	0.685400	0.033600	0.590100	10.18258	0.43993	7.83228
N	N3	0.314600	0.533600	0.409900	4.67382	6.98653	5.74145
C	C37	0.258800	0.136400	0.989400	3.84484	1.78591	14.79123
C	C37	0.741200	0.636400	0.010600	11.01156	8.33251	-1.21749

N	N4	0.851800	0.139200	0.659800	12.65468	1.82257	8.59818
N	N4	0.148200	0.639200	0.340200	2.20172	8.36917	4.97555
F	F3	0.723100	0.669700	0.088000	10.74266	8.76852	0.01106
F	F3	0.276900	0.169700	0.912000	4.11374	2.22192	13.56267
F	F5	0.276000	0.707400	0.629000	4.10037	9.26213	9.19565
F	F5	0.724000	0.207400	0.371000	10.75603	2.71553	4.37809
F	F7	0.925300	0.219500	0.368100	13.74663	2.87396	3.95822
F	F7	0.074700	0.719500	0.631900	1.10977	9.42056	9.61551
N	N6	0.567900	0.900100	0.906700	8.43695	11.78519	12.93861
N	N6	0.432100	0.400100	0.093300	6.41945	5.23859	0.63512
O	O6	0.141500	0.134700	0.096700	2.10218	1.76365	1.22910
O	O6	0.858500	0.634700	0.903300	12.75422	8.31025	12.34463
O	O5	0.857600	0.777800	0.002100	12.74085	10.18389	-1.56560
O	O5	0.142400	0.277800	0.997900	2.11555	3.63729	15.13934
N	N7	0.531900	0.652100	0.385500	7.90212	8.53808	4.95988
N	N7	0.468100	0.152100	0.614500	6.95428	1.99148	8.61386
N	N5	0.129300	0.639200	0.994500	1.92093	8.36917	15.11126
N	N5	0.870700	0.139200	0.005500	12.93547	1.82257	-1.53753
C	C10	0.145600	0.606000	0.075900	2.16309	7.93448	0.90037
C	C10	0.854400	0.106000	0.924100	12.69331	1.38788	12.67336
O	O8	0.473100	0.697000	0.666400	7.02856	9.12596	9.40572
O	O8	0.526900	0.197000	0.333600	7.82784	2.57936	4.16801
C	C17	0.625200	0.924900	0.851100	9.28822	12.10990	11.97354
C	C17	0.374800	0.424900	0.148900	5.56818	5.56330	1.60019
O	O10	0.452100	0.595900	0.792600	6.71658	7.80224	11.39302
O	O10	0.547900	0.095900	0.207400	8.13982	1.25564	2.18072
O	O13	0.085500	0.341000	0.435200	1.27022	4.46478	6.55891
O	O13	0.914500	0.841000	0.564800	13.58618	11.01138	7.01483
C	C7	0.935000	0.076800	0.674900	13.89073	1.00556	8.67625
C	C7	0.065000	0.576800	0.325100	0.96567	7.55216	4.89748
H	H7A	0.986094	0.116113	0.656905	14.64981	1.52029	8.30325
H	H7A	0.013906	0.616113	0.343095	0.20659	8.06689	5.27048
H	H7B	0.927501	0.014165	0.638843	13.77933	0.18547	8.13361
H	H7B	0.072499	0.514165	0.361157	1.07707	6.73207	5.44012
C	C30	0.129200	0.745900	0.311500	1.91945	9.76622	4.56791
C	C30	0.870800	0.245900	0.688500	12.93695	3.21962	9.00582
H	H30A	0.099987	0.783024	0.356269	1.48545	10.25229	5.31345
H	H30A	0.900013	0.283024	0.643731	13.37095	3.70569	8.26029
H	H30B	0.912170	0.246367	0.743702	13.55156	3.22573	9.78090
H	H30B	0.087830	0.746367	0.256298	1.30484	9.77233	3.79284
O	O7	0.089100	0.112500	0.942800	1.32371	1.47299	14.38807
O	O7	0.910900	0.612500	0.057200	13.53269	8.01959	-0.81434
C	C12	0.155200	0.746700	0.970700	2.30571	9.77669	14.69560
C	C12	0.844800	0.246700	0.029300	12.55069	3.23009	-1.12186
F	F1	0.273700	0.036700	0.992400	4.06620	0.48052	14.80977
F	F1	0.726300	0.536700	0.007600	10.79020	7.02712	-1.23604
N	N8	0.220400	0.898700	0.290600	3.27435	11.76686	4.07534

N	N8	0.779600	0.398700	0.709400	11.58205	5.22026	9.49840
C	C31	0.217000	0.798000	0.298200	3.22384	10.44837	4.19899
C	C31	0.783000	0.298000	0.701800	11.63256	3.90177	9.37474
N	N2	0.713600	0.886800	0.732100	10.60153	11.61105	9.97180
N	N2	0.286400	0.386800	0.267900	4.25487	5.06445	3.60193
O	O14	0.050300	0.322000	0.818100	0.74728	4.21601	12.53536
O	O14	0.949700	0.822000	0.181900	14.10912	10.76261	1.03837
H	H14	0.066817	0.307812	0.870754	0.99266	4.03024	13.31741
H	H14	0.933183	0.807812	0.129246	13.86374	10.57684	0.25632
N	N1	0.879300	0.992700	0.803200	13.06323	12.99762	10.76062
N	N1	0.120700	0.492700	0.196800	1.79317	6.45102	2.81311
C	C24	0.549900	0.113000	0.632000	8.16953	1.47953	8.73158
C	C24	0.450100	0.613000	0.368000	6.68687	8.02613	4.84215
O	O11	0.836600	0.679300	0.538000	12.42886	8.89421	6.74627
O	O11	0.163400	0.179300	0.462000	2.42754	2.34761	6.82747
F	F4	0.256200	0.615000	0.739300	3.80621	8.05232	10.93525
F	F4	0.743800	0.115000	0.260700	11.05019	1.50572	2.63848
O	O12	0.962100	0.721200	0.459100	14.29334	9.44282	5.29443
O	O12	0.037900	0.221200	0.540900	0.56306	2.89622	8.27931
O	O9	0.599600	0.031800	0.353600	8.90790	0.41636	4.34128
O	O9	0.400400	0.531800	0.646400	5.94850	6.96296	9.23245
C	C8	0.955300	0.047800	0.770500	14.19232	0.62585	10.11421
C	C8	0.044700	0.547800	0.229500	0.66408	7.17245	3.45952
H	H8A	0.990433	0.503956	0.221658	14.71427	6.59840	1.57622
H	H8A	0.009567	0.003956	0.778342	0.14213	0.05180	11.99752
H	H8B	0.031285	0.610506	0.194440	0.46478	7.99348	2.94329
H	H8B	0.968715	0.110506	0.805560	14.39162	1.44688	10.63044
C	C19	0.567600	0.955700	0.991800	8.43249	12.51317	14.25287
C	C19	0.432400	0.455700	0.008200	6.42391	5.96657	-0.67914
C	C32	0.862700	0.459000	0.718200	12.81662	6.00978	9.47940
C	C32	0.137300	0.959000	0.281800	2.03978	12.55638	4.09433
H	H32A	0.914406	0.413717	0.733285	13.58478	5.41688	9.61592
H	H32A	0.085594	0.913717	0.266715	1.27162	11.96348	3.95781
H	H32B	0.139209	0.010058	0.235668	2.06814	0.13169	3.37863
H	H32B	0.860791	0.510058	0.764332	12.78825	6.67829	10.19510
H	H32C	0.131554	0.993467	0.337188	1.95442	13.00766	4.96007
H	H32C	0.868446	0.493467	0.662812	12.90198	6.46106	8.61366
C	C15	0.112200	0.824100	0.026800	1.66689	10.79011	0.20464
C	C15	0.887800	0.324100	0.973200	13.18951	4.24351	13.36909
H	H15A	0.139407	0.817869	0.087697	2.07109	10.70852	1.09402
H	H15A	0.860593	0.317869	0.912303	12.78531	4.16192	12.47971
H	H15B	0.047370	0.810929	0.023044	0.70375	10.61766	0.26746
H	H15B	0.952630	0.310929	0.976956	14.15265	4.07106	13.30627
H	H15C	0.877905	0.393329	0.994225	13.04251	5.14994	13.71209
H	H15C	0.122095	0.893329	0.005775	1.81389	11.69654	-0.13836
C	C6	0.816600	0.140400	0.564600	12.13174	1.83829	7.19416
C	C6	0.183400	0.640400	0.435400	2.72466	8.38489	6.37957

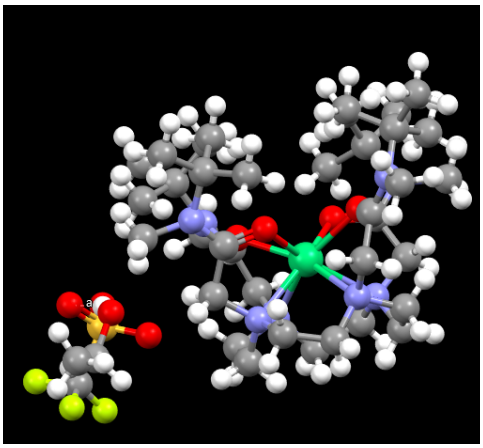
H	H6A	0.867828	0.144996	0.529955	12.89280	1.89846	6.56389
H	H6A	0.132172	0.644996	0.470045	1.96360	8.44506	7.00985
H	H6B	0.778505	0.201631	0.551696	11.56578	2.64000	7.06595
H	H6B	0.221495	0.701631	0.448304	3.29062	9.18660	6.50779
C	C11	0.910900	0.068900	0.074700	13.53269	0.90212	-0.54419
C	C11	0.089100	0.568900	0.925300	1.32371	7.44872	14.11792
H	H11A	0.908671	0.998836	0.052274	13.49958	13.07796	-0.88623
H	H11A	0.091329	0.498836	0.947726	1.35682	6.53136	14.45996
H	H11B	0.876899	0.073007	0.124954	13.02756	0.95590	0.29494
H	H11B	0.123101	0.573007	0.875046	1.82884	7.50250	13.27879
H	H11C	0.973617	0.088368	0.092885	14.46444	1.15702	-0.38033
H	H11C	0.026383	0.588368	0.907115	0.39196	7.70362	13.95406
C	C5	0.762300	0.046400	0.537700	11.32503	0.60752	6.88008
C	C5	0.237700	0.546400	0.462300	3.53137	7.15412	6.69365
H	H5A	0.261295	0.551437	0.524980	3.88190	7.22007	7.61728
H	H5A	0.738705	0.051437	0.475020	10.97450	0.67347	5.95645
H	H5B	0.198230	0.485582	0.454453	2.94498	6.35782	6.64606
H	H5B	0.801770	0.985582	0.545547	11.91142	12.90442	6.92767
C	C22	0.662300	0.957400	0.042200	9.83939	12.53543	-0.58266
C	C22	0.337700	0.457400	0.957800	5.01701	5.98883	14.15640
H	H22A	0.685446	0.887506	0.048835	10.18326	11.62029	-0.52337
H	H22A	0.314554	0.387506	0.951165	4.67314	5.07369	14.09710
H	H22B	0.659945	0.987579	0.099983	9.80441	12.93057	0.31373
H	H22B	0.340055	0.487579	0.900017	5.05199	6.38397	13.26001
H	H22C	0.702042	0.998298	0.010075	10.42982	13.07092	-1.15263
H	H22C	0.297958	0.498298	0.989925	4.42658	6.52432	14.72637
C	C4	0.349700	0.427400	0.420500	5.19528	5.59603	5.83968
C	C4	0.650300	0.927400	0.579500	9.66112	12.14263	7.73405
H	H4A	0.650501	0.905678	0.518057	9.66410	11.85822	6.78518
H	H4A	0.349499	0.405678	0.481943	5.19230	5.31162	6.78856
H	H4B	0.587309	0.925652	0.592760	8.72530	12.11975	8.05612
H	H4B	0.412691	0.425652	0.407240	6.13110	5.57315	5.51761
C	C23	0.389000	0.603400	0.440100	5.77914	7.90044	6.06902
C	C23	0.611000	0.103400	0.559900	9.07726	1.35384	7.50472
H	H23A	0.576300	0.076370	0.506011	8.56174	0.99993	6.73748
H	H23A	0.423700	0.576370	0.493989	6.29466	7.54653	6.83625
H	H23B	0.364885	0.671280	0.453239	5.42088	8.78920	6.31678
H	H23B	0.635115	0.171280	0.546761	9.43552	2.24260	7.25695
C	C34	0.703700	0.567300	0.708300	10.45445	7.42777	9.62285
C	C34	0.296300	0.067300	0.291700	4.40195	0.88117	3.95089
H	H34A	0.727894	0.583556	0.653778	10.81388	7.64062	8.73610
H	H34A	0.272106	0.083556	0.346222	4.04252	1.09402	4.83763
H	H34B	0.746187	0.590226	0.757992	11.08565	7.72795	10.31078
H	H34B	0.253813	0.090226	0.242008	3.77075	1.18135	3.26296
H	H34C	0.645954	0.602194	0.709299	9.59655	7.88465	9.74587
H	H34C	0.354046	0.102194	0.290701	5.25985	1.33805	3.82786
C	C1	0.121300	0.384200	0.223000	1.80208	5.03041	3.21645

C	C1	0.878700	0.884200	0.777000	13.05432	11.57701	10.35729
H	H1A	0.073041	0.347493	0.185793	1.08513	4.54980	2.73200
H	H1A	0.926959	0.847493	0.814207	13.77127	11.09640	10.84173
H	H1B	0.108331	0.379332	0.284247	1.60941	4.96667	4.18609
H	H1B	0.891669	0.879332	0.715753	13.24699	11.51327	9.38764
C	C2	0.210600	0.333600	0.215100	3.12876	4.36789	2.92810
C	C2	0.789400	0.833600	0.784900	11.72764	10.91449	10.64564
H	H2A	0.208509	0.261788	0.234730	3.09769	3.42764	3.23502
H	H2A	0.791491	0.761788	0.765270	11.75871	9.97424	10.33871
H	H2B	0.221186	0.333372	0.153071	3.28603	4.36491	1.95082
H	H2B	0.778814	0.833372	0.846929	11.57037	10.91151	11.62291
C	C39	0.994900	0.675900	0.620400	14.78063	8.84969	7.72331
C	C39	0.005100	0.175900	0.379600	0.07577	2.30309	5.85042
C	C16	0.629600	0.861600	0.768800	9.35359	11.28110	10.69487
C	C16	0.370400	0.361600	0.231200	5.50281	4.73450	2.87887
H	H16A	0.371389	0.287933	0.216901	5.51750	3.76996	2.65629
H	H16A	0.628611	0.787933	0.783099	9.33890	10.31656	10.91745
H	H16B	0.576892	0.876825	0.725407	8.57054	11.48045	10.12322
H	H16B	0.423108	0.376825	0.274593	6.28586	4.93385	3.45051
C	C9	0.889000	0.001600	0.899600	13.20734	0.02095	12.23068
C	C9	0.111000	0.501600	0.100400	1.64906	6.56755	1.34305
H	H9A	0.046910	0.493979	0.076263	0.69691	6.46777	1.08987
H	H9A	0.953090	0.993979	0.923737	14.15949	13.01437	12.48386
H	H9B	0.145805	0.446923	0.075650	2.16614	5.85165	0.89613
H	H9B	0.854195	0.946923	0.924350	12.69026	12.39825	12.67761
C	C3	0.706700	0.853400	0.639300	10.49902	11.17374	8.55210
C	C3	0.293300	0.353400	0.360700	4.35738	4.62714	5.02164
H	H3A	0.679159	0.784576	0.633593	10.08986	10.27261	8.51532
H	H3A	0.320841	0.284576	0.366407	4.76654	3.72601	5.05842
H	H3B	0.767809	0.848741	0.621356	11.40688	11.11274	8.16123
H	H3B	0.232191	0.348741	0.378644	3.44952	4.56614	5.41251
C	C21	0.532600	0.064100	0.974600	7.91252	0.83927	14.05257
C	C21	0.467400	0.564100	0.025400	6.94388	7.38587	-0.47884
H	H21A	0.427403	0.600950	0.060169	6.34967	7.86836	0.13243
H	H21A	0.572597	0.100950	0.939831	8.50673	1.32176	13.44131
H	H21B	0.469223	0.599419	0.969689	6.97096	7.84831	14.09485
H	H21B	0.530777	0.099419	0.030311	7.88544	1.30171	-0.52112
H	H21C	0.528178	0.561527	0.057397	7.84682	7.35219	-0.09815
H	H21C	0.471822	0.061527	0.942603	7.00958	0.80559	13.67188
C	C27	0.316300	0.206800	0.648900	4.69908	2.70767	9.42775
C	C27	0.683700	0.706800	0.351100	10.15732	9.25427	4.14598
H	H27A	0.286104	0.158527	0.606381	4.25048	2.07563	8.82765
H	H27A	0.713896	0.658527	0.393619	10.60592	8.62223	4.74609
H	H27B	0.324893	0.272065	0.620012	4.82674	3.56220	8.96579
H	H27B	0.675107	0.772065	0.379988	10.02966	10.10880	4.60794
H	H27C	0.279115	0.217467	0.696106	4.14664	2.84734	10.22576
H	H27C	0.720885	0.717467	0.303894	10.70976	9.39394	3.34797

C	C36	0.622500	0.420600	0.635900	9.24811	5.50700	8.65651
C	C36	0.377500	0.920600	0.364100	5.60829	12.05360	4.91723
H	H36A	0.568017	0.462347	0.634597	8.43869	6.05360	8.73791
H	H36A	0.431983	0.962347	0.365403	6.41771	12.60020	4.83582
H	H36B	0.393108	0.848374	0.359037	5.84017	11.10793	4.80999
H	H36B	0.606892	0.348374	0.640963	9.01623	4.56133	8.76375
H	H36C	0.649487	0.431308	0.581928	9.64904	5.64720	7.77305
H	H36C	0.350513	0.931308	0.418072	5.20736	12.19380	5.80069
C	C26	0.408000	0.163500	0.686800	6.06141	2.14074	9.84195
C	C26	0.592000	0.663500	0.313200	8.79499	8.68734	3.73179
C	C33	0.690000	0.451700	0.714400	10.25092	5.91420	9.74254
C	C33	0.310000	0.951700	0.285600	4.60548	12.46080	3.83119
C	C20	0.506100	0.900100	0.048900	7.51882	11.78519	-0.18818
C	C20	0.493900	0.400100	0.951100	7.33758	5.23859	13.76191
H	H20A	0.556154	0.402166	0.979620	8.26245	5.26564	14.08617
H	H20A	0.443846	0.902166	0.020380	6.59395	11.81224	-0.51244
H	H20B	0.509640	0.933706	0.105924	7.57142	12.22520	0.68551
H	H20B	0.490360	0.433706	0.894076	7.28498	5.67860	12.88822
H	H20C	0.525505	0.828859	0.056793	7.80711	10.85242	-0.10249
H	H20C	0.474495	0.328859	0.943207	7.04929	4.30582	13.67622
C	C14	0.258000	0.756200	0.980800	3.83295	9.90108	14.65996
C	C14	0.742000	0.256200	0.019200	11.02345	3.35448	-1.08623
H	H14A	0.725362	0.324677	0.037080	10.77627	4.25106	-0.77921
H	H14A	0.274638	0.824677	0.962920	4.08013	10.79766	14.35294
H	H14B	0.717271	0.205061	0.055939	10.65606	2.68490	-0.47300
H	H14B	0.282729	0.705061	0.944061	4.20033	9.23150	14.04674
H	H14C	0.717762	0.244871	0.957985	10.66336	3.20614	13.45106
H	H14C	0.282238	0.744871	0.042015	4.19304	9.75274	0.12268
C	C13	0.118900	0.769000	0.874600	1.76643	10.06867	13.27973
C	C13	0.881100	0.269000	0.125400	13.08997	3.52207	0.29400
H	H13A	0.053016	0.766016	0.867205	0.78763	10.02960	13.28834
H	H13A	0.946984	0.266016	0.132795	14.06877	3.48300	0.28539
H	H13B	0.142362	0.717947	0.836862	2.11499	9.40022	12.65345
H	H13B	0.857638	0.217947	0.163138	12.74141	2.85362	0.92028
H	H13C	0.861638	0.337220	0.141299	12.80084	4.41529	0.57570
H	H13C	0.138362	0.837220	0.858701	2.05556	10.96189	12.99803
O	O15	0.226600	0.976800	0.513100	3.36646	12.78944	7.49854
O	O15	0.773400	0.476800	0.486900	11.48994	6.24284	6.07520
H	H15	0.793111	0.528864	0.514752	11.78277	6.92452	6.46842
H	H15	0.206889	0.028864	0.485248	3.07363	0.37792	7.10531
C	C29	0.606900	0.559100	0.273600	9.01635	7.32041	3.09271
C	C29	0.393100	0.059100	0.726400	5.84005	0.77381	10.48102
H	H29A	0.347165	0.064732	0.766153	5.15762	0.84755	11.18028
H	H29A	0.652835	0.564732	0.233847	9.69878	7.39415	2.39345
H	H29B	0.550409	0.534954	0.241295	8.17710	7.00426	2.69928
H	H29B	0.449591	0.034954	0.758705	6.67930	0.45766	10.87445
H	H29C	0.627121	0.510640	0.320351	9.31676	6.68591	3.77673

H	H29C	0.372879	0.010640	0.679649	5.53964	0.13931	9.79700
C	C35	0.657400	0.426700	0.800700	9.76660	5.58687	11.13551
C	C35	0.342600	0.926700	0.199300	5.08980	12.13347	2.43822
H	H35A	0.296194	0.945583	0.151467	4.40038	12.38071	1.78629
H	H35A	0.703806	0.445583	0.848533	10.45602	5.83411	11.78744
H	H35B	0.354903	0.853384	0.196494	5.27258	11.17353	2.37198
H	H35B	0.645097	0.353384	0.803506	9.58382	4.62693	11.20175
H	H35C	0.602167	0.465101	0.806182	8.94603	6.08966	11.32305
H	H35C	0.397833	0.965101	0.193818	5.91037	12.63626	2.25068
C	C38	0.313500	0.677500	0.708900	4.65748	8.87064	10.35919
C	C38	0.686500	0.177500	0.291100	10.19892	2.32404	3.21454
C	C28	0.451600	0.238100	0.754700	6.70915	3.11749	10.80888
C	C28	0.548400	0.738100	0.245300	8.14725	9.66409	2.76485
H	H28A	0.530482	0.799974	0.274523	7.88105	10.47422	3.24936
H	H28A	0.469518	0.299974	0.725477	6.97535	3.92762	10.32438
H	H28B	0.495072	0.706438	0.212873	7.35499	9.24953	2.36364
H	H28B	0.504928	0.206438	0.787127	7.50141	2.70293	11.21009
H	H28C	0.591375	0.756080	0.204888	8.78570	9.89951	2.06093
H	H28C	0.408625	0.256080	0.795112	6.07070	3.35291	11.51281
C	C40	0.124600	0.315500	0.770600	1.85111	4.13090	11.66365
C	C40	0.875400	0.815500	0.229400	13.00529	10.67750	1.91008
H	H40A	0.877279	0.748957	0.260010	13.03321	9.80624	2.37911
H	H40A	0.122721	0.248957	0.739990	1.82319	3.25964	11.19463
H	H40B	0.180696	0.317769	0.811885	2.68449	4.16061	12.19645
H	H40B	0.819304	0.817769	0.188115	12.17191	10.70721	1.37729
C	C42	0.845700	0.426100	0.452600	12.56406	5.57901	5.41098
C	C42	0.154300	0.926100	0.547400	2.29234	12.12561	8.16275
H	H42A	0.163372	0.851283	0.545038	2.42712	11.14602	8.10938
H	H42A	0.836628	0.351283	0.454962	12.42928	4.59942	5.46435
H	H42B	0.903076	0.442667	0.488916	13.41646	5.79593	5.86468
H	H42B	0.096924	0.942667	0.511084	1.43994	12.34253	7.70905
C	C43	0.851300	0.457500	0.360200	12.64725	5.99014	3.97416
C	C43	0.148700	0.957500	0.639800	2.20915	12.53674	9.59957
H	H43A	0.204769	0.939277	0.676206	3.04213	12.29814	10.05710
H	H43A	0.795231	0.439277	0.323794	11.81427	5.75154	3.51663
H	H43B	0.901900	0.422382	0.338516	13.39899	5.53033	3.54514
H	H43B	0.098100	0.922382	0.661484	1.45741	12.07693	10.02860
H	H43C	0.860484	0.531536	0.357750	12.78369	6.95951	3.91923
H	H43C	0.139516	0.031536	0.642250	2.07271	0.41291	9.65451
C	C18	0.498600	0.822200	0.881500	7.40740	10.76523	12.67873
C	C18	0.501400	0.322200	0.118500	7.44900	4.21863	0.89500
H	H18A	0.505349	0.309546	0.181445	7.50767	4.05295	1.85933
H	H18A	0.494651	0.809546	0.818555	7.34873	10.59955	11.71440
H	H18B	0.440294	0.846505	0.895826	6.54118	11.08346	13.00853
H	H18B	0.559706	0.346505	0.104174	8.31522	4.53686	0.56521
H	H18C	0.514742	0.758730	0.913260	7.64721	9.93420	13.13893
H	H18C	0.485258	0.258730	0.086740	7.20919	3.38760	0.43480

C	C25	0.436000	0.187100	0.525900	6.47739	2.44974	7.30594
C	C25	0.564000	0.687100	0.474100	8.37901	8.99634	6.26779
H	H25A	0.579740	0.759681	0.472536	8.61285	9.94666	6.21432
H	H25A	0.420260	0.259681	0.527464	6.24355	3.40006	7.35942
H	H25B	0.382745	0.147605	0.502753	5.68621	1.93262	7.04785
H	H25B	0.617255	0.647605	0.497247	9.17019	8.47922	6.52588
H	H25C	0.483496	0.177474	0.488386	7.18301	2.32370	6.63833
H	H25C	0.516504	0.677474	0.511614	7.67339	8.87030	6.93540
C	C41	0.126900	0.394500	0.708700	1.88528	5.16527	10.70381
C	C41	0.873100	0.894500	0.291300	12.97112	11.71187	2.86992
H	H41A	0.890457	0.959096	0.266070	13.22898	12.55764	2.44810
H	H41A	0.109543	0.459096	0.733930	1.62741	6.01104	11.12563
H	H41B	0.084858	0.378667	0.656593	1.26068	4.95796	9.97777
H	H41B	0.915142	0.878667	0.343407	13.59572	11.50456	3.59596
H	H41C	0.187977	0.400522	0.692593	2.79266	5.24411	10.34136
H	H41C	0.812023	0.900522	0.307407	12.06374	11.79071	3.23238



Highlighted coordinates used for tilt angle calculation.

Vectors between

O1-O3

$$\begin{pmatrix} -3.40658 \\ -0.95917 \\ -1.9837 \end{pmatrix}$$

N1-N3

$$\begin{pmatrix} -2.88065 \\ -12.55769 \\ -2.92834 \end{pmatrix}$$

Cos(θ)= Dot product of vectors/magnitude of vector1 x magnitude of vector 2

Cos(θ)= 27.66707/(4.057x13.21245237)

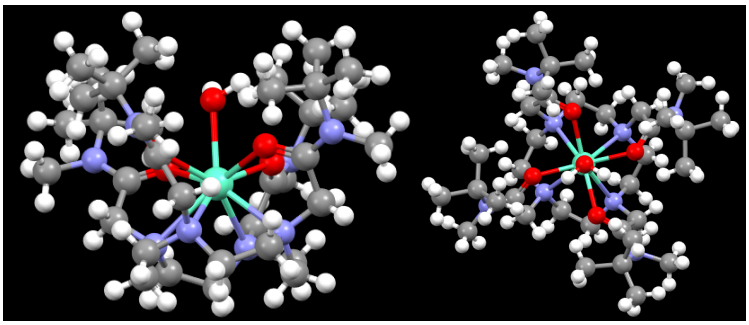
θ = 58.93°

[Eu(DTtBuMA)] $^{3+}$

Crystal Structure

Generated by CrystalMaker X for Windows (http://crystalmaker.com)
Coordinates for "esy_abseu_b"
Unit cell parameters:-
a = 12.93210; b = 13.68360; c = 18.38320 Å
alpha = 84.8780; beta = 75.8570; gamma = 79.2570 °
Listing of all 248 visible atoms:

		Fractional Coordinates			Orthogonal Coordinates [Å]		
Elmt	Label	x	y	z	xor	yor	zor
Eu	Eu1	0.652640	0.728410	0.767720	8.06446	11.32218	17.06525
Eu	Eu1	0.347360	0.271590	0.232280	4.29222	4.44381	5.69944
O	O4	0.498400	0.209900	0.284100	6.15857	3.92581	7.05396
O	O4	0.501600	0.790100	0.715900	6.19811	11.84017	15.71073
O	O2	0.159200	0.325400	0.269200	1.96718	4.77508	5.84933
O	O2	0.840800	0.674600	0.730800	10.38950	10.99091	16.91537
O	O1	0.645600	0.573400	0.719500	7.97747	9.19451	15.96720
O	O1	0.354400	0.426600	0.280500	4.37921	6.57148	6.79749
O	O5	0.288000	0.261600	0.372800	3.55872	4.18080	8.08288
O	O5	0.712000	0.738400	0.627200	8.79796	11.58519	14.68182
H	H5A	0.218237	0.236107	0.392829	2.69669	3.68427	8.19949
H	H5A	0.781763	0.763893	0.607171	9.66000	12.08171	14.56520
H	H5B	0.335958	0.211495	0.398719	4.15133	3.60041	8.64968
H	H5B	0.664042	0.788505	0.601281	8.20536	12.16558	14.11501
O	O3	0.299700	0.112700	0.272700	3.70330	2.17645	6.09779
O	O3	0.700300	0.887300	0.727300	8.65338	13.58954	16.66691
N	N4	0.478100	0.827200	0.857900	5.90773	12.29559	18.29221
N	N4	0.521900	0.172800	0.142100	6.44895	3.47040	4.47248
N	N2	0.250700	0.389300	0.135600	3.09782	5.84151	3.76052
N	N2	0.749300	0.610700	0.864400	9.25886	9.92448	19.00417
N	N5	0.458500	0.520200	0.314300	5.66554	8.06961	7.86213
N	N5	0.541500	0.479800	0.685700	6.69114	7.69637	14.90256
N	N1	0.526300	0.609000	0.855000	6.50332	9.42475	18.12464
N	N1	0.473700	0.391000	0.145000	5.85336	6.34123	4.64005
N	N7	0.172900	0.012500	0.289600	2.13647	0.53985	5.88539
N	N7	0.827100	0.987500	0.710400	10.22021	15.22613	16.87931
C	C8	0.441000	0.659800	0.914700	5.44930	9.93482	19.01464
C	C8	0.559000	0.340200	0.085300	6.90738	5.83117	3.75005
H	H8A	0.528887	0.334598	0.041519	6.53529	5.69047	2.84322
H	H8A	0.471113	0.665402	0.958481	5.82139	10.07552	19.92147
H	H8B	0.382050	0.620100	0.931141	4.72087	9.26777	19.08211
H	H8B	0.617950	0.379900	0.068859	7.63581	6.49822	3.68258
N	N3	0.703000	0.829100	0.865900	8.68675	12.80210	19.15225
N	N3	0.297000	0.170900	0.134100	3.66993	2.96389	3.61244
C	C31	0.428700	0.863200	0.737200	5.29731	12.68066	15.96124
C	C31	0.571300	0.136800	0.262800	7.05937	3.08532	6.80345
C	C3	0.803800	0.670000	0.902500	9.93230	10.84914	19.94923
C	C3	0.196200	0.330000	0.097500	2.42438	4.91684	2.81546



Highlighted coordinates used for tilt angle calculation.
Vectors between
O1-O3

$$\begin{pmatrix} 4.27417 \\ 8.01806 \\ 9.869417 \end{pmatrix}$$

N1-N3

$$\begin{pmatrix} -2.18343 \\ -3.37735 \\ -1.027617 \end{pmatrix}$$

Cos(θ) = Dot product of vectors/magnitude of vector1 x magnitude of vector 2
Cos(θ)= -46.55446 /(13.41504 x 4.15089)
θ = 146^{O} = -33.27^{O}

Appendix III: Unsuccessful reactions

pH probes: unsuccessful synthesis attempts

DO3A-4-acetylpyridine

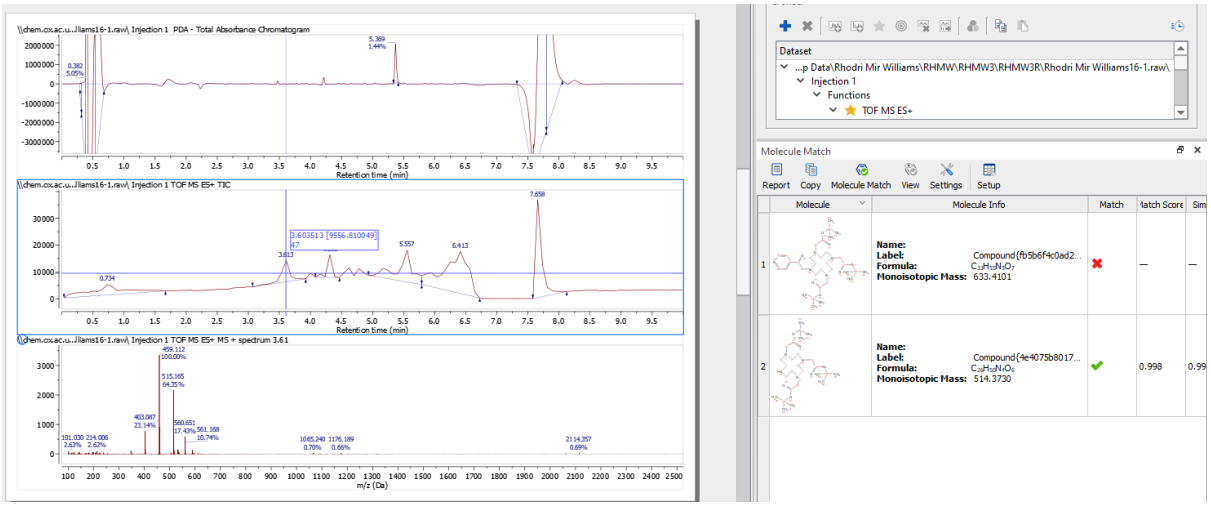
4-(Bromoacetyl) pyridine hydrobromide (0.34 g, 1.21 mmol), DO3A-triester (0.565 g, 1.1 mmol), KI (0.02 g) and Cs_2CO_3 (0.395 g, 1.21 mmol) were dissolved in DMF (5 ml) under nitrogen. The reaction was heated up to 50 ^oC. The reaction was stirred for 24H in total (TLC confirmed reaction had finished 9:1 DCM/EtOH). The mixture was filtered. The solvent was removed until the product was dry. This was then analysed by NMR and HPLC-mass spectrometry. The product was them columned. HPLC-MS showed no extractable amount of product.

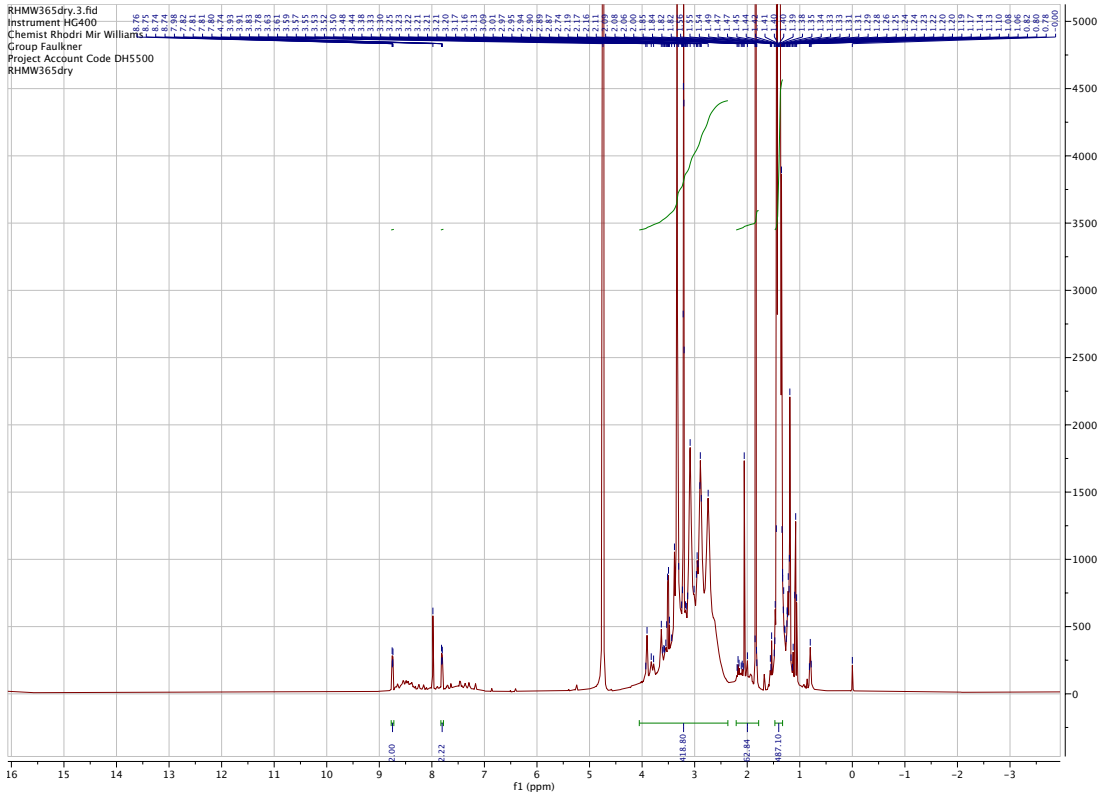
DO3A-4-acetylpyridine

A solution in CH3CN (5 mL) of DO3A(tBu)3 (100 mg, 0.19 mmol), 4-(bromoacetyl)pyridine hydrobromide (60 mg, 0.212 mmol) was left stirring, Cs_2CO_3 (297 mg, 0.96 mmol) . The reaction mixture was stirred for 2 days at 65 ^oC and then filtered, evaporated in vacuo and then purified by silica gel chromatography (99:1 CH_2Cl_2–MeOH) to afford impure DO3A(tBu)4-acetylpyridine.

This was treated as an intermediate and deprotected by stirring in DCM/TFA (1:1, 5 mL) for 12 h. After 12 h, the solvent was evaporated. The product was then dissolved in MeOH and diluted with diethyl ether. This yielded 10 mg of crude product insufficient for HPLC purification.

Crude HPLC-MS and NMR



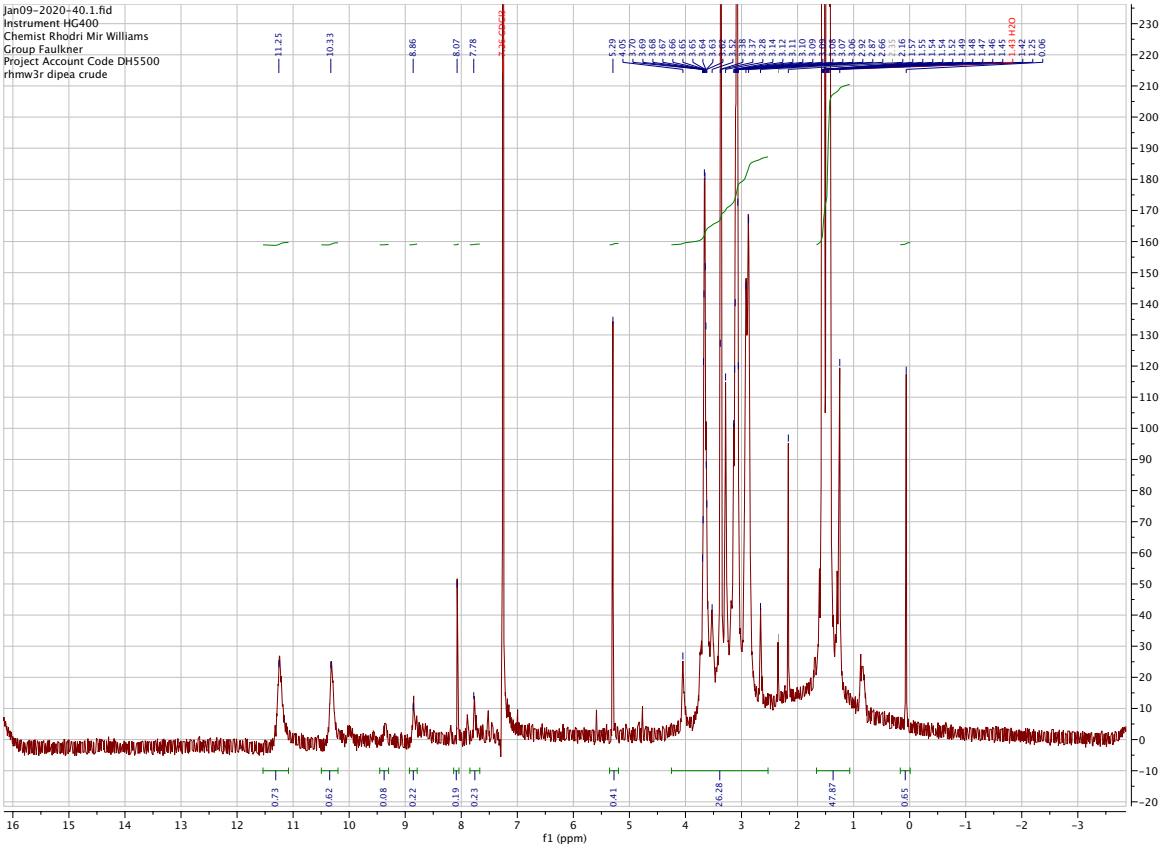


DO3A-4-acetylpyridine

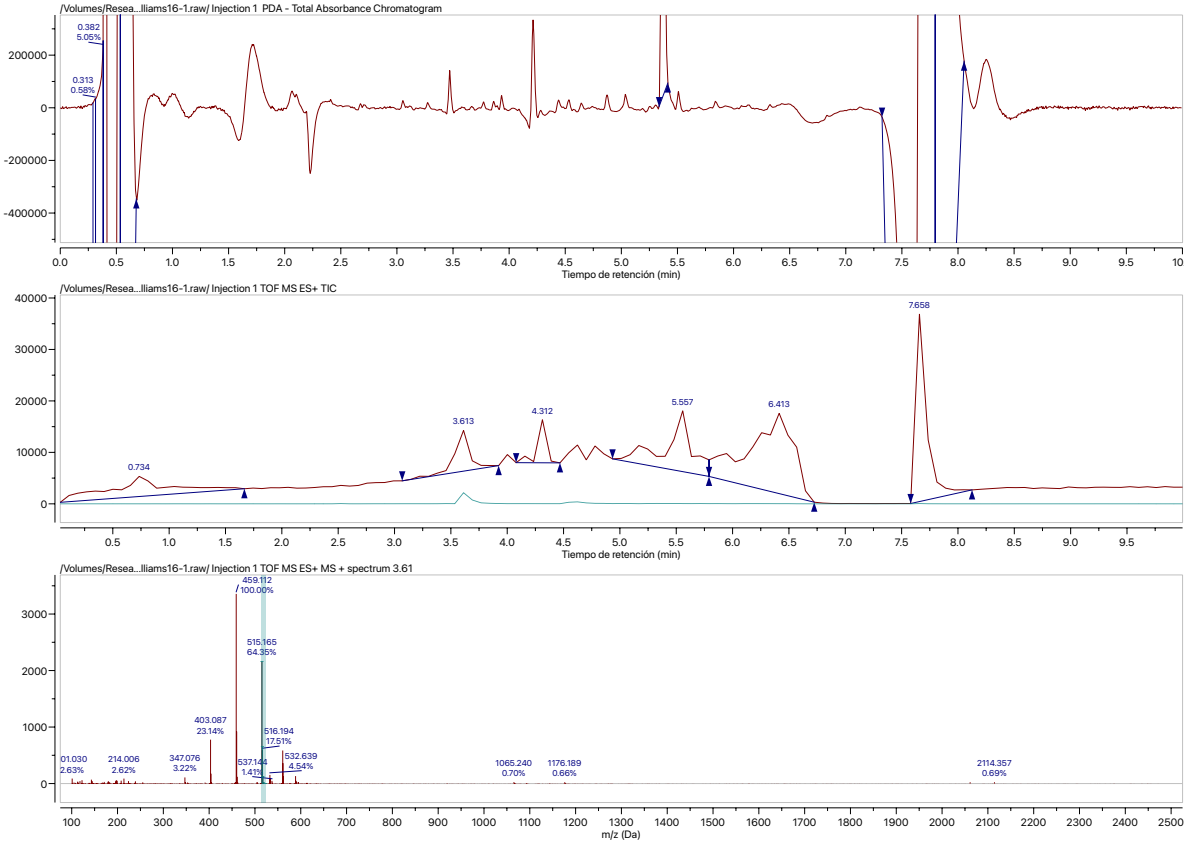
4-(Bromoacetyl)pyridine Hydrobromide (0.065 g, 0.21 mmol), DO3A-triester(0.1 g, 0.194 mmol) and DIPEA (0.1 mL, 0.485 mmol) were dissolved in DMF (2.59 ml) under nitrogen. The reaction was stirred fortnight. The DMF was removed by a column in ACN:H2O (10:0 - 9:1). The sample was submitted to HPLC-MS and NMR presence of product was confirmed

but also the presence of unremoved DMF. It was attempted to remove the DMF by forming an azeotrope with toluene. The toluene was added and removed 4 times. After 40 mins the sample was not DMF free. The sample was then azeotropically evaporated with heptane twice and once more with toluene to yield a dryer sample. HPLC-MS and NMR showed that not much product had been produced and so synthesis was halted.

Crude NMR



Crude HPLC-MS

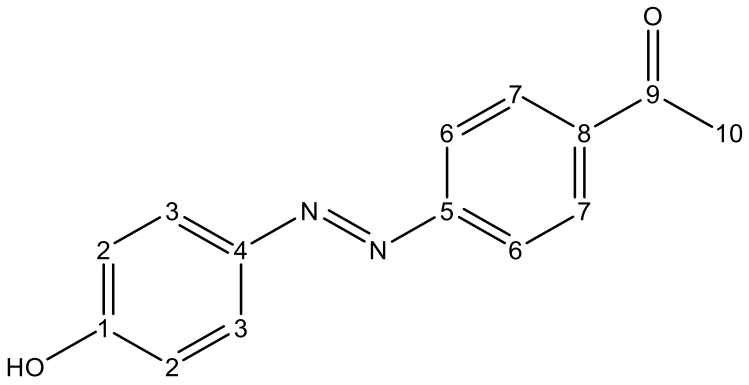


Redox: Attempted ‘arm’ syntheses

The initial part of the synthesis (the azo dye formation) was successful but the attempted brominations were unsuccessful due to over bromination combined with incomplete reaction. Therefore, yields were not recorded.

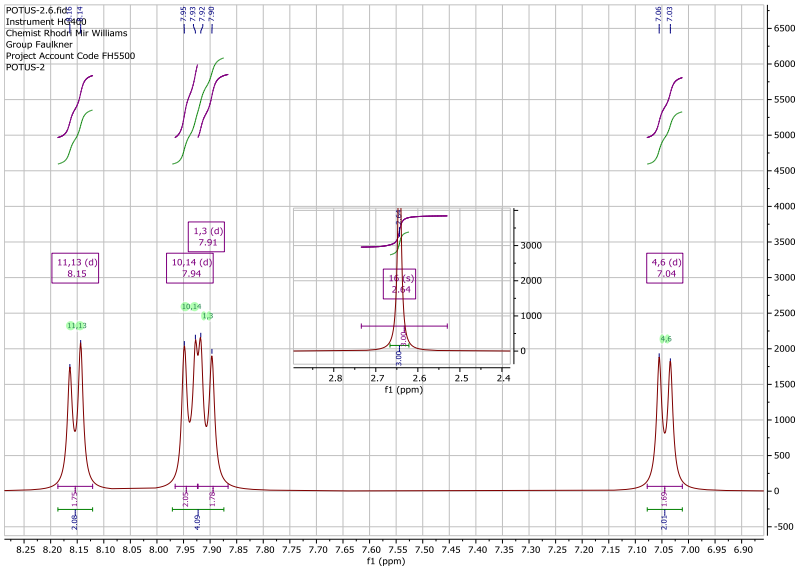
Synthesis of 1-(4-((4-hydroxyphenyl)diazenyl)phenyl)ethan-1-one

To a solution of 4-aminoacetophenone (500 mg, 3.71 mmol, 1 equiv.) in 9.25 mL of distilled water and 1.57 mL of concentrated HCl, was added dropwise (at 0 °C) a solution of KNO2 (0.457 g, 5.37 mmol, 1.45 equiv.) dissolved in 9.25 mL of distilled water. At the same temperature, a solution of sodium hydroxide (192 mg, 4.81 mmol,1.3 equiv.), sodium carbonate (1.76 g, 16.65 mmol, 4.5 equiv.) and phenol (500 mg, 5.3 mmol, 1.44 equiv.) in 9.25 mL of distilled water was added slowly to the resulting diazonium salt solution. The reaction mixture was stirred for 1 hour keeping the solution at 0 °C. The reaction temperature was gradually raised to r.t. The mixture was acidified with concentrated HCl. The product precipitated as a dark red-orange solid. It was filtered and washed with water. The solid was then dissolved into acetone to transfer into a vial and dried in vacuo (890mg, 3.65 mmol, 99%).



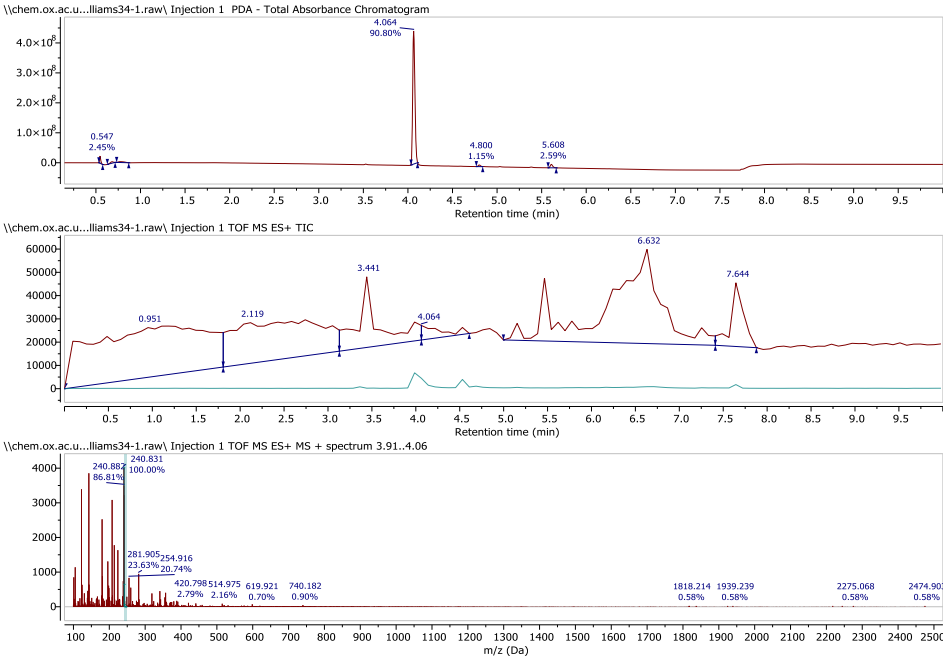
HNMR

δ_H (400 MHz, Acetone-d_6) 8.15 (2 H, d, *J* 8.1, 7), 7.94 (2 H, d, *J* 8.3, 6), 7.91 (2 H, d, *J* 8.4, 3), 7.04 (2 H, d, *J* 8.4, 2), 2.64 (3 H, s, 13).



Mass spectrometry

HPLC-LRMS-$[M-H]^+$ = 240.090 Da (R.T. 4.064 min.)

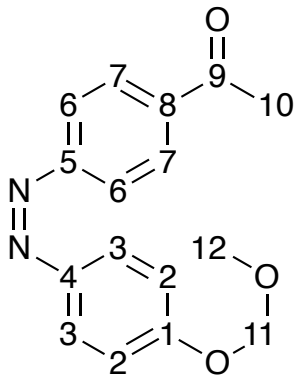


Reference: Applied Surface Science, Vol. 452, 2018, 337-35

MOM protection of OH group (1-(4-((4-(methoxymethoxy)phenyl)diazenyl)phenyl)ethan-1-one)

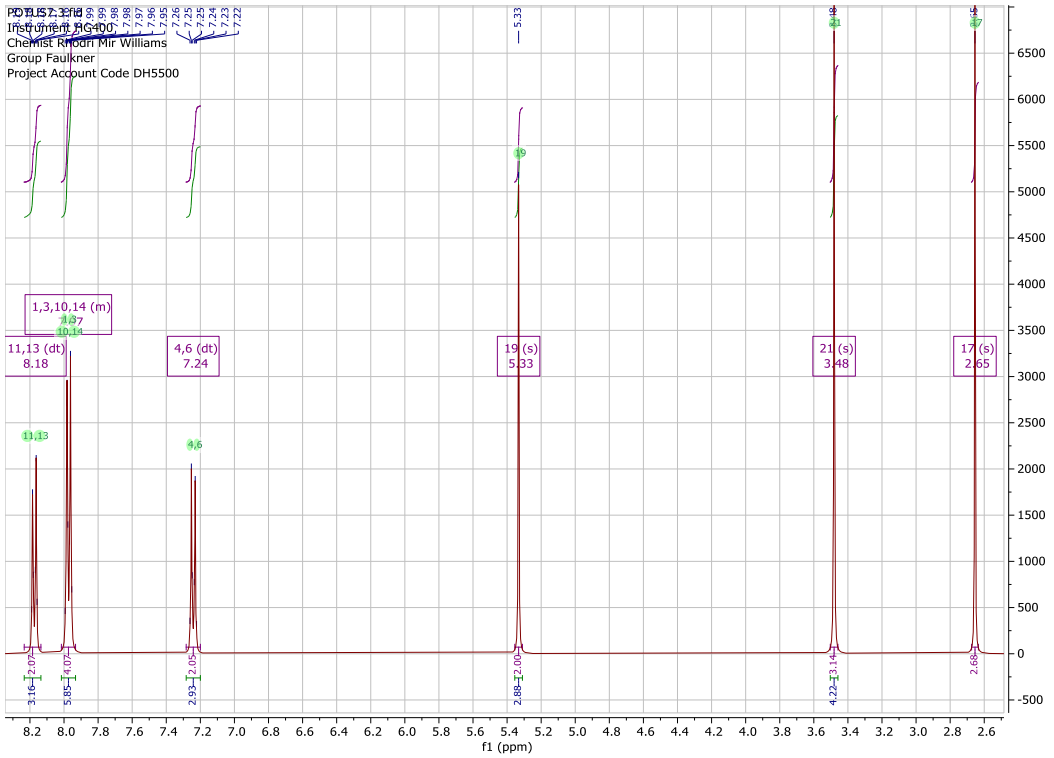
MOMCl (0.05 mL, 51 mg ,0.63 mmol, 1.5 equiv.) was added to a stirred solution of POTUS-2 (100 mg, 0.42 mmol, 1 equiv.) in dry CH_2Cl_2(10 mL) at 0 °C. Diisopropylethyl amine (0.150 mL, 108 mg ,0.84 mmol, 2 equiv.) was slowly added to the reaction mixture. The ice bath was removed, and the mixture was stirred at room temperature for a total of 2h (TLC confirmed reaction was successful). The reaction was diluted with diethyl ether (20 mL) and then washed with brine (3 x 10 mL). The organic phase was concentrated then redissolved in acetone and filtered to remove salt.

The filtrate was concentrated to yield a red solid (95.7 mg, 0.34mmol,80%).



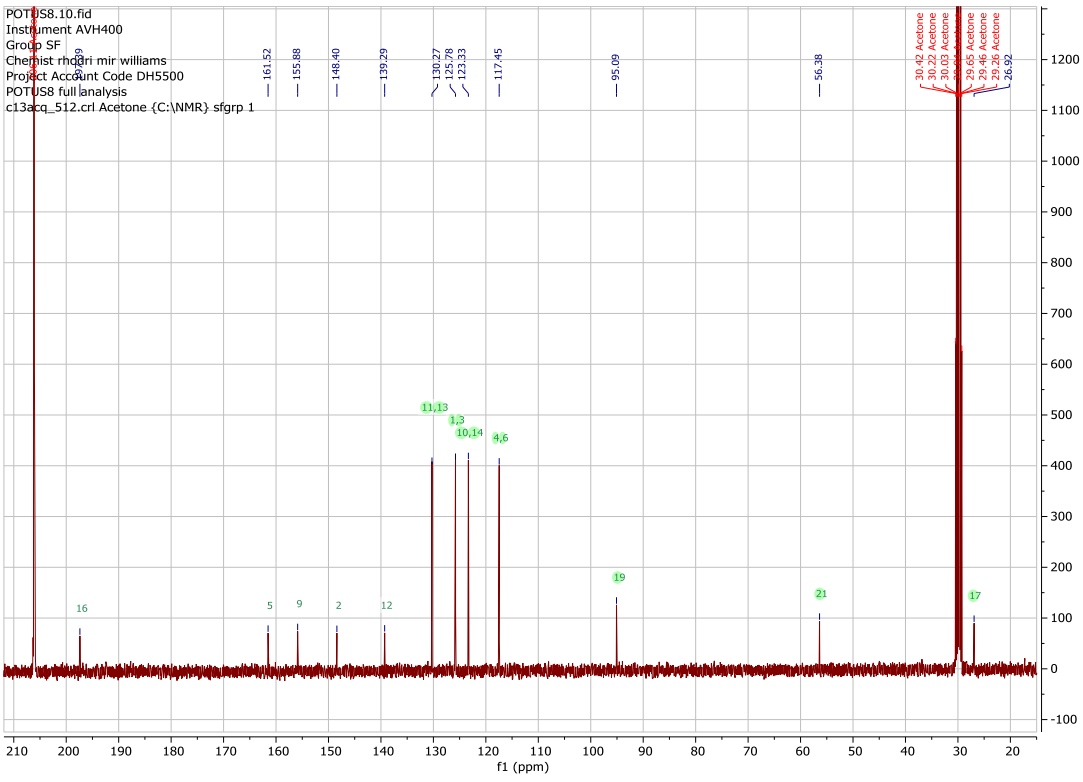
HNMR

δ_H (400 MHz, Acetone) 8.18 (2 H, dt, *J* 8.6, 1.8, 7), 8.02 – 7.93 (4 H, m, 3,6), 7.24 (2 H, dt, *J* 9.0, 2.0, 2), 5.33 (2 H, s, 11), 3.48 (3 H, s, 12), 2.65 (3 H, s, 10).



CNMR

δ_C (101 MHz, Acetone) 197.39 (9), 161.52 (1), 155.88 (5), 148.40 (4), 139.29 (8), 130.27 (7), 125.78 (3), 123.33 (6), 117.45 (2), 95.09 (11), 56.38 (12), 26.92 (10).

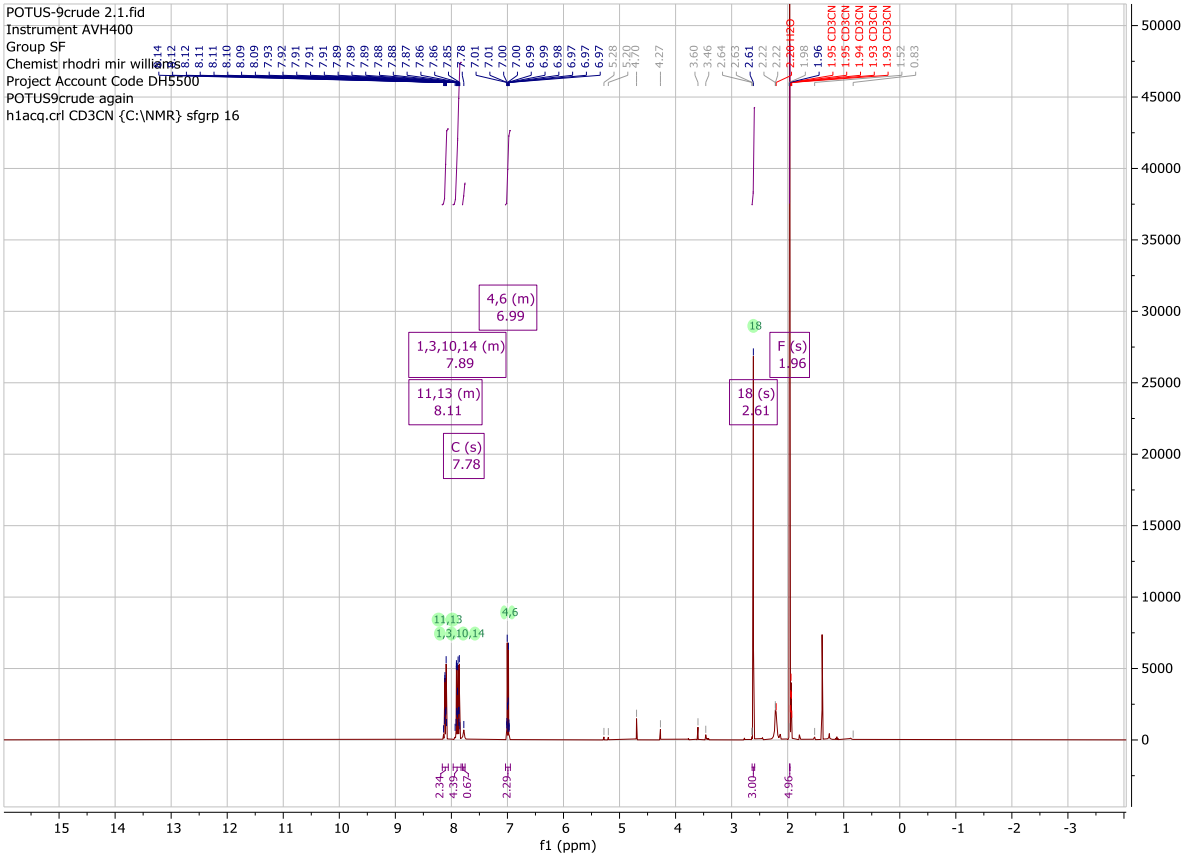


Brominations

Br_2

1-(4-((4-(methoxymethoxy)phenyl)diazenyl)phenyl)ethan-1-one (30 mg, 0.1 mmol, 1 equiv) was dissolved in diethyl ether (0.05 mL) and dioxane (0.026 mL) and the mixture sonicated in an ice bath while Br_2 was added dropwise (5.12 µL, 0.1 mmol, 1 equiv.). The reaction was left stirring at RT monitoring its progression by TLC (Diethyl ether/Pentane, 1:1). TLC showed very little reaction after 3h. The temperature was increased to 40 ^{O}C. After 3 hours TLC still showed a lack of reaction. NMR showed no reaction whatsoever.

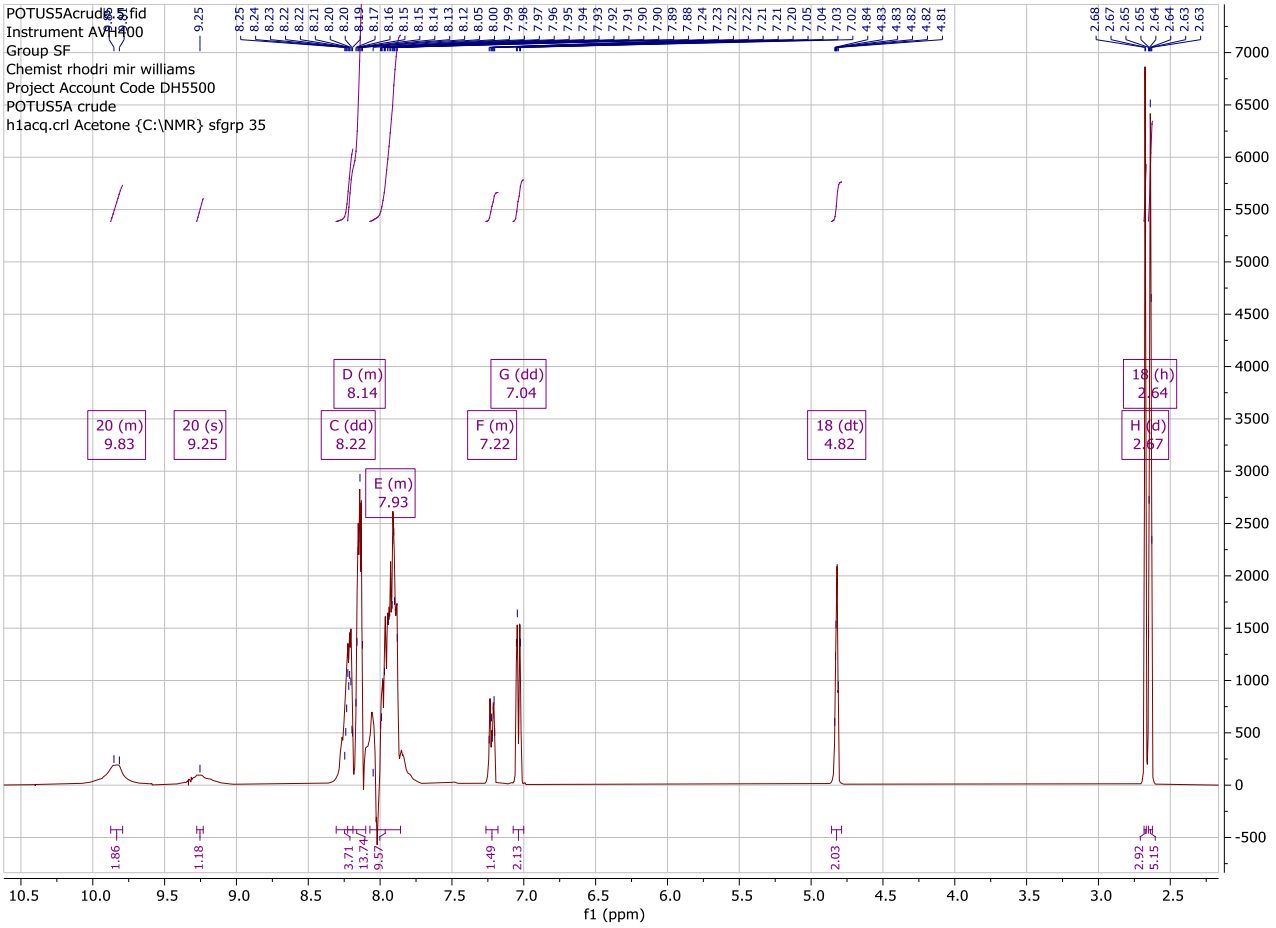
HNMR



NBS-TMS-OTf

1-(4-((4-hydroxyphenyl)diazenyl)phenyl)ethan-1-one (50 mg, 0.207 mmol, 1 eq) was dissolved in acetonitrile and trimethylsilyl trifluoromethanesulfonate (TMS-OTf) (2.05). *N*-bromosuccinimide (NBS) (41 mg, 0.23 mmol, 1.1 eq) was added in portions over 20 minutes. The reaction was stirred at room temperature overnight (monitored by TLC), diluted with diethyl ether (50 mL), washed with H_2O (3 ×7 ml), dried over $MgSO_4$ and concentrated. This yielded of a black oil. NMR of the sample showed that it was a mixture of brominated, dibrominated, some products of self-reaction with the brominated product with and mostly unreacted starting material.

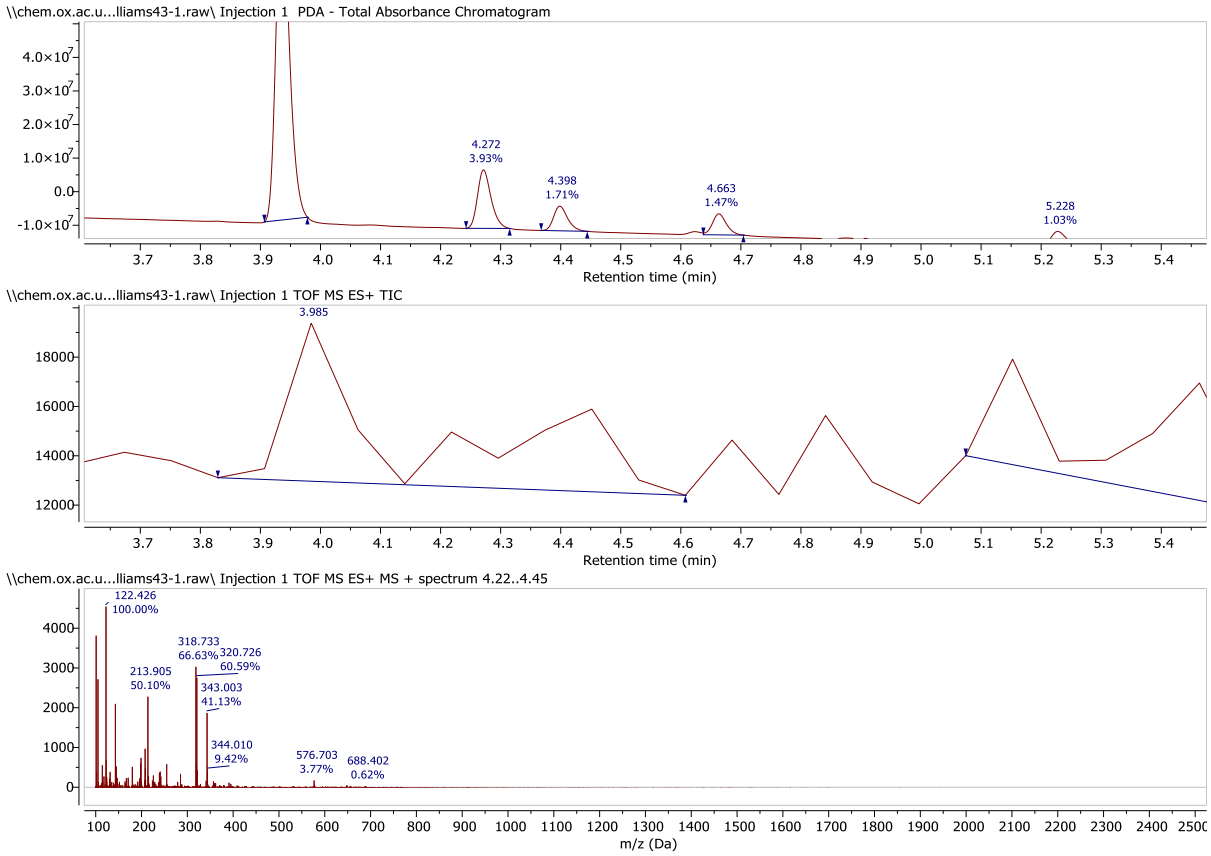
HNMR



$CuBr_2$

1-(4-((4-hydroxyphenyl)diazenyl)phenyl)ethan-1-one (50 mg, 0.21 mmol, 1 equiv.) was dissolved in minimum H_2CCl_2. To this solution, Cu(II)Br_2 (51 mg, 0.23 mmol, 1.1equiv.) was added. The solution was heated to 70 ^oC under a N_2 atmosphere. After 23H glacial acetic acid was added to catalyse. The solid in the flask turned from black to colourless.. The solution was cooled to room temperature. The solid was removed by filtration through a cellite pad and washed with $CHCl_3$. The combined filtrates were concentrated. This yielded 41 mg of crude product and HPLC-MS showed mostly starting material and low amounts of various brominated products.

Mass spectrometry



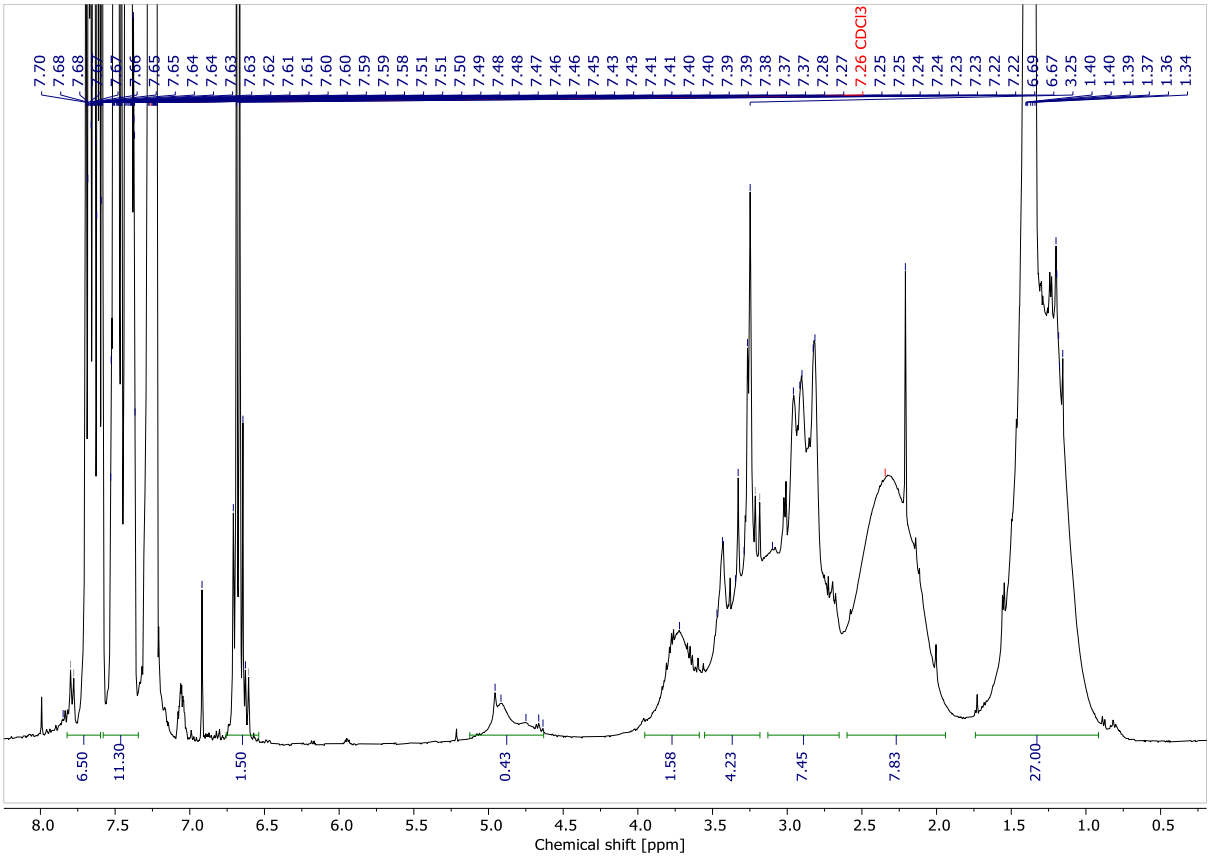
Peaks at 4.727 and 4.398 minutes have $[M-H]^+$ = 318 Da which match up to the values expected for the compound although only 6% of the products from UV chromatograph.

Reductions of azido group

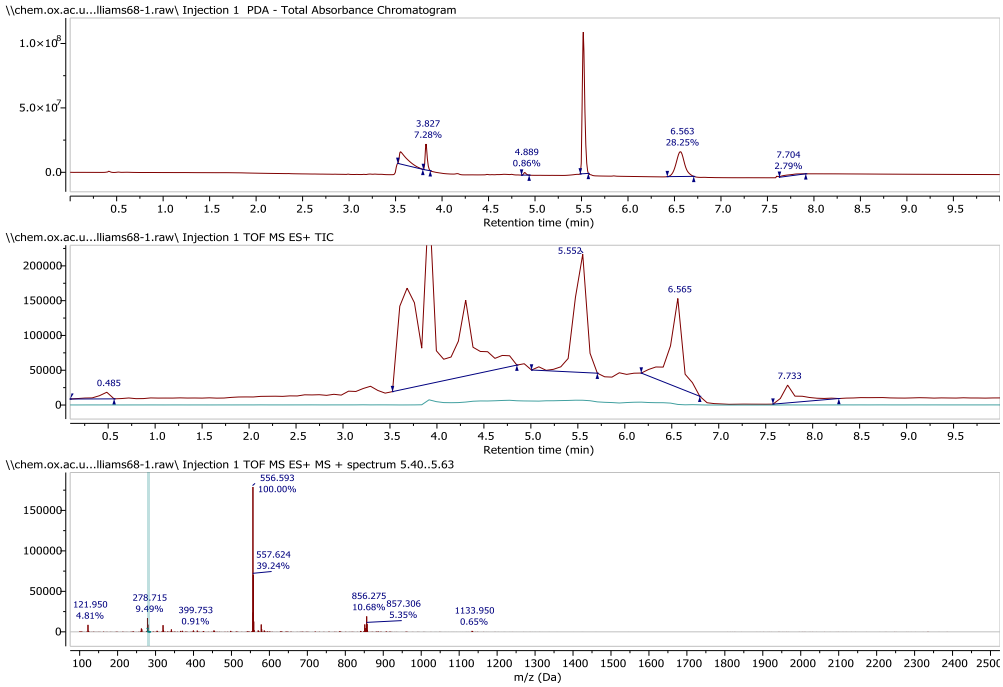
Staudinger reaction

tri-tert-butyl 2,2',2''-(10-(2-(4-azidophenyl)-2-oxoethyl)-1,4,7,10-tetraazacyclododecane-1,4,7-triyl)triacetate (500 mg, 0.84 mmol, 1 equiv.) was dissolved in THF(10 mL) and H2O (11 mL). Triphenylphosphine (264.30 mg, 1 mmol, 1.2 equiv) was added in small portions at room temperature. After stirring at room temperature for 24 h, THF was evaporated under reduced pressure and the remained aqueous phase was extracted with EtOAc (3 x 50 mL). The combined organic layers were dried over anhydrous Na_2SO_4 and concentrated under reduced pressure. This yielded the crude product (644 mg) this was not collected due to doubts on whether the reaction had worked.

NMR



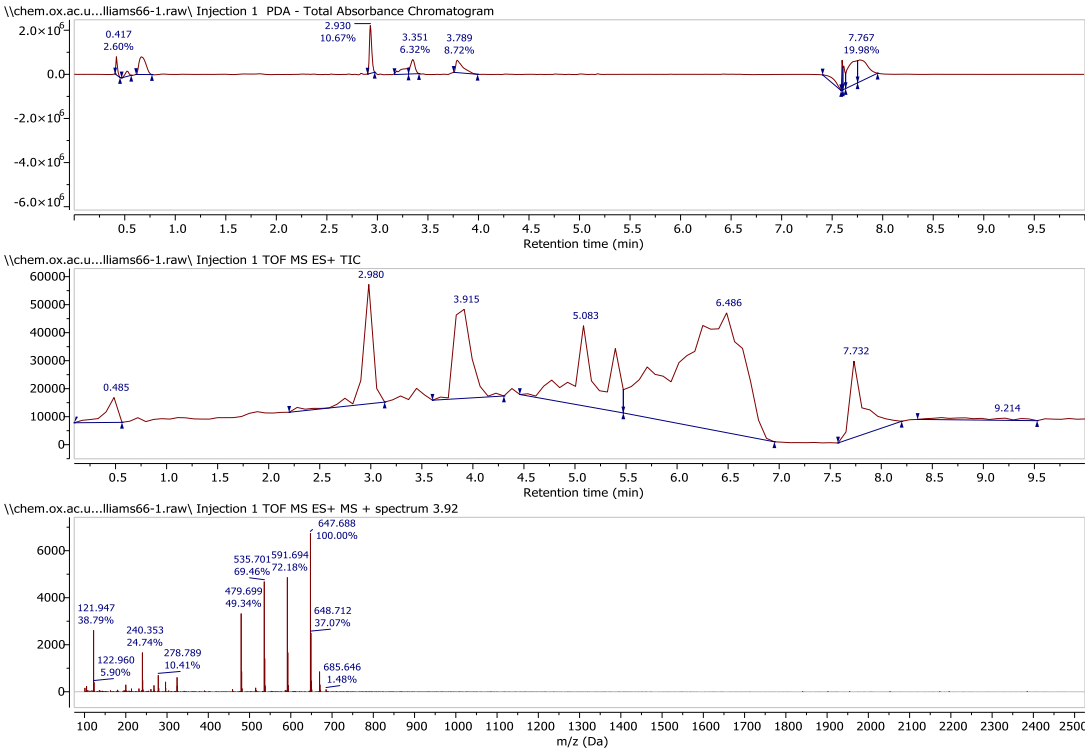
Mass Spectrometry



MS of strongest peak in UV chromatogram shows peak at 556 Da. This corresponds to the synthetic target although this was noted later during the compilation of the experimental section.

Zn, NH_4Cl

To a solution of tri-tert-butyl 2,2',2''-(10-(2-(4-azidophenyl)-2-oxoethyl)-1,4,7,10-tetraazacyclododecane-1,4,7-triyl)triacetate (51 mg, 0.075 mmol) and ammonium chloride (9.36 mg, 0.175mmol) in ethyl alcohol (0.2 mL) and water (0.07 mL), zinc powder (6.55 mg, 0.1 mmol) was added. The mixture was then stirred vigorously at reflux. After the reaction is over (monitored by TLC), ethyl acetate (0.5 mL) and aqueous ammonia (0.003 mL) was added. The mixture was filtered, and the filtrate was washed with brine, dried over anhydrous sodium sulfate. After removal of solvent under reduced pressure, the residue characterised by mass spectrometry which showed some product present but at the time this was misinterpreted and then disposed.



$[M-H]^+$ = 647 Da corresponds to desired product.